UNIVERSITY OF OKLAHOMA

GRADUATE COLLEGE

Disentangling the Formation Pathways of Protostars

A DISSERTATION

SUBMITTED TO THE GRADUATE FACULTY

in partial fulfillment of the requirements for the

Degree of

DOCTOR OF PHILOSOPHY

By

NICKALAS REYNOLDS
Norman, Oklahoma
2023

Disentangling the Formation Pathways of Protostars

A DISSERTATION APPROVED FOR THE
HOMER L. DODGE DEPARTMENT OF PHYSICS AND ASTRONOMY

BY THE COMMITTEE CONSISTING OF

Dr. Nathan Kaib, (Chair)

Dr. Megan Elwood-Madden

Dr. John Tobin

Dr. Howard Baer

Dr. Karen Leighly

To my first mentors, Carol and Sean, who instilled in me the drive to pursue astronomy,

to my husband, Son, who supported and inspired me in this journey,

and to the community of friends and family that help me along the way.

Acknowledgements

I can only begin by expressing my sincere appreciation to my Ph.D. advisor Dr. Nathan Kaib and my research advisor Dr. John J. Tobin. Their combined advocacy, support, and guidance throughout my journey is what allowed me to produce this work, a culmination of seven years of research.

My interest in astronomy started after many years of discussions with my first mentor, Carol Moloney. She first taught me calculus, physics, and after watching many documentaries I was determined to be an astrophysicist. Fast forward to first semester of undergraduate at Clemson University. Dr. Sean Brittain gave a guest lecture during one of the first seminars at CU and it was there I knew I wanted to study star formation. I spent my time learning about YSOs and getting my first experience of research, reducing infrared data.

Four years later I was set to graduate from Clemson and during my search I learned that Dr. John Tobin was joining the University of Oklahoma faculty. I applied for OU and in the summer of 2016, I became Dr. Tobin's first graduate student at OU.

I highly value Dr. Tobin's teachings and patience over the past seven years. I first learned about and reduced radio data under his guidance, and even built my first (and second) radio observatories with him. He has been a great mentor and from the first semester, he has put a lot of effort so I can grow as a scientist. He spent many hours training me on various telescopes and observation techniques from infrared to radio, teaching me how to reduce and interpret the complex products of radio interferometry, and even more hours editing my proposals and

published papers. I see in him the scientist I wish to be and I sincerely look forward to many more years of working together as we puzzle out the physics of star formation.

This work has many collaborators, whose invaluable insights and contributions were critical. In particular Dr. Patrick Sheehan was a great collaborator and peer. He helped perfect my code abilities, make my calculations more statistically rigorous, but also was supportive in my endeavors. For details on each of the collaborations, please refer to the publications noted in the footnotes of Chapters 2-5. The funding for this work was provided by: National Science Foundation grant AST-1814762 to OU.

This research is based on data collected at Atacama Large millimeter/submillimeter Array, a radio interferometer located in Atacama, Chile. ALMA is a partnership of ESO (representing its member states), NSF (USA) and NINS (Japan), together with NRC (Canada), MOST and ASIAA (Taiwan), and KASI (Republic of Korea), in cooperation with the Republic of Chile. The Joint ALMA Observatory is operated by ESO, AUI/NRAO and NAOJ. I also wish to acknowledge the critical importance of the NRAO operators, staff, and employees, who all played vital roles in the observations and data reductions.

I would also like to acknowledge the custodial, administrative, and IT staff in the Homer L. Dodge Department of Physics and Astronomy, in particular Cynthia Pack and Jennifer Absha-gen who provided constant assistance throughout the years. The success of the department is dependent upon the care, time, effort that the staff devote to keeping our buildings clean and computers operational.

The supercomputing for this work was largely performed at the OU Supercomputing Center for Education & Research (OSCER). I thank all the support staff but in particular Dr. Henry

Newman, Dr. Soumya Bhattacharya, and Dr. Horst Severini for their time and expertise.

This research was enabled, in no small part, by the efforts of countless software developers who tirelessly and selflessly provide and maintain tools for the public. This includes, but is not limited to, the developers of the following tools: Python (Van Rossum & Drake Jr, 1995), NumPy (Harris et al., 2020), SciPy (Virtanen et al., 2020), emcee (Foreman-Mackey et al., 2013), dynesty (Speagle, 2020), Matplotlib (Hunter, 2007), Astropy (Astropy Collaboration et al., 2013; Price-Whelan et al., 2018), and CASA (McMullin et al., 2007).

Long before OU was established, the land on which the University now resides was the traditional home of the "Hasinais" Caddo Nation and "Kirikiris" Wichita & Affiliated Tribes. We acknowledge this territory once also served as a hunting ground, trade exchange point, and migration route for the Apache, Comanche, Kiowa and Osage nations. Today, 39 tribal nations dwell in the state of Oklahoma as a result of settler and colonial policies that were designed to assimilate Native people.

OU recognizes the historical connection our university has with its Indigenous community. We acknowledge, honor and respect the diverse Indigenous peoples connected to this land. We fully recognize, support and advocate for the sovereign rights of all of Oklahoma's 39 tribal nations. This acknowledgement is aligned with our university's core value of creating a diverse and inclusive community. It is an institutional responsibility to recognize and acknowledge the people, culture and history that make up our entire OU Community.

Table of Contents

Abstract

The aim of this dissertation is to characterize the first stages of star formation, particularly the youngest systems forming multiple stars. Recent studies of star-forming regions and field stars in the Milky Way galaxy have shown more than half of all stars form with companion stars. However, despite these surveys, the relevance and importance of the various formation processes and exact evolution paths are not clear. To do so, I observe several protostellar systems, some that are forming multiples and others that are single protostars in order to disentangle the formation processes. I present high resolution and high sensitivity observations towards each of these systems and undertake rigorous modeling to estimate the physical parameters.

First, in Chapter 2, I discuss the radio observations of L1448 IRS3B/A, a protostellar system with multiple protostars in the Perseus molecular cloud. I resolve the disk and spirals of L1448 IRS3B and estimate the total dynamical mass of the system as constrained by the dust observations ($\sim$0.3 $M_\odot$) against the gravitational potential mass ($\sim$1.1 $M_\odot$). I find the protostellar companions embedded within the massive disk are likely formed in-situ via gravitational instabilities, while the tertiary companion, L1448 IRS3A likely formed via tubulent fragmentation from the parent cloud.

Secondly, in Chapter 3, I observe the nearly edge-on, isolated protostar BHR7-mms, in an effort to characterize the kinematics of the system at the scales of the circumstellar disk. After performing rigorous modeling, I confirm the disk is in Keplerian rotation, consistent with a central potential mass of $\sim$1.17 $M_\odot$. I also estimate the mass of the circumstellar disk to be

$\sim$0.24 $M_\odot$ and find the disk is likely marginally gravitationally unstable.

Thirdly, in Chapter 4, I return to BHR7-mms, to link the full transfer of angular momentum from the scales of the core (d$\sim$0.1 pc) down to the disk. The processes by which angular momentum can be efficiently liberated from the system after infall from large scales is not well understood and I propose ways to trace the motions from the envelope down to the disk.

Next, in Chapter 5, I undertake a high resolution continuum survey of twelve known protostellar systems in Perseus to observe the relative orientation vectors of the compact circumstellar disk as compared to the binary orbital inclinations. This method is theorized to be the best proxy for the angular momentum of the protostar and should save the signature of their formation mechanism. These systems are known to have formed companions but prior observations had insufficient sensitivity or resolution to discern the kinematics. I find this particular sample is consistent with gravitational instability and turbulent fragmentation pathways and detail statistical tests performed to determine the formation mechanism.

Finally, in Chapter 6, I summarize the findings of my collection of works and contributions to the field of multiple-star formation. I also explore the ongoing works and future studies that are being conducted as a direct result of these findings. These findings can directly inform theoretical hydrodynamical simulations of protostar formation and prompt further, large-scale high-resolution surveys of protostar clusters.

List of Publications

This dissertation comes from the following works:

- *"Kinematic Analysis of a Protostellar Multiple System: Measuring the Protostar Masses and Assessing Gravitational Instability in the Disks of L1448 IRS3B and L1448 IRS3A"*

  Reynolds, N. K., Tobin, J. J., Sheehan, P. D., Sadavoy, S. I., Kratter, K. M., Li, Z., Chandler, C. J., Segura-Cox, D., Looney, L. W., Dunham, M. M., 2021 ApJL, 907, L10,

- *"Investigating the Isolated Protostar BHR7-mms. I. Characterizing the Keplerian Disk"*

  Reynolds, N. K., Tobin, J. J., Bos, S., Dunham, M., Bourke, T., van der Marel, N., Kratter, K. M., Sheehan, P. D., Looney, L. W., Sadavoy, S. M., Segura-Cox, D., van't Hoff, M., Chen, C., and Li, Z., 2023 in subm.a,

- *"Investigating the Isolated Protostar BHR7-mms. II. Coupling of Infall and Keplerian Kinematics"*

  Reynolds, N. K., Tobin, J. J., Bos, S., Dunham, M., Bourke, T., van der Marel, N., Kratter, K. M., Sheehan, P. D., Looney, L. W., Sadavoy, S. M., Segura-Cox, D., van't Hoff, M., Chen, C., and Li, Z., 2023 in subm.b,

- *"The Disk Orientations of Perseus Protostellar Multiples at ∼8 au Resolution"*

  Reynolds, N. K., Tobin, J. J., Kratter, K. M., Sheehan, P. D., Looney, L. W., Sadavoy, S. I., Segura-Cox, D., Kaib, N., Li, Z., 2023 in subm.c,

and other publications related to this dissertation:

- *"Disks and Outflows in the Intermediate-mass Star-forming Region NGC 2071 IR"*

  Cheng, Yu , Tobin, John J. , Yang, Yao-Lun , van't Hoff, Merel L. R. , Sadavoy, Sarah I. , Osorio, Mayra , Díaz-Rodríguez, Ana Karla , Anglada, Guillem , Karnath, Nicole , Sheehan, Patrick D. , Li, Zhi-Yun , **Reynolds, N. K.** and 4 authors, 2022 ApJ, 933, 178.

- *"The VLA/ALMA Nascent Disk and Multiplicity (VANDAM) Survey of Orion Protostars. A Statistical Characterization of Class 0 and I Proto- stellar Disks"*

  Tobin, J. J., Sheehan, P., Megeath, S. T., Diaz-Rodriguez, A. K., Offner, S. S. R., Murillo,

N. M., van't Hoff, M., van Dishoeck, E. F.,Osorio, M., Anglada, G., Furlan, E., Stutz, A. M., **Reynolds, N. K.** and 23 authors, 2020, ApJ, 890, 130.

- *"The VLA/ALMA Nascent Disk and Multiplicity (VANDAM) Survey of Orion Protostars IV. Unveiling the Embedded Intermediate-Mass Protostar and Disk within OMC2-FIR3/HOPS-370"*

  Tobin, J. J., Sheehan, P., **Reynolds, N. K.** and 13 authors, 2020, ApJ 933, 178.

- *"Detection of Irregular, Sub-mm Opaque Structures in the Orion Molecular Clouds: Protostars within 10000 years of formation?"*

  Karnath, N., Megeath, S. T., Tobin, J. J., Stutz, A., Li, Z. Y., Sheehan, P., **Reynolds, N. K.** and 6 authors, 2020, ApJ, 890, 129.

- *"The VLA/ALMA Nascent Disk and Multiplicity (VANDAM) Survey of Orion Protostars. I. Identifying and Characterizing the Protostellar Content of the OMC2-FIR4 and OMC2-FIR3 Regions"*

  Tobin, J. J., Megeath, S. T., van't Hoff, M., Diaz-Rodriguez, A. K., **Reynolds, N. K.** and 29 authors, 2019, ApJ, 886, 6.

Chapter 1

Introduction

1.1. Prelude

What is a planet and how did the planets in our Solar system form? How did the Sun form? What are our origins in the universe? These are the basic questions that have driven people since we first looked up in the sky. The first known astronomers were found in ancient Babylonia and despite the simplicity of the time, they were the first to use mathematical models to predict the movements of celestial bodies, predicting and observing the motions of Venus. Other records indicate similar, independent developments happened across the globe; in China they made detailed star catalogues prior to 400 BCE, even recording the first observed supernova (SN185) and in India, they mathematically detailed the precession of Earth's equinoxes. For we all stand upon the shoulders of giants.

1.2. Formation of Stars

Most stars form in massive (M$\sim 10^{5-6}$ M$_\odot$, size$\sim$50 pc; Lynds, 1962; Myers et al., 1983; Clemens & Barvainis, 1988; Williams & McKee, 1997; Lee & Myers, 1999) complexes of dust and gas called molecular clouds. These clouds are predominately composed of molecular hydrogen (H_2) with only a small fraction contained within icy dust particles (gas to dust ratio, of 100:1 Bohlin, 1975; Spitzer & Jenkins, 1975; Bohlin et al., 1978a; Lombardi et al., 2014a,b; Liseau et al., 2015). These clouds are cold and dense (T$\approx$10-20 K, $\langle n_{H_2} \rangle \approx 10^5$ cm^{-3}; Wilson et al., 1997; Ward-Thompson et al., 1994). The dust particles are often made of carbonaceous materials and simple silicates, initially forming μm-sized solid surfaces. These dust grains influence the ISM thermal properties by the efficient absorption and thermal reprocessing of stellar light. Additionally, in more shielded environments, these grains provide surfaces for gas phase molecules to deposit. D'Hendecourt et al. (1985); Hasegawa et al. (1992) found abundances of H_2O to be $\sim 10^{-8}$ in local, cold molecular clouds and because of the inefficiency of the gas phase chemical routes, the use of grain surface chemistry is required to explain the

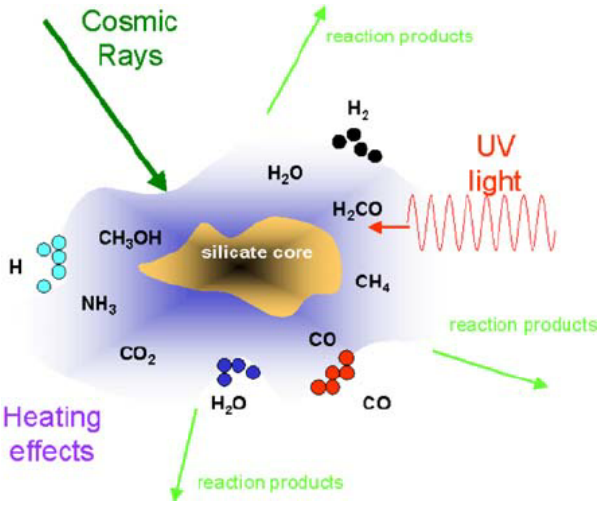

Figure 1.1: : Build up of ice layers on the surface of amorphous dust grains. As the cold gas in the ISM-like environment pass over the silicate and carbonaceous core dust grains, ices form on the surface, causing the grain to form a "sticky" mantle. This mantle grows in mass and ability to collect additional ices. These molecules, subject to external radiation fields and heating, form surfaces by which complex chemistry can occur. *image credit Srama et al. (2009b)

observations. In cold (T$\leq$20 K) environments, gases (H_2,He_2, OH, CO, NH_3) can accumulate on these grains in the form of ice (Frerking et al., 1982; Papoular, 2005) where H_2, HD, and D_2 can form the first layers on the grains (Cazaux et al., 2008). Once the first layer is formed, the mantle becomes more conducive, providing a "sticky" surface (Figure 1.1) by which additional reagents can more easily deposit (Papoular, 2005). These icy mantles, which are sensitive to hard photons, are thought to play a critical role in the creation of complex molecules found in the ISM. Once in contact with hard photons, like that of UV and x-rays from nearby O&B type stars, (Herbst & Klemperer, 1973), molecules can be liberated or provided with an energy kick to ionize without destroying the grain (see sputtering). These reactants can then chemically interact with surrounding material, including re-depositing onto the mantle, forming new products. It is thought via these processes, that organic molecules which are found in the Solar system, e.g. simple hydrocarbons (CH_4, C_2H_2, C_2H_4), including complex amines and ethers (CH_3NH_2, NH_2CHO, CH_3OCH_3, $CH_3OC_2H_5$), up to chained 12+ component species, are formed (Müller et al., 2001, 2005; Srama et al., 2009a; Endres et al., 2016).

The molecular clouds by which stars (and eventually planets) form are cold (few 10s of K) and dense (10^4-10^6 particles cm^{-3} Ward-Thompson et al., 1994; Bergin & Tafalla, 2007). However, molecular clouds can vary greatly in physical and chemical properties, both in terms of the

cloud-to-cloud comparison but also vary greatly across the cloud complex (Ward-Thompson et al., 2007).

Even the low mass molecular clouds (M$\sim$100s of $M_{\odot}$) are observed to form filamentary structures (Bally et al., 1987; di Francesco et al., 2007; Myers, 2009; André et al., 2010; Molinari et al., 2010; Kirk et al., 2013; Li et al., 2016), in which overdensities occur and prestellar cores begin to condense (Andre et al., 1993; Lada & Lada, 2003; André et al., 2014). At this stage, pressure, turbulence, self-gravity, and magnetic fields heavily influence the structure of the clouds (Crutcher, 1999; McKee & Ostriker, 2007; Kim & Ostriker, 2007; Boss & Keiser, 2013; Inutsuka et al., 2015) and eventually these clouds undergo localized regions of anisotropic collapse along the filament (Williams & McKee, 1997). Fundamentally, the molecular cloud filament is the locus of mass flow along a local minima in the aggregate potentials for the region (Lin et al., 1965).

The collapse of protostars quickly becomes a form of "tug-of-war" between the rapid spin-up of the protostar from infalling material and effects that efficiently dissipate angular momentum. It is known the protostellar environment harbors magnetic fields, yet ideal magnetic-hydrodynamics is not a good approximation for the formation of protostars as even moderate magnetic fields completely suppress the formation of rotationally supported disks (Mellon & Li, 2008). Additional effects may contribute to reducing the efficiency of angular momentum dissipation via magnetic field interactions. It is expected from simulations and observations that non-ideal magnetic effects such as the Hall effect, Ohmic diffusion, and ambipolar diffusion may play important roles to reduce the efficiency of angular momentum dissipation Tsukamoto et al. (2015). The exact weighted importance of turbulence, gravity, and magnetic field potentials is still being explored.

The collapse of a core is defined by the Jeans criteria, which define the internal thermal motions' support against the self gravity of the cloud. This requires cold and dense structures, such that when the cloud breaks equilibrium, due to a localized region of density that exceeds the Jeans criteria, the cloud undergoes collapse. However, this process of star formation is not very efficient (SFE), with $<$5% of the molecular cloud mass being converted into stars (Alves et al., 2007); yet these clouds can coalesce to form optically thick, dense cores, whose SFE can reach $\sim$30% (Evans et al., 2009; Offner & Arce, 2014).

As these optically thick cores form, the local pressures and temperatures increase, halting the infall into so-called First Hydrostatic Stellar Core (FHSC). These optically thick regions continue to increase in temperature from the prior collapse, until the H_2 dissociates (T$\sim$2000 K), leading to further collapse until the thermal pressures and gravitational pressures stabilize, resulting in the second hydrostatic core. Thus the protostar forms (Larson, 1969). As the remaining cloud collapses around the protostar, due to the conservation of angular momentum, a rotationally supported disk (RSD) forms (Section 1.3.2.1). RSDs have been frequently observed around YSOs (Williams & Cieza, 2011), including in deeply embedded Class 0/I sources (Tobin et al., 2012, 2013).

1.3. Protostar Characteristics

Protostars have been extensively studied for decades and a common classification, dubbed "Classes 0-III", has been established (Lada, 1987; Andre et al., 1993). These classes describe the observed characteristics of the protostars and are thought to describe the evolutionary path of the protostars. It also stands to reason that the protostars should follow an evolutionary path, beginning with characteristics similar to the Interstellar Medium (ISM) and ending with characteristics like that of field stars, open clusters, or our Solar System.

1.3.1. Classification Techniques of Protostars

With high resolution and sensitivity instruments from recent space and ground based facilities spanning optical to radio wavelengths, we can begin to accurately classify these young stellar objects.

The first method of defining the classes was based on multi-wavelength observations of the spectral energy distribution (SED) (a measure of source brightness as a function of wavelength or frequency). (Lada & Wilking, 1984) categorized the classes corresponding to the spectral index at infrared wavelengths, defined as

$$\alpha_\lambda = \frac{dlog\lambda F_\lambda}{dlog\lambda}, \tag{1.1}$$

for λ =2-25 μm, (Lada, 1987). These α_λ values correspond to physically different systems, with the steep positive slopes indicating cold, dust grains and the increasingly negative slopes

indicating less photon reprocessing (less intervening dust). Class I sources are defined as having $0 < \alpha_\lambda \leq 3$, Class II $-2 < \alpha_\lambda \leq 0$, and the bluest, most evolved sources Class III $-3 < \alpha_\lambda \leq -2$. Andre et al. (1993) discovered an even redder type of source and dubbed Class 0 and a new classification technique was employed to categorize the Class 0 from the Class I objects via the ratio of the submillimeter luminosity ($0.35\ mm < \lambda < 1\ mm$) to the total luminosity, with Class 0 sources having an $L_{submm}/L_{bol} \geq 0.5\%$, indicating a large amount of small, cold dust emission. Myers & Ladd (1993) offered another parameter to classify the sources based on the SED, T_{bol}, which is the temperature of a black body with the same flux-weighted mean frequency as the observed SED (see also Chen et al., 1995a; Myers et al., 1998). However, T_{bol} is subject to degeneracies in viewing angle inclination and models by Young & Evans (2005) and Dunham et al. (2010) suggest L_{bol}/L_{submm} is better evolutionary tracers.

It is now understood that each of the classes corresponding to a particular evolutionary state of the protostar, an illustration is provided in Figure 1.2. For the purpose of this dissertation, I focus on Class 0 and Class I protostars, which directly seed the next stages of protostar evolution and the formation of planets which occurs in the disks.

Class 0

Class 0 protostellar sources are deeply embedded within the molecular clouds and their cores, and the mass of the surrounding envelope dominates the system as evident by the excess in very-far-infrared and submillimeter continuum emission (Andre et al., 1993). The sources typically feature prominent outflows and high velocity ($v > 30$ km s^{-1}) bipolar jets that reach separations of $\sim$10s of thousands of au. As the envelope infalls towards the protostar, the conservation of angular momentum causes a spin up and flattening along the plane orthogonal to the angular momentum rotation axis, into a disk (Terebey et al., 1984; Bodenheimer et al., 1990). These structures have been observationally confirmed (Tobin et al., 2012; Dunham et al., 2014; Maury et al., 2019), but the rotation rates (assuming conservation of angular momentum) are slower than expected. Simulations have shown that magnetic braking due to the compression of the magnetic fields is thought to assist with the dispersal of angular momentum (Allen et al., 2003b,a; Allen, 2004), but due to the high efficiency to transport angular momentum, either do not produce rotationally supported disks or produce disks much smaller

than observed (Mellon & Li, 2008). Many non-ideal MHD effects can be applied which can act to modify the efficiency of angular momentum transport in disks; such as outflows carrying away the magnetic field (Dapp et al., 2012) and Ohmic dissipation (Nakano et al., 2002)

Another facet of Class 0 protostars is luminosity excess, with a majority of the luminosity stemming from accretion onto the surface of the protostar from the disk. The disk accretion rates as derived from the accretion luminosity ($\dot{M}$ $>10^{-5}$-10^{-7} $M_{\odot}$ yr^{-1}; Tobin et al., 2012; Reynolds et al., 2021) are the highest at this stage as the central mass of the protostar and disk grow the fastest. This accretion rate is also thought to be variable, with some periods of enhanced accretion expected to appear as outburst and increased volumetric knots along the poles due to enhanced outflow rate (Safron et al., 2015; Plunkett et al., 2015).

Class I

At the Class I stage, the young stellar object has evolved, accreting significant amounts of the mass from the envelope into the protostar and disk, but still surrounded by an infalling envelope, changing the shape of the SED. The outflows, which entrain the slower moving circumstellar material, work to disperse the envelope, forming a cavity and slowing the accretion of material Arce & Sargent (2006); Offner & Arce (2014). At this stage, the outflows would be less prominent, due to interactions with the surrounding material and reduction of accretion. By the end of the Class I stage, the envelope will be entirely evacuated and the disk will have significantly accreted onto the protostars. The protostars will also be exposed at the end of this stage, with significant hot radiation from the protostar present in the SED.

Class II+

Beyond the Class I stage, the so-called Class II, and III, solid and gas exo-planets have been directly observed to have formed and already undergone significant evolution (Keppler et al., 2018; Müller et al., 2018; Currie et al., 2022; Pinte et al., 2023). Thus it is likely the planets have at least begun their formation, prior to the Class II stage, when the disk is still massive. While there have been many studies of Class II protostars that have shown features indicative of planets/companions (rings, spirals, gaps, asymetries, warps; Andrews et al., 2018; Jennings et al., 2022a,b, respectively), to date no direct observations of planets have been confirmed within the disks of Class 0 protostars. There is a growing body evidence that disk substructure

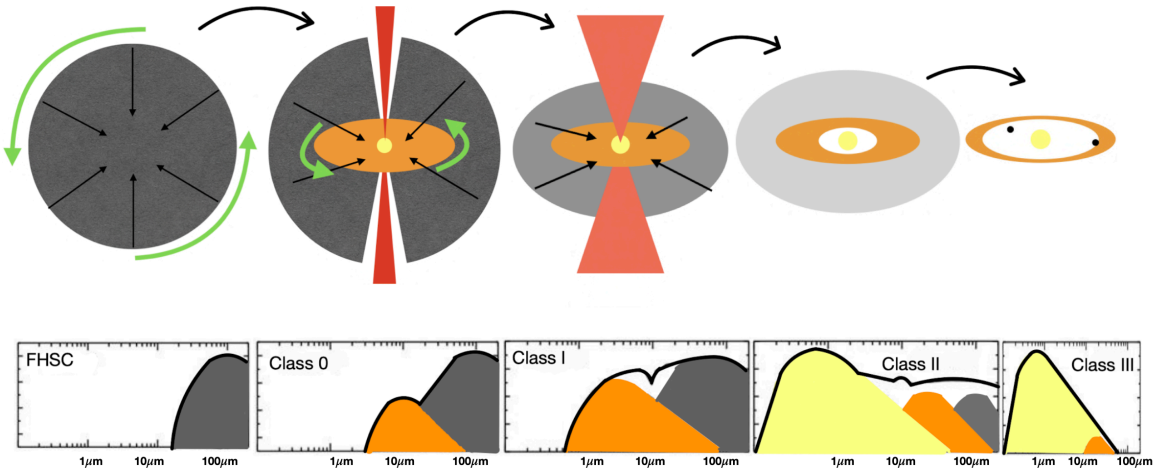

Figure 1.2: : Illustration of the various evolutionary stages of protostars, from Class 0 to III. Class 0 protostars are heavily embedded in an envelope shown in black and the SED is dominated by cold, dense dust grains. The class I sources have a less massive envelope than the Class 0 and the disk is flatter, but both still dominate the SED. By the Class II stage, the so-called protoplanetary and debris disk stage, much of the mass has been accreted to the protostar, whose light is now less shielded by the disk and envelope. The outflows are less energetic. In the Class III stage, the disk would have either fully accreted to the protostar or the material locked into planets/planetesimals. (M_{disk} ~1%; Andrews et al., 2018).

could signify the existence of proto-planets forming (Sheehan & Eisner, 2017a; Fedele et al., 2018; Pinte et al., 2019a; Segura-Cox et al., 2020, Yamamoto et al., 2023 sub.).

1.3.2. Multiplicity

While the above scenarios and Figure 1.2 only consider single, isolated stars, it is well established that most stars form in clusters, and during the evolution of the protostars, the protostars were all likely to have been in close proximity (~10,000 au) to another star (Perseus and Taurus molecular clouds; Tobin et al., 2018b; Andrews et al., 2018). However, the multiplicity of stars evolves and in the more evolved Class I and II environments, the multiplicity appears to be lower (Orion molecular clouds; Tobin et al., 2020), with the lowest companion multiplicity in field star surveys (Worley, 1962; Reipurth & Zinnecker, 1993). That is to say, we observe a decrease in multiplicity fraction from Class 0 to I sources.

1.3.2.1. Mechanisms for Formation

Current theories suggest two favored pathways for forming multiple systems, that appear to operate simultaneously:

- gravitational instabilities within disks (on scales ∼100s of au; e.g. Adams et al., 1989; Stamatellos & Whitworth, 2009; Kratter et al., 2010a),
- and/or turbulent fragmentation (on scales ∼1000s of au; e.g. Fisher, 2004; Padoan & Nordlund, 2004; Offner et al., 2010; Boss & Keiser, 2013).

Gravitational instability forms companions at more compact companions (<100s of au), the size scale of the disk. Additionally, the circumstellar disk is required to be massive ($\frac{M_d}{M_\odot} >$ 10%) and locally fragment. These fragments rapidly form within a few thousand of years and can form low mass brown dwarfs (Stamatellos & Whitworth, 2009), stellar mass companions (Kratter & Lodato, 2016), and possibly giant gas planets (Baehr, 2023). Tobin et al. (2016a); Burns et al. (2023) show observations of gravitationally unstable disks which mirror that of simulations from Kratter et al. (2010a); Bate (2012, 2018), with prominent spirals arms, indicating density enhancements and instabilities in the disk. Tobin et al. (2016a) found there was likely enhanced mass build-up occuring in the disk, causing gravitational instabilities to fragment the disk, forming the multiples via analysis of the Toomre Q parameter, a measure of disk stability, (more on this in Chapter 2).

However, for the most compact companions (≤10 au separations), a fundamental limit exists for gravitational instability, set by the radius of the first hydrostratic core (R_{core}∼7 au, regardless of initial condiations; Larson, 1969), inside which in-situ fragmentation is fundamentally prohibited (Bate, 1998). Despite forming in the outer disk, the companions could migrate inwards due to disk drag or multi-body interactions to form more compact systems, similar to the Type II migrations found in planet interactions with a viscous disk (D'Angelo & Lubow, 2008, 2010).

Turbulent fragmentation of a self-gravitating core can produce widely separated sources (1000s of au) which then may dynamically evolve to more compact separations (Bate et al., 2002; Moeckel & Bate, 2010; Reipurth & Mikkola, 2012). Turbulent perturbations within

the core can produce pockets of enhanced densities, causing localized regions to collapse on timescales faster than the whole core. Then, depending on the relative velocity vectors with respect to the core, the system could be unbounded or contract the relative separations. This could explain systems of multiples that have wide or compact companions with randomly aligned disk orientations with respect to the dynamical orbits of the companions (Jensen et al., 2004; Scholz et al., 2010; Jensen & Akeson, 2014; Offner & Arce, 2014; Lee et al., 2019a; Offner et al., 2022b).

Dynamical interactions of the protostars can result in compact binaries (Bate, 2000) or can lead to ejection of loosely bound objects via 3+ body chaotic interactions (Hut & Bahcall, 1983). Price & Podsiadlowski (1995) showed that passage of stars may perturb cores, forcing small displacements of the protostar from the core center, and creating a new protostar. This process could act multiple times from multiple passages of nearby stars in dense environments. Subsequently, these formed protostars could further dynamically interact or undergo orbital decay, either contributing to ejected stars or compressing the orbital separations to form compact multiples (Bate et al., 2002; Reipurth & Mikkola, 2012). Possible markers for this mechanism would be compact multiples with random alignments, highly off-axis cores and protostars or cores and protostars with different system velocities.

Formation of Disks

Up until now, we neglected the formation of the disk which is critical for understanding protostars. The initial formation of the disk is heavily regulated by the FHSC (for reference; Section 1.2). During this process of collapse, from the second core collapse resulting from the deuterium burning, a rotationally supported disk is formed outside of the FHSC interior region as the collapse continues to bring in material. Disks at all stages of YSOs have been extensively studied (Pudritz & Wilson, 1996; Maury et al., 2010; Tobin et al., 2016b; Gerin et al., 2017; Segura-Cox et al., 2018; Tobin et al., 2018b; Andrews et al., 2018, and references therein), yet many more questions remain:

1. The angular momentum problem, which refers fact that if angular momentum of the parent cloud is conserved (R$\sim 10^5$ au) as it infalls to the core (R$\sim$10s of au), then the YSO

would rotate much faster than the break up speed. Additionally, with the large angular momentum present, the core material could orbit at extended radii, much larger than observed. Despite typical clouds rotating slowly (Goodman et al., 1993; Caselli et al., 2002b), the specific angular momentum still needs to decrease 4–5 orders of magnitude, without disrupting the system. Possible solutions to this are fragmentation of the disk (Section 1.3.2) or other mechanisms to carry away momentum (e.g. outflows described in Chapter 4, or magnetic braking (Allen et al., 2003b,a; Allen, 2004))

2. The disk, which may be massive as it accretes matter from the surrounding environment may not efficiently accrete onto the protostar. This causes a buildup of excess mass in the disk, and if the self-gravity of the mass exceeds the kinematic energies of the disk, the disk could fragment into additional components. These components could be brown dwarfs to stellar-sized objects depending on the size of the disk and efficiency of accretion, which could further accrete material from the disk. This possibility is explored more in depth in Chapter 2.
3. The magnetic braking problem, which is possibly a solution to the angular momentum problem, instead operates too efficiently, suppressing disk formation completely (Mestel & Spitzer, 1956; Allen et al., 2003b,a; Allen, 2004). Cores are observed to have strong magnetic fields (Troland & Crutcher, 2008), and during the collapse stage, the magnetic field provides a long distance "lever arm" to slow the rotation of the core. However, it is expected non-ideal MHD effects can act to reduce the efficiency of magnetic braking (Nakano et al., 2002; Dapp et al., 2012; Tsukamoto et al., 2015).
4. Outflows may hold the key to solve these problems. Outflows, which are known to be a signature of accretion, are likely a result of inefficient accretion of matter from the disk onto the protostar. Some of the accreted material becomes heated, ionized, and driven away from the protostar via bi-polar outflows. These outflows have several components, a slower moving (V$\leq$ 10 km s^{-1}), wide angle ($\theta \sim 45°$) component and a fast moving (V$>$ 15 km s^{-1}), collimated ($\theta \sim 5°$) jet. The outflow is also thought to interact with the slowly rotating envelope as well, slowing additional accretion, and itself rotating and precessing; however, the exact importance of this effect is still under debate.
5. The temperature profile of the disks are still poorly understood due to the complexity

of the disks. The YSO disk is geometrically thick, with the upper layers expected to experience radiative heating while the lower layers are more shielded. The effects of turbulence from accretion can induce an internal heating mechanism. Additionally, the lower layers, which we expect to be more dense, will have higher kinetic temperatures, providing another heating mechanism. This results in a vertical and radial temperature gradient across the disk.

6. Dust grains, which experience a headwind of sub-Keplerian gas, will efficiently radially drift across the disk. This can quickly deplete the disk of $\sim$mm-sized dust grains unless some mechanism can either halt their march inwards or cause them to grow to $\sim$meter-sized, in which the grains are large enough to not be heavily influenced by the gas kinematics.
7. The complexity in the temperature and density radial profiles directly affect the chemical formation of the disk, which has been extensively studied by van 't Hoff et al. (2018); van 't Hoff (2019); van 't Hoff et al. (2020). Henning & Semenov (2013); Dutrey et al. (2014); Bianchi et al. (2022); Miotello et al. (2022); Hsieh et al. (2023) observed vertical stratification of multiple molecules, where the heavy molecules settle and freeze onto the large dust grains of the disk (reproduced in Figure 1.3; Miotello et al., 2022). The disk midplane ($T_{avg} \approx 25-40$ K) is heavily obscured from the central protostar and shielded from back radiation of the surrounding field making the environment relatively quiescent for molecules to become ices. Further from the midplane, the average temperature increases, liberating molecules from the grains. This region becomes "flared" as UV photons destroy the dust grains and thermal motions cause the gas molecules to occupy a finite range of relative velocities.

Thus with these questions/limitations in mind, we can construct a model of the disk. There seems to exist a layered model of the disk, restricted by the various freeze-out points of molecules, resulting in a stratification of the species. This "onion-like" model for cores was proposed by Bergin & Tafalla (2007) and results in "freeze-out" holes in the observations. Additionally, the dust particles will settle towards the midplane and subsequently radially drift inwards. Pile-ups of mass can occur and cause local instabilities in the disk where the self-gravity of localized regions exceeds that which is supported via thermal motions.

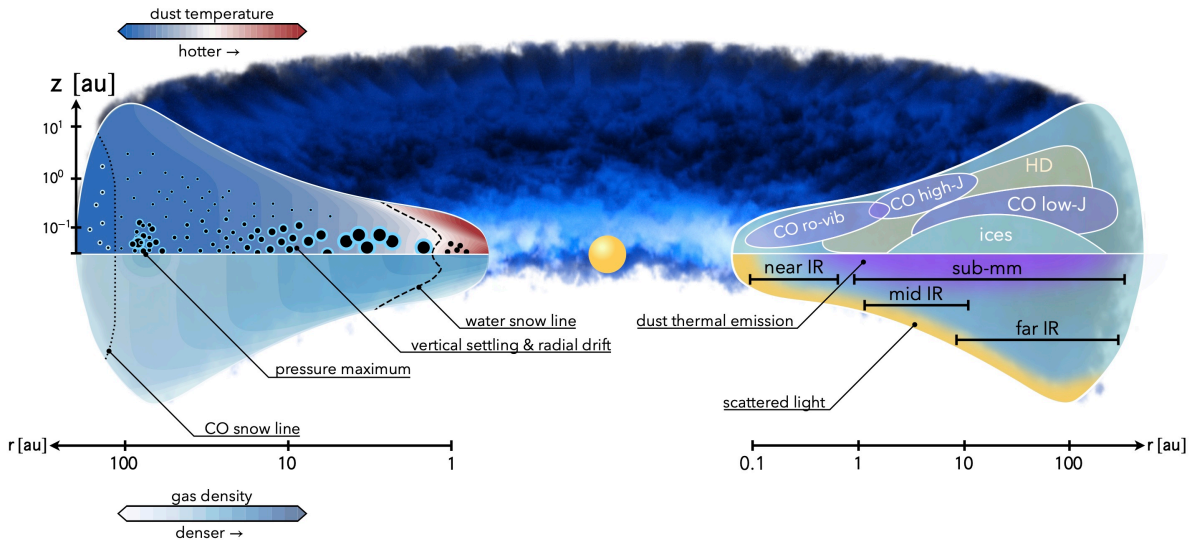

Figure 1.3: : Simplified profile visualization of a YSO protoplanetary disk. These sources have less gas and dust than their younger counterparts, but this visualization is simply to aid the reader in understanding the stratification present in both dust and gas. The central protostar is indicated at the center and, for protostars, is enshrouded in hot gas and dust accreting to the surface. The left side details the dust settling that occurs and the vertical and horizontal disk temperature gradients as a function of scale height. The right side details various layers of gas, and the surfaces that particular transitions of the abundance molecular lines probe. Miotello et al. (image credit 2022).

1.3.2.2. Determination of Disk Mass: Dust Component

If we assume the continuum emission originates as thermal dust emission (valid for millimeter/submillimeter wavelengths), we can estimate the dust contribution to the disk mass for the protostars. If we make the assumption that the disk is isothermal, optically thin, without scattering, and the dust and gas are well mixed, then we can derive the disk mass from the equation (Hildebrand, 1983):

$$M_{dust} = \frac{D^2 F_\lambda}{\kappa_\lambda B_\lambda(T_{dust})} \tag{1.2}$$

where D is the distance to the region, F_λ is the flux density, κ_λ is the dust opacity, B_λ is the Planck function evaluated at T_{dust}, where T_{dust} is taken to be the average temperature of a typical protostar disk. The κ_λ parameter would be a function of wavelength and could be described as a power-law at long wavelengths. The slope of this power law would be determined by the physical properties of the emitting grains. If the grains have thin icy mantles, the opacity value would be lower, thus increasing the disk mass, whereas larger values of κ_λ at a given wavelength indicates larger grains. In Class 0 protostars, dust opacity models of dense

cores with thin icy-mantles (Ossenkopf & Henning, 1994) are typically chosen, with values of 0.899 cm^2 g^{-1} for 879 μm. However, the opacity changes as a function of wavelength, which can be appropriately scaled via:

$$\kappa_{0.879mm} = \kappa_{1.3mm} \times \left(\frac{1.3mm}{0.879mm} \right)^{\beta}. \tag{1.3}$$

We note that β values typical for protostars range from 1 (significant grain growth) to 1.8 (ISM value) (Kwon et al., 2009; Sadavoy, 2013). Beckwith et al. (1990) conducted a survey of protostars and estimated β <1.6 with the average of their sample $\beta = 0.65$.

Typically, the disk mass is determined from the thermal dust emission by assuming some abundance ratio between the gas and dust. For Class 0 protostars, which are still heavily embedded within the envelopes and the star has not dispersed the gas away, it is expected the gas-to-dust ratio (GDR) would be inherited from the ISM (∼100:1).

1.3.2.3. Determination of Disk Mass: Gas Component

A more direct way of estimating the gas component of the circumstellar disk would be to directly measure the gas. Then the two components, gas and dust, could simply be added to determine the total disk mass.

Molecular H_2 is the most abundant molecule in protostellar environments but does not have a permanent dipole moment, owing to the symmetry of the molecule. Along with the low molecular weight, the energy structure excludes transitions at radio wavelengths that would be observable at the temperatures of cold, molecular gas. Thus we have to look towards other molecules that are asymmetric and less abundant.

CO , the next most abundant molecule, has abundances of order 10,000× less than molecular hydrogen in the ISM (Wilson & Rood, 1994), with relatively well understood gas phase chemistry. The molecule, due to its high molecular weight and asymmetric nuclear configuration, is readily observed from near-infrared to radio wavelengths, where the dust is optically thin.

However, despite being 4 orders of magnitude less abundant, the ^{12}CO molecule is still optically thick in these regions making it a poor direct tracer for the gas mass of the disk.

Also, the CO molecule photodissociation sensitivity is controlled by indirect line processes (as opposed to direct continuum processes) that are initiated by the discrete absorption of photons into predissociative bound states and is thus subject to self and mutual shielding (Bally & Langer, 1982; van Dishoeck & Black, 1988).

^{13}CO/C^{17}O/C^{18}O , which are CO isotopologues, are much less abundant ($[H_2/^{12}CO] \approx$ 2,000, $[^{12}C/^{13}C] \approx 70$, $[^{16}O/^{17}O] \approx 2000$, $[^{18}O/^{17}O] \approx 4.16$) and the lines appear more optically thin, saturating deeper in the disk midplane (van Zadelhoff et al., 2001; Dartois et al., 2003). Bruderer (2013) showed for CO column density of about 10^{15} cm^{-2}, the UV absorption lines saturate and the photodissociation rate decreases sharply, allowing CO to survive in the midplane of the disk. Because the ^{12}CO isotopologue relative abundances are lower, they largely are not self-shielded until closer to the midplane. In particular, this makes the photodissociation processes highly isotope-selective, in which C^{18}O and C^{17}O are less affected. Therefore, the combination of several isotopologues can be used to investigate the radial/vertical gas profile of the disk.

In particular, C^{18}O and C^{17}O have been used to probe the outer and inner regions of disks, respectively, tracing the Keplerian components (Arce & Sargent, 2006; Thomas & Fuller, 2008; Tobin et al., 2016a; Frimann et al., 2017). Additionally, the CO freeze-out temperature is 25 K, restricting observations of CO to the inner $\sim$1000 au, where heating will liberate the CO molecules from the dust grains. Using optically thin isotopologues, Goldsmith et al. (1997); Goldsmith & Langer (1999) showed a conversion from the observed emission to the gas mass. However, we observe gas masses to be much smaller than expected from ISM abundance values and dust measurements (Crapsi et al., 2005). Further rigorous modeling of this discrepancy has found observations of CO can under-represent the gas component by a factor of 2-10 (Chen, 2010; Alonso-Albi et al., 2010).

N$_2$D+/N$_2$H+ ; Further out in the disk, the temperature reaches $\sim$10 K, where CO and other carbon bearing molecules have long been frozen onto the dust grains, while remaining dense (n$\sim 10^5$ cm^{-2}). Nitrogen-bearing species appear able to exist at lower temperature, with N$_2$H+ and the deuterated N$_2$D+ were some of the first molecular ions observed in the ISM (Turner,

1974; Green et al., 1974; Caselli et al., 1995, 2002a; Crapsi et al., 2005). N_2H+ is thought to have formed via the reactions

$$H_2 + c.r. \rightarrow H_2+$$
$$H_2+ + H_2 \rightarrow H_3+ + H$$
$$H_3+ + N_2 \rightarrow N_2H+ + H_2$$
$$and$$
$$D_2H+ + N_2 \rightarrow N_2D+ + HD$$
$$H_3+ + HD \Leftrightarrow H_2D+ + H + \Delta E$$
$$H_2D+ + N_2 \rightarrow N_2D+ + H_2$$

Additionally, closer to the disk scales, where the temperatures reach values $\geq$20-K, CO sublimates from the dust grains and reacts destructively with nitrogen-bearing species via the reactions:

$$N_2H+ + CO \rightarrow HCO+ + N_2 \tag{1.4}$$

The N_2H+ molecule also has hyperfine structure, by which the line excitation temperature and total optical depth can be estimated by simultaneously fitting the hyperfine structure and comparing against the statistical abundance. As such, these molecules are best for probing the cold, dense environment around the protostar, in the envelope.

1.3.2.4. Molecular Lines

With the complex conditions of protostellar environments, with cold outer envelopes, warm inner disks, energetic outflows, there exist steep radial, azimuthal, and vertical gradients in density, radiation field, and temperature. It stands to reason that several molecules, beyond CO, with varying critical densities, excitation temperatures, and abundances must be observed in order to probe the full structure of these systems.

However, not all molecules will exist equally and with equal abundance. Due to relative populations owing to the physical conditions and to chemical processes, molecules will be

visible at regions where the gas phase abundance and Einstein A coefficient is the largest. Thus, with a careful considerations of molecules, we can use the specific transitions of lines as probes of particular regions or conditions.

The more abundant molecules, like that of ^{12}CO, become optically thick quickly, and effects like line opacity can become important. For these optically thick lines ($\tau >> 1$), the observed brightness temperature, defined as,

$$T_b = T_{ex} \left(1 - e^{-\tau}\right), \tag{1.5}$$

approaches the excitation temperature T_{ex} of the observed molecule for optically thick observations ($\tau >> 1$). Where the brightness temperature of the observed intensity can be determined from the equation:

$$T_b = \frac{\lambda^2 S_\lambda}{2k_b \Omega}, \tag{1.6}$$

where λ is the observing wavelength, S_λ is the flux density observed at that particular wavelength, k_b is the Stefan-Boltzmann constants, and Ω is the characteristic solid angle of the observing resolution element (beam).

Low energy transitions of molecular lines, in particular the CO lines, can be close to Local Thermodynamic Equilibrium (LTE) when certain conditions are present ($n_{crit,CO}$ $\approx$1.1$\times10^4$, $n_{crit,C^{18}O}$ $\approx$9.5$\times10^3$, $n_{crit,^{13}CO}$ $\approx$9.6$\times10^3$) and thus the excitation temperature is close to the kinetic temperature of the localized gas. This makes optically thick molecular lines viable gas temperature estimators (and similarly for dust continuum observations) at the $\tau \approx 1$ surface (e.g. protoplanetary disks; Weaver et al., 2018).

From molecular lines, we obtain channel maps, in which each channel corresponds to the spatial distribution (2D image) of the particular emission at the specified velocity. For each particular velocity, the emission corresponds to the depth at which the velocity of the emitting surface is constant. Beckwith & Sargent (1993) and Horne & Marsh (1986) showed that due to the Keplerian rotation of the disk, the surface appears as a "butterfly" pattern in velocity.

Reducing the dimensionality of the channel maps comes as a logical next step, reducing the inherent 3D nature of the data cubes into 2D (image) or 1D (spectral) representations. One thing to note in particular, the channel maps only integrate emission over a narrow bandwidth

(typically $\sim$0.15 km s^{-1}), the resulting image in each channel have higher noise levels than the MFS continuum. One way to reduce the cube is to integrate across the frequency axis, into a so-called "moment maps". The first three moments are most common, with the zeroth moment map defined as integrating the spectra at each pixel position, revealing the overall geometry of the emission and the first moment map is the intensity weighting average velocity image, while the third moment map is the intensity-weighted velocity dispersion (line width).

Determination of stellar mass starts by assuming the gravity is dominated by a central star, there are only two-body interactions, and neglecting pressure gradients. The expression for mid-plane Keplerian velocity is given by the balance between the gravity and centrifugal forces:

$$F_{cent} = F_{grav} => \frac{1}{2}\frac{mv^2}{R} = \frac{1}{2}\frac{GM_* m}{R^2}, \tag{1.7}$$

$$v^2 = \frac{GM_*}{R}, \tag{1.8}$$

where M_* is the mass of the central potential and "v" is the tangential velocity at the radius R. This tangential velocity is related to the observed velocity in the channel maps (with a factor of sin(i)) from the rest frequency of the chosen molecular line. One should note, disks have non-zero radial pressure gradients, which are parameterized by the disk sound speed and density structure, which typically decrease radially. This induces a negative pressure gradient, thus at a given radius, the gas orbits at sub-Keplerian speeds, although this affect is typically $< 1\%$ ($V_\theta/V_{Kep} \approx 0.995$). It is also obvious, an inherent limitation of any dynamical mass estimate from data cubes is the degeneracy with the inclination viewing angle. The inclination can be estimated, however, from well resolved images of the protostellar disk and modeling of the SED.

1.3.3. Observations

Due to the ISM-like environments (small μm-sized dust grains, and temperatures only a few 10s of K), these cores and subsequent protostar sources are optically thick from optical to ultraviolet wavelengths. However, the reprocessed thermal radiation from photon absorption at the dust grains in infrared and radio wavelengths escapes the dense environment, emitting

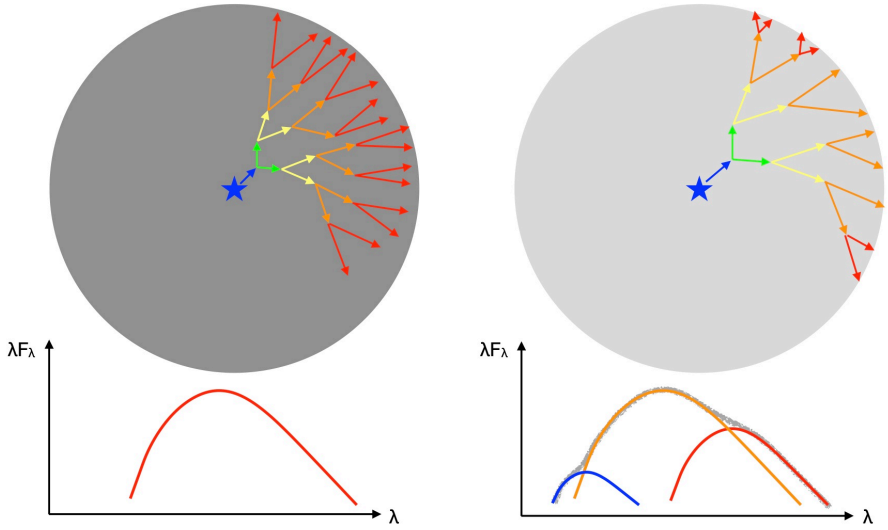

Figure 1.4: : Visualization of the effects from absorption and emission of photons from a central emitter. The left column indicates an early-type core, that inherits the characteristics of the ISM and contains a majority of the mass as small grains in the envelope/core. Photons, emitted from the center of the core, get efficiently absorbed by grains with cross-sections larger than the photon wavelength. The grains heat up and isotropically emit like a blackbody, radiating away the energy as thermal radiation. This process continues until the photons are liberated from the surface, possibly re-processing many times, and being observed as a cold blackbody The right panel is consistent with a core that has accreted some envelope material into the central part of the core or into a disk. The photons emitted experience less re-processing as the surrounding environment is less dense. This can be observed as a sum of several thermal gray bodies, based on the temperature of each of the emitting surfaces, such as the central protostar (if photons are able to escape with minimal reprocessing), the disk, and the envelope. *image credit Jonathan Williams

at much longer wavelengths (redder and colder) than first emitted (Figure 1.4).

However, since radio and infrared wavelengths are $\geq$1 order of magnitude larger than optical wavelengths (1 mm versus 600 nm; $\sim 10^3$), and resolution is proportional to wavelength via the equation,

$$\theta = \frac{1.22\lambda}{D}, \tag{1.9}$$

in order to achieve the same resolution as optical wavelengths, we would need to construct radio telescopes on the order of kilometers, which quickly becomes an engineering nightmare. An interferometer works by interfering light from two (or more) different apertures and allows for greater increase of resolution as compared to the single aperture. Michelson and Morley first used the interference of light waves to create a tabletop interferometer, which formed the basis for astrometric interferometry. Later, Michelson & Pease (1921), constructed an optical

interferometer which achieved sufficient resolution to observe the diameter of Betelgeuse.

The simplest form of an interferometer, is a few individualized segments of a larger mirror. These segments, whose combined surface area only represent a fraction of the full mirror, would ideally would act as a single telescope. These individual segments could then be separated to even larger distances and combined to produce higher resolutions. To combine these segments, taking into consideration of the phase-delay of the individual antennas, one could directly combine the light waves using high-throughput fiber optics; however, this becomes impractical at 100s of km.

Thus, with clever tools in mathematics and signal processing, one can construct interferometers with baselines out to kilometers (or even 100s-1000s of km), much larger than any single individual telescope. This works by time-stamping each observation with extremely high-precision hydrogen-maser atomic clocks and later phase-correcting and interfering the light waves through a so-called "correlator". We then replace "D" in Equation 1.9 with the maximum baseline length, and we now have the maximum resolution of the combined array.

It should be noted several limitations to this method exist, such as incomplete sampling of the observing plane, the so-called *uv*-visibility plane, which defines the overall sensitivity, resolution, and maximum recoverable angular "on-sky" scales. The resolution of the interferometer is not infinite but is a complex 2D geometry as a function of sky position (called *uv*-sampling). The interferometer, which inherently has incomplete uv-visibility coverage, will have reduced sensitivity as compared to a telescope of the same geometry. Also the data products yielded by the telescope scales exponentially with the number of non-degenerate antennas included in the array as $\frac{N(N-1)}{2}$ possible baseline pairs are correlated.

The idea of astronomical interferometry has been around for over a century (Michelson & Pease, 1921; Jennison, 1958), but only in recent decades, with the advent of state-of-the-art receivers, capable of observing thousands of frequencies simultaneously, and computing advancements, have we been able to achieve the necessary sensitivities and resolutions to probe these dense star forming regions.

Figure 1.5: : The Atacama Large millimeter/submillimeter array, composed of 66 antennas, fifty in the primary, configurable 12-meter array, four in the compact 12-meter array, and twelve 7-meter tertiary antenna. This flexibility in the specific configurations and class of telescopes allows for robust observations that can be tailored to astronomers needs. * credit David. Wilner, *Fifteenth Synthesis Imaging Workshop, 2016*

1.3.3.1. Facilities

The Atacama Large Millimeter/submillimeter Array (ALMA), Figure 1.5, is an incredibly powerful interferometer, operated as a single telescope located on Llano de Chajnantor plateau in the Atacama region of Chile at an elevation of ∼5000 meters. The main array consists of 50, 12-meter antennas, operating at frequencies of ∼100-1,000 GHz (λ∼0.32-3.6 mm). An additional fixed, compact array of four, 12-meter antennas and a tertiary array of 12, 7-meter antennas enhances the sensitivity of the array by filling in the compact baselines of the uv-visibilities, making it one of the most sensitive telescopes. The full array of 50 antennas operate as a single telescope, yet can be re-configured across the Atacama desert, spanning up to 16 km in separations. These various configurations provide varying degrees of spatial scale sensitivity and resolutions, depending on the required science. The advent of ALMA has revolutionized many fields and the telescope is able to probe the both the local Universe and the early Universe with unprecedented levels of sensitivity and resolution.

1.3.3.2. Data Products

In this dissertation, I focus on ALMA observations in the millimeter/submillimeter regime, with each observation inherently four dimensional data products. The process to recover the final data product from the raw, sampled real and imaginary visibility amplitudes is lengthy and requires a mathematically rigorous treatment, the derivation of which is extensively described in Högbom (1974), Brouw (1975), Readhead & Wilkinson (1978), Pearson & Readhead (1984),

Sramek & Schwab (1989), Wilkinson (1989), Conway et al. (1990), Wilkinson (1990), Cornwell et al. (1995), Cornwell & Fomalont (1999), Bracewell (2000), Frey & Mosoni (2009), Condon & Ransom (2016), and Thompson et al. (2017). Many improvements have been made to the original algorithms, (Briggs weighting, w-plane consideration, and self calibration; Briggs, 1995a,b; Cornwell, 2008; Cornwell et al., 2008; Rau et al., 2009), but we will focus on two specific techniques of data reduction.

The final, calibrated data product has four axes of: polarization, frequencies, and two spatial axes corresponding to the on-sky coordinates. For the purposes of this dissertation, we will only consider amplitude of the dual polarization as we tuned the observations to achieve the highest sensitivities. The resulting product can be described as either a:

1. data cube (3D): Each channel of the data cube corresponds to the spatial distribution of the particular emission at the specified frequency. The frequency axis can be converted to a Doppler shifted line-of-sight velocity as a function of a chosen rest frequency. Typically, data cube central frequencies are chosen such that observations cover particular transitions of molecular lines (more on this in Section 1.3.2.4),
2. Multi-frequency synthesis (MFS) image (2D): standard continuum image, where the aforementioned data cube has specific channels corresponding to molecules line emission removed (Figure 1.6) and the remaining channels across a (wide) range in frequencies are mapped onto a single wideband image (Conway et al., 1990). This spectral averaging across several widebands could result in spectral smearing of the final image, thus Taylor term expansion is conducted and a spectral index is derived. Following Rau & Cornwell (2011), this can be further refined by smoothing each Taylor residual image during reduction for each scale size and compute the coefficient that best reduces the residuals.

1.4. Broader Contexts and Overview

In this dissertation, I will discuss my efforts to characterize the formation of protostellar multiples and the signatures of the formation pathways. Namely, I will focus on observations at the radio wavelengths ($\sim$0.87-3 mm), using the state-of-the-art Atacama Large millimeter/-submillimeter Array. These observations will contain dust continuum and molecular line data

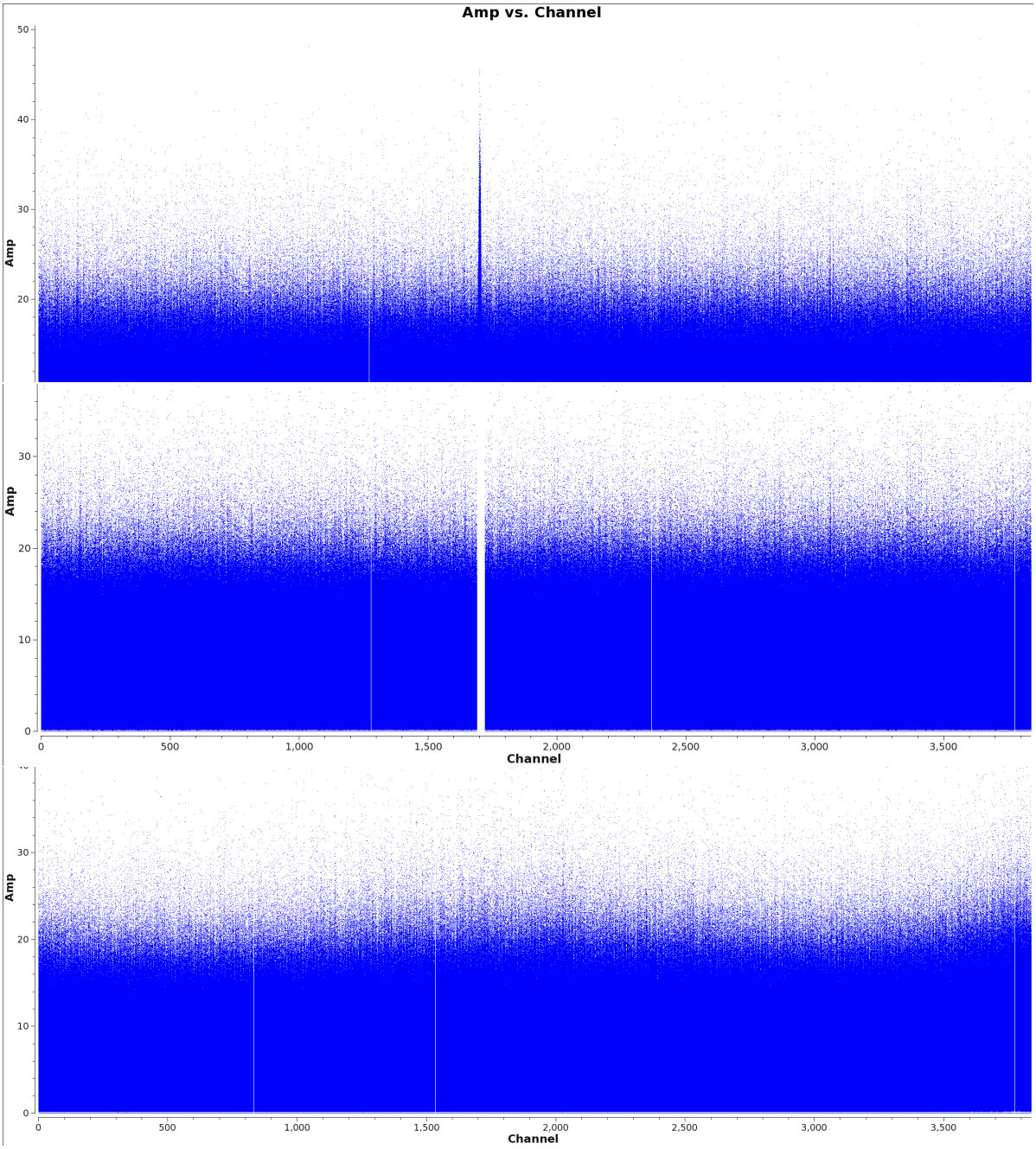

Figure 1.6: : Example observation of the protoplanetary system TW Hydrae with ALMA. ALMA has exquisite spectral resolution (R$\sim$15,000,000$\approx$15 kHz), and in this particular example, has $\sim$3800 channels of emission. The first row is a spectral window that is dominated by continuum (zero level linear offset in emission) and a narrow line of emission towards the center of the window, likely corresponding to a particular molecular line transition. The second row is masking out channels near that particular emission and the final row is a line-emission free (continuum only) spectral window. These final two spectra windows can be combined to form just under 7600 channels of continuum, doubling the sensitivity of the continuum observations. Meanwhile, the masked channels can be extracted to isolate the emission from that particular transition. The resulting calibrated datasets observed from ALMA have a typical amplitude error of $\sim$10%. *image from *https://casaguides.nrao.edu/index.php?title=First_Look_at_Imaging_CASA_6*

to discern disk structures and kinematic profiles. The observations constraints will be used to inform the priors for the analytical models and statistical tests of star formation theory.

In Chapter 2, I analyzed observations at 879 μm of the protostellar multiple system L1448 IRS3B, found in the Perseus molecular cloud (d$\sim$300 pc). I conducted observations targeting disk tracing kinematic lines such as $C^{17}O$, $H^{13}CO+$, and ^{13}CO along with shock and outflow tracers SiO and ^{12}CO. This enabled me to characterize the Keplerian motions and outflow properties, in a known multiple. These observations are critical for laying the groundwork for understanding what molecular lines tracers are best suited for tracing the kinematics of Class 0 systems. I also found the system to be gravitationally unstable, likely forming the close companions (a$<$ 500 au) in-situ. I described rigorous radiative transfer modeling along with Bayesian inference methods to constrain the parameters of the source. These models simultaneously fit the SED along with the ALMA uv-visibility products, to accurately fit the physical parameters.

In Chapter 3, I conducted observations at 1.3 mm towards the isolated protostar, BHR7-mms. This Class 0 protostar is located in a nearby Vela cometary globule (d$\sim$400 pc) and was thought to have a nearly edge-on, Keplerian disk. I confirm Keplerian rotation on the scales of the disk with the disk tracer $C^{18}O$ and determine the mass of the disk from continuum observations. I found the protostar is likely marginally gravitationally unstable, consistent with a $M_{disk}/M_* \approx 0.26/1.17$.

In Chapter 4, I continued my investigations of BHR7-mms, this time to focus on tracing the angular momentum from the cloud scales down to the disk. I conducted complementary observations of BHR7-mms at 3 mm, with the dense, cold gas tracers N_2H+. I confirmed the rotation and infall in the envelope and furthermore, estimated the envelope and disk accretion rates. These indicate an imbalance in mass transfer and likely point to future instabilities or high accretion events.

In Chapter 5, a relatively new observational approach is taken to constrain the formation pathway of twelve Perseus protomultiple systems. These observations leverage the high resolution ($\sim$8 au) capabilities of ALMA with the exquisite sensitivities to observe the compact circumstellar disks around each of the companions to determine the orientation angles of the circumstellar disk relative to the companion orbital plane. I found the subsample of compact

(<300 au) companions to be most consistent with a preferentially aligned distribution while the subsample of wide (>500 au) companions to be most consistent with a randomly aligned distribution. These indicate the compact companions likely formed via gravitational instability, which theory tends preserve the relative alignments as compare to turbulent fragmentation and subsequent dynamical interaction which form randomly aligned systems.

I summarize the dissertation in Chapter 6 and discuss the broader impact of my work. In particular I outline the additional questions that have arisen as I tackled the hard problems of protomultiple formation pathways and discuss the future research endeavors I am pursuing.

Chapter 2

Characterizing the Kinematics of the Protostellar Multiple L1448 IRS3B[1]

Preface

We present new Atacama Large Millimeter/submillimeter Array (ALMA) observations towards a compact ($\sim$230 au separation) triple protostar system, L1448 IRS3B, at 879 μm with $0.''11 \times 0.''05$ resolution. Spiral arm structure within the circum-multiple disk is well resolved in dust continuum toward IRS3B, and we detected the known wide ($\sim$2300 au) companion, IRS3A, also resolving possible spiral substructure. Using dense gas tracers, $C^{17}O$ (J = 3$\rightarrow$2), $H^{13}CO+$ (J = 4$\rightarrow$3), and $H^{13}CN$ (J = 4$\rightarrow$3), we resolved the Keplerian rotation for both the circum-triple disk in IRS3B and the disk around IRS3A. Furthermore, we used the molecular line kinematic data and radiative transfer modeling of the molecular line emission to confirm that the disks are in Keplerian rotation with fitted masses of $1.19^{+0.13}_{-0.07} M_\odot$ for IRS3B-ab, $1.51^{+0.06}_{-0.07}$ $M_\odot$ for IRS3A, and placed an upper limit on the central protostar mass for the tertiary IRS3B-c of 0.2 $M_\odot$. We measured the mass of the fragmenting disk of IRS3B to be $\sim$0.29 $M_\odot$ from the dust continuum emission of the circum-multiple disk and estimated the mass of the clump surrounding IRS3B-c to be 0.07 $M_\odot$. We also found that the disk around IRS3A has a mass of $\sim$0.04 $M_\odot$. By analyzing the Toomre Q parameter, we found the IRS3A circumstellar disk is gravitationally stable (Q$>$5), while the IRS3B disk is consistent with a gravitationally unstable disk (Q$<$1) between the radii $\sim$200-500 au. This coincides with the location of the spiral arms and the tertiary companion IRS3B-c, supporting the hypothesis that IRS3B-c was formed in situ via fragmentation of a gravitationally unstable disk.

[1]Chapter reproduced from (Reynolds et al., 2021).

2.1. Introduction

Star formation takes place in dense cores within molecular clouds (Shu et al., 1987) that are generally found within filamentary structures (André et al., 2014). The Perseus Molecular Cloud, in particular, hosts a plethora of young stellar objects (YSOs; Enoch et al., 2009; Sadavoy et al., 2014) and is nearby (d$\sim$288$\pm$22 pc; e.g., Ortiz-León et al., 2018; Zucker et al., 2019), making its protostellar population ideal for high-spatial resolution studies. By observing these YSOs during the early stages of star formation, we can learn about how cores collapse and evolve into protostellar and/or proto-multiple systems, and how their disks may form into proto-planetary systems.

Protostellar systems have been classified into several groups following an evolutionary sequence: Class 0, the youngest and most embedded objects characterized by low L_{bol}/L_{submm} ($< 5 \times 10^{-3}$; Andre et al., 1993) and T_{bol} $\leq$70 K, Class I sources which are still enshrouded by an envelope that is less dense than the Class 0 envelope, with $T_{bol} <= 650$ K, Flat Spectrum sources, which are a transition phase between Class I and Class II, and Class II objects, which have shed their envelope and consist of a pre-main sequence star (pre-MS) and a protoplanetary disk. Most stellar mass build-up is expected to occur during the Class 0 and Class I phases ($< 5 \times 10^5$ yr; e.g. Lada, 1987; Kristensen & Dunham, 2018), because by the time the system has evolved to the Class II stage, most of the mass of the envelope has been either accreted onto the disk/protostar or blown away by outflows (Arce & Sargent, 2006; Offner & Arce, 2014).

Studies of multiplicity in field stars have observed multiplicity fractions of 63% for nearby stars (Worley, 1962), 44-72% for Sun-like stars (Abt, 1983; Raghavan et al., 2010a), 50% for F-G type nearby stars (Duquennoy & Mayor, 1991), 84% for A-type stars (Moe & Di Stefano, 2017), and 60% for pre-MS stars (Mathieu, 1994). These studies demonstrate the high frequency of stellar multiples and motivates the need for further multiplicity surveys toward young stars to understand their formation mechanisms.

Current theories suggest four favored pathways for forming multiple systems: turbulent fragmentation (on scales $\sim$1000s of au; e.g. Fisher, 2004; Padoan & Nordlund, 2004), thermal fragmentation (on scales $\sim$1000s of au; e.g. Offner et al., 2010; Boss & Keiser, 2013), gravitational instabilities within disks (on scales $\sim$100s of au; e.g. Adams et al., 1989; Stamatellos &

Whitworth, 2009; Kratter et al., 2010a), and/or loose dynamical capture of cores ($\sim 10^{4-5}$ au scales Bate et al., 2002; Lee et al., 2019b). Additionally, stellar multiples may evolve via multi-body dynamical interactions which can alter their hierarchies early in the star formation process (Bate et al., 2002; Moeckel & Bate, 2010; Reipurth & Mikkola, 2012). In order to fully understand star formation and multiple-star formation, it is important to target the youngest systems to characterize the initial conditions.

The VLA Nascent Disk and Multiplicity (VANDAM) survey (Tobin et al., 2016b) targeted all known protostars down to 20 au scales within the Perseus Molecular Cloud using the Karl G. Jansky Very Large Array (VLA) to better characterize protostellar multiplicity. They found the multiplicity fraction (MF) of Class 0 protostars to be $\sim$57% (15-10,000 au scales) and $\sim$28% for close companions (15-1,000 au scales), while, for Class I protostars, the MF for companions (15-10,000 au scales) is 23% and 27% for close companions (15-1,000 au scales). This empirical distinction in MF motivates the need to observe Class 0 protostars to resolve the dynamics before the systems evolve. It was during this survey that the multiplicity of L1448 IRS3B, a compact ($\sim$230 au) triple system, was discovered. Tobin et al. (2016a) observed this source at 1.3 mm, resolving spiral arms, kinematic rotation signatures in $C^{18}O$, ^{13}CO, and H_2CO, with strong outflows originating from the IRS3B system.

L1448 IRS3B has a hierarchical configuration, which features an inner binary (separation $0.''25 \approx 75$ au, denoted -a and -b, respectively) and an embedded tertiary (separation $0.''8 \approx 230$ au, denoted -c). The IRS3B-c source is deeply embedded within a clump positioned within the IRS3B disk, thus we reference the still forming protostar as IRS3B-c and the observed compact emission as a "clump" around IRS3B-c. Tobin et al. (2016a) found evidence for Keplerian rotation around the disks of IRS3B and IRS3A. They also found that the circum-triple disk was likely gravitationally unstable.

Theory suggests that during stellar mass assembly via disk accretion, fragmentation via gravitational instability (hereafter GI) may occur if the disk is sufficiently massive, cold, and rapidly accreting(Adams et al., 1989; Yorke & Bodenheimer, 1999; Kratter et al., 2010a). Due to the scales of fragmentation, and on-going infall, fragments likely turn into stellar or brown dwarf mass companions, and GI is a favored pathway for the formation of compact multi-systems ($\lesssim$100 au). Since observations show that the youngest systems, like L1448 IRS3B,

have higher disk masses than their more evolved counterparts (Tobin et al., 2020), we would also expect observational signatures of disk instability and fragmentation to be most prevalent in the Class 0 stage.

The wide and compact proto-multiple configurations of IRS3A and IRS3B contained within a single system provides a test bed for multiple star formation pathways to determine which theories best describe this system. Here we detail our follow-up observations to Tobin et al. (2016a) of L1448 IRS3B with the Atacama Large Millimeter/submillimeter Array (ALMA) in Band 7, with $2\times$ higher resolution and $6\times$ higher sensitivity. We resolvedthe kinematics toward both IRS3B and IRS3A with much higher fidelity that the previous observations, enabling us to characterize the nature of the rotation in the disks, measure the protostar masses, and characterize the stability of both disks. We show our observations of this system and describe the data reduction techniques in Section 2.2, we discuss our empirical results and our use of molecular lines in Section 2.3, we further analyze the molecular line kinematics in Section 2.4, we further detail our models and the results in Section 2.5, and we interpret our findings in Section 2.6, where we discuss the implications of our empirical and model results and future endeavors.

2.2. Observations

We observed L1448 IRS3B with ALMA in Band 7 (879 μm) during Cycle 4 in two configurations, an extended (C40-6) and a compact (C40-3) configuration in order to fully recover the total flux out to $\sim5''$ angular scales in addition to resolving the structure in the disk. C40-6, was used on 2016 October 1 and 4 with 45 antennas. The baselines ranged from 15 to 3200 meters, for a total of 4495 seconds on source (8052 seconds total) for both executions. C40-3, was used on 19 December 2016 with 41 antennas. The baselines covered 15 to 490 meters for a total of 1335 seconds on source (3098 seconds total).

The complex gain calibrator was J0336+3218, the bandpass calibrator was J0237+2848, and the flux calibrator was the monitored quasar J0238+1636. The observations were centered on IRS3B. IRS3A, the wide companion, is detected further out in the primary beam with a beam efficiency $\sim$60%.We summarize the observations in Tables 2.1 and 2.2 and further detail our observations and reductions in Appendix 2.A.

It should also be noted there is possible line blending of $H^{13}CN$ (J = 4→3) and SO_2 (J = $13_{2,12}$ →$12_{1,11}$) (Lis et al., 1997) (Table 2.2). The SO_2 line has an Einstein A coefficient of 2.4×10^{-4} s^{-1} with an upper level energy of 93 K, demonstrating the transition line strength could be strong. SO_2 provides another shock tracer which could be present toward the protostars. We label $H^{13}CN$ and SO_2 together for the rest of this analysis to emphasize the possible line blending of these molecular lines. Additionally, the ^{12}CO and SiO emission primarily trace outflowing material and analysis of these data is beyond the scope of this paper, but the integrated intensity maps of select velocity ranges are shown in Appendix 2.D.1 and 2.D.2. The results of this analysis are summarized for each of the sources in Table 2.3.

2.3. Results

2.3.1. 879 μm Dust Continuum

The observations contain the known wide-binary system L1448 IRS3A and L1448 IRS3B and strongly detect continuum disks towards each protostellar system (Figures 2.1 and 2.2). We resolvedthe extended disk surrounding IRS3A (Briggs robust weight $= 0.5$: Figure 2.1, superuniform: Figure 2.3).

2.3.1.1. IRS3B

We resolvedthe extended circum-multiple disk of IRS3B and the spiral arm structure that extends asymmetrically to ∼600 au North-South in diameter. Figure 2.2 shows a zoom in on the IRS3B circumstellar disk, which exhibit clear substructure. Furthermore, we observed the three distinct continuum sources within the disk of IRS3B as identified by Tobin et al. (2016a), but with our superior resolution and sensitivity (∼2× higher), our observations are able to marginally resolve smaller-scale detail closer to the inner pair of sources, IRS3B-a and -b (Figure 2.2). We can now constrain the origin point of the two spiral arm structures. Looking towards IRS3B-ab, we noticed a decline in the disk continuum surface brightness in the inner region, north-eastward of IRS3B-ab. We also observed a "clump" ∼50 au East of IRS3B-b. However, given that this feature is located with apparent symmetry to IRS3B-a, it is possible that the two features ("clump" and IRS3B-a) are a part of an inner disk structure as there appears a slight deficit of emission located between them ("deficit"), while IRS3B-b is just outside of the inner region.

2.3.1.2. IRS3B-ab

To best determine the position angle and inclination of the circum-multiple disk, we first removed the tertiary source that is embedded within the disk using the *imfit* task in CASA by fitting two 2-D Gaussians with a constant emission offset (detailed fully in Appendix 2.F). We fitted the semi-major and semi-minor axis of the IRS3B-ab disk with a 2-D Gaussian using the task *imfit* in CASA. To fit the general shape of the disk and not fit the shape of the spiral arms, we smoothed the underlying disk structure (taper the uv visibilities at 500 kλ during deconvolution using the CASA *clean* task), yielding more appropriate image for single 2D Gaussian fitting.

From this fit, we recovered the disk size, inclination, and position angle, which are summarized in Table 2.3. The protostellar disk of IRS3B has a deconvolved major axis and minor axis FWHM of 1.″73±0.″05 and 1.″22±0.″04 (497±17 au × 351±12 au), respectively. This corresponds to an inclination angle of $45.0^{\circ}{}^{+2.2}_{-2.2}$ assuming the disk is symmetric and geometrically thin, where an inclination angle of 0° corresponds to a face-on disk. We estimated the inclination angle uncertainty to be as much as 25% by considering the south-east side of the disk as asymmetric and more extended. The position angle of the disk corresponds to 28±4° East-of-North.

2.3.1.3. IRS3B-c

In the process of removing the clump around the tertiary companion IRS3B-c, we construct a model image of this clump that can be analyzed through the same methods. We recover a deconvolved major axis and minor axis FWHM of 0.″28±0.″05 and 0.″25±0.″04 (80±17 au × 71±12 au), respectively, corresponding to a radius ∼40 au (assuming the disk is symmetric). This corresponds to an inclination angle of $27.0^{\circ}{}^{+19}_{-19}$ and we fit a position angle of 21±1° East-of-North. We note the inclination estimates for IRS3B-c may not be realistic since the internal structure of the source (oblate, spherical, etc.) cannot be constrained from these observations, thus the reported angles are assuming a flat, circular internal structure, similar to a disk.

2.3.1.4. IRS3A

The protostellar disk of IRS3A has a FWHM radius of ∼100 au and has a deconvolved major axis and minor axis of $0.''69^{+0.01}_{-0.01}$ and $0.''25^{+0.1}_{-0.1}$ (197±3 au × 72±3 au), respectively. This corresponds to an inclination angle of 68.6±1.2° assuming the disk is axially symmetric. The position angle of the disk corresponds to 133±1° East-of-North. We marginally resolved two emission deficits one beamwidth off IRS3A, along the major axis of the disk. The potential spirals appear to originate along the minor axis of the disk; however, due to the reconstructed beam elongation along the minor axis of the disk, we cannot fully resolve the substructure of the disk around IRS3A, limiting the characterization that we can perform on it.

2.3.2. Disk Masses

The traditional way to estimate the disk mass is via the dust component which dominates the disk continuum emission at millimeter wavelengths. If we make the assumption that the disk is isothermal, optically thin, without scattering, and the dust and gas are well mixed, then we can derive the disk mass from the equation:

$$M_{dust} = \frac{D^2 F_\lambda}{\kappa_\lambda B_\lambda(T_{dust})} \tag{2.1}$$

where D is the distance to the region (288 pc), F_λ is the flux density, κ_λ is the dust opacity, B_λ is the Planck function for a dust temperature, and T_{dust} is taken to be the average temperature of a typical protostar disk. The κ_λ at λ = 1.3 mm was adopted from dust opacity models with value of 0.899 cm^2 g^{-1}, typical of dense cores with thin icy-mantles (Ossenkopf & Henning, 1994). We then appropriately scale the opacity:

$$\kappa_{0.879mm} = \kappa_{1.3mm} \times \left(\frac{1.3mm}{0.879mm}\right)^{\beta} \tag{2.2}$$

assuming β=1.78. We note that β values typical for protostars range from 1-1.8 (Kwon et al., 2009; Sadavoy, 2013). If we assume significant grain growth has occurred, typical of more evolved protoplanetary disks like that of Andrews et al. (2009), we would then adopt a $\kappa_{0.899\mu m} \approx$ 3.5 cm^2 g^{-1} and β=1, which would lower our reported masses by a factor of 2.

The assumed luminosities of the sources are 13.0 L$_\odot$ and 14.4 L$_\odot$ for IRS3B and IRS3A

at a distance of 300 pc, respectively (8.3 $L_\odot$ and 9.2 $L_\odot$ for IRS3B and IRS3A, respectively at 230 pc; Tobin et al., 2016a). We note that in the literature there are several luminosity values for IRS3B, differing from our adopted value by a factor of a few. Reconciling this is outside of the scope of this paper, but the difference could arise from source confusion in the crowded field and differences in SED modeling.

We adopt a $T_{dust} \approx 40\ K$ for the IRS3B disk dust temperatures from the equation $T_{dust} = 30\ K \times (L_*/L_\odot)^{1/4}$, which is comparable to temperatures derived from protostellar models (43 K: Tobin et al., 2013) and larger than temperatures assumed for the more evolved protoplanetary disks (25 K: Andrews et al., 2013). The compact clump around IRS3B-c has a peak brightness temperature of 55 K. Thus we adopt a T_{dust} = 55 K since the emission may be optically thick ($T_{dust} \sim T_B$). We determined the peak brightness temperature of this clump by first converting the dust continuum image from Jy into K via the Rayleigh-Jean's Law[2]. We adopt a T_{dust} = 51 K for the IRS3A source.

If we assume the canonical ISM gas-to-dust mass ratio of 100:1 (Bohlin et al., 1978b), we estimate the total mass of the IRS3B-ab disk (IRS3B-c subtracted) to be 0.29 $M_\odot$ for $\kappa_{0.879\ mm}$ =1.80 cm^2 g^{-1}, $T_{dust} \approx 40\ K$ (Tobin et al., 2019), and $F_\lambda \approx 1.51\ Jy$. We note that the dust to gas ratio is expected to decrease as disks evolved from Class 0 to Class II (Williams & Best, 2014), but for such a young disk, we expect it to still be gas rich and therefore have a gas to dust ratio more comparable with the ISM. We estimate 0.07 $M_\odot$ to be associated with the circumstellar dust around IRS3B-c, from this analysis, for a T_{dust} = 55 K. We perform the same analysis towards IRS3A and arrive at a disk mass estimate of 0.04 $M_\odot$, for a T_{dust} = 51 K and $F_\lambda \approx 0.19\ Jy$.

The dust around the tertiary source, IRS3B-c, is compact and it is the highest peak intensity source in the system, and thus the optical depth needs to be constrained. An optically thick disk will be more massive than what we calculate while an optically thin disk will be more closely aligned with our estimates. We calculate the average deprojected, cumulative surface density

[2](T = $1.222\times10^3 \frac{I\ mJy\ beam^{-1}}{(\nu\ GHz)^2(\theta_{major}\ arcsec)(\theta_{minor}\ arcsec)}$ K, Wilson et al., 2009)

from the mass and radius provided in Table 2.3, and determined the optical depth via

$$\begin{aligned}\tau_{0.879\ mm} &= \kappa_{0.879mm}\Sigma \\ &= \frac{D^2 F_\lambda}{\pi R_{disk}^2 B_\lambda(T_{dust})}\end{aligned}$$

from (Tobin et al., 2016a). The dust surrounding the tertiary source has an average dust surface density (Σ) of $\sim$2.6 g cm^{-2} and an optical depth (τ) of $\sim$2.14, indicative of being optically thick, while IRS3B-ab (IRS3B-c clump subtracted) is not optically thick if we assume dust is equally distributed throughout the disk with an average dust surface density of $\sim$0.17 g cm^{-2} and an optical depth of 0.34. However, since spiral structure is present, these regions of concentrated dust particles are likely much more dense. L1448 IRS3A has an average dust surface density of 0.32 g cm^{-2} and an optical depth of 0.57. Optically thick emission indicates that our dust continuum mass estimates are likely lower limits for the mass enclosed in the clump surrounding IRS3B-c, while the IRS3B-ab circum-multiple disk and the IRS3A circumstellar disk are probably optically thin except for the inner regions.

An effect that could impact our measurements of disk masses and surface densities is scattering. Scattering reduces the emission of optically thick regions of the disk and causes them to appear optically thin, thus underestimating the optical depth. Zhu et al. (2019), showed that in the lower limit of extended (> 100 au) disks, this effect underestimates the disk masses by a factor of 2. However, towards the inner regions, this effect might be enhanced to factors > 10. Sierra & Lizano (2020) show that for wavelengths $\sim$870 μm and 100 μm size particles, only a $\Sigma \approx 3.2$ (g cm^{-2}) is needed for the particles to be optically thick. Thus our masses could be several factors higher.

2.3.3. Molecular Line Kinematics

Additionally, we observed a number of molecular lines (^{12}CO, SiO, H^{13}CO+, H^{13}CN/SO_2, C^{17}O) towards IRS3B and IRS3A and used them to resolve outflows, envelope, and disk kinematics, with the goal of disentangling the dynamics of the systems. We summarize the observations of each of the molecules below and provide a more rigorous analysis towards molecules tracing disk kinematics. While outflows are important for the evolution and characterization of

YSOs, the analysis of these complex structures is beyond the scope of this paper because we are focused on the disk and envelope. We found ^{12}CO and SiO emission primarily traces outflows, H^{13}CO+ emission traces the inner envelope, H^{13}CN/SO_2 emission traces energetic gas which can take the form of outflow launch locations or inner disk rotations, and C^{17}O primarily traced the disk. Non-disk/envelope tracing molecular lines (^{12}CO and SiO) are discussed in Appendix 2.D.

We constructed moment 0 maps, which integrate the data cube over the frequency axis, to reduce the 3D nature of datacubes to 2D images. These images show spatial locations of strong emission and deficits. To help preserve some frequency information from the datacubes, we integrated at specified velocities to separate the various kinematics in these systems. However, when integrating over any velocity ranges, we did not preserve the full velocity information of the emission, thus we provided spectral profiles of C^{17}O emission toward the IRS3B-ab, IRS3B-c, and IRS3A sources in Appendix 2.E.

2.3.3.1. C^{17}O Line Emission

The C^{17}O emission (Figure 2.4, 2.5, and 2.6) appears to trace the gas kinematics within the circumstellar disks because the emission is largely confined to the scales of the continuum disks for both IRS3B and IRS3A, appears orthogonal to the outflows, and has a well-ordered data cube indicative of rotation (Figure 2.6). C^{17}O is a less abundant molecule (ISM [^{12}CO]/[C^{17}O] $\approx$1700:1; e.g. Wilson & Rood, 1994) isotopologue of ^{12}CO (ISM $[H_2]/[^{12}\mathrm{CO}] \approx 10^4$:1; e.g. Visser et al., 2009), and thus traces gas closer to the disk midplane. Towards IRS3B, the emission extends out to $\sim$1.$''$8 ($\sim$530 au), further than the continuum disk ($\sim$500 au) and has a velocity gradient indicative of Keplerian rotation. Towards IRS3A, the emission is much fainter, however, from the moment 0 maps, C^{17}O still appears to trace the same region as the continuum disk.

2.3.3.2. H^{13}CO+ Line Emission

The H^{13}CO+ emission (Figure 2.7 and 2.8) detected within these observations probe large scale structures (>5$''$), much larger than the size of the continuum disk of IRS3B and scales $\sim$1.$''$5 towards IRS3A. For IRS3B, the emission structure is fairly complicated with multiple emission peaks near line center and emission deficits near the sources IRS3B-ab+c, while

appearing faint towards IRS3A. The data cube appears kinematically well ordered, indicating possible rotating structures. Previous studies suggested HCO+ observations are less sensitive to the outer envelope structure, probing densities $\geq 10^5$ cm^{-3} and temperatures > 25 K (Evans, 1999). However, follow up surveys (Jørgensen et al., 2009) found this molecule to primarily trace the outer-circumstellar disk and inner envelope kinematics, and were unable to observe the disks of Class 0 protostars from these observations alone. Jørgensen et al. (2009) postulated that in order to disentangle dynamical structures on <100 au scales, a less abundant or more optically thin tracer (like that of H^{13}CO+) would be required with high resolutions. However, this molecular line, as shown in the integrated intensity map of H^{13}CO+ (Figure 2.7 and 2.8) traces scales much larger than the continuum or gaseous disk of IRS3B and IRS3A and thus is likely tracing the inner envelope.

2.3.3.3. H^{13}CN Line Emission

The H^{13}CN/SO_2 emission (Figures 2.9 and 2.10) is a blended molecular line, with a separation of 1 km s^{-1} (Table 2.2). The integrated intensity maps towards IRS3B appear to trace an apparent outflow launch location from the IRS3B-c protostar (Figure 2.9) based on the spatial location and parallel orientation to the outflows. The H^{13}CN/SO_2 emission towards IRS3B is nearly orthogonal to the disk continuum major axis position angle and indicates that the emission towards IRS3B is tracing predominantly SO_2 and not H^{13}CN.

2.4. Keplerian Rotation

To determine the stability of the circumstellar disks around IRS3B and IRS3A, the gravitational potentials of the central sources must be constrained. The protostars are completely obscured at $\lambda < 3$ μm, rendering spectral typing impossible and kinematic measurements of the protostar masses from disk rotation are required to characterize the protostars themselves. Assuming the gravitational potential is dominated by the central protostellar source(s), one would expect the disk to follow a Keplerian rotation pattern if the rotation velocities are large enough to support the disk against the protostellar gravity. These Keplerian motions will be observed as Doppler shifts in the emission lines of molecules due to their relative motion within the disk. Well-resolved disks with Keplerian rotation are observed as the characteristic "butterfly" pattern around the central gravitational potential: high velocity emission at small radii

to low velocity emission at larger radii, and back to high velocity emission at small radii on opposite sides of the disk (e.g., Rosenfeld et al., 2013; Pinte et al., 2018a).

2.4.1. PV Diagrams

To analyze the kinematics of these sources, we first examined the moment 0 (integrated intensity) maps of the red- and blue-Doppler shifted $C^{17}O$ emission to determine if the emission appears well ordered (Figure 2.4) and consistent with $H^{13}CO+$ (Figure 2.7). We then examined the sources using a position-velocity (PV) diagram which collapses the 3-D nature of these data cubes (RA, DEC, velocity) into a 2-D spectral image. We specified the number of integrated pixels across the minor axis to limit bias from the large scale structure of the envelope and select emission originating from the disk. This allows for an estimation of several parameters via examining the respective Doppler shifted components.

2.4.1.1. IRS3B

The PV diagrams for IRS3B are generated over a 105 pixel (2.″1) width strip at a position angle 28°. The PV diagram velocity axis is centered on the system velocity of 4.8 km s^{-1} (Tobin et al., 2016a) and spans $\pm$5 km s^{-1} on either side, while the position axis is centered just off of the inner binary, determined to be the kinematic center, and spans 5″ ($\sim$1500 au) on either side.

$C^{17}O$ appears to trace the gas within the disk of IRS3B on the scale of the continuum disk (Figure 2.4). It is less abundant and therefore less affected by outflow emission. We used it as a tracer for the kinematics of the disk (PV-diagram indicating Keplerian rotation; Figure 2.11). The $C^{17}O$ emission extends to radii beyond the continuum disk, likely extending into the inner envelope of the protostar, while the $H^{13}CO+$ emission (Figure 2.7) appears to trace larger scale emission surrounding the disk of IRS3B and emission within the spatial scales of the disk has lower intensity. This is indicative of emission from the inner envelope as shown by the larger angular scales the emission extends to with respect to $C^{17}O$ ($H^{13}CO+$ PV-diagram; Figure 2.12). Finally, the blended molecular line, $H^{13}CN/SO_2$ appears to trace shocks in the outflows and not the disk kinematics for IRS3B. For these reasons, we do not plot the PV diagram of $H^{13}CN/SO_2$.

2.4.1.2. IRS3A

The PV diagrams for IRS3A are generated with a 31 pixel (0.″62) width strip at a position angle 133°. $C^{17}O$ is faint and diffuse towards the IRS3A disk (Figure 2.13) but still traces a velocity gradient consistent with rotation (Figure 2.5) and has a well ordered PV diagram (Figure 2.13). $H^{13}CN/SO_2$, (Figure 2.10), appears to trace the kinematics of the inner disk due to the compactness of the emission near the protostar and the appearance within the disk plane (Figure 2.14). The velocity cut is centered on the system velocity of 5.4 km s^{-1} and spans 6.2 km s^{-1} on either side. The emission from the blended $H^{13}CN/SO_2$ is likely dominated by $H^{13}CN$ instead of SO_2, due to the similar system velocity that is observed. SO_2 would have $\sim$1.05 km s^{-1} offset which is not observed in IRS3A.

Similar to IRS3B, the $H^{13}CO+$ emission likely traces the inner envelope, indicated in Figure 2.8, as it extends well beyond the continuum emission but still traces a velocity gradient consistent with rotation (Figure 2.15). The circumstellar disk emission is less resolved, however, due to the compact nature of the source and has lower sensitivity to emission because it is located $\sim$8 arcsec (beam efficiency$\sim$60%) from the primary beam center.

2.4.2. Protostar Masses: Modeling Keplerian Rotation

The kinematic structure, as evidenced by the blue- and red-shifted integrated intensity maps (e.g., Figures 2.4 and 2.5) indicates rotation on the scale of the continuum disk. The disk red- and blue-emission are oriented along the disk major axis and and not along the disk minor axis, which would be expected if the emission was contaminated by outflow kinematics. We first determined the protostellar mass by analyzing the PV diagram to determine regions indicative of Keplerian rotation. We summarized the results of our PV mass fitting in Table 2.4. PV diagram fitting provides a reasonable measurement of protostellar masses in the absence of a more rigorous modeling approach. The Keplerian rotation-velocity formula, $V(R) = (GM/R)^{0.5}$ allows several system parameters to be constrained: system velocity, kinematic center position, and protostellar mass. There is a degeneracy between mass determination and the inclination angle of the Keplerian disk, with more inclined sources being less reliable due to higher uncertainty in the line-of-sight velocities. We accounted for inclination in fitting the mass using the constraint from the major and minor axis ratio of the continuum emission.

2.4.2.1. IRS3B-ab

When calculating the gravitational potential using kinematic line tracers, one must first define the position of the center of mass. For circum-multiple systems, the center of mass is non trivial to measure, because it is defined by the combined mass of each object and the distribution can be asymmetric. Figure 2.16 compares various "kinematic centers" for the circumstellar disk of IRS3B depending on the methodology used. First, by fitting the mid-point between highest velocity $C^{17}O$ emission channels, where both red and blue emission is present, for IRS3B-ab using the respective red and blue-shifted emission, the recovered center is $03^h25^m36.32^s$ $30°45'14.''92$ which is very near IRS3B-a. The second method, fitting symmetry in the PV-diagram, however, requires a different center in order to reflect the best symmetry of the emission arising from the disk, at $03^h25^m36.33^s$ $30°45'15.''04$ which corresponds to a position north-east of the binary pair, which is close to a region of reduced continuum emission ("deficit" in Figure 2.2). The first method of fitting the highest velocity emission assumes these highest velocity channels correspond to regions that are closest to the center of mass and the emission is symmetric at a given position angle. We chose the $C^{17}O$ molecule, which is not affected by the strong outflows, appears to trace the continuum disk the best, and has no outflow contamination, for fitting. The second method of fitting the PV-diagram center assumes the source is symmetric and well described by a simple Keplerian disk across the position angle of the PV cut, ignoring the asymmetry along the minor axis. Finally, we included two other positions corresponding to the peak emission in the highest velocity blue- and red- Doppler shifted channels, respectively. Unsurprisingly, these positions are on either side of the peak fit. The difference in the position of the kinematic centers is within $\sim$2 resolution elements of the $C^{17}O$ map and does not significantly affect our mass determination, as demonstrated in our following analysis.

We used a method of numerically fitting the $C^{17}O$ PV diagrams employed by Ginsburg et al. (2018) and Seifried et al. (2016), by fitting the emission that is still coupled to the disk and not a part of the envelope emission. This helps to provide better constraints on the kinematic center for the Keplerian circum-multiple disk. This was achieved by extracting points in the PV-diagram that have emission 10 σ along the position axis for a given velocity channel and fitting these positions against the standard Keplerian rotation-velocity formula. The Keplerian

velocity is the max velocity at a given radius but each position within a disk will include a superposition of lower velocity components due to projection effects.

The fitting procedure was achieved using a Markov Chain Monte Carlo (MCMC) employed by the Python MCMC program *emcee* (Foreman-Mackey et al., 2013). Initial prior sampling limits of the mass were set to 0.1-2 $M_\odot$. Outside of these regimes would be highly inconsistent with prior and current observations of the system. Uncertainty in the distance (22 pc) from the *Gaia* survey (Ortiz-León et al., 2018) and an estimate of the inclination error (10°) were included while the parameters (M and V_{sys}) were allowed to explore phase space. These place approximate limits to the geometry of the disk. The cyan lines in Figure 2.11 trace the Keplerian rotation curve with M=1.15 $M_\odot$ with 3-σ uncertainty$= 0.09$ $M_\odot$, which fits the edge of the $C^{17}O$ emission from the source. This mass estimate describes the total combined mass of the gravitating source(s). Thus if the two clumps (IRS3B-a and -b) are each forming protostars, this mass would be divided between them. However with the current observations, we cannot constrain the mass ratio of the clumps. Thus, we can consider two scenarios (Section 2.6.7), an equal mass binary and a single, dominate central potential.

The $H^{13}CO+$ PV-diagram (Figure 2.12) shows high asymmetry emission towards the source. However, the $H^{13}CO+$ emission is still consistent with the central protostellar mass measured using $C^{17}O$ emission of 1.15 $M_\odot$ (indicated by the white dashed line). This added asymmetry is most likely due to $H^{13}CO+$ emission being dominated by envelope emission, in contrast to the $C^{17}O$ being dominated by the disk. There is considerably more spatially extended and low velocity emission that extends beyond the Keplerian curve and cannot be reasonably fitted with any Keplerian curve. Additionally, there is a significant amount of $H^{13}CO+$ emission that is resolved out near line-center, appearing as negative emission, whereas, the $C^{17}O$ emission did not have as much spatial filtering as the $H^{13}CO+$ emission.

2.4.2.2. IRS3B-c

We also analyzed the $C^{17}O$ kinematics near the tertiary, IRS3B-c, to search for indications of the tertiary mass influencing the disk kinematics. In Figure 2.17, we showed the PV diagram of $C^{17}O$ within a 2.″0 region centered on the tertiary and plot velocities corresponding to Keplerian rotation at the location of IRS3B-c within the disk, to provide an upper bound on the

possible protostellar mass within IRS3B-c. Emission in excess of the red-dashed lines could be attributed to the tertiary altering the gas kinematics. The velocity profile at IRS3B-c shows no evidence of any excess beyond the Keplerian profile from the main disk, indicating that it has very low mass. Based on the non-detection, we can place upper limits on the mass of the IRS3B-c source of $<$0.2 $M_\odot$ as shown by the white dotted lines in Figure 2.17. A protostellar mass much in excess of this would be inconsistent with the range of velocities observed.

2.4.2.3. IRS3A

For the IRS3A circumstellar disk, the dense gas tracers $H^{13}CN$ and $C^{17}O$ were used to analyze disk characteristics and are shown in Figures 2.13 and 2.14. The position cut is centered on the continuum source (coincides with kinematic center), and spans 2″($\sim$576 au) on either side. This provides a large enough window to collect all of the emission from the source. The dotted white lines show the Keplerian velocity corresponding to a M=1.4 $M_\odot$ central protostar which is consistent with the PV diagram.

The spatial compactness of IRS3A limits the utility of the $H^{13}CN$ PV-diagram with the previous MCMC fitting routine. We found evidence of rotation in this line tracer from the velocity selected moment 0 map series and PV-diagram. However, from the PV diagram alone, strong constraints cannot be determined due to the compactness of the $H^{13}CN$ emission and the low S/N of $C^{17}O$.

2.5. Application of Radiative Transfer Models

To further analyze the disk kinematics, we utilized the methods described in Sheehan et al. (2019) and further described in Appendix 2.C for modeling the molecular line emission presented thus far. The modeling framework uses RADMC-3D (Dullemond et al., 2012) to calculate the synthetic channel maps using 2D axisymmetric radiative transfer models in the limit of local local thermodynamic equilibrium (LTE) and GALARIO (Tazzari et al., 2018) to generate the model visibilities from those synthetic channel maps. We sampled the posterior distributions of the parameters to provide fits to the visibilities by utilizing a MCMC approach (*pdspy*; Sheehan et al., 2019). *pdspy* uses the full velocity range given by the frequency limit of the input visibilities in modeling.

Some of the parameters are less constrained than others due to asymmetry of the disks and

discussion of these parameters falls outside the scope of the kinematic models sought in this paper. Our focus for the kinematic models are: position angle (p.a.), inclination (inc.), stellar mass (M_*), disk radius (R_D), and system velocity (V_{sys}). We provide a summary of our model results in Table 2.5.

The combined fitting of the models is computationally expensive (fitting 200 models simultaneously per "walker integration time-step"), requiring on average $1 - 2 \times 10^4$ core-hours per source to reach convergence. We ran these models across 5 nodes with 24 cores/nodes each for $\sim$150 hours on the OU (University of Oklahoma) Supercomputing Center for Education and Research supercomputers (OSCER) to reach sufficient convergence in the parameters. The convergence state is determined when the *emcee* "walkers" reach a steady state solution where the ensemble of walkers is not changing by an appreciable amount, simply oscillating around some median value with a statistical variance.

2.5.1. IRS3B

The *pdspy* kinematic flared disk model results for IRS3B are shown in Figure 2.18 with the Keplerian disk fit compared to the data. The system velocity fitted is in agreement with the PV-diagram analysis. There is some uncertainty in the kinematic center, due to the diffuse, extended emission near the system velocity ($<$1 km s^{-1}) which yielded degeneracy when fitting. The models yielded similar stellar masses as compared to the PV/Gaussian fitting (3-σ uncertainties listed, *pdspy* $1.19^{+0.13}_{-0.07}$ $M_\odot$; PV: $1.15^{+0.09}_{-0.09}$ $M_\odot$), similar position angles (*pdspy*: $27^\circ{}^{+1.8}_{-2.9}$; PV:$\sim$28°), and while the inclinations are not similar (*pdspy*: $66^\circ{}^{+3.0}_{-4.6}$; Gaussian:$\sim$45°), this discrepancy in inclination is most likely due to a difference in asymmetric gas and dust emission. With the tertiary subtraction method (Appendix 2.F), we fitted a Gaussian the dust continuum of IRS3B-c to preserve the underlying disk structure, then fit the IRS3B-ab disk with a single gaussian. Using the PV-diagram fitting, we attempted to fit symmetric Keplerian curves to the PV-diagram. *pdspy* attempts to also fit the asymmetric southeast side of the disk, which is an asymmetric feature, with the model symmetric Keplerian disk. Upon further inspection of the residual map, there is significant residual emission on the south-eastern side of the disk which is likely a second order effect in the fit, however it is confined spatially and spectrally and should not have a major effect on the overall fit.

2.5.2. IRS3A

The *pdspy* kinematic flared disk model results for IRS3A are shown in Figure 2.19, primarily fitting the inner disk. The models demonstrate the gas disk is well represented by a truncated disk with a maximum radius of the disk of ∼40 au (most likely due to the compact nature of the emission). This disk size of 40 au is smaller than the continuum disk and results from the compact emission of $H^{13}CN$. The models find a system velocity near 5.3 km s^{-1} in agreement with the PV-diagram. The system velocity of numerous molecules ($H^{13}CO+$, $C^{17}O$, and $H^{13}CN$) are in agreement and thus likely tracing the same structure in the system. The models yielded a similar stellar mass ($1.51^{+0.06}_{-0.07}$ $M_\odot$, 3-σ uncertainties listed) to the estimate from the PV-diagram. Also the disk orientation of inclination (69°) and position angle (∼122°) agree with the estimate from the continuum Gaussian fit.

2.6. Discussion

2.6.1. Origin of Triple System and Wide Companion

Protomultiple systems like that of IRS3B and IRS3A can form via several possible pathways: thermal fragmentation (on scales ∼1000s of au), turbulent fragmentation (on scales ∼1000s of au), gravitational instabilities within disks (on scales ∼100s of au), and/or loose dynamical capture of cores (on scales $\sim 10^{4-5}$ au). To constrain the main pathways for forming multiple systems, we must first constrain the protostellar geometrical parameters and then the (in)stability of the circum-multiple disk. Previous studies towards L1448 IRS3B (see Tobin et al., 2016a) achieved ∼0.″4 molecular line resolution, roughly constraining the protostellar mass. The high resolution and high sensitivity data we presented allows constraints on the stability of the circumstellar disk of IRS3B and sheds light on the formation pathways of the compact triple system and the wide companion. The circumstellar disk around the wide companion, IRS3A, has an orthogonal major axis orientation to the circumstellar disk of IRS3B, favoring formation mechanisms that result in wider companions forming with independent angular momentum vectors. The circumstellar disk around IRS3B is massive, has an embedded companion (IRS3B-c), and has spiral arms, which are indicative of gravitational instability, and we will more quantitatively examine the (in)stability of the disk in Section 2.6.3.

2.6.2. Signatures of an Embedded Companion in Disk Kinematics

Hydrodynamic simulations show that massive embedded companions within viscous disks should impact the Keplerian velocity pattern in a detectable manner (Perez et al., 2015). Pérez et al. (2018) showed the signatures of a massive companion embedded within a viscous, non-self gravitating disk.Their model observations are higher ($\sim$2$\times$) spectral and angular resolution, and more sensitive ($\sim$5$\times$) than the presented observations. They show a 10 M_J mass source should be easily detectable with about 1000 orbits of evolution by analyzing the moment 1 maps. More recently, several studies of protoplanetary disks have confirmed these predictions of localized Keplerian velocity deviations for moderately massive planets (Pinte et al., 2018b, 2019b). However, these systems are much more evolved ($>$ 3 Myr), with quiescent, non-self gravitating disks, and likely experienced thousands of stable orbits compared to IRS3B, a self-gravitating and actively accreting Class 0 source, with a companion that likely has completed only a few dynamically changing orbits.

Hall et al. (2020) performed simulations of a viscous, self-gravitating disk (0.3 $M_\odot$) around a 0.6 $M_\odot$ source, which showed that the effects of self gravity will provide "kinks" at high resolution and sensitivity. Additionally, Vorobyov & Basu (2011) showed that due to angular momentum exchange between the fragment and the disk or dispersal due to tidal torques, the fragmentation radius could drastically change up to an order-of-magnitude over the evolution time scales of the disk. This reordering of the disk structure can work to mask definitive observable kinematic deviations of embedded companions in the disk.

2.6.3. Disk Structure

With the high resolution observations, we can construct a radial profile of the continuum emission to analyze disk structure. The circumstellar disk of IRS3B has prominent spiral arms but the radial profile will azimuthally average this emission. In order to construct the radial profile, we have to define: an image center to begin the extraction, the geometry (position angle and inclination) of the source, and the size of each annulus. The system geometry and image center were all adapted from the PV diagram fit parameters and the radius of the annuli was defined as half the average synthesized beamsize (Nyquist Sampling; Nyquist, 1928). We converted from flux density to mass via Equation 2.1 and further constructed a disk mass surface

density profile. To convert from flux density into dust mass, we adopted a radial temperature power law with a slope of -0.5, assuming the disk at 100 au can be described with a temperature of (30 K)$\times(L_*/L_\odot)^{0.25}$. The temperature profile has a minimum value of 20 K, based on models of disks embedded within envelopes (Whitney et al., 2003). While we adopted a temperature law profile , protostellar multiples are expected to complicate simple radial temperature profiles.

Towards IRS3B, in order to mitigate the effects of the tertiary source in the surface density calculations, we used the tertiary subtracted images, described in the Appendix 2.F. The system geometric parameters used for the annuli correspond to an inclination of 45° and a position angle of 28°. The PV/Gaussian fits were used here for ease of reproducibility and utilizing the *pdspy* results would still be consistent. The largest annulus extends out to 5″, corresponding to the largest angular scale on which we can recover most emission. The temperature at 100 au for IRS3B-ab is taken to be ≈40.1 K. We showed both the extracted flux radial profile and radial surface density profile for IRS3B-ab in Figure 2.20. The radial surface density profile shows a flat surface density profile out to ∼400 au.

Towards IRS3A, the system geometry parameters used for the annuli correspond to an inclination of 69° and a position angle of 133°. With this method, we constructed a radial surface density profile to analyze the stability of the disk (Figure 2.21). The temperature at 100 au for IRS3A is taken to be ≈50.9 K. The circumstellar disk of IRS3A is much more compact than the circumstellar disk of IRS3B, with the IRS3A disk radius ∼150 au, and thus the assumed temperature at 100 au is a good approximation for the median disk temperature.

2.6.3.1. Disk Stability

The radial surface density profiles allow us to characterize the stability of the disk to its self-gravity as a function of radius. The Toomre Q parameter (herein Q) can be used as a metric for analyzing the stability of a disk. It is defined as the ratio of the rotational shear and thermal pressure of the disk versus the self-gravity of the disk, susceptible to fragmentation. When the Q parameter is <1, it indicates a gravitationally unstable region of the disk.

Q is defined as:

$$Q = \frac{c_s \kappa}{\pi G \Sigma} \tag{2.3}$$

where the sound speed is c_s, the epicyclic frequency is κ corresponding to the orbital frequency ($\kappa = \Omega$ in the case of a Keplerian disk), and the surface density is Σ, and G is the gravitational constant.

We further assumed the disk is thermalized and the disk sound speed radial profile is given by the kinetic theory of gases:

$$c_s\left(T\right) = \left(\frac{k_b T}{m_H \mu}\right)^{0.5} \tag{2.4}$$

where T is the gas temperature and μ is the mean molecular weight (2.37). We then evaluated the angular frequency as a function of radius,

$$\Omega\left(R\right) = \left(\frac{GM_*}{R^3}\right)^{0.5} \tag{2.5}$$

where $M_* = 1.15\ M_\odot$.

Simulations have shown that values of Q<1.7 (calculated in 1D) can be sufficient for self-gravity to drive spiral arm formation within massive disks while Q $\approx$1 is required for fragmentation to occur in the disks (Kratter et al., 2010b). Figure 2.22 shows the Q radial profile for the circumstellar disk of L1448 IRS3B, which varies by an order of magnitude across the plotted range (0.4-4). The disk has Q$<$ 1 and therefore is gravitationally unstable starting near $\sim$120 au, interior to the location of the embedded tertiary within the disk and extending out to the outer parts of the disk ($\sim$500 au) as indicated by the IRS3B Toomre Q radial profile. The prominent spiral features present in the circumstellar disk span a large range of radii (10s-500 au).

Figure 2.23 shows the Toomre Q radial profile for the circumstellar disk of L1448 IRS3A. The IRS3A dust continuum emission, while having possible spiral arm detection (Figure 2.1), is more indicative of a gravitationally stable disk through the analysis of the Toomre Q radial profile (Q>5 for the entire disk). This is due to the higher mass central protostar and lower disk surface density, as compared to the circumstellar disk of IRS3B. Thus substructures in IRS3A may not be gravitationally driven spiral arms and could reflect other substructure. The circumstellar disk around IRS3A has a mass of 0.04 $M_\odot$ and the protostar has a mass of 1.4 $M_\odot$.

2.6.4. Interpretation of the Formation Pathway

The formation mechanism for the IRS3A source, IRS3B system as a whole, and the more widely separated L1448 NW source Tobin et al. (2016b), is most likely turbulent fragmentation, which works on the 100s-1000s au scales (Offner et al., 2010; Lee et al., 2019b). Companions formed via turbulent fragmentation are not expected to have similar orbital configurations and thus are expected to have different V_{sys}, position angle, inclination, and outflow orientations. For the wide companion, IRS3A, the disk and outflows are nearly orthogonal to IRS3B and have different system velocities (e.g., 5.3 km s^{-1} and 4.9 km s^{-1}, respectively; Tables 2.4 and 2.5). McBride & Kounkel (2019) has shown protostellar systems dynamically ejected from multi-body interactions are less likely to be disk bearing. Considering the low systemic velocity offset (IRS3A: 5.3 km s^{-1}, IRS3B: 4.9 km s^{-1}), the well ordered Keplerian disk of IRS3A, and relative alignment along the long axis of the natal core (Sadavoy & Stahler, 2017), the systems would not likely have formed via the dynamical ejection scenario from the IRS3B system (Reipurth & Mikkola, 2012).

In contrast, the triple system IRS3B appears to have originated via disk fragmentation. The well organized $C^{17}O$ emission, which traces the disk continuum emission, indicates that the circum-multiple disk in IRS3B is in Keplerian rotation at both compact and extended spatial scales (0.″2 to >2.″0; 50 au to >600 au) (see Figure 2.4). The derived disk mass ($M_d/M_s \sim 25\%$) is high, such that the effects of self-gravity are important (Lin & Pringle, 1990). The low-m (azimuthal wavenumber) spiral arms observed in the disk are consistent with the high mass (Kratter & Lodato, 2016). The protostellar disk is provided stability on scales near the central potential due to the shear effects of Keplerian rotation and higher temperatures, while, at larger radii, the rotation velocity falls off and the local temperature is lower, allowing for local gravitational instability. Moreover, as seen in Figure 2.22, Toomre's Q falls below unity at radii > 120 au, coincident with the spatial location of the tertiary IRS3B-c, as expected if recently formed via gravitational instability in the disk. Additionally the inner binary, IRS3B-ab, could have formed via disk fragmentation prior to the IRS3B-c, resulting in the well-ordered kinematics surrounding IRS3B-ab.

The PV analysis of IRS3B-c also suggests that the central mass of the tertiary continuum

source is low enough ($\sim$ 0.02 $M_\odot$) to not significantly alter the kinematics of the disk (Figures 2.4 and 2.6)

The apparent co-planarity of IRS3B-abc and the well-organized kinematics of both the disk and envelope tracers, $C^{17}O$ and $H^{13}CO+$, argue against the turbulent fragmentation pathway within the subsystem. The PV-diagram of IRS3B-ab is well structured in various disk tracing molecules and the outflow orientation of IRS3B-c is aligned with the angular momentum vector of IRS3B-ab, making dynamical capture unlikely.

2.6.5. Protostar Masses

Comparing the masses of IRS3A (1.51 $M_\odot$) and IRS3B (1.15 $M_\odot$) to the initial mass function (IMF) (young cluster IMF towards binaries; Chabrier, 2005) shows these protostars will probably enter the main sequence as typical, stars once mass accretion from the infalling envelope and massive disks completes. IRS3B-a and -b are likely to continue accreting matter from the disk and envelope and grow substantially in size.

In addition to the symmetry in the inner clumps, further analysis towards IRS3B-ab of the spatial location of the kinematic centers indicate that the kinematic center is consistent with being centered on the deficit ("deficit"; Figure 2.2) with a surrounding inner disk, where IRS3B-a is a bright clump moving into the inner disk. The continuum source IRS3B-b would be just outside the possible inner disk radius. These various kinematic centers are within one resolving element of the $C^{17}O$ beam, and thus we are unable to break the degeneracy of the results from these observations alone. Higher resolution kinematics and continuum observations are required to understand the architecture of the inner disk and whether each dust clump corresponds to a protostar, or if the clumps are components of the inner disk and the central protostar is not apparent from dust emission in our observations.

If we assume the IRS3B-ab clumps surround a single central source, this source would most likely form an A-type ($M_* \approx 1.6 - 2.4$ $M_\odot$) star, depending on the efficiency of accretion (10-15%; Jørgensen et al., 2007). Similarly, IRS3A is likely to form an A-type star. If the IRS3B-ab clumps each represent a forming protostar, then each source would most likely form a F or G-type ($M_* \approx 0.8 - 1.4$ $M_\odot$) star depending on the ratio of the masses between the IRS3B-a and IRS3B-b components. IRS3B-c, while currently estimated to have a mass < 0.2 $M_\odot$, it

could still accrete a substantial amount mass of the disk and limit the accretion onto the central IRS3B-ab sources. This mechanism can operate without the need to open a gap (Artymowicz & Lubow, 1996), which remains unobserved in these systems.

More recently, Maret et al. (2020) targeted several (7) Class 0 protostars in Perseus with marginal resolution and sensitivities, to fit the molecular lines emission against Keplerian curves to derive protostellar masses. Their fitting method is similar to our own PV diagram fitting and has an average protostellar mass of $\sim$0.5 $M_\odot$. If IRS3B-ab is a single source protostar, then this source would be significantly higher mass ($M_*\sim$1.2 $M_\odot$) than the average mass of the sample, similar for IRS3A ($M_*\sim$1.4 $M_\odot$). However, if IRS3B-ab is a multiple protostellar source of two equally mass protostars ($M_*\sim$0.56 $M_\odot$), then these sources would be consistent with the survey's average protostellar mass. Maret et al. (2020) included IRS3B (labeled L1448-NB), using the molecules ^{13}CO, C^{18}O, and SO, and the protostellar parameters are consistent with the results we derived here ($M_*\sim$1.4 $M_\odot$, $PA\sim$29.5°, and $i\sim$45°), despite lower sensitivities and resolutions compared to our observations.

Yen et al. (2017) targeted several well known Class 0 protostars and compared their stellar properties against other well known sources (see reference Table 5 and Figure 10), to determine the star/disk evolution. They derived an empirical power-law relation for Class 0 towards their observations $R_d = (44\pm8)\times\left(\frac{M_*}{0.1\ M_\odot}\right)^{0.8\pm0.14}$ au and a Class 0+I relation of $R_d = (161\pm16)\times\left(\frac{M_*}{1.0\ M_\odot}\right)^{0.24\pm0.12}$ au. The L1448 IRS3B system, with a combined mass $\sim$1.15 $M_\odot$, disk mass of $\sim$0.29 $M_\odot$, and a FWHM Keplerian gaseous disk radius of $\sim$300 au, positions the target well into the Class 0 stage ($\sim$245-500 au for the Yen et al. (2017) relation) and $\sim$2-3$\times$ the average stellar mass and radius of these other well known targets. The protostellar mass of IRS3B is larger relative to the sample of protostars observed in Yen et al. (2017), which had typical central masses 0.2 to 0.5 $M_\odot$. However, this is the combined mass of the inner binary and each component could have a lower mass. L1448 IRS3A, which has a much more compact disk (FWHM Keplerian disk radius of $\sim$158 au) and a higher central mass than IRS3B ($\sim$1.4 $M_\odot$), is more indicative of a Class I source using these diagnostics. We note there is substantial scatter in the empirically derived relations (Tobin et al., 2020), thus the true correspondence of disk radii to an evolutionary state of the YSOs is highly uncertain and we observed no evidence for an evolutionary trend with disk radii.

2.6.6. Gravitational Potential Energy of IRS3B-c

In analyzing the gravitational stability of the IRS3B circumstellar disk, we can also analyze the stability of the clump surrounding IRS3B-c. If the clump around IRS3B-c is sub-virial (i.e., not supported by thermal gas pressure) it would be likely unstable to gravitational collapse, undergoing rapid (dynamical timescale, τ_{dyn}) collapse resulting in elevated accretion rates compared to the collapse of virialized clumps Additionally, it would be unlikely to observe this short-lived state during the first orbit of the clump. Dust clumps embedded within protostellar disks are expected to quickly (t$< 10^5 - yr$) migrate from their initial position to a quasi-stable orbit much closer to the parent star (Vorobyov & Elbakyan, 2019). Thus observing the IRS3B-c clump at the wide separation within the disk is likely due to it recently forming in-situ. The virial theorem states $2E_{kin} + E_{pot} = 0$, or in other words we can define an $\mathcal{R}$ such that $\mathcal{R} := \frac{2E_{kin}}{|E_{pot}|}$ will be < 1 for a gravitationally collapsing clump and > 1 for a clump to undergo expansion. Assuming the ideal gas scenario of N particles, we arrived at $E_{kin} = 1.5Nk_bT_{clump}$ where k is the Planck constant and T_{clump} is the average temperature of the particles. The potential energy takes the classic form $E_{pot} = \frac{-3}{5}\frac{GM_{clump}^2}{R_{clump}}$. We can define $N = \frac{M_{clump}}{\mu m_H}$ where μ is the mean molecular weight (2.37) and m_H is the mass of hydrogen. Assuming the clump is thermalized to the $T_{peak} = 54.6$ K, the mass of the clump is 0.07 $M_\odot$, the upper bound for the IRS3B-c protostar is 0.2 $M_\odot$, and the diameter is 78.5 au (Table 2.3), we calculated $\mathcal{R} \approx 1.4$ for the dust clump alone (this $\mathcal{R}$ is likely an upper bound since our mass estimate for the dust is likely a lower limit due to the high optical depths) and ≈ 0.3 for the combined dust clump and protostar. This $\mathcal{R}$ is likely an lower bound since our mass estimate for the protostar an upper limit due to be consistent with the kinematic observations. This is indicative that the core could be virialized but could also reflect a circumstellar accretion disk around IRS3B-c, or in the upper limit of the protostellar mass, could undergo contraction.

2.6.7. Mass Accretion

The mass in the circumstellar disks and envelopes provide a reservoir for additional mass transfer onto the protostars. However, this mass accretion can be reduced by mass outflow due to protostellar winds, thus we need to determine the maximal mass transport rate of the system to determine if winds are needed to carry away momentum (Wilkin & Stahler, 1998). While

these observations do not place a direct constraint on $\dot{M}$, from our constraints on M_* and the observed total luminosity we can estimate the mass accretion rate. In a viscous, accreting disk, the total luminosity is the sum of the stellar and accretion luminosity:

$$L_{bol} \sim L_* + L_{acc} \tag{2.6}$$

and the L_{acc} is:

$$L_{acc} = \frac{GM_*\dot{M}}{R_*} \tag{2.7}$$

half of which is liberated through the accretion disk and half emitted from the stellar surface. From our observations, we can directly constrain the stellar mass and thus, using the stellar birth-line in Hartmann et al. (1997) (adopting the models with protostellar surface cooling which provides lower-estimates), we can estimate the protostellar radius. From these calculations we can estimate the mass accretion rate of the protostars. The results are tabulated in Table 2.6 but are also summarized here. For the single protostar IRS3A this is straight-forward, but for the binary source IRS3B-ab, care must be taken. We adopted the two scenarios for the system configuration: 1.) the protostellar masses are equally divided (two 0.575 $M_\odot$ protostars) and 2.) one protostar dominates the potential (one 1.15 $M_\odot$ protostar). From Figure 3 in Hartmann et al. (1997) we estimated the stellar radius to be 2.5 $R_\odot$, 2.5 $R_\odot$, and 2 $R_\odot$ for stellar masses 0.575 $M_\odot$, 1.15 $M_\odot$, and 1.51 $M_\odot$, respectively. From Figure 3 in Hartmann et al. (1997) we estimated the stellar luminosity to be 1.9 $L_\odot$, 3.6 $L_\odot$, and 2.5 $L_\odot$ for stellar masses 0.575 $M_\odot$, 1.15 $M_\odot$, and 1.4 $M_\odot$, respectively (see Section 2.3.2).

Considering the bolometric luminosities for IRS3B and IRS3A given in Section 2.3.2, we found the $\dot{M} \sim 4.95 \times 10^{-7}$ $M_\odot$ yr^{-1} for IRS3A. Then for IRS3B-ab, in the first scenario (two 0.575 $M_\odot$ protostars), we found $\dot{M} \sim 1.5 \times 10^{-6}$ $M_\odot$ yr^{-1} and in the second scenario (one 1.15 $M_\odot$ protostar), we found $\dot{M} \sim 6.6 \times 10^{-7}$ $M_\odot$ yr^{-1}. These accretion rates are unable to build up the observed protostellar masses within the typical lifetime of the Class 0 stage ($\sim$160 kyr) and thus require periods of higher accretion events to explain the observed protostellar masses. This possibly indicates the IRS3B-ab system is more consistent as an equal mass binary system. However, further, more sensitive and higher resolution observations to fully resolve out the dynamics of the inner disk are needed to fully characterize the sources.

We further compared the accretion rates derived here with a similar survey towards Class 0+I protostars (Yen et al., 2017). We found IRS3A is consistent with L1489 IRS, a Class I protostar with a $M_* \sim 1.6\,M_\odot$ (Green et al., 2013) and a $\dot{M} \sim 2.3 \times 10^{-7}\,M_\odot\,yr^{-1}$ (Yen et al., 2014). Furthermore, in the case IRS3B-ab is an equal mass binary, the derived accretion rates as compared with the sources in Yen et al. (2017) are in the upper echelon of rates. However, in the case IRS3B-ab is best described as a single mass protostar, the derived accretion rates are consistent with TMC-1 and TMC-1A, other Class 0+I sources in Yen et al. (2017).

2.7. Summary

We presented the highest sensitivity and resolution observations tracing the disk kinematics toward L1448 IRS3B and IRS3A to date, ($C^{17}O$/$C^{18}O$ comparison: $\sim$5$\times$ higher S/N at 4.0 km s^{-1}, $\sim$3$\times$ higher resolution, and $\sim$2$\times$ better velocity resolution as compared to Tobin et al. (2016a)). Our observations resolve three dust continuum sources within the circum-multiple disk with spiral structure and trace the kinematic structures using $C^{17}O$, $H^{13}CN$/SO_2, and $H^{13}CO+$ surrounding the proto-multiple sources. The central gravitating mass in IRS3B, near -a and -b, dominates the potential as shown by the organized rotation in $C^{17}O$ emission. We compared the high fidelity observations with radiative transfer models of the line emission components of the disk. The presence of the tertiary source within the circum-multiple disk, detection of dust continuum spiral arms, and the Toomre Q analysis are indicative of the disk around IRS3B being gravitationally unstable.

We summarize our empirical and modeled results:

1. We resolved the spiral arm structure of IRS3B with high fidelity and observed IRS3B-c, the tertiary, to be embedded within one of the spiral arms. Furthermore, a possible symmetric inner disk and inner depression is marginally resolved near IRS3B-ab. IRS3B-b may be a high density clump just outside of the inner disk. We also marginally resolved possible spiral substructure in the disk of IRS3A. We calculated the mass of the disk surrounding IRS3B to be $\sim$0.29 $M_\odot$ with $\sim$0.07 $M_\odot$ surrounding the tertiary companion, IRS3B-c. IRS3A has a disk mass of $\sim$0.04 $M_\odot$.
2. We found that the $C^{17}O$ emission is indicative of Keplerian rotation at the scale of the continuum disk, and fit a central mass of $1.15^{+0.09}_{-0.09}$ $M_\odot$ for IRS3B using a fit to the PV

diagram. $H^{13}CO+$ traces the larger structure, corresponding to the outer disk and inner envelope for IRS3B. Meanwhile, the $H^{13}CN/SO_2$ blended line most likely reflects SO_2 emission, tracing outflow launch locations near IRS3B-c. The *pdspy* modeling of IRS3B finds a mass of $1.19^{+0.13}_{-0.07}$ $M_\odot$, comparable to the PV diagram fit of $1.15^{+0.09}_{-0.09}$ $M_\odot$.

3. We found that the tertiary companion is forming a central protostar that is less than 0.2 $M_\odot$. This upper limit is based on its lack of significant disturbance of the disk kinematics. Moreover, we found that there is a jet originating from the clump, confirming that a protostar is present.
4. For IRS3A, the $H^{13}CN/SO_2$ emission likely reflects $H^{13}CN$ emission due to a consistent velocity with $C^{17}O$. $H^{13}CN$ emission indicates Keplerian rotation at the scale of the continuum disk corresponding to a central mass of 1.4 $M_\odot$. The molecular line, $C^{17}O$, is also detected but is much fainter in the source but consistent with a central mass results of 1.4 $M_\odot$. The *pdspy* modeling fit for IRS3A yields mass $1.51^{+0.06}_{-0.07}$ $M_\odot$ which is also comparable to the PV diagram estimate of 1.4 $M_\odot$.
5. The azimuthally averaged radial surface density profiles enable us to analyze the gravitational stability as a function of radius for the disks of IRS3B and IRS3A. We found the circum-multiple disk of IRS3B is gravitationally unstable ($Q < 1$) for radii > 120 au. We found the protostellar disk of IRS3A is gravitationally stable ($Q > 5$) for the entire disk. We marginally detected substructure in IRS3A, but at our resolution, we cannot definitely differentiate between spiral structure and a gap in the disk. If the substructure is spiral arms due to gravitational instabilities, then the disk mass must be underestimated by a factor of 2-4 from our Toomre Q analysis.

Through the presented analysis, we determined that the most probable formation pathway for the IRS3B and its spiral structure, is through the self-gravity and fragmentation of its massive disk. The larger IRS3A/B system (including the even wider companion L1448 NW) likely formed via turbulent fragmentation of the core during the early core collapse, as evidenced by the nearly orthogonal disk orientation and different system velocity for IRS3A and IRS3B.

Table 2.1: Summary of Observations

Source	RA (J2000)	Dec (J2000)	Config.[a]	Resolution	LAS[b]	Date (UT)	Calibrators (Gain, Bandpass, Flux)
L1448 IRS3B	03:25:36.382	30:45:14.715	C40-6	$0.''12$	$1.''3$	1 and 4 October 2016	J0336+3218,J0237+2848,J0238+1636
L1448 IRS3B	03:25:36.382	30:45:14.715	C40-3	$0.''59$	$5.''6$	19 December 2016	J0336+3218,J0237+2848,J0238+1636

[a]C40-6 - Extended and C40-3 - Compact

[b]LAS- Largest Angular Scale

Table 2.2: Continuum and Spectral Line Data

	MFS Continuum[a]	^{12}CO	SiO[b]	H^{13}CN/SO$_2$[c]	H^{13}CO+	C^{17}O	335.5GHz Continuum
Rest. Freq. (GHz)	341.0	346.0	347.000030579	345.339756	346.998347	337.061104	335.5
Center Freq. (GHz)	341.0	346.778059	347.2698586	345.3520738	347.010582	337.0730133	335.4708304
Chan. Width (km/s)	2747.96	0.212	0.210	0.053	0.053	0.054	0.873
Num. Chan.	1	1920	1920	1920	1920	3840	1920
RMS/chan. (mJy)	0.069	4.0	0.5	4.5	4.5	3.7	-
Integr. (Jy) IRS3B[d]	1.5	512.7,809.8[e]	7.8, 3.5[e]	0.2, 0.1[e]	2.6, 4.1[e]	2.9, 3.2[e]	-
Integr. (Jy) IRS3A*d*	0.2	3.16,67.6[e]	0,0 [e]	2.3, 2.7[e]	0.2, 0.4[e]	0.1, 0.1[e]	-
Synth. Beam[f]	$0.''11\times0.''05$	$0.''19\times0.''11$	$0.''85\times0.''52$	$0.''22\times0.''14$	$0.''21\times0.''13$	$0.''21\times0.''13$	$0.''21\times0.''13$
Briggs Robust	0.5	0.5	0.5	0.5	0.5	0.5	-
Taper (kλ)	-	-	-	1000	1500	1500	-

NOTE—The setup of the correlator for the observations

[a] Multi-Frequency Synthesis (MFS) utilizing the extracted emission from line free spectral channels

[b] SiO was tuned incorrectly for the C40-6 observations.

[c] The H^{13}CN line is blended with the SO_2 line (345.3385377 GHz) and have a velocity separation of $\sim$1.06 km s^{-1}.

[d] The integrated flux density for the source, measured by integrated the full emission whose origin is the source. In the case of continuum emission, this is given in *Jy*; in the case of molecular line emission this is given in *Jy km s*$^{-1}$.

[e] The molecular line emission is given as the total integrated flux (Jy km s^{-1}) for the blue and red-Doppler shifted emission, denote blue, red, respectively.

[f] The synthesized beam size is provided from the *clean* task for the molecular lines (or continuum for the MFS column) using the briggs robust weighing parameter of 0.5 during image reconstruction.

Table 2.3: Source Properties

Source	RA (J2000)	Dec (J2000)	Inc.[a] (°)	P.A.[b] (°)	Outflow?	V_{sys} (km s^{-1})	L_{bol} ($L_\odot$)	M_{dust} ($M_\odot$)	$Major_{Dust}$[c] ($''$, au)	$Minor_{Dust}$[c] ($''$, au)	$Major_{Gas}$[c] ($''$, au)	$Minor_{Gas}$[c] ($''$, au)	$<T_0>$ (K)	$<\tau>$
IRS3B-ab	03:25:36.317	30:45:15.005	45	28	Joint	4.75	13.0[e]	0.29	1.73±0.05, 498±14	1.22±0.04, 351±12	2.38±0.09, 685±26	2.25±0.08, 648±23	40	0.34
IRS3B-c	03:25:36.382	30:45:14.715	27	21	Yes	4.75	-[d]	0.07	0.28±0.05, 81±14	0.25±0.04, 72±12	-	-	55	2.14
IRS3A	03:25:36.502	30:45:21.859	69	133	No	5.2	14.4[e]	0.04	0.70±0.02, 202±6	0.25±0.01, 72±3	0.52±0.08, 150±23	0.42±0.07, 121±20	51	0.57

NOTE—Summary of the empirical parameters based from the observations of the system. The sizes were derived from a 2-D Gaussian fit to the continuum and moment 0 emission maps, directly to the visibilities. IRS3B-c is blended with the underlying disk continuum and estimates here are extracted from a 2-D gaussian fit with a zero-level offset to preserve the underlying disk flux and is discussed in Appendix 2.F.

[a] Inclination is defined such that 0° is a face-on disk.

[b] Position angle is defined such that at 0°, the major axis of the disk is aligned North and the angle corresponds to East-of-North.

[c] The circumstellar disks surround IRS3B and IRS3A are ellipsoidal in the dust continuum and molecular line emission. Values are given as FWHM.

[d] The bolometric luminosity is not known at this time.

[e] The bolometric luminosity is scaled to a distance of 288 pc from Tobin et al. (2016a).

Table 2.4: PV Diagram Fitting

Source	Center RA ($''$)	Center Dec ($''$)	Inclination ($^\circ$)	Position Angle ($^\circ$)	Stellar Mass ($M_\odot$)	Velocity (km s^{-1})
IRS3B	$03^h25^m36.317^s$	$30^\circ45'15.''005$	45	29	$1.15^{+0.09}_{-0.09}$	4.8
IRS3B-c	$03^h25^m36.382^s$	$30^\circ45'14.''715$	-	-	$<0.2^a$	-
IRS3A	$03^h25^m36.502^s$	$30^\circ45'21.''859$	69	125	1.4^b	5.4

NOTE—Summary of PV diagram stellar parameter estimates with 3-σ confidence interval of the best fit walkers generated from emcee. The inclination and position angle estimates are provided by 2-D Gaussian fitting of the uv-truncated data and is further confirmed with the PV diagram analysis.

[a]The upper limit for IRS3B-c of <0.2 $M_\odot$ is derived from its apparent lack of significant influence on the disk kinematics within its immediate proximity. Furthermore, we estimated from the dust emission that the mass of the gas and dust clum surrounding the protostar is $\sim$0.07 $M_\odot$. So the combined mass of the clump and protostar must be <0.2 $M_\odot$. Figure 2.17 shows the mass limit estimates of the tertiary of the source, with emission outside of the dotted lines indicating additional mass if perturbing the disk.

[b]IRS3A, was marginally resolved and no sufficient numeric fits could be achieved with simple PV-diagram fitting. These estimates are provided by fitting the curve by eye and are not designated to be the final results and simply provide further constraints for the priors for the more rigorous kinematic modeling.

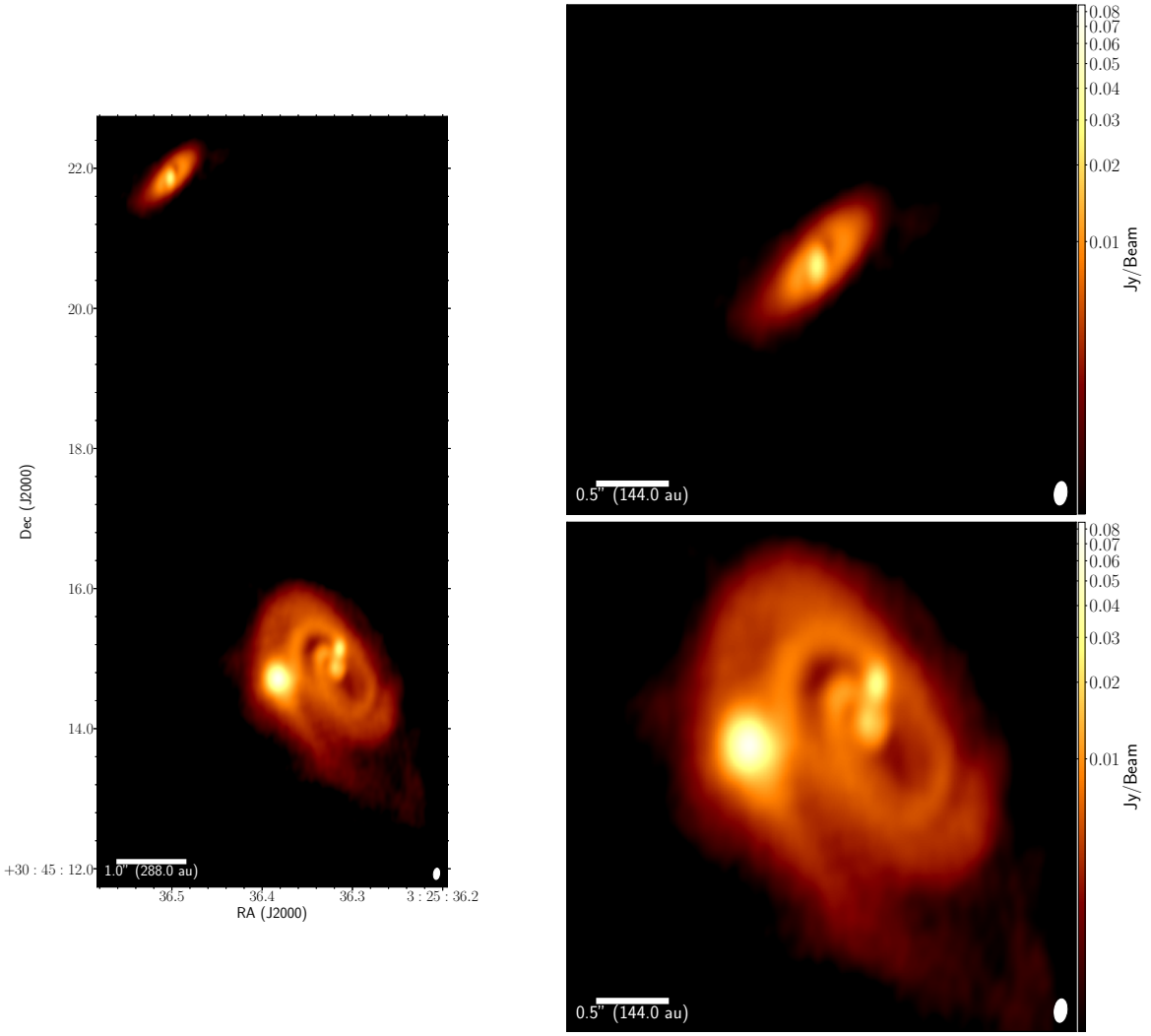

Figure 2.1: : ALMA 879 μm continuum observations of the triple protostellar system L1448 IRS3B and its wide companion IRS3A (**left**). The right panels are $\sim$2$\times$ zoom-ins on IRS3B and IRS3A. The top right image shows the wide companion, IRS3A, (d$\sim$7.$''$9$\approx$2300 au), featuring possible spiral structure. The bottom right image zooms in on the proto-multiple system, IRS3B. The inner binary is separated by 0.$''$25 (75 au) and has a spiral circum-binary disk with the embedded source $\sim$0.$''$8 (230 au) away from the binary within one of the arms. The beam size of each panel is shown in lower right (0.$''$11$\times$0.$''$05).

Table 2.5: Kinematic *pdspy*Modeling

Source	RA Offset ($''$)	Dec Offset ($''$)	Inc. ($^\circ$)	P.A. ($^\circ$)	M_* ($M_\odot$)	M_{gas}[a] ($M_\odot$)	R_{disk} (au)	V_{sys} (km s^{-1})	Turbulence (km s^{-1})	Surface Density Index γ	T_0 (K)
IRS3B	$0.031^{+0.019}_{-0.011}$	$0.025^{+0.020}_{-0.015}$	$66.0^{+3.0}_{-4.6}$	$26.7^{+1.8}_{-2.9}$	$1.19^{+0.13}_{-0.07}$	$0.079^{+0.021}_{-0.016}$	$299.0^{+24.9}_{-47.6}$	$4.880^{+0.110}_{-0.090}$	$0.012^{+0.005}_{-0.003}$	$1.2^{+0.1}_{-0.1}$	50^{+3}_{-5}
IRS3A	$0.034^{+0.003}_{-0.003}$	$0.015^{+0.003}_{-0.003}$	$69.5^{0.38}_{0.37}$	$122.4^{1.4}_{1.4}$	$1.51^{+0.06}_{-0.07}$	$6.3^{+1.6}_{-1.3}x10^{-6}$	$39.9^{+2.4}_{-1.4}$	$5.288^{+0.090}_{-0.084}$	$0.015^{+0.06}_{-0.009}$	$0.4^{+0.2}_{-0.1}$	163^{+9}_{-8}

NOTE—Summary of kinematic model parameters. The RA and DEC offsets of the *pdspy*modeling are defined from the central positions given in PV Analysis, Table 2.4. The errors presented are the 3-σ confidence intervals of the best fit walkers generated from *emcee*.

[a]The reported values of M_{gas} depend on the assumed abundance for each of the molecules. For the IRS3B source, we used the $C^{17}O$ emission, which has an assumed abundance of 2×10^{-7} relative to H_2, while for the IRS3A source we used the $H^{13}CN$ emission which has an assumed abundance of 2.9×10^{-11} relative to H_2.

Table 2.6: Mass Accretion

Source	L_{bol} ($L_\odot$)	M_* ($M_\odot$)	R_* ($R_\odot$)	L_* ($L_\odot$)	$\dot{M}_{acc}$ (10^{-7} $M_\odot$ yr^{-1})
IRS3B-ab[a]	13.0[b]	(0.575, 1.2)	(2.5, 2.5)	(1.91, 3.57)	(15.3, 6.56)
IRS3A	14.4[b]	1.5	2	2.53	5.43

NOTE—Summary of the derived parameters from Hartmann et al. (1997) to estimate the amount of mass accretion that is consistent with protostellar models and the observations. The methodology for estimating R_*, L_*, $\dot{M}$, and $M_{accreted}$ are provided in Section 2.6.7.

[a] When constraining R_*, L_*, $\dot{M}$, and $M_{accreted}$, IRS3B can be analyzed at two scenarios, 1.) equally mass binary and 2.) one protostar with most of the mass; we reference these delineations as (equal mass, single massive protostar), respectively.

[b] The bolometric luminosity is scaled to a distance of 288 pc from Tobin et al. (2016b).

Table 2.7: Self-Calibration

Step	RMS (mJy beam^{-1})	IRS3B S/N	IRS3A S/N	Iterations	Solution Integration (s)
No-selfcal.	6.5 | 74	82 | 43	26 | 13	100 | 100	
phase-cal. 1	4.2 | 25	140 | 140	48 | 40	100 | 110	"inf"
phase-cal. 2	1.7 | 11	310 | 330	120 | 100	300 | 500	30.25
phase-cal. 3	1.3 | 5.8	540 | 620	200 | 190	3000 | 1500	12.1
ampl.-cal.	0.7 | 4.3	1000 | 840	390 | 260	2500 | 2500	"inf"

NOTE—Summary of the parameters required to reproduced the gain and amplitude self-calibrations. The configurations are delineated as C40-6 | C40-3, respectively in the table. "inf" indicates the entire scan length, dictated by the time on a single pointing, which is typically 6.05 seconds.

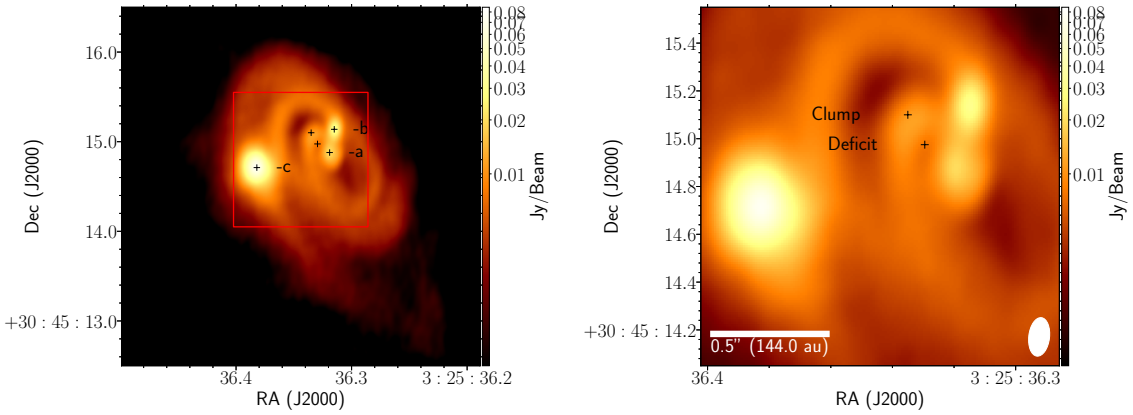

Figure 2.2: : ALMA 879 μm continuum observations of the triple protostellar system L1448 IRS3B with the difference continuum sources marked. The left colored image is zoomed in on IRS3B and is plotting with a log color stretch. The inner binary is separated by 0.″25 (75 AU) and has a circum-binary disk with spiral structure and the tertiary is separated from the binary by ∼0.″8 (230 AU) within one of the arms. The "protostars" are the continuum positions previously discovered in Tobin et al. (2016a), while the "clump" is a new feature, resolved in these observations. The "deficit" indicates the location of depression of flux between IRS3B-a and the "clump". This is discussed in Sections 2.3.1 and 2.6. The beam size of each panel is shown in lower right (0.″11×0.″05 using Briggs Robust parameter of 0.5).

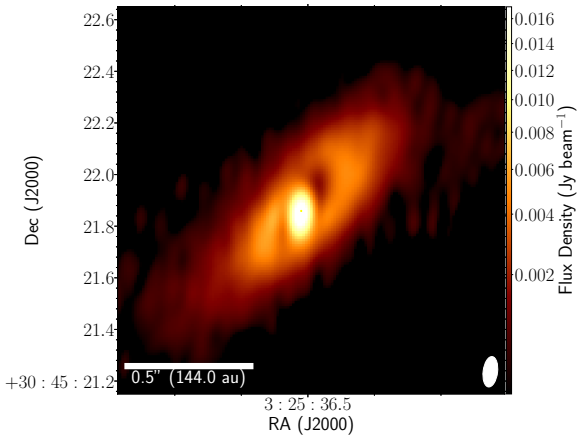

Figure 2.3: : Continuum (879 μm) image of IRS3A, reconstructed with the *superuniform* weighing scheme, half of the cell size, and zoomed 2x from the images in Figure 2.1 to highlight the possible spiral substructure.

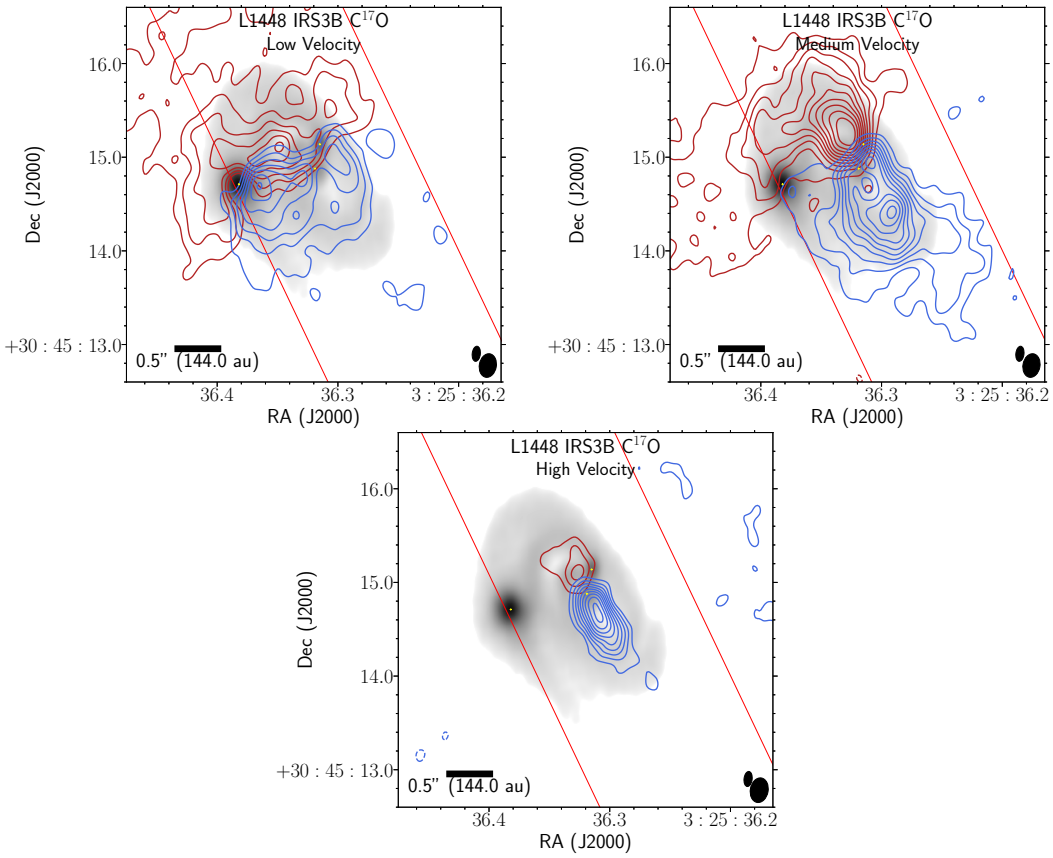

Figure 2.4: : $C^{17}O$ integrated intensity maps towards IRS3B over a selected range of velocities overlayed on continuum (grayscale). The $C^{17}O$ emission traces the rotating gas within the disk via Doppler-shifted emission. The panels correspond to low, medium, and high velocity ranges which are delineated as red(blue), respectively. Negative contours are not present in these integrated intensity maps; however, at the location of IRS3B-c, there is strong absorption that is evident in the high spectral resolution data cube, but is not represented here. The red lines indicate the region extracted for PV diagram construction, along the position angle of the major axis. **Low Velocity:** Velocity range starts at 4.68→5.67 km s^{-1} (3.58→4.68 km s^{-1}) and contours start at 8(8)σ and iterate by 3(3)σ with the 1σ level starting at 0.0023(0.0025) Jy beam^{-1} for the red(blue) channels respectively. **Medium Velocity:** Velocity range starts at 5.67→6.66 km s^{-1} (2.48→3.58 km s^{-1}) and contours start at 3(5)σ and iterate by 3(3)σ with the 1σ level starting at 0.002(0.0016) Jy beam^{-1} for the red(blue) channels respectively. **High Velocity:** Velocity range starts at 6.66→7.65 km s^{-1} (1.27→2.48 km s^{-1}) and contours start at 5(5)σ and iterate by 3(3)σ with the 1σ level starting at 0.0018(0.0012) Jy beam^{-1} for the red(blue) channels respectively. The $C^{17}O$ synthesized beam (0.″21×0.″13) is the bottom-right most ellipse on each of the panels and the continuum synthesized beam (0.″11×0.″05) is offset diagonally.

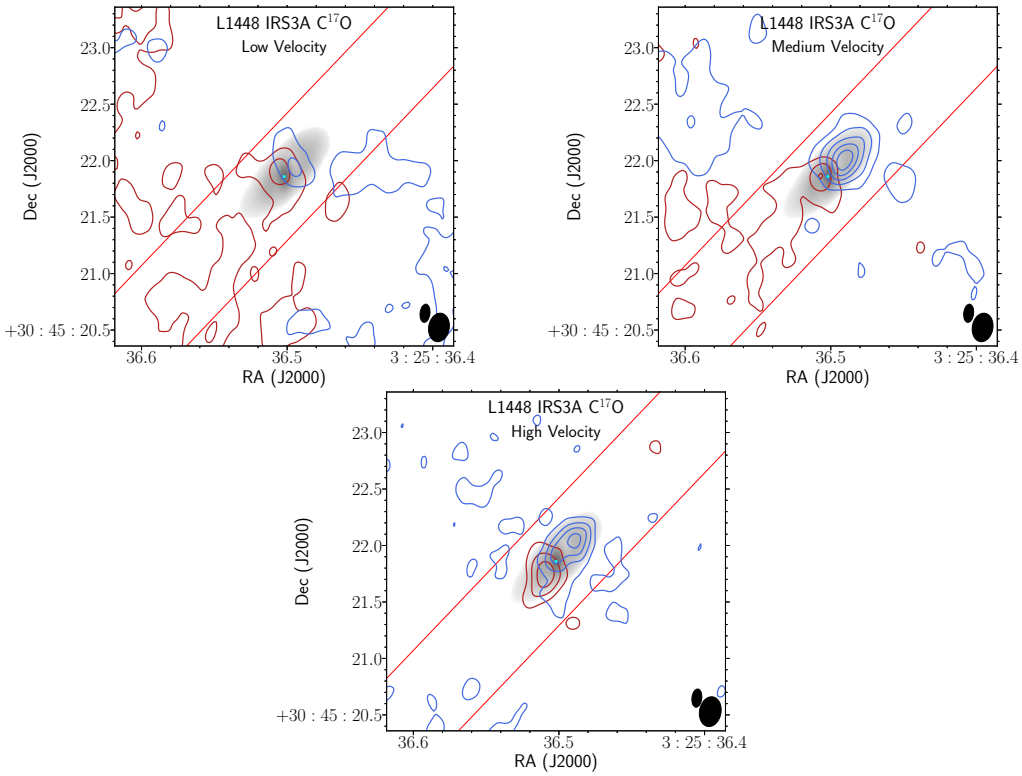

Figure 2.5: : $C^{17}O$ integrated intensity maps toward IRS3A over a selected range of velocities overlayed on continuum (grayscale). The $C^{17}O$ emission exhibits a velocity gradient across the continuum emission. However, S/N is low in comparison to IRS3B. The panels correspond to low, medium, and high velocity ranges which are delineated as red(blue), respectively. The red lines indicate the region extracted for PV diagram construction, along the position angle of the major axis. **Low Velocity:** velocity ranges 5.2→6.5 km s^{-1}(4.1→5.2 km s^{-1}), contours start at 3(3)σ and iterate by 3(3)σ with the 1σ level starting at 0.0023(0.0025) Jy beam^{-1} for the red(blue) channels respectively. **Medium Velocity:** velocity ranges 6.5→7.4 km s^{-1}(3.0→4.1 km s^{-1}), contours start at 3(3)σ and iterate by 3(3)σ with the 1σ level starting at 0.002(0.0016) Jy beam^{-1} for the red (blue) channels respectively. **High Velocity:** velocity ranges 7.4→8.6 km s^{-1}(1.8→3.0 km s^{-1}), contours start at 3(3)σ and iterate by 3(3)σ with the 1σ level starting at 0.0018(0.0012) Jy beam^{-1} for the red(blue) channels respectively. The $C^{17}O$ synthesized beam (0.″21×0.″13) is the bottom-right most ellipse on each of the panels and the continuum synthesized beam (0.″11×0.″05) is offset diagonally.

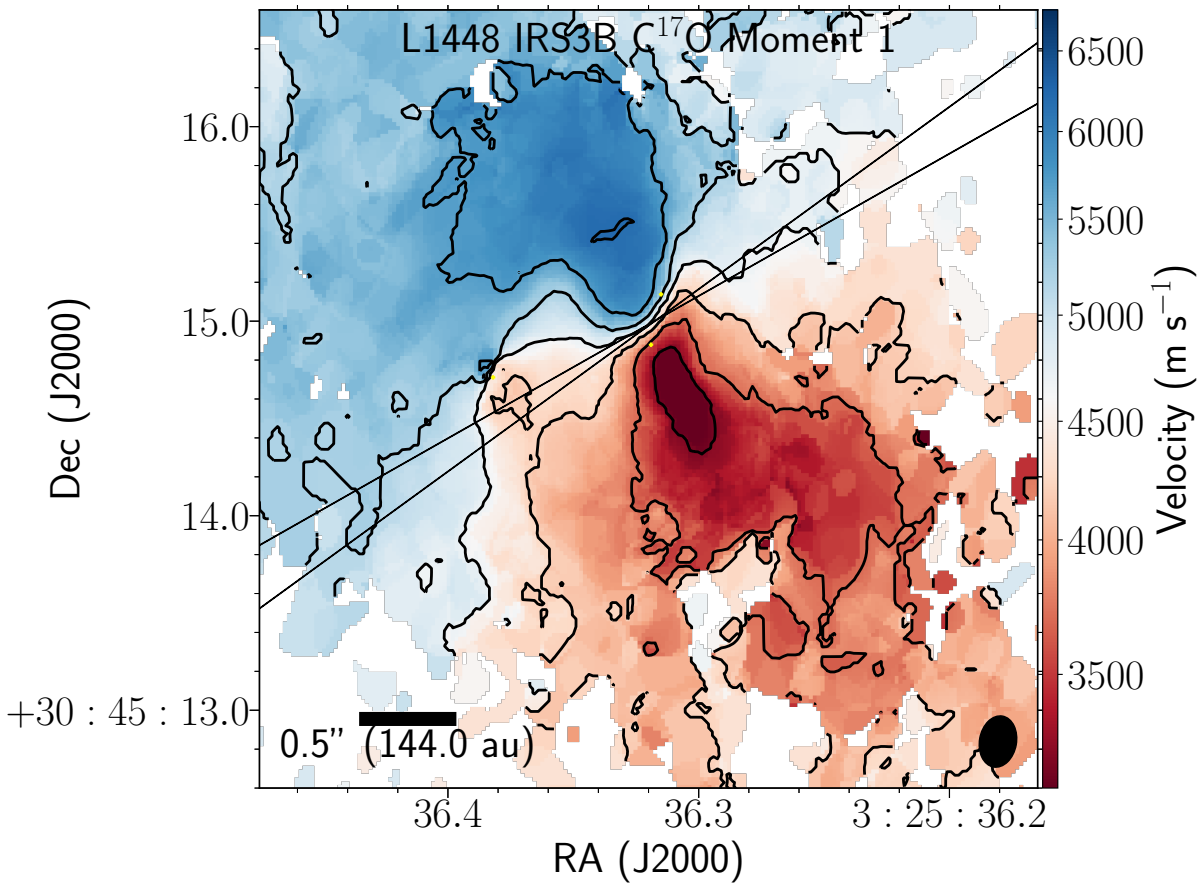

Figure 2.6: : $C^{17}O$ velocity-weighted integrated intensity maps toward IRS3B and IRS3A over a selected range of velocities (1.27→7.65 km s^{-1}) The $C^{17}O$ emission appears well ordered across the semi-major axis. The contours denote the 0.5 km s^{-1} velocity offsets from system velocity of 4.8 km s^{-1}. The yellow markers indicate the three continuum sources. The black lines indicate the position angle of the minor disk estimates as given by the *pdspy* fitting routine in Table 2.4, of $90 + 26.7^{+1.8}_{-2.9}$°. The $C^{17}O$ synthesized beam (0.″21×0.″13) is the bottom-right most ellipse.

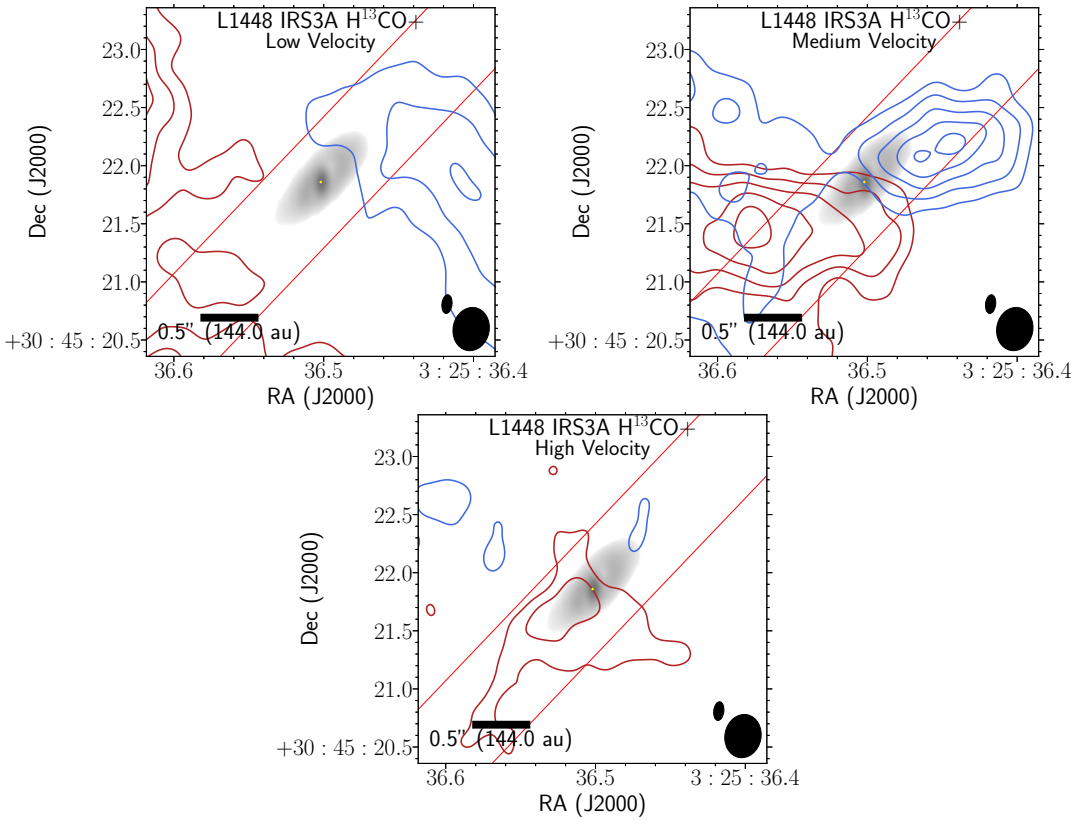

Figure 2.7: : $H^{13}CO+$ integrated intensity maps towards IRS3B over a selected range of velocities overlayed on continuum (grayscale). The top row spatial scale is set to match those of Figure 2.4 and the bottom row scale is set to encapsulate the entire IRS3B system, to better demonstrate the spatial scales probed with this molecule. The top row is tapered with a 400 kλ Gaussian to best reduce the amount of noise and show the proper resolution to the spatial scales shown. The $H^{13}CO+$ emission is primarily tracing the intermediate dense, gaseous material within the inner envelope, but the higher-velocity emission does originate near the protostars. The columns correspond to similar velocity ranges of $C^{17}O$ emission as shown in the previous figure, with low, medium, and high Doppler-shifted velocity ranges delineated as red(blue), respectively. Negative contours do not show additional structure and are suppressed for visual aid. The red lines indicate the region extracted for PV diagram construction, along the position angle of the major axis in a region much larger than the $C^{17}O$ PV diagram extraction to fully capture the emission. **Low Velocity:** velocity ranges 4.7$\rightarrow$5.7 km s^{-1}(3.6$\rightarrow$4.7 km s^{-1})), contours start at 10(10)σ and iterate by 2(2)σ with the 1σ level starting at 0.003(0.003) Jy beam^{-1} for the top row and 0.005(0.005) Jy beam^{-1} for the bottom row, red(blue) channels respectively. **Medium Velocity:** velocity ranges 5.7$\rightarrow$6.7 km s^{-1}(2.4$\rightarrow$3.5 km s^{-1}), contours start at 5(5)σ and iterate by 5(3)σ with the 1σ level starting at 0.005(0.005) Jy beam^{-1} for the top row and 0.005(0.005) Jy beam^{-1} for the bottom row, red(blue) channels respectively. **High Velocity:** velocity ranges 6.7$\rightarrow$7.7 km s^{-1}(1.3$\rightarrow$2.4 km s^{-1}), contours start at 5(5)σ and iterate by 2(2)σ with the 1σ level starting at 0.002(0.002) Jy beam^{-1} for the top row and 0.005(0.005) Jy beam^{-1} for the bottom row, for the red(blue) channels respectively. The $H^{13}CO+$ synthesized beam (top:0.″374$\times$0.″310, bottom: 0.″85$\times$0.″52) is the bottom-right most ellipse on each of the panels and the continuum synthesized beam (0.″11$\times$0.″05) is offset diagonally.

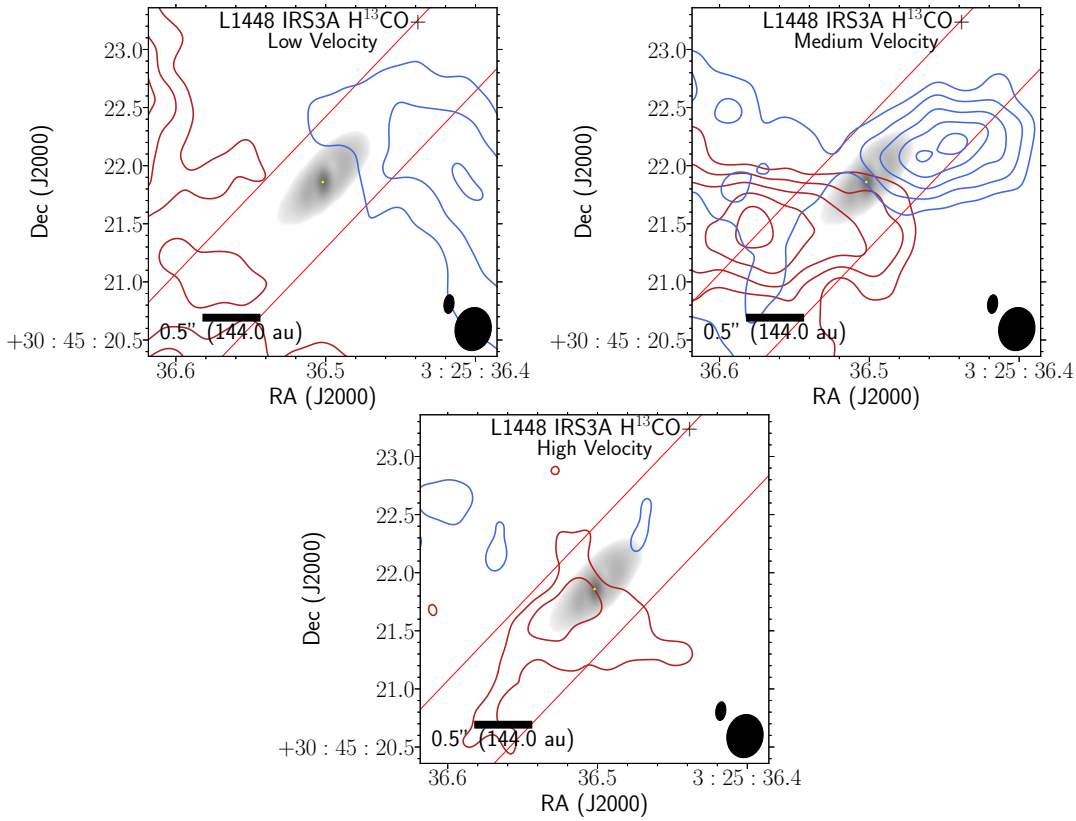

Figure 2.8: : $H^{13}CO+$ integrated intensity map towards IRS3A generated at a position angle of 125°; whose emission predominately traces the intermediate dense, gaseous material of the inner envelope. The image is tapered with a 400 kλ Gaussian to best reduce the amount of noise and show the proper resolution to the spatial scales shown. The $H^{13}CO+$ emission might trace a velocity gradient across the source, but the lack of strong emission coming from the disk itself hinders resolving the kinematics. The columns correspond to low, medium, and high velocity ranges which are delineated as red(blue), respectively. **Low Velocity:** velocity ranges 5.2→6.5 km s^{-1}(4.1→5.2 km s^{-1}), contours start at 5(5)σ and iterate by 2(2)σ with the 1σ level starting at 0.004(0.007) Jy beam^{-1} for the red(blue) channels respectively. **Medium Velocity:** velocity ranges 6.5→7.4 km s^{-1}(3.0→4.1 km s^{-1}), contours start at 3(3)σ and iterate by 2(2)σ with the 1σ level starting at 0.003(0.003) Jy beam^{-1} for the red (blue) channels respectively. **High Velocity:** velocity ranges 7.4→8.6 km s^{-1}(1.8→3.0 km s^{-1}), contours start at 3(3)σ and iterate by 2(2)σ with the 1σ level starting at 0.002(0.0025) Jy beam^{-1} for the red(blue) channels respectively. The $H^{13}CO+$ synthesized beam (0.″85×0.″52) is the bottom-right most ellipse on each of the panels and the continuum synthesized beam (0.″11×0.″05) is offset diagonally.

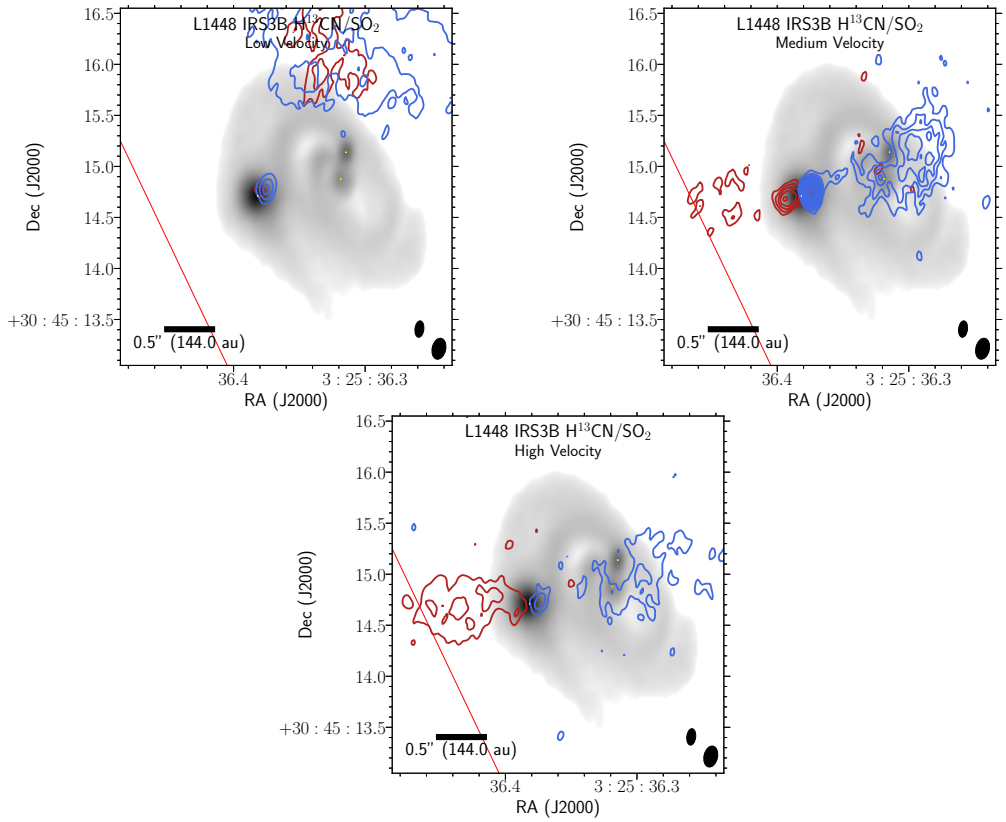

Figure 2.9: : $H^{13}CN/SO_2$ integrated intensity map towards IRS3B, appears to trace near the outflow launch location from the tertiary, IRS3B-c. There is pretty large asymmetry in the velocity channels covered by the red and blue-shifted emission. The panels correspond to low, medium, and high velocity ranges which are delineated as red(blue), respectively. **Low Velocity:** velocity ranges 5.2→7.2 km s^{-1}(4→4.8 km s^{-1}), contours start at 5(5)σ and iterate by 2(5)σ with the 1σ level starting at 0.0025(0.0021) Jy $beam^{-1}$ for the red(blue) channels respectively. **Medium Velocity:** velocity ranges 7.2→9.2 km s^{-1}(3.2→4 km s^{-1}), contours start at 5(5)σ and iterate by 2(2)σ with the 1σ level starting at 0.0016(0.0016) Jy $beam^{-1}$ for the red(blue) channels respectively. **High Velocity:** velocity ranges 9.2→11.2 km s^{-1}(1.6→3.2 km s^{-1}), contours start at 4(4)σ and iterate by 3(3)σ with the 1σ level starting at 0.0021(0.0021) Jy $beam^{-1}$ for the red(blue) channels respectively. The $H^{13}CN$ synthesized beam (0.″22×0.″14) is the bottom-right most ellipse on each of the panels and the continuum synthesized beam (0.″11×0.″05) is offset diagonally.

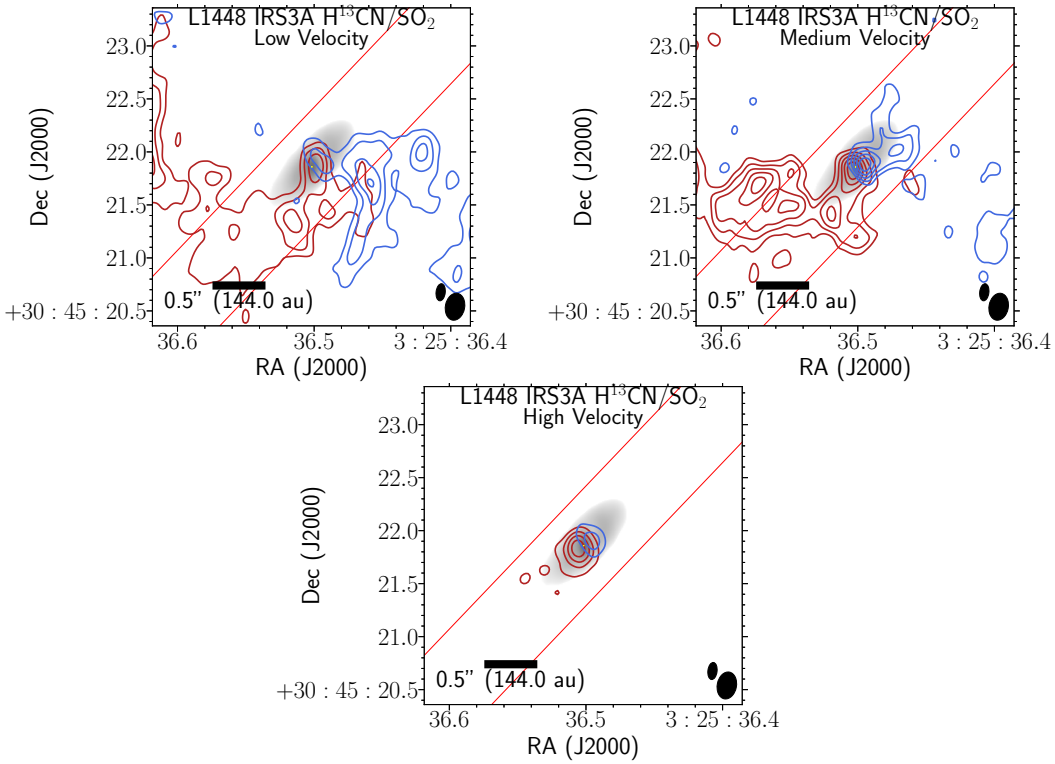

Figure 2.10: : $H^{13}CN/SO_2$ integrated intensity map towards IRS3A; whose emission appears to trace rotation within the inner disk. The panels correspond to low, medium, and high velocity ranges which are delineated as red(blue), respectively. The system velocity of the $H^{13}CN/SO_2$ emission ($\sim$5.4 km s^{-1}) agrees with system velocity of $C^{17}O$, likely tracing $H^{13}CN$ emission and not SO_2 emission. **Low Velocity:** velocity ranges 5.2$\rightarrow$6.5 km s^{-1}(4.1$\rightarrow$5.2 km s^{-1}), contours start at 4(4)σ and iterate by 2(2)σ with the 1σ level starting at 0.0021(0.0021) Jy beam^{-1} for the red(blue) channels respectively. **Medium Velocity:** velocity ranges 6.5$\rightarrow$7.4 km s^{-1}(3.0$\rightarrow$4.1 km s^{-1}), contours start at 4(4)σ and iterate by 2(2)σ with the 1σ level starting at 0.0016(0.0016) Jy beam^{-1} for the red (blue) channels respectively. **High Velocity:** velocity ranges 7.4$\rightarrow$8.6 km s^{-1}(1.8$\rightarrow$3.0 km s^{-1}), contours start at 4(4)σ and iterate by 3(3)σ with the 1σ level starting at 0.0021(0.0021) Jy beam^{-1} for the red(blue) channels respectively. The $H^{13}CN$ synthesized beam (0.$''$22$\times$0.$''$14) is the bottom-right most ellipse on each of the panels and the continuum synthesized beam (0.$''$11$\times$0.$''$05) is offset diagonally.

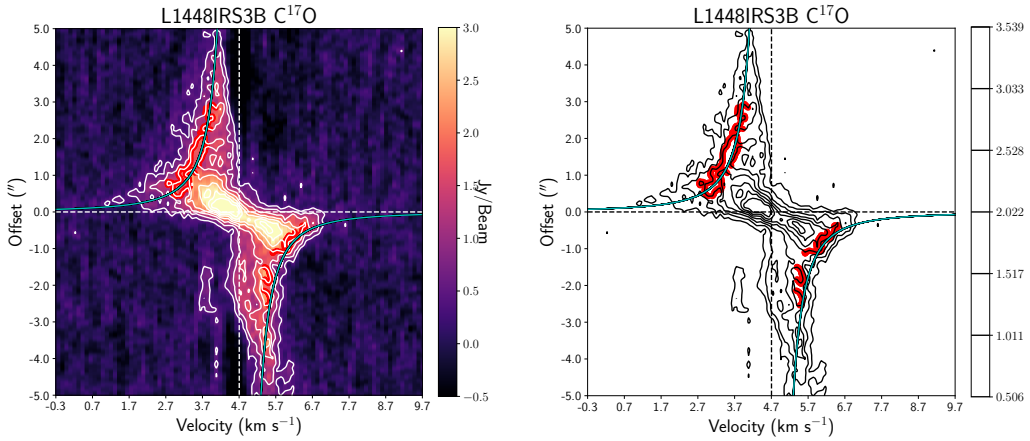

Figure 2.11: : PV-diagrams of IRS3B $C^{17}O$ emission generated at a position angle of 29°, with the cyan lines corresponding to the fit of 1.15 $M_{\odot}$, demonstrating the data could be reproduced reasonably well with a Keplerian disk orbiting a 1.15 $M_{\odot}$ protostar. The cyan line traces the median fit for numeric Keplerian orbital fit routine while the black lines represent 100 randomly sampled MCMC fits, used to estimate errors. As evident, this methodology selectively fits the highest velocity emission that is symmetric in the protostellar system. The white/black contours trace regions starting from 3σ at 2σ intervals, where σ $\approx$0.14 Jy beam^{-1}. The red contours trace the regions selected for the MCMC fit which are defined as the 10 and 12σ levels as to not fit the diffuse large-scale emission.

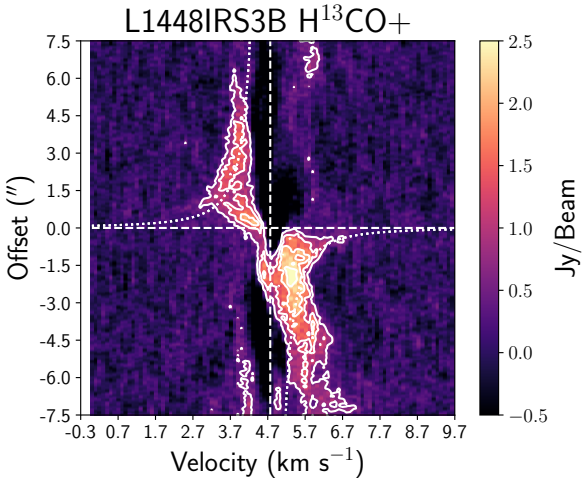

Figure 2.12: : $H^{13}CO+$ emission towards IRS3B generated at a position angle of 29°, with the white dashed lines corresponding to the Keplerian fit of 1.15 $M_\odot$ from the fit to $C^{17}O$, demonstrating the data are not inconsistent with a 1.15 $M_\odot$ protostar, similarly demonstrated from the $C^{17}O$ emission Keplerian fits. The PV diagram shows a large amount of asymmetry in the molecular line emission close to system velocity, with emission at velocities in excess of Keplerian particularly at the red-shifted velocities. These are possible indications of infalling material from the envelope given the spatial location this emission. The white contours trace regions starting from 3σ at 2σ intervals, where $\sigma \approx 0.15$ Jy

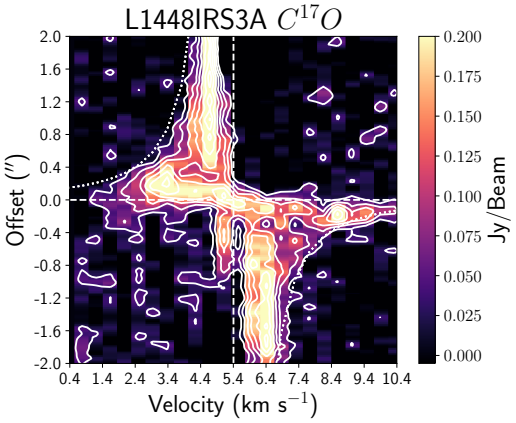

Figure 2.13: : Position-velocity diagrams of IRS3A $C^{17}O$ emission generated at a position angle of 125°, with the dotted lines corresponding to 1.4 $M_\odot$. The emission suffers from the lower spatial sampling across the source and the extended, resolved-out emission from the IRS3B+A envelope/core. Similarly, strong spatial integration (width of slice 0.″3) restrictions were placed when making the PV diagram to limit the inclusion of large-scale emission. The white contours trace regions starting from 3σ at 2σ intervals, where $\sigma \approx 0.15$ Jy.

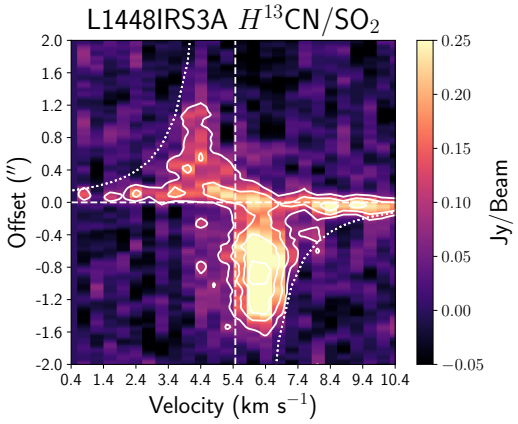

Figure 2.14: : Position-velocity diagram of IRS3A $H^{13}CN/SO_2$ emission with the dotted lines corresponding to Keplerian velocities for a 1.4 $M_\odot$ protostar. This PV diagram places a constraint on the possible protostellar mass parameter of $\sim$1.4 $M_\odot$. The IRS3A mass is less well constrained due to the compactness of the emission. Strong spatial integration (width of slice 0.″3) restrictions were placed when making the PV diagram to help limit the inclusion of large scale emission.

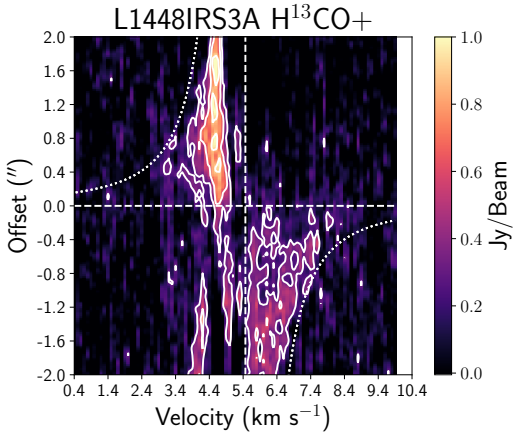

Figure 2.15: : Position-velocity diagram of IRS3A $H^{13}CO+$ generated at a position angle of 125°; whose emission predominately traces the intermediate dense, gaseous material of the inner envelope. The emission is fainter and is coming from the outerdisk/inner-envelope. The dotted line corresponds to a central protostellar mass of 1.4 $M_\odot$.

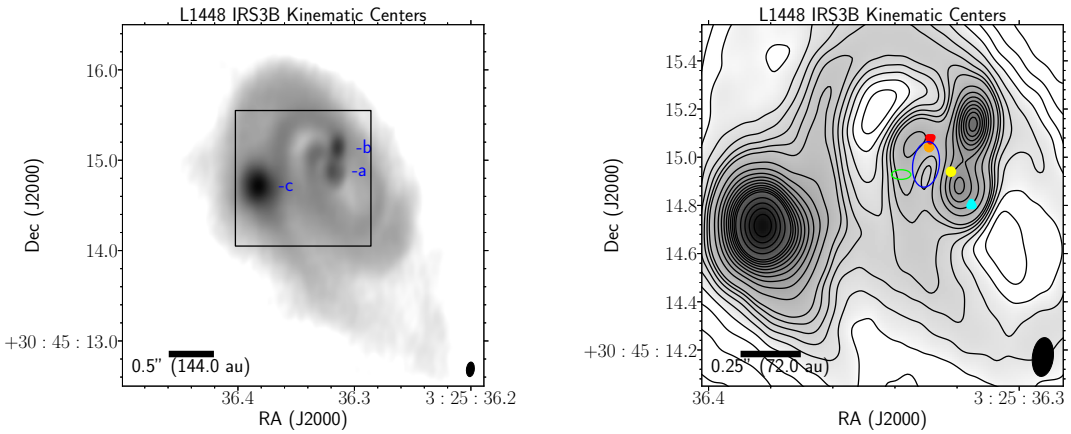

Figure 2.16: : Positions of the various "kinematic centers" that have been fit from $C^{17}O$ emission at IRS3B in relation to continuum structure. The grayscale is the dust continuum from Figure 2.1. Left: The red colored texts detail the locations of continuum sources, presumed to be protostars. Right: A zoom in on the region indicated by the black rectangle in the left image. The red and blue triangles indicate the central Gaussian fit of the highest Doppler-shifted velocity emission with the yellow circle indicating the midpoint. The orange circle indicates the center that best constructs the PV diagram symmetrically. The green ellipse is the model Keplerian centroid fit with the respective error as indicated by the size of the ellipse (see Section 2.5). The blue ellipse is the $C^{17}O$ beam ($0.''21 \times 0.''13$) centered on the region of emission deficit for size comparison. The contours start at 10σ and iterate by 10σ with the 1σ level starting at 8.5×10^{-5} Jy beam^{-1}. The region of deficit, first identified in Figure 2.2 is shown to be centered within the three various kinematic center fits and are marginally separated by less than a few beams.

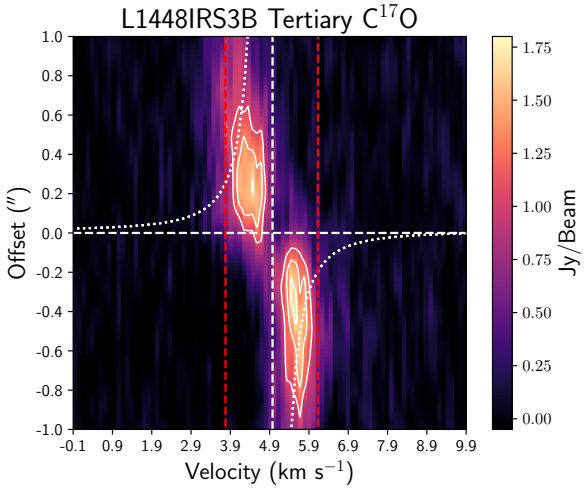

Figure 2.17: : PV-diagram of $C^{17}O$ toward IRS3B-c, the tertiary. The white lines corresponding to a Keplerian curve of a 0.2 $M_\odot$ protostellar source. These fits place an upper limit to the mass of the tertiary companion to $<$0.2 $M_\odot$, since any larger mass and we would expect to see emission extending to high velocity, indicating the tertiary would be affecting disk kinematics. The red dashed lines indicate the maximum Keplerian velocities at the radius of IRS3B-c in the rotating disk corresponding to the 1.15 $M_\odot$ mass of the central potential. Emission outside of these bounds could be due to the tertiary affecting disk kinematics, but from this analysis, we could not detect an obvious effect of the tertiary on the disk kinematics. The white/black contours trace regions starting from 14σ at 4σ intervals, where $\sigma \approx$0.1 Jy beam^{-1}.

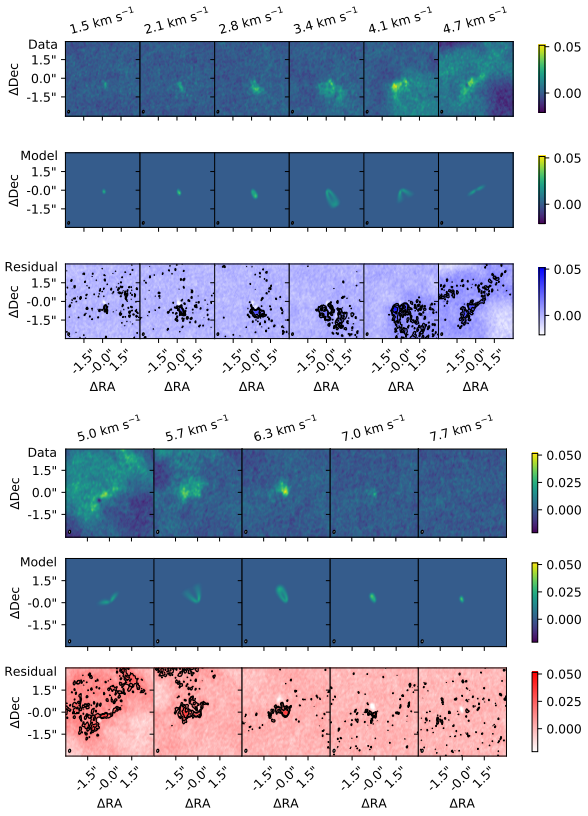

Figure 2.18: : IRS3B Kinematic Model comparison: A representative selection of channel maps that demonstrate the fit of the model to the data. The top figure is the blue Doppler shifted emission while the bottom figure is the red Doppler shifted emission. The first row contours are the model contours, generated at the 2, 3, 5, and 10σ level overlaid the data channels selected at the same velocity. The second row is the residual contours (2 and 3σ) overlaid the same data channels. System velocity is $\sim$4.8 km s^{-1}. It should be noted the highly correlated structure visible in the residuals. This reflects an imperfect fit to the data given that the circumstellar disk itself is asymmetric.

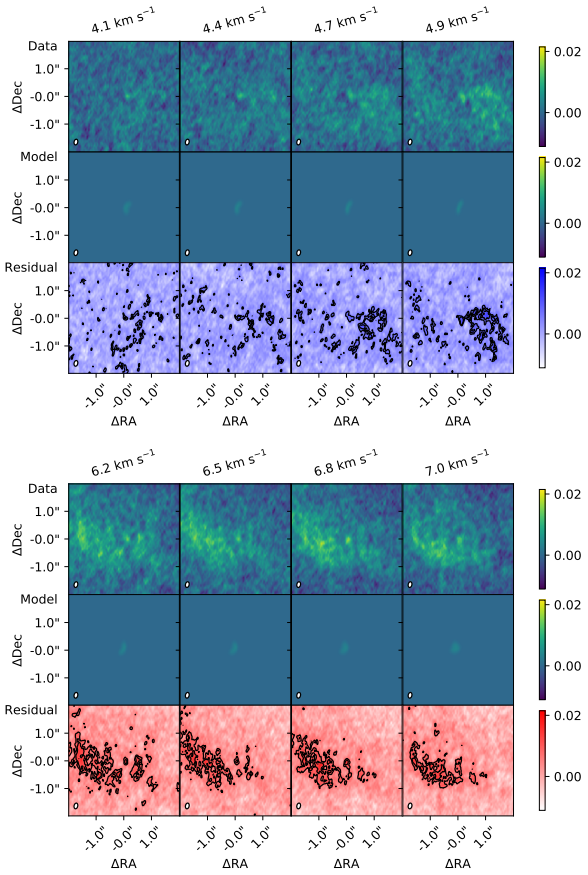

Figure 2.19: : IRS3A Kinematic Model comparison: A representative selection of channel maps that demonstrate the fit of the model to the data. The top figure is the blue Doppler shifted emission while the bottom figure is the red Doppler shifted emission. The first row contours are the model contours, generated at the 2, 3, 5, and 10σ level overlaid the data channels selected at the same velocity to not overshadow the emission. The second row is the residual contours overlaid the same data channels. System velocity is $\sim$5.2 km s^{-1}. There is residual emission at scales much larger than the continuum disk, especially prevalent near the system velocity, likely due to large scale emission from the cloud that is not included in the disk.

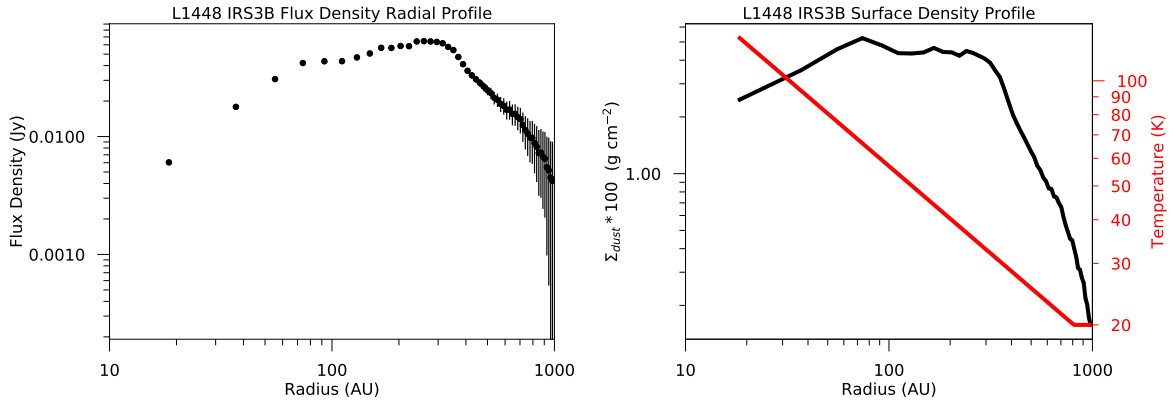

Figure 2.20: : The left plot is the continuum flux density radial profile of IRS3B. The right plot is the deprojected radial surface density profile of the dust continuum in black , while the red line is the radial temperature profile of the disk. The temperature profile is $\propto$ R$^{-0.5}$ and is scaled such that at 100 AU is described via (30 K)$\times(L_*/\mathrm{L}_\odot)^{0.25} \approx 40.1$ K.

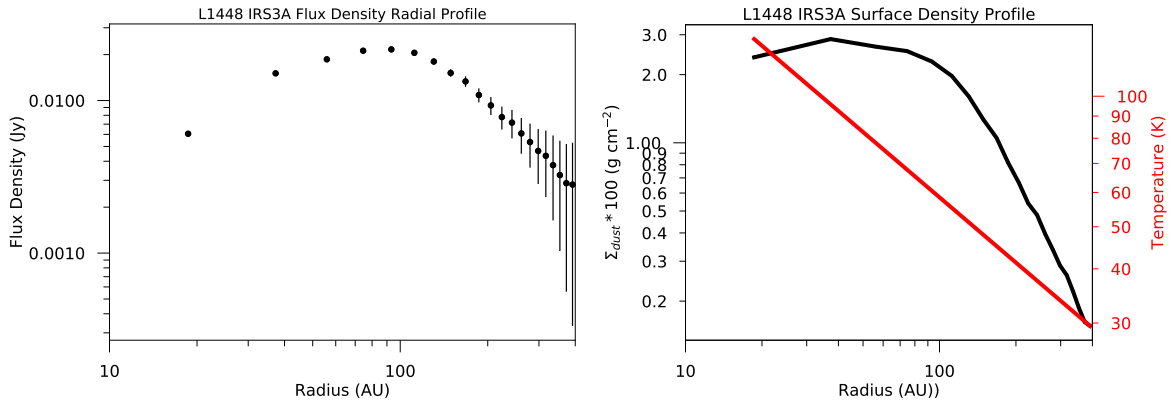

Figure 2.21: : The left plot is the continuum flux density radial profile of IRS3A. The right plot is the radial surface density profile of the dust continuum in black, while the red line is the radial temperature profile of the disk. The temperature profile is $\propto$ R$^{-0.5}$ and is scaled such that at 100 AU is described via (30 K)$\times(L_*/\mathrm{L}_\odot)^{0.25} \approx 53.1$ K.

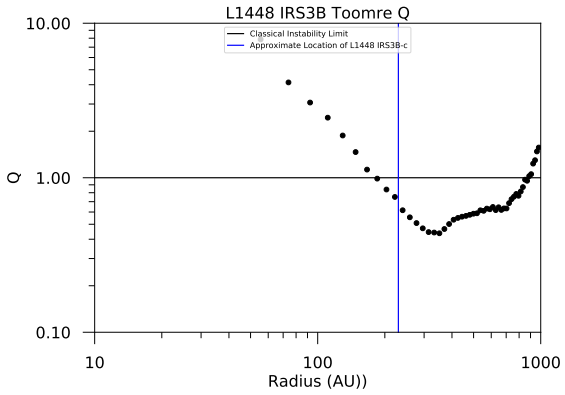

Figure 2.22: : Toomre Q parameter plotted as a function of deprojected radius for IRS3B. The horizontal line indicates a Toomre Q parameter of one, at which the disk would be gravitationally unstable. As indicated, the disk Toomre Q parameter drops below 1 at a radius of $\sim$120 AU. The vertical line corresponds to the deprojected radius of IRS3B-c. The observed spiral arms also become most prominent at R $>$100 AU, where Toomre Q approaches 1.

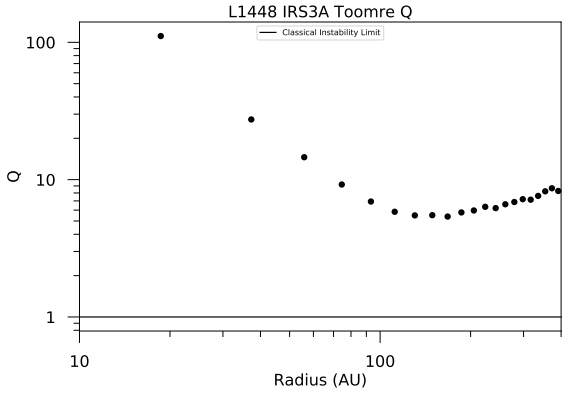

Figure 2.23: : Toomre Q parameter plotted as a function of deprojected radius for IRS3A. The horizontal line indicates a Toomre Q parameter of one, at which the disk would be gravitationally unstable. The circumstellar disk of IRS3A is much less massive than IRS3B, coupled with a more massive protostar, the disk is more stable against gravitational instabilities.

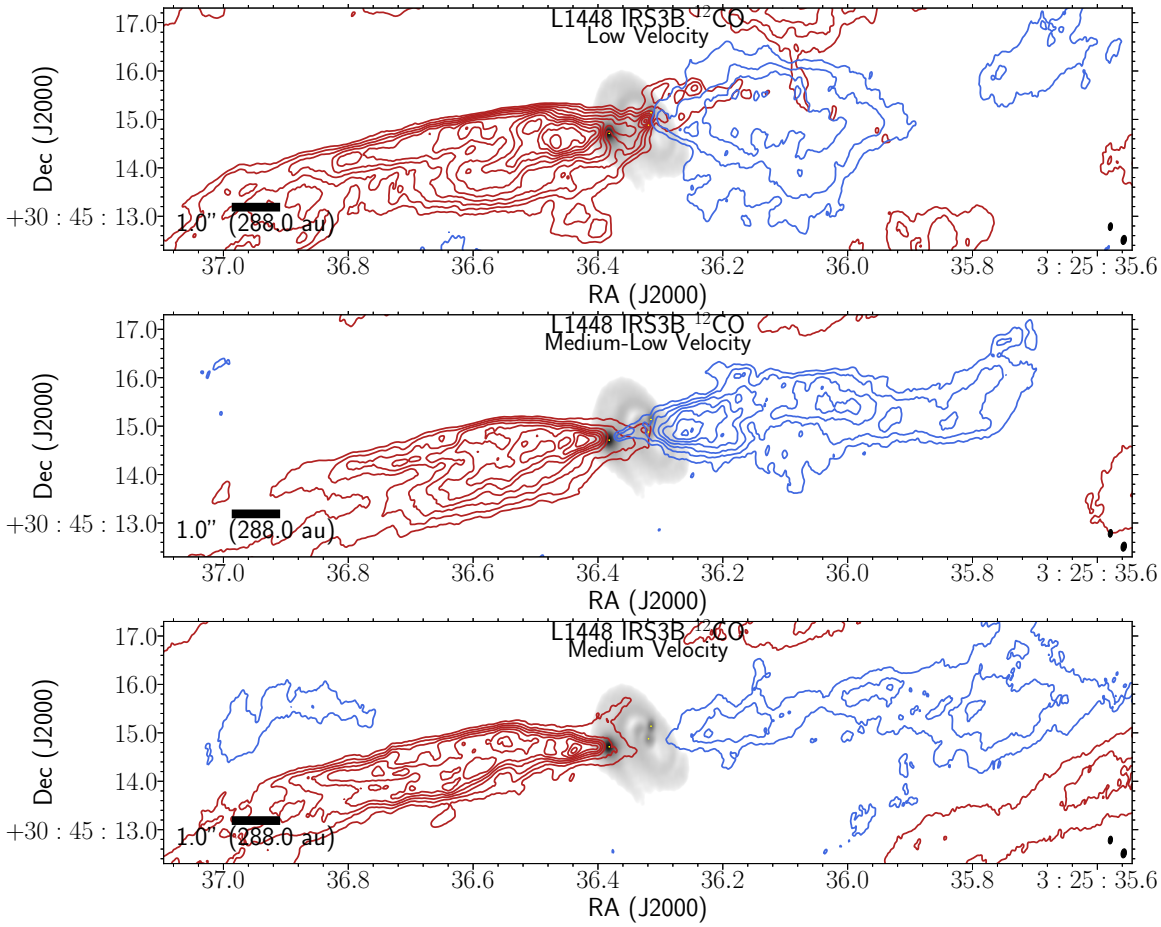

Figure 2.24: : Moment 0 map (integrated intensity) of ^{12}CO, overlaid on the continuum (grayscale) image from Figure 2.1, split up according to velocity ranges, providing exquisite detailing of the location and collimated of the IRS3B outflows. The central outflow from IRS3B extends 10″ (2880 au), beyond the edge of the primary beam of ALMA at 879 micron, from launch location on either side. The panels correspond to low, medium-low, and medium velocity ranges which are delineated as red(blue), respectively. **Low Velocity:** velocity ranges 5.5→10.5 km s^{-1} (4→-1 km s^{-1}), contours start at 3(3) σ and iterate by 2(2) σ with the 1-σ level starting at 0.1(0.1) Jy beam^{-1} for the red(blue) channels respectively. **Medium-low Velocity:** velocity ranges 10.5→15.5 km s^{-1} (-6→-4 km s^{-1}), contours start at 5(5) σ and iterate by 3(2) σ with the 1-σ level starting at 0.04(0.004) Jy beam^{-1} for the red(blue) channels respectively. **Medium Velocity:** velocity ranges 15.5→20.5 km s^{-1} (-11→-6 km s^{-1}), contours start at 10(10) σ and iterate by 4(4) σ with the 1-σ level starting at 0.02(0.02) Jy beam^{-1} for the red(blue) channels respectively. The ^{12}CO synthesized beam (0.″19×0.″11) is the bottom-right most overlay on each of the panels and the continuum synthesized beam (0.″11×0.″05) is offset diagonally.

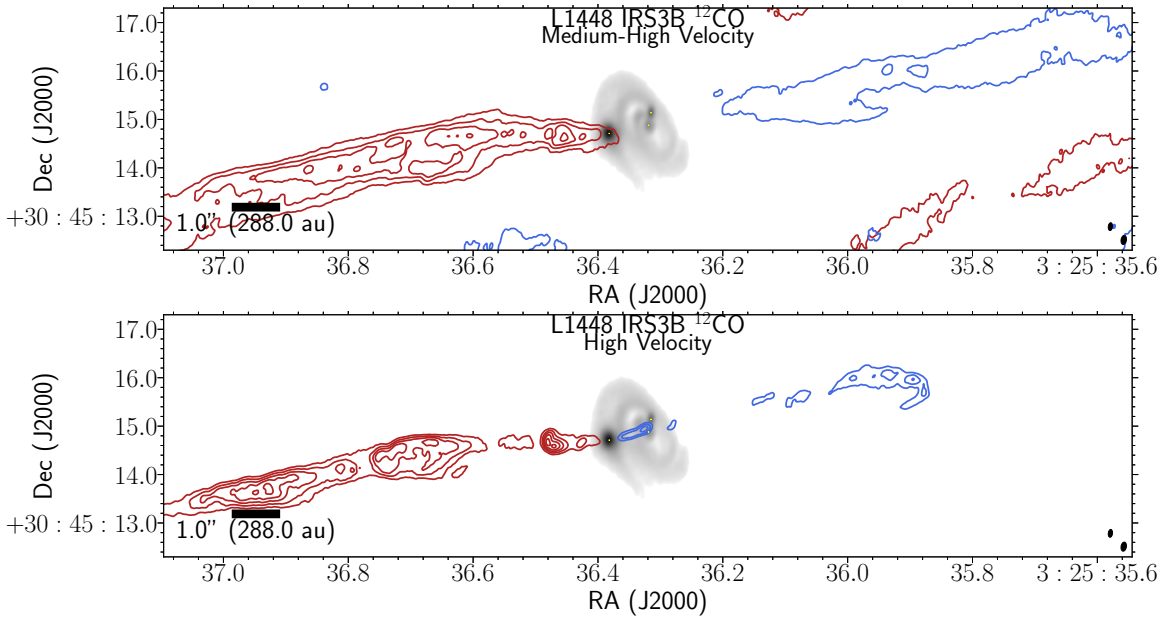

Figure 2.25: : Same as Figure 2.24 but for the **Medium-high Velocity:** velocity ranges 20.5→25.5 km s^{-1} (-16→-11 km s^{-1}), contours start at 3(3) σ and iterate by 4(4) σ with the 1-σ level starting at 0.04(0.04) Jy beam^{-1} for the red(blue) channels respectively. **High Velocity:** velocity ranges 25.5→30.5 km s^{-1} (-21→-16 km s^{-1}), contours start at 5(5) σ and iterate by 2(2) σ with the 1-σ level starting at 0.04(0.04) Jy beam^{-1} for the red(blue) channels respectively. The ^{12}CO synthesized beam (0.″19×0.″11) is the bottom-right most overlay on each of the panels and the continuum synthesized beam (0.″11×0.″05) is offset diagonally.

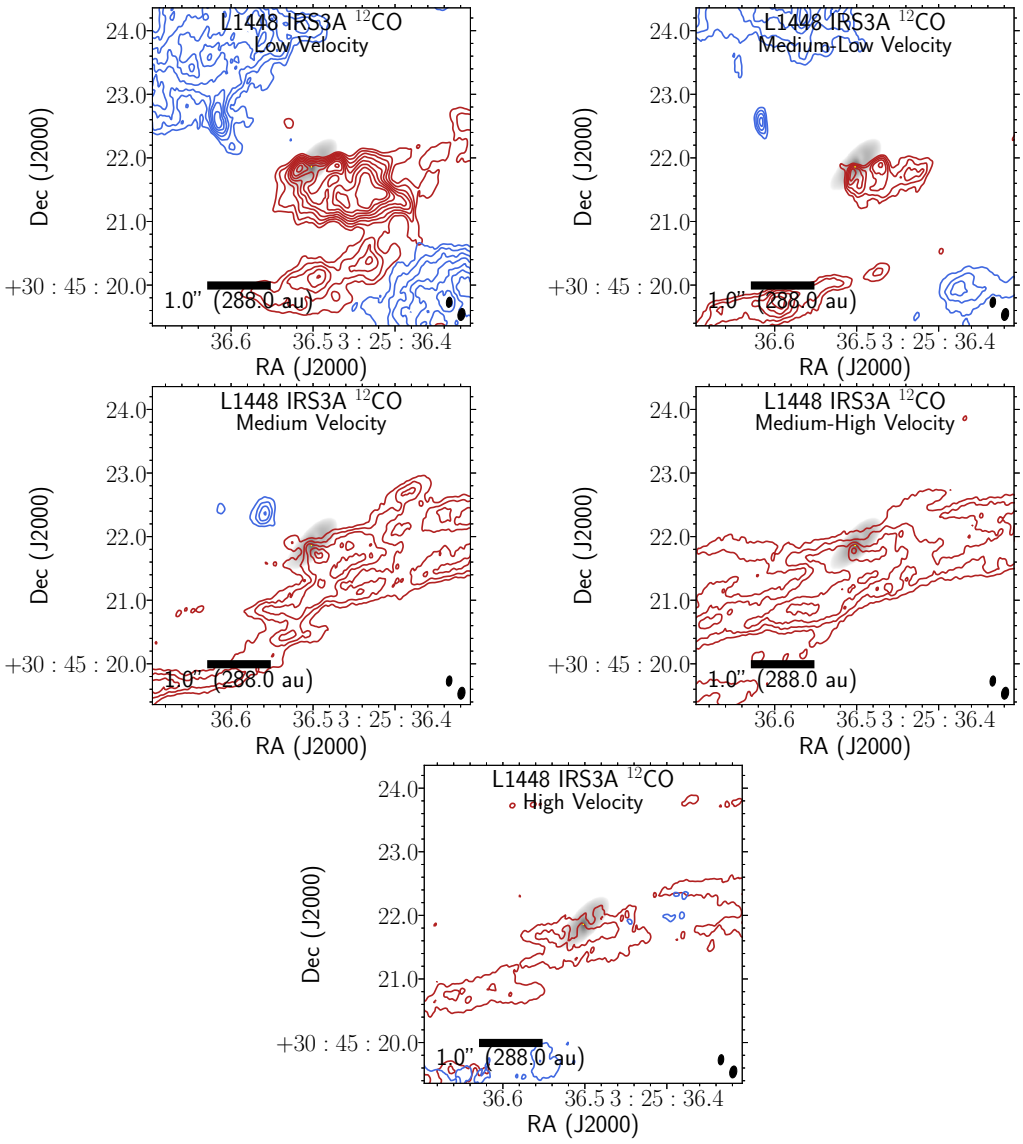

Figure 2.26: : Similar to Figures 2.24 and 2.25 towards the IRS3A source with the same velocity ranges. **Low Velocity:** velocity ranges 5.5→10.5 km s^{-1} (4→-1 km s^{-1}), contours start at 5(5) σ and iterate by 4(2) σ with the 1-σ level starting at 0.1(0.1) Jy beam^{-1} for the red(blue) channels respectively. **Medium-low Velocity:** velocity ranges 10.5→15.5 km s^{-1} (-6→-4 km s^{-1}), contours start at 5(5) σ and iterate by 2(2) σ with the 1-σ level starting at 0.04(0.004) Jy beam^{-1} for the red(blue) channels respectively. **Medium Velocity:** velocity ranges 15.5→20.5 km s^{-1} (-11→-6 km s^{-1}), contours start at 5(5) σ and iterate by 2(2) σ with the 1-σ level starting at 0.02(0.02) Jy beam^{-1} for the red(blue) channels respectively. **Medium-high Velocity:** velocity ranges 20.5→25.5 km s^{-1} (-16→-11 km s^{-1}), contours start at 3(3) σ and iterate by 2(2) σ with the 1-σ level starting at 0.04(0.04) Jy beam^{-1} for the red(blue) channels respectively. **High Velocity:** velocity ranges 25.5→30.5 km s^{-1} (-21→-16 km s^{-1}), contours start at 3(3) σ and iterate by 2(2) σ with the 1-σ level starting at 0.04(0.04) Jy beam^{-1} for the red(blue) channels respectively. The ^{12}CO synthesized beam (0.″19×0.″11) is the bottom-right most overlay on each of the panels and the continuum synthesized beam (0.″11×0.″05) is offset diagonally.

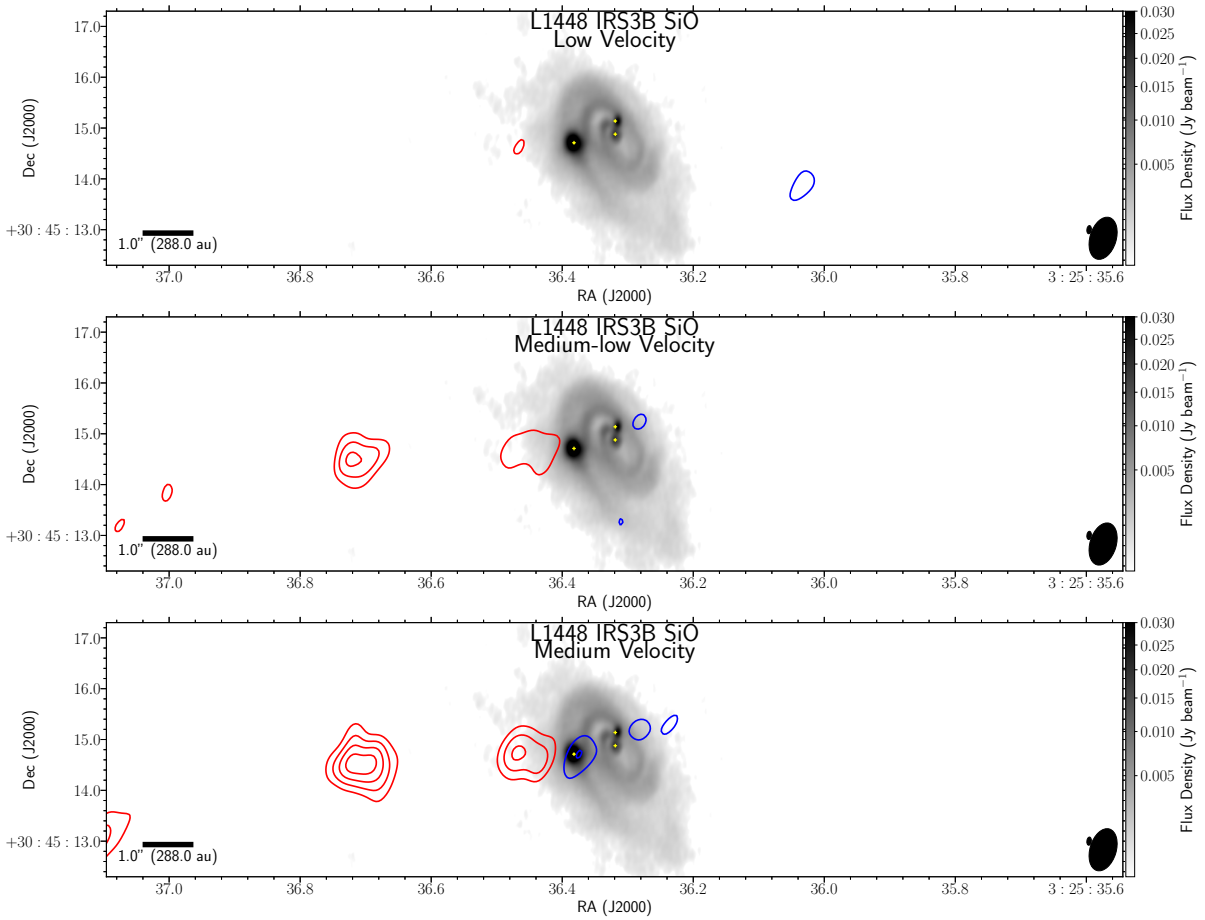

Figure 2.27: : Moment 0 map (integrated intensity) of SiO, overlaid on the continuum (grayscale) image from Figure 2.1. SiO shows locations of shocked gas fronts. The panels correspond to low, medium-low, and medium velocity ranges which are delineated as red(blue), respectively. **Low Velocity:** velocity ranges 5.5→10.5 km s^{-1} (4→-1 km s^{-1}), contours start at 5(5) σ and iterate by 3(3) σ with the 1-σ level starting at 0.11(0.09) Jy beam^{-1} for the red(blue) channels respectively. **Medium-low Velocity:** velocity ranges 10.5→15.5 km s^{-1} (-6→-4 km s^{-1}), contours start at 5(5) σ and iterate by 3(3) σ with the 1-σ level starting at 0.01(0.01) Jy beam^{-1} for the red(blue) channels respectively. **Medium Velocity:** velocity ranges 15.5→20.5 km s^{-1} (-11→-6 km s^{-1}), contours start at 5(5) σ and iterate by 3(3) σ with the 1-σ level starting at 0.009(0.012) Jy beam^{-1} for the red(blue) channels respectively. The SiO synthesized beam (0.″85×0.″52) is the bottom-right most overlay on each of the panels and the continuum synthesized beam (0.″11×0.″05) is offset diagonally.

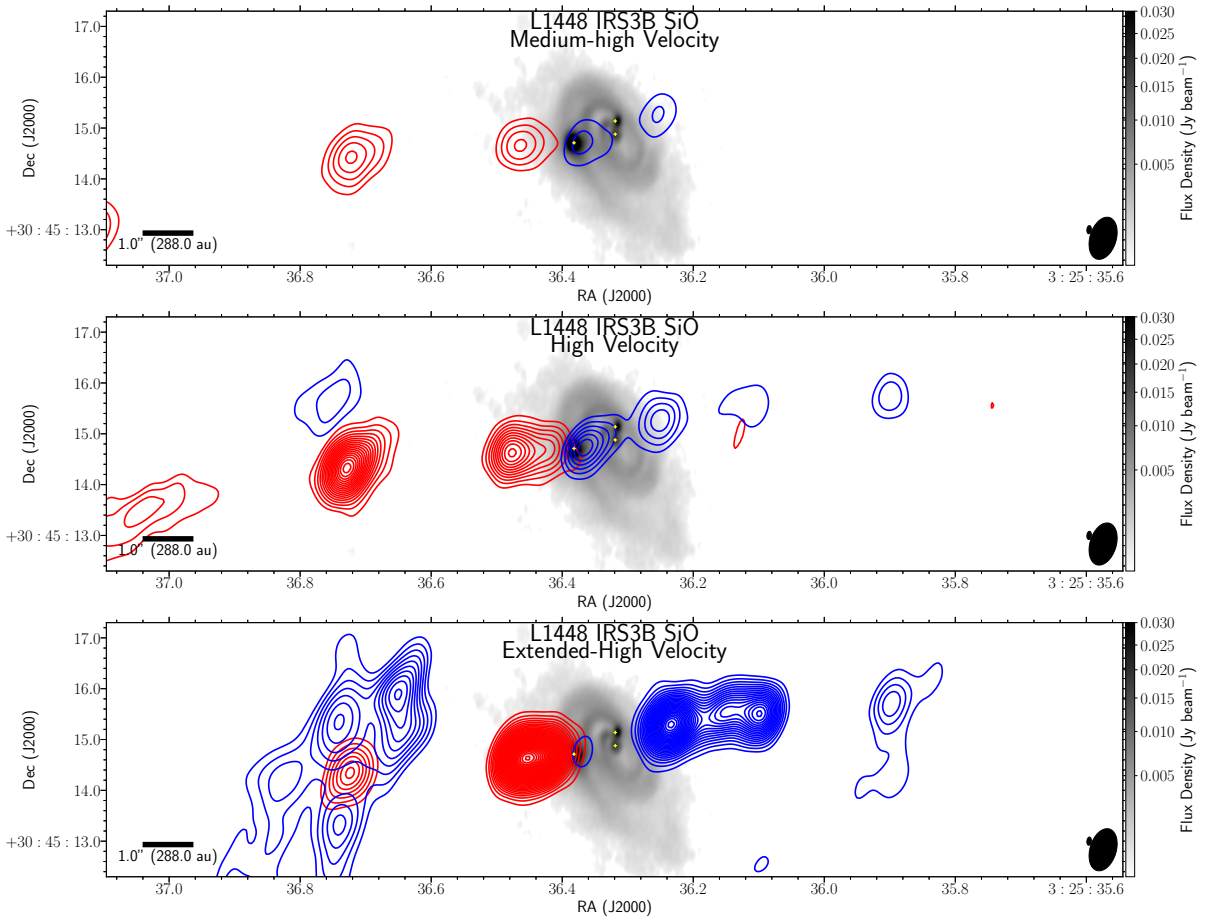

Figure 2.28: : Similar to Figure 2.27 but for the **Medium-high Velocity:** velocity ranges 20.5→25.5 km s^{-1} (-16→-11 km s^{-1}), contours start at 5(5) σ and iterate by 3(3) σ with the 1-σ level starting at 0.012(0.015) Jy beam^{-1} for the red(blue) channels respectively. **High Velocity:** velocity ranges 25.5→30.5 km s^{-1} (-21→-16 km s^{-1}), contours start at 5(5) σ and iterate by 3(3) σ with the 1-σ level starting at 0.008(0.015) Jy beam^{-1} for the red(blue) channels respectively. **Extended-High Velocity:** velocity ranges 30.5→50 km s^{-1} (-40→-21 km s^{-1}), contours start at 5(5) σ and iterate by 3(3) σ with the 1-σ level starting at 0.025(0.025) Jy beam^{-1} for the red(blue) channels respectively. There is significant blue-shifted emission on the eastern side of the image, in the same location as the red-shifted outflow, which is coming from the L1448-C outflow, located $\sim$3′south of L1448 IRS3B. The SiO has additional emission well beyond the velocity range of the emission in ^{12}CO and is presented as an additional panel ("extended-high velocity") which only features the red-shifted emission. The SiO synthesized beam (0.″85×0.″52) is the bottom-right most overlay on each of the panels and the continuum synthesized beam (0.″11×0.″05) is offset diagonally.

Appendix

2.A. Observations

The ALMA correlator was configured to observe CO, $C^{17}O$, $H^{13}CO+$, $H^{13}CN$, SiO, and a broad 2 GHz continuum band centered at 335.5 GHz (894 μm). A summary of the correlator setup is provided in Table 2.2. The raw data were reduced using the Cycle 4 ALMA pipeline within the *Common Astronomy Software Application* (CASA) (McMullin et al., 2007) version 4.7.0. All further processing was done using the CASA version 4.7.2 and the reduction sequence is described here. To maximize the sensitivity of the continuum observations, emission free channels from the higher resolution windows were added to the continuum after appropriate flagging of line emission. The total bandwidth recovered from this method was $\sim$1.2 GHz, which, in conjunction with the continuum spectral window bandwidth of 1.875 GHz, yields $\sim$3 GHz of aggregate continuum bandwidth with an average frequency center of 341.0 GHz. Given the high signal-to-noise (S/N) of the sources, we performed self-calibration (summary to reproduce in Table 2.7) on the separate configurations (C40-3 and C40-6) to further increase the S/N by correcting short timescale phase and amplitude fluctuations. During the phase-only self-calibration, the solution intervals for each additional iteration were: "inf" (The entire scan length, dictated by the time on a single pointing), 30.25 seconds (5 integrations), and 12.1 seconds (2 integrations). During the amplitude self-calibration, the solution interval of "inf" was used. The final self-calibrated measurement sets from the two configurations were concatenated using the CASA task *concat*. The resulting images were generated from this concatenated dataset using *Briggs weighting* with a *robust* parameter of 0.5 (Figure 2.1). The beamsize of the combined continuum image is $0.''11\times0.''05$ (32×15 au). We achieved 69 μJy beam^{-1} sensitivity for the aggregate continuum data and the full list of frequencies, bandwidths, beamsizes, sensitivities, and tapering for the suite of molecules is provided in Table 2.2.

During the high-resolution execution, the central frequency of the SiO spectral window was set to 347.01 GHz with a bandwidth of 469 MHz, falling outside of the emission range for the target molecule. However, for the C40-3 configuration, the spectral setup was corrected

and SiO was observed.

2.B. Optimal Disk tracing Molecular lines

To infer properties about the central potential from the circumstellar disk characteristics, we must disentangle the envelope and disk kinematics from the molecular line emission. Previous observations conducted by Tobin et al. (2016a) of IRS3B included molecular lines $C^{18}O$ and ^{13}CO. However, while emission from $C^{18}O$ spatially coincides with the disk and is optically thin, it can have resolved-out emission towards the molecular line center, under-representing the underlying gas structure and reducing the fidelity of the tracer (Booth & Ilee, 2020). Furthermore, ^{13}CO is a poor kinematic tracer for embedded Class 0 disks because it is a more abundant molecule that will have a high optical depth (and subsequently a larger degree of spatial filtering which limits the velocity range it is sensitive to) and confusion with the outflow. This tracer is better suited towards more evolved Class I sources (possibly IRS3A). Combining all previous observations of the sources, we found $C^{17}O$ is possibly the best tracer for Class 0 disks, being the least abundant molecule and thus experiencing the least amount of spatial filtering, both of which allow for accurate emission reconstruction near the line center. However, due to the low abundance, this molecule requires substantial integration time and is not suited for Class I disks.

2.C. Application of Radiative Transfer Models

We generated a set of *priors* for the protostellar parameters based on the observational constraints. These *priors* are then sampled via a uniform distribution and fed into *emcee* to generate the samples, each sample describing a unique set of model parameters. These parameters are used to generate synthetic channel maps for the lines of interest, computed with RADMC-3D. These synthetic data cubes are Fourier transformed to recover a synthetic visibility dataset. These are re-gridded and subsequently cross-compared with the observed data in the uv-plane. The likelihood of the parameters for this comparison is then updated internally, the MCMC either probabilistically accepts the sample and migrates to this new point, or does not accept it by comparing the new likelihood to the previous sample. The whole process is repeated until convergence.

We assumed the kinematic rotation of the disk is described by a Keplerian orbit, with an

azimuthal velocity (in cylindrical coordinates) of $V(R) = \sqrt{GM/R}$. We assumed the molecular line emission comes from a flared disk geometry as motivated by viscous and irradiated disk evolution, where the mass density profile is described, in cylindrical coordinates with the origin at the gravitational source, by the equation:

$$\rho\left(R,z\right) = \frac{\Sigma(R)}{\sqrt{2\pi}h(R)} exp\left(-0.5\left(\frac{z}{h(R)}\right)^2\right) \tag{2.8}$$

where R is the distance in the radial direction in cylindrical coordinates, Σ is the surface mass density of each molecule species, and *h* is the disk scale height. We assumed the disk can be described via a power-law surface mass density profile that is truncated at some outer radius, of the form:

$$\Sigma\left(R\right) = \Sigma_0 \times R^{-\gamma}. \tag{2.9}$$

We also defined

$$\Sigma_0 = \frac{(2-\gamma)M_{disk}}{2\pi\left(R_{out}^{2-\gamma} - R_{in}^{2-\gamma}\right)} \tag{2.10}$$

where R_{out} is the outer cutoff radius, R_{in} is the inner cutoff radius, and γ is the surface density power law exponent.

Another assumption we made is that the vertical structure of the disk is set by Local Hydrostatic Equilibrium (LHSE) with a vertically isothermal temperature profile and a radial power-law temperature profile of the form:

$$T\left(R\right) = T_0\left(\frac{R}{1\ au}\right)^{-q} \tag{2.11}$$

which then sets the scale height of the disk, under the balance of thermal pressure and gravity, to be

$$h\left(R\right) = \left(\frac{k_b R^3 T(R)}{GM\mu m_H}\right)^{1/2} \tag{2.12}$$

where k_b is the Boltzmann constant, G is the gravitational constant, m_H is the mass of hydrogen, and μ is the mean molecular weight (assuming classic protostellar mean molecular weight, $\mu \approx 2.37$; Lodders, 2003). Additionally, chemical variations such as gas freeze-out onto dust grains towards the midplane and outer disk are excluded from the models.

Combining the aforementioned parameters that describe the disk structure plus the inclusion of disk geometric orientations, we have the following free parameters: position angle (p.a.), inclination (inc.), temperature (T_0), stellar mass (M_*), disk radius (R_D), disk mass (M_{disk}), surface density power law (γ), system source velocity (V_{sys}), and uniform microturbulent line broadening (α) (Table 2.5). Furthermore, we have a number of fixed parameters that are used throughout the models but are not fit: molecular gas-to-H_2 abundance ratio (for IRS3B $C^{17}O$ =5.88×10^{-8}; for IRS3A $H^{13}CN$ =2.04×10^{-7}), inner disk cutoff radius (R_{in} = 0.1 au), and the temperature power law index (q = 0.35).

The combined fitting is computationally expensive, requiring on order 10^4 core-hours to reach convergence. A bulk of the computation time (up to 10 minutes per individual model) is used when RADMC-3D attempts to ray-trace massive disks.

2.D. Outflows

2.D.1. ^{12}CO Line Emission

The second most abundant molecule to H_2, ^{12}CO, is shown as moment 0 maps in Figures 2.24, 2.25, and 2.26. The ^{12}CO integrated intensity maps towards IRS3B (Figures 2.24 and 2.25) show clear signs of a collimated outflow originating from a region near IRS3B-ab and IRS3B-c that extends to $\sim$20″. Outflows are thought to be a signature of stellar birth with the highest velocity outflows (>20 km s^{-1}) and high collimation are frequently found toward Class 0 protostars (Andre et al., 1993). We observed asymmetric emission of the ^{12}CO outflows with excess red-shifted emission dominating the data cube. The low velocity outflows appear to originate from IRS3B-ab while the high velocity jets appear to originate from both IRS3B-ab and -c. The outflows from IRS3B-ab and IRS3B-c are highly entangled at the lower velocity emission ($<$ 10 km s^{-1}) but become more easily separated at higher velocity emission ($>$ 20 km s^{-1}). The outflows of IRS3B-ab and IRS3B-c appear aligned within the wide opening angle ($\sim$45°) of the IRS3B-ab emission. However, both of these sources are marginally misaligned from the IRS3B-ab continuum disk minor axis ($<$ 10°). In the blue-shifted emission, there appears a faint but very wide opening angle ($\sim$65°) for the outflows which is resolved out in these observations but more clear in Tobin et al. (2016a). Additionally, there is a crescent shaped over-density along the blue-shifted emission, which could be due to orbital movement of the

tertiary and/or precessions of the outflows. In the red-shifted emission there are 3 main over densities that occur along the line of the outflow, possibly indicative of irregular, high accretion events in the past. ^{12}CO integrated intensity maps towards IRS3A (Figure 2.26) show low velocity, wide angle outflows towards line center, unlike the collimated outflows towards IRS3B.

2.D.2. SiO Line Emission

The SiO emission (Figures 2.27 and 2.28) corresponds to shocks along the outflow. SiO most probably forms via dust grain sputtering which can inject either silicon atoms or SiO molecules into the gas (Caselli et al., 1997). This happens from neutral particle impacts on charged grains in addition to grain-grain collisions at sufficient velocities (25-35 km s^{-1}; Caselli et al., 1997). Furthermore, we observed a relatively high asymmetry in the emission intensity between the red- and blue-shifted, while the radial extent (distance from launch location) is more symmetric about the outflow launch origin. Unlike the ^{12}CO emission, the outflow launch location from SiO seems to coincide with IRS3B-c for both the high and low velocity emission rather than IRS3B-ab. However, the lower resolution leaves some ambiguity as to the true launch location.

2.E. Molecular Line Spectra

In order to visualize the structure and dynamics in 3D datacubes, we constructed moment 0 maps and PV diagrams to reduce the number of axis by either integrating along the frequency axis or along slices across the minor axis, respectively. We can also construct spectra, centered on the sources, and integrated radially outwards in annuli.

Figure 2.E.1 is the C^{17}O spectra for the IRS3B-c system. We extracted the emission within an ellipse centered on IRS3B-c to define the main core of the IRS3B-c spectra in "red" and an annulus just outside of this ellipse to define the comparative IRS3B-ab disk spectra in "red". The IRS3B-c spectra features a deficit of emission towards line center due to the high optical depths towards this clump. Figure 2.E.2 is the C^{17}O spectra for the IRS3B system. This spectra is centered on the kinematic center of the disk (Table 2.4) and is integrated out to the size of the gaseous disk (Table 2.3). Figure 2.E.3 is the C^{17}O emission towards IRS3A which is faint in these observations, making it not a suitable molecule for tracing disk kinematics.

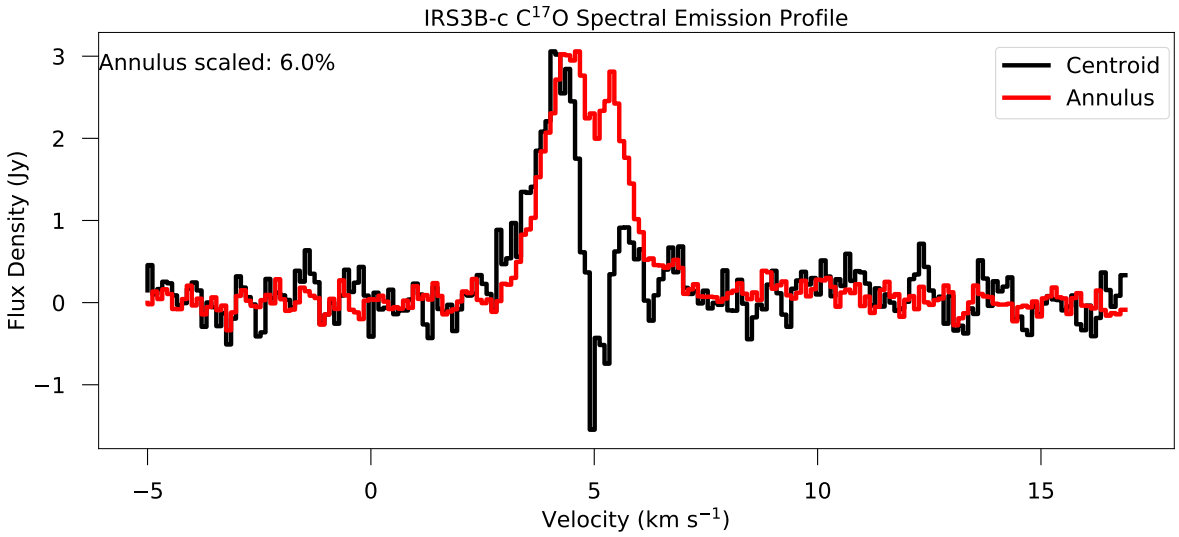

Figure 2.E.1: : $C^{17}O$ integrated spectral emission profile of IRS3B-c, set to the rest frequency of $C^{17}O$. The profiles were extracted by integrating the emission within an annulus, where the co-center of the annuli is set to the center point of IRS3B-c, while the inclination and position angle of the annuli is set to the IRS3B-ab parameters. The "black" profile is extracted from a central ellipse 2 times the size of the restoring beam, while the "red" profile is extracted from an annulus with the same width as the average restoring beam, three beam widths off of the source. The central emission features a deficit of emission towards line center. The profiles are normalized to highlight the emission profiles rather than the actual values of the emission.

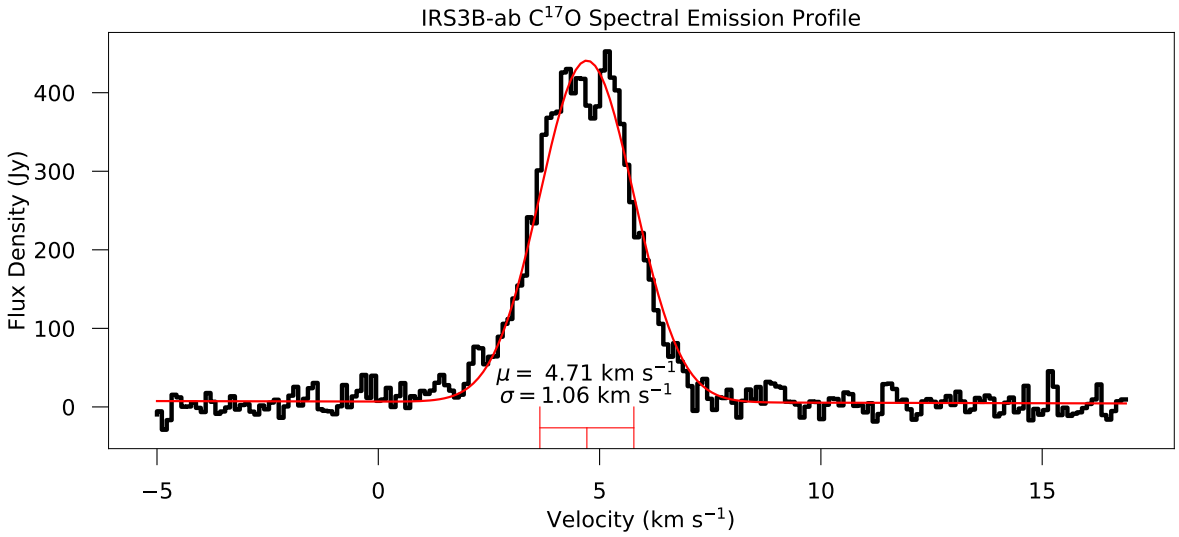

Figure 2.E.2: : $C^{17}O$ integrated spectral emission profile of IRS3B-ab, set to the rest frequency of $C^{17}O$. The profile is extracted by integrating the emission within an ellipse, where the center, inclination, and position angle are set to the center point of IRS3B-ab. The "black" profile is extracted from a central ellipse the same size as the gaseous disk in Table 2.3. The red line is a Gaussian fit to the spectra, with parameters $\mu = 4.71^{+0.02}_{-0.02}$ km s^{-1} and $\sigma = 1.06^{+0.02}_{-0.02}$ km s^{-1}.

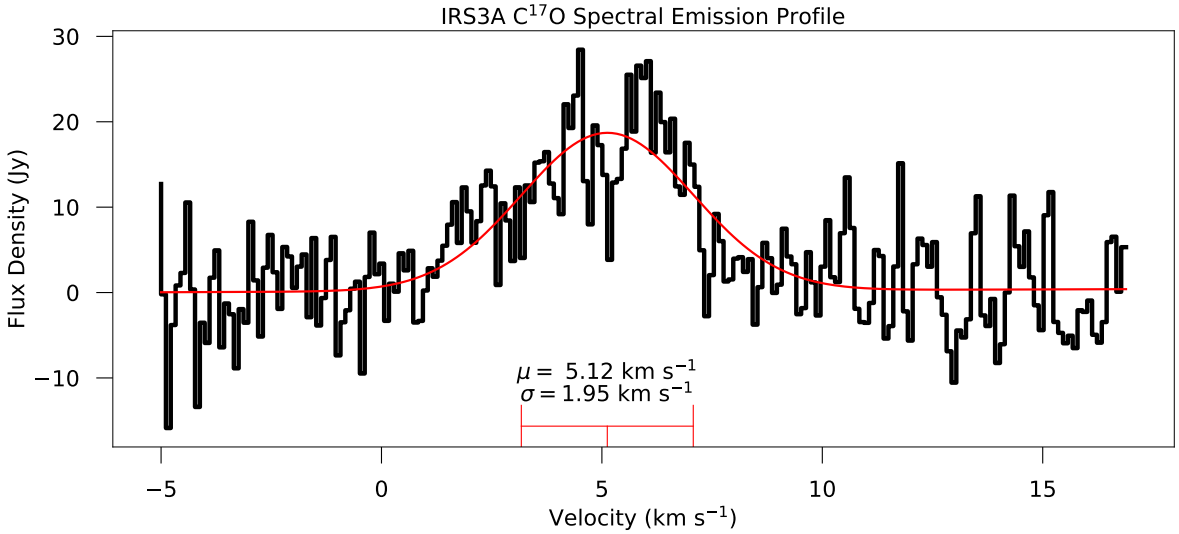

Figure 2.E.3: : $C^{17}O$ integrated spectral emission profile of IRS3A, set to the rest frequency of $C^{17}O$. The profiles were extracted by integrating the emission within an ellipse, where the center, inclination, and position angle are set to the center point of IRS3A. The "black" profile is extracted from a central ellipse the same size as the gaseous disk in Table 2.3. The $C^{17}O$ emission towards this source is fainter than the emission from other dense gas tracers, thought to trace disk kinematics like that of $H^{13}CN$. The red line is a Gaussian fit to the spectra, with parameters $\mu = 5.12^{+0.15}_{-0.15}$ km s^{-1} and $\sigma = 1.95^{+0.75}_{-0.17}$ km s^{-1}.

2.F. Tertiary Subtraction and Gaussian Fitting

The continuum emission of the bright, embedded source, IRS3B-c, biases the analysis of the radial disk structure and circumstellar disk mass estimate of the IRS3B system. By removing this source, we can independently examine the disk and the tertiary source in order to characterize their properties separately (Figure 2.F.1). In order to remove the tertiary source, we fitted two Gaussians with a zero-level offset to the position of the source using the *imfit* task in CASA (a point source and single Gaussian did not provide adequate fit while preserving the underlying disk emission). The offset serves to preserve the emission from the underlying IRS3B-ab disk emission. We also restricted the imfit task to a $0.''8 \times 0.''7$ ellipse around the source such that the fit does not extend into the surrounding emission from the spiral arms. With these parameters generated from the imfit task, we then constructed a model image of the tertiary. We used the CASA task *setjy* to Fourier transform the model image and fill the model column of the measurement set with the model visibility data. We then used the task *uvsub* to subtract this model from the data, producing the residual visibilities without the tertiary. A tertiary subtracted image is generated from this residual dataset and shown in Figure 2.F.1 along with the model of the tertiary used to construct this dataset. The masses generated from this fit is $\sim$0.07 $M_{\odot}$, as described in Section 2.3.1 and provided in Table 2.4. We then are able to reconstruct and taper the resulting visibilities to smooth over the substructure of the disk, in order to better fit the circum-multiple disk. The image (Figure 2.F.2) is fit with a 2-D Gaussian using the *imfit* in CASA and the results of the fit are provided in Table 2.3.

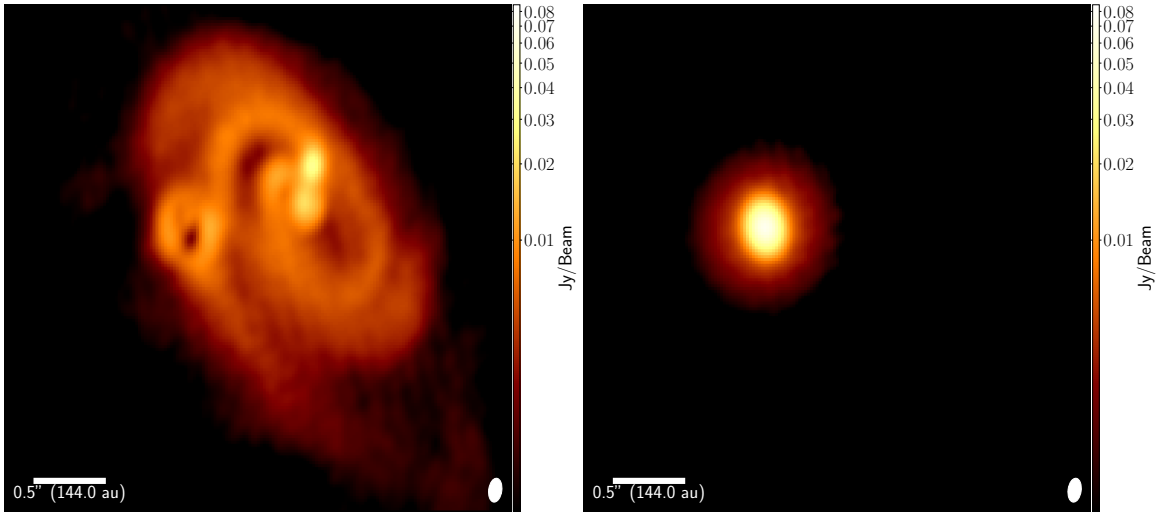

Figure 2.F.1: : Continuum (879 μm) images of IRS3B with the tertiary clump removed (left image) for analysis and the model of the tertiary clump (right image). The tertiary model was constructed using two 2D Gaussians with a zero-level offset in order to properly restore the underlying disk emission without introducing additional features. The left image was used to exclude the embedded tertiary mass from the dust component of the circumstellar disk while the right image image was then used for analysis of the compact dust emission around the tertiary.

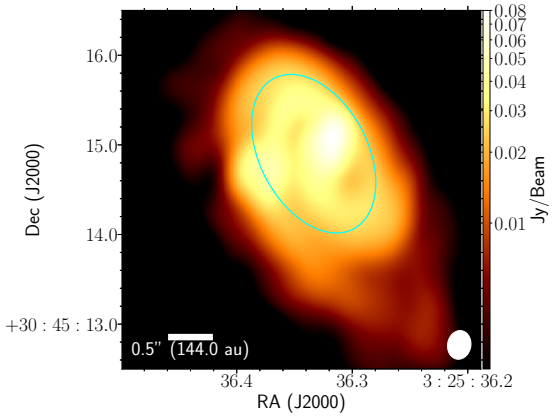

Figure 2.F.2: : Continuum (879 μm) image of IRS3B with the tertiary removed, reconstructed with Briggs weighing robust parameter of 2 and tapered to 500kλ. This smooths over the substructure of the continuum disk to enable fitting of the disk with a single 2-D Gaussian profile, without over-fitting the substructure. The cyan line is the Gaussian fit of the circum-multiple disk of IRS3B, with the major and minor axis of the ellipses defined by the FWHM major and minor axis of the 2-D Gaussian fit.

CHAPTER 3

Characterizing the Keplerian Disk around the isolated protostar BHR7-mms[1]

Preface

We present the analysis of the kinematic structure of the disk (resolution$\sim 0.''11 \approx 44$ au) towards the isolated protostar, BHR7-mms (d$\sim$400 pc) with the Atacama Large Millimeter/-submillimeter Array at 1.3 mm. We resolved the nearly edge-on circumstellar disk and observe several gas tracers, such as ^{12}CO, C^{18}O, ^{13}CO, SO, and H_2CO. We used the molecular line kinematic observations of C^{18}O and ^{13}CO to confirm that the disks are in Keplerian rotation with a central gravitating mass of 1.17$\pm$0.02 $M_\odot$ from radiative transfer modeling. Our analytic models are consistent with a central mass between 0.5-1.4 $M_\odot$. Furthermore, we estimate the mass of circumstellar disk to be at least 0.16 $M_\odot$ from the 1.3 mm dust continuum emission. By analyzing the Toomre Q parameter, we found the BHR7-mms circumstellar disk is likely gravitationally unstable, with a Q=0.5-1.4.

[1]Chapter reproduced from work in submission.

3.1. Introduction

Star formation takes place within dense cores within molecular clouds (Shu et al., 1987) and dense cores generally form within filametary structures (André et al., 2014). Although there are a few instances of cores forming isolated from any nearby structure (e.g. Clemens & Barvainis, 1988; Bourke et al., 1995a). Once a core undergoes collapse, a disk forms around the central, gravitating potential. Once this disk forms due to the conservation of angular momentum, the stellar mass assembly will be primarily regulated by the accretion of material from the circumstellar disk. Furthermore, if the disk is sufficiently massive, the disk can undergo fragmentation due to gravitational instability (e.g. Kratter & Lodato, 2016), potentially leading to the formation of spirals, stellar companions, and possibly giant planets. However, it is not generally understood how many stars have disks massive enough to undergo gravitational instability and at what stage in the evolution of the protostar these disks can fragment. Additionally, high-resolution interferometric imaging of the more evolved protoplanetary disks (Andrews et al., 2018), has uncovered a diversity of "substructure" features that deviate from otherwise smooth, power-law radial surface brightness distributions previously observed. However, these substructures uncovered are not results of gravitational instabilities but likely stem from other processes like planet formation from core accretion.

We present observations of a nearby (d$\sim$400$\pm$10 pc; Woermann et al., 2001) isolated protostar BHR7-mms (Tobin et al., 2018a), located in the dark cloud BHR7, within the Vela cometary globule (Hartley et al., 1986; Bourke et al., 1995a,b), using ALMA Band 6 (1.3 mm) at high resolution. Woermann et al. (2001) estimates the distance to the center of the Vela cometary globule shell to be $\sim$400 pc, with a system velocity of 10 km s^{-1}. Considering our V$_{sys}\sim$4.9 km s^{-1}, it is likely BHR7 is located on the near side of the expanding shell, decreasing the distance but for the purpose of this work we adopted 400 pc, but it is possible BHR7 is somewhat closer than 400 pc, enhancing the masses derived herein.

The isolated nature of BHR7-mms makes it an ideal target to examine what is expected to be prototypical star formation, free of confusion and interaction with neighboring protostars. Tobin et al. (2018a) followed up this source, solidifying its characterization of a Class 0 protostar with a bolometric luminosity of 9.3 L$_\odot$ and a bolometric temperature of 50.5 K. The

source exhibits a beautiful bipolar outflow structure in ^{12}CO, extending over 20″≈8,000 au and about 20 km s^{-1} from line center. According to Tobin et al. (2018a), the C^{18}O and ^{13}CO gas kinematic motion at a scale of 200 au around the protostar could be dominated by Keplerian rotation, consistent with a 1.1 $M_\odot$ gravitational mass. Additionally, they found BHR7-mms to have an unresolved disk mass of at least 0.42 $M_\odot$ (assuming the puffy, edge-on disk is optically thin), thus making it a good candidate for a gravitationally unstable source.

The organization of this paper (Paper I) is as follows: details of our observations in Section 3.2, summary of our continuum and kinematic observations in Section 3.3, radiative transfer models in Section 3.4, further characterization of the system in Section 3.5, and summary of our findings in Section 3.6.

3.2. Observations

The Atacama Large Millimeter/submillimeter Array (ALMA) is a state-of-the-art interferometer located on Llano de Chajnantor plateau in the Atacama region of Chile at an elevation of ∼5000 meters). The observations of BHR7-mms took place across two configurations, associated with project 2019.1.00463.S. We summarize the correlator setup in Table 3.2.1 and the scheduling block in Table 3.2.2.

The correlator was configured to observe both continuum and molecular line emission with a central frequency of 226 GHz, with spectral windows set to observe ^{12}CO, ^{13}CO, C^{18}O (J = 2-1), H_2CO (J = 3_{22} - 2_{21}), H_2CO (J = 3_{21} - 2_{20}), H_2CO (J = 3_{03} - 2_{02}), SO (J = 6_5-5_4), and N_2D+ (J = 3-2)with a wide-bandwidth (1.875 GHz), coarse resolution (1.5 km s^{-1}) spectral window allotted for continuum. The CO and N_2D+ lines were each observed with a 234 MHz spectral window while the remaining lines were observed with a 59 MHz spectral window. ^{13}CO and C^{18}O were observed with a spectral resolution of 0.083 km s^{-1}, CO and N_2D+ were observed with a spectral resolution of 0.31 km s^{-1}, and the remaining lines were observed with a spectral resolution of 0.167 km s^{-1}. The aggregate continuum bandwidth after flagging line emission is 2.8 GHz.

Compact Configuration The first set of observations utilized 46 antennas on 2019 October 30. The total on source time for the compact configuration observations was 8 minutes and

covered baselines between 15.1 meters to 670 meters. The raw visibility data was pipeline calibrated by the North American ARC staff using Common Astronomy Software Applications (CASA) version 5.6.1-8. The observations have a typical angular resolution of 0.″5 (200 au) with a continuum sensitivity of 50 μJy beam^{-1} when reconstructed with Briggs robust weighting parameter of 0.5 and a signal-to-noise ratio (SNR) of $\sim$1,000. We performed 7 rounds of phase-only self-calibration on the short-baseline dataset and a final round of amplitude self-calibrations (summarized in Table 3.2.3).

3.2.0.0.1 Extended Configuration The second set of observations utilized 40 antennas and took place on 2021 July 07 with baselines spanning 41 meters to 3,600 meters with a total on source time of 32 minutes. The raw visibility data were pipeline calibrated using *CASA* version 6.1.1-15. The observations have a typical angular resolution of 0.″1 (40 au) with a continuum sensitivity of 54 μJy beam^{-1} when reconstructed with Briggs robust weighting parameter of 0.5 and a signal-to-noise ratio (SNR) of $\sim$200. We performed 7 rounds of phase-only self-calibration on the extended baseline observations and a final round of amplitude self-calibrations (summarized in Table 3.2.3).

3.2.0.0.2 Imaging With the self-calibrated uv-visibilities in hand, we utilized the *CASA* (McMullin et al., 2007) task *tclean* (version 6.5.2) to reconstruct the molecular line data cubes and continuum images. In order to take advantage of the full spectral range of line-free continuum emission, we used the multi-frequency synthesis (MFS) imaging mode. We also utilized the multi-Taylor-term, multi-scale (MTMFS) algorithm on the continuum with the scales set to "0" (point like), "5" (minor axis of the beam), and "30" ($\sim$3$\times$ beam major axis), applying conservative masks around the regions of emission as to not clean the beam sidelobes. Images were produced at a range of Briggs robust weighting parameter from -2 to 2, but for the purpose of this work, we show the Briggs robust 0.5 image, which balances the compact and extended baseline weights to achieve moderate resolution and sensitivity. The pixel size of the continuum images was set to 0.″02, which achieves $\sim$5 pixels across the minor beam axis for the Briggs robust 0.5 synthesized beam. The images were constructed $\sim$30″ wide, centered on the protostar, to recover any emission compact or large-scale, that could be found at high

separations.

The continuum-subtracted molecular line uv-visibilities were reconstructed using the "cube" imaging mode, in order to retain information regarding the velocity structure. We utilized the well known "Clark" algorithm during the imaging process, also applying conservative masks around the regions of emission as to assist the deconvolve process and not clean the sidelobes of the beam. Images were produced at a range of Briggs robust weighting parameter from 0 to 2. For the purpose of this work, we show the natural weight image, which is formally the Briggs robust weighting value of 2, to achieve the highest sensitivities. The pixel size of the line images was set to match the continuum images of $0.''02$, which achieves $\sim$20 pixels across the minor beam axis for the natural synthesized beam.

Table 3.2.1: Correlator Setup

	Aggregate Continuum[a]	Continuum	CO	^{13}CO	C^{18}O	H_2CO[b]
Rest Freq. (GHz)	226.3162	233.5	230.538	220.398684	219.560358	218.222192
Chan. Width (km s^{-1})	1.45	1.45	0.635	0.167	0.167	0.167
Num. Chan.	-	3840	1920	1920	1920	960
RMS Chan^{-1}. (mJy beam^{-1})	48×10^{-3}	65×10^{-3}	15.3	13.4	9.5	8.3
Peak Intensity (mJy beam^{-1})	28.26		689.93	309.86	161.76	115.92
Brightness Temperature (K)	45.72		62.42	29.48	16.00	11.57
Synthesized Beam[d]	0.14×0.10	0.14×0.10	0.53×0.48	0.54×0.49	0.53×0.48	0.53×0.48

NOTE—The setup of the correlator for the observations.

[a]Multi-Taylor term Multi-Frequency Synthesis (MTMFS) utilizing the extracted continuum emission from averaging line-free spectral channels.

[b]We set the correlator such that the spectral window would cover three transitions of H_2CO. The H_2CO-1, H_2CO-2, and H_2CO-3 correspond to the H_2CO (J = 3_{03} - 2_{02}), H_2CO (J = 3_{21} - 2_{20}), and H_2CO (J = 3_{22} - 2_{21}), respectively.

[d]The synthesized beam size is provided from the *tclean* task for the molecular lines (or continuum for the MTMFS column) using the Briggs robust weighing parameter of 0.5 during image reconstruction.

Table 3.2.2: 1.3 mm Scheduling Block

Name	Baselines (m)	Date	Phase Cal.	Bandpass Cal.	Flux Cal.	Time on Source (minutes)
short	15-697	2019 October 30	J0743-3803	J0538-4405	J0747-3310	8.06
long	41-3,600	2021 June 07	J0743-3803	J0538-4405	J0747-3310	32.16

NOTE—S.B. is the scheduling block identifier.

NOTE—E.B. is the number of execution blocks.

3.3. Results

3.3.1. 1.3 mm Dust Continuum

The 1.3 mm continuum observations unveil the structure of the dusty protostellar disk. The source appears to be nearly edge-on in near-infrared (NIR) images (Tobin et al., 2018a). In agreement with those observations, we resolve the edge-on disk (resolution$\sim$0.$''$11$\times$0.$''$06, sensitivity$\sim$50 μJy beam^{-1}), with a relative smooth surface brightness distribution, elongated in the east-west direction (Figure 3.3.1). The smooth surface brightness distribution could be explained by either no substructures being present in the source or from inclination viewing projection effects that inhibit the identification of structure. With nearly edge-on sources, we are limited by the disk optical depth and are less sensitive to the azimuthal sub-structures that may be present (Bate, 2018).

We can use the *CASA imfit* to estimate the size of the continuum disk by fitting multi-component 2D Gaussians to the emission. The deconvolved size (major and minor axis given by *imfit*) of the continuum source is 0.$''$580$\pm$0.006$\times$0.$''$253$\pm$0.003$\approx$232$\times$101 au with a position angle of 87.481°$\pm$0.006°. This is suggestive of a relatively compact continuum disk with a R$\sim$116 au. We estimated the inclination to be 64.1° by taking the inverse cosine of the minor/major axis of the fits. This method of determining the inclination of the continuum disk relies on the assumption the disk is azimuthially symmetric and vertically thin. Determination of the inclination from this method becomes less accurate towards edge-on sources

Table 3.2.3: 1.3 mm Self-Calibration

Step	RMS (mJy beam^{-1})	BHR7 S/N	Solution Integration (s)
Short-Baseline Self-calibration			
No-selfcal.	0.22	617	
phase-cal. 1	0.14	973	"inf"
phase-cal. 2	0.13	997	"inf"
phase-cal. 3	0.13	1014	241.92
phase-cal. 4	0.13	1025	120.96
phase-cal. 5	0.13	1045	60.48
phase-cal. 6	0.13	1069	30.24
phase-cal. 7	0.13	1093	12.1
ampl.-cal.	0.12	1092	"int"
Long-Baseline Self-calibration			
No-selfcal.	0.15	164	
phase-cal. 1	0.12	227	"inf"
phase-cal. 2	0.12	240	"inf"
phase-cal. 3	0.10	350	90.72
phase-cal. 4	0.09	456	42.34
phase-cal. 5	0.06	481	18.14
ampl.-cal	0.06	509	"int"

NOTE—Summary of the parameters required to reproduced the gain and amplitude self-calibrations.

NOTE—"inf" indicates the entire scan length and "int" indicates a single integration, typically 6.05 seconds for the short-baseline observations and 9.07 seconds for the long baseline observations.

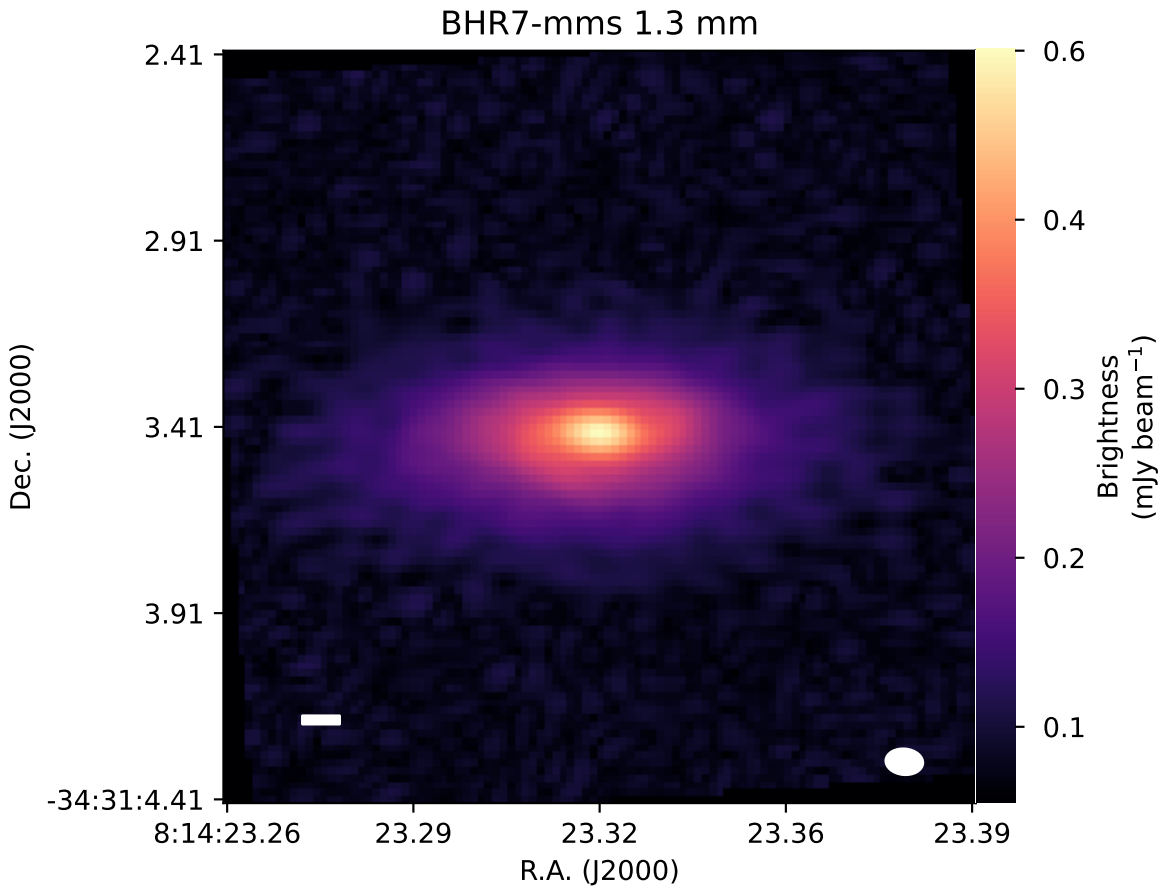

Figure 3.3.1: : Continuum images at 1.3 mm of the protostar BHR7-mms, constructed with Briggs robust weighting of 0.5. A 0.″1 (40 au) scalebar is shown in the lower left and the respective restoring beam is shown in the lower right.

if the disk has significant disk vertical thickness. The integrated intensity of the source is 205.9±2.2 mJy (peak≈5.24±0.07 mJy beam^{-1}). These high resolution observations are less sensitive to the large scale emission from the envelope but the flux density remains consistent with prior lower-resolution data observed at the same wavelength. The integrated flux density from the extended SMA and compact observations were, respectively, ∼197 mJy and 273 mJy (Tobin et al., 2018a). This indicates the observed emission is dominated by the compact disk with little contribution from the envelope at this wavelength.

Analyzing the visibility amplitude can give additional insights into the protostar. A better estimate of the total integrated flux density would be to find the flux density of the most compact baselines (25 kλ), which gives a value of ∼0.234 mJy.

3.3.1.0.1 Mass Estimates It is common to estimate the disk mass via the dust continuum emission at millimeter wavelengths. If we make the assumption that the disk is isothermal, optically thin, without scattering, and the dust and gas are well mixed, then we can derive the disk mass from the equation

$$M_{dust} = \frac{D^2 F_\nu}{\kappa_\nu B_\nu(T_{dust})}, \tag{3.1}$$

where D is the distance to the protostar (400 pc), F_ν is the flux density, κ_ν is the dust opacity, B_ν is the Planck function for a dust temperature, and T_{dust} is taken to be the average temperature of a typical protostar disk. The κ_ν at λ = 1.3 mm was adopted from dust opacity models with a value of 0.899 cm^2 g^{-1}, typical of dense cores with thin icy-mantles (Ossenkopf & Henning, 1994). We note the opacity chosen will directly determine the estimated dust mass, but the value should be between 0.899-2.3 cm^2 g^{-1}. This M$_{dust}$ is thought to be a proxy for the total mass of the disk by applying a correction factor that accounts for the gas contribution. We adopted a gas-to-dust ratio (GDR) of 100:1, typical for the ISM (Bohlin et al., 1978b).

There are several ways to approximate the average temperature of the dust in the disk. One method is to adopt T$_{disk}$ =43 K$\left(\times\frac{L_*}{L_\odot}\right)^{1/4}$ = 75 K, which is higher than temperatures derived from protostellar models (43 K; Tobin et al., 2013) and much higher than the more evolved protoplanetary disks (20 K; Andrews et al., 2013). We provide a range of temperatures T$_{disk}$=20, 48, and 75 K to be 20 K, typical of the more evolved protoplanetary disks (Andrews et al., 2013; Tobin et al., 2020).

We found the mass of the disk to be 0.16 M$_\odot$ (T=75 K),0.26 M$_\odot$ (T=48 K), and 0.74 M$_\odot$ (T=20 K) for a flux density value of 0.21 Jy. While our visibility amplitude analysis indicates we are underestimating our flux by $\sim$12%, we considered the flux density derived from the image-plane fit. If we adopt a 2$\times$ higher dust mass opacity, indicative of larger grains, we would decrease our mass by the same factor. Considering these limitations, we adopted a disk mass of 0.26 M$_\odot$, with the understanding this mass is likely the lower bound for the disk mass. Since the source appears at such a large inclination angle $> 60°$, additional emission may be reduced by optical depth effects, underestimating the amount of mass in the disk.

3.3.2. Molecular Lines

An isolated Class 0 source with an inclination of $>60^{\circ}$ is an ideal candidate to examine the kinematic properties of the infalling envelope. The lack of nearby sources and the clear geometric orientation simplify the interpretation of molecular line kinematic data. The observations in the extended and compact configuration were set up to focus on the kinematic tracers of the disk and inner envelope (^{13}CO, C^{18}O, H_2CO). The analysis of the larger-scale envelope is left for a subsequent paper.

3.3.2.1. Molecular Line Observations

We summarize the observations of each molecule below and provide a more rigorous analysis of molecules tracing disk kinematics. While outflows are important for the evolution and characterization of YSOs and the envelope component is important for replenishing the mass of the disk, the analysis of these complex structures is beyond the scope of this paper because we are focused on the disk. We found CO emission primarily traces outflows; ^{13}CO and H_2CO primarily traces the inner envelope and outer disk; and C^{18}O primarily traces the disk.

To aid in the analysis of the molecular line observations, we employed several methods to reduce the dimensionality of the 3D datacubes. We construct moment 0 maps, which integrate the data cube over the frequency axis, to construct 2D images. These images show spatial locations of strong emission. To help preserve some frequency information from the data cubes, we performed velocity-weighted integrated emission, so called moment 1 map. However, when integrating over any velocity ranges, we do not preserve the full velocity information of the emission; thus we provide spectral profiles and position velocity diagrams of the molecular lines as well.

3.3.2.1.1 C^{18}O The C^{18}O emission (Figure 3.3.2) appears to trace the gas kinematics within the outer circumstellar disk (r<2″), the axis of rotation is orthogonal to the outflows, and has a well-ordered data cube indicative of rotation. C^{18}O, is a less abundant isotopologue of CO, ISM values $[^{18}O/^{16}O]$ ≈560:1 Wilson & Rood (1994), which has been shown as a proxy for the total gas abundance, ISM values $[H_2]\,/\,[^{12}CO] \approx 10^4$:1 Visser et al. (2009). The emission extends out to 1.″8 (∼720 au) on either side of the disk, much further than the continuum

(∼232 au).

Figure 3.3.2 shows the moment 0 map overlaid in black on the moment 1 map, shown with the respective red-blue Doppler shifted emission on the left. The emission shows an obvious velocity gradient that may trace Keplerian rotation, with the system velocity of ∼4.8 km s^{-1}. We also show the $C^{18}O$ spectra in Figure 3.3.3, extracted by integrating the emission found within a 2″ mask centered on the continuum center. We calculated a 1D Gaussian fit to the spectra, masking the central channels out because we are likely resolving-out the large-scale emission of the envelope that is found in the central channels.

3.3.2.1.2 ^{13}CO The ^{13}CO emission appears to trace the gas out to scales <4″ (Figure 3.3.4). On the left side, the axis of rotation is orthogonal to the outflows and the inner 0.″5 is missing flux. This deficit of flux is likely due to resolving out the large-scale emission which can be seen from the spectra in Figure 3.3.5.

3.3.2.1.3 H_2CO The H_2CO emission, similar to the $C^{18}O$ emission, appears to trace the gas out to scales <3″ (Figure 3.3.6). We observed 3 H_2CO transitions, H_2CO (J = 3_{03} - 2_{02}) E_{up} = 10.4834 K, H_2CO (J = 3_{21} - 2_{20}) E_{up} = 57.6120 K, and H_2CO (J = 3_{22} - 2_{21}) E_{up} = 57.6086 K, with the higher-energy transitions having lower surface brightness. All 3 transitions are provided, but for the purpose of the analysis, since the higher energy transitions are several factors less abundant, we only considered the H_2CO (J = 3_{03} - 2_{02}) transition.

The emission of H_2CO appears to trace larger scales ∼3× larger than the $C^{18}O$ scales (Figure 3.3.2) and comparable to the scales traced by ^{13}CO (Figure 3.3.4). Figure 3.3.6 features a deficit of emission along the inner ∼0.5 km s^{-1} channels from line center, likely from resolving-out the large scale emission and the most-abundant species being likely optically thick as shown in the first column spectra in Figure 3.3.7.

3.3.3. Position-Velocity Diagram Analysis

To aid in the analysis of the molecular line observations, we constructed 2D position-velocity (PV) diagrams of the data cubes. The PV diagrams are extracted by summing the pixels within a defined region at each position along a particular axis of the disk. When probing disk kinematics, it is useful to restrict the PV diagram to widths to the size of the disk to

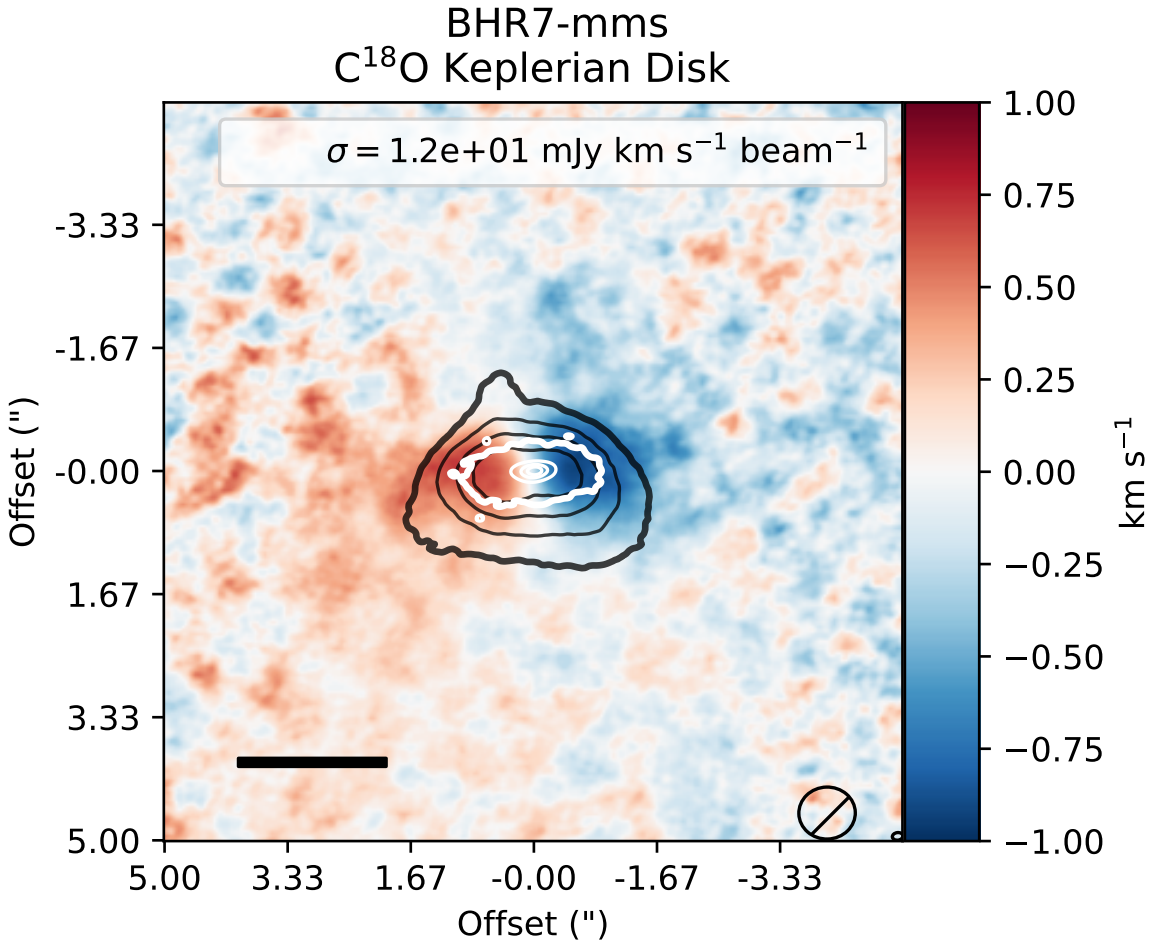

Figure 3.3.2: : The first moment map of $C^{18}O$ in red-blue scale, the $C^{18}O$ moment 0 contour map overplotted in the black contour lines (starting at 10-σ, iterating by 5-σ), and finally the compact black contours at the center of the image indicate the 1.3 mm dust continuum (starting at 10-σ, iterating by 300-σ). The $C^{18}O$ emission appears to extend beyond the edge of the continuum disk, to $\sim$600 au. The first moment map indicates well-ordered kinematics on the size-scale of the disk. We discuss this further in Section 3.3.2.

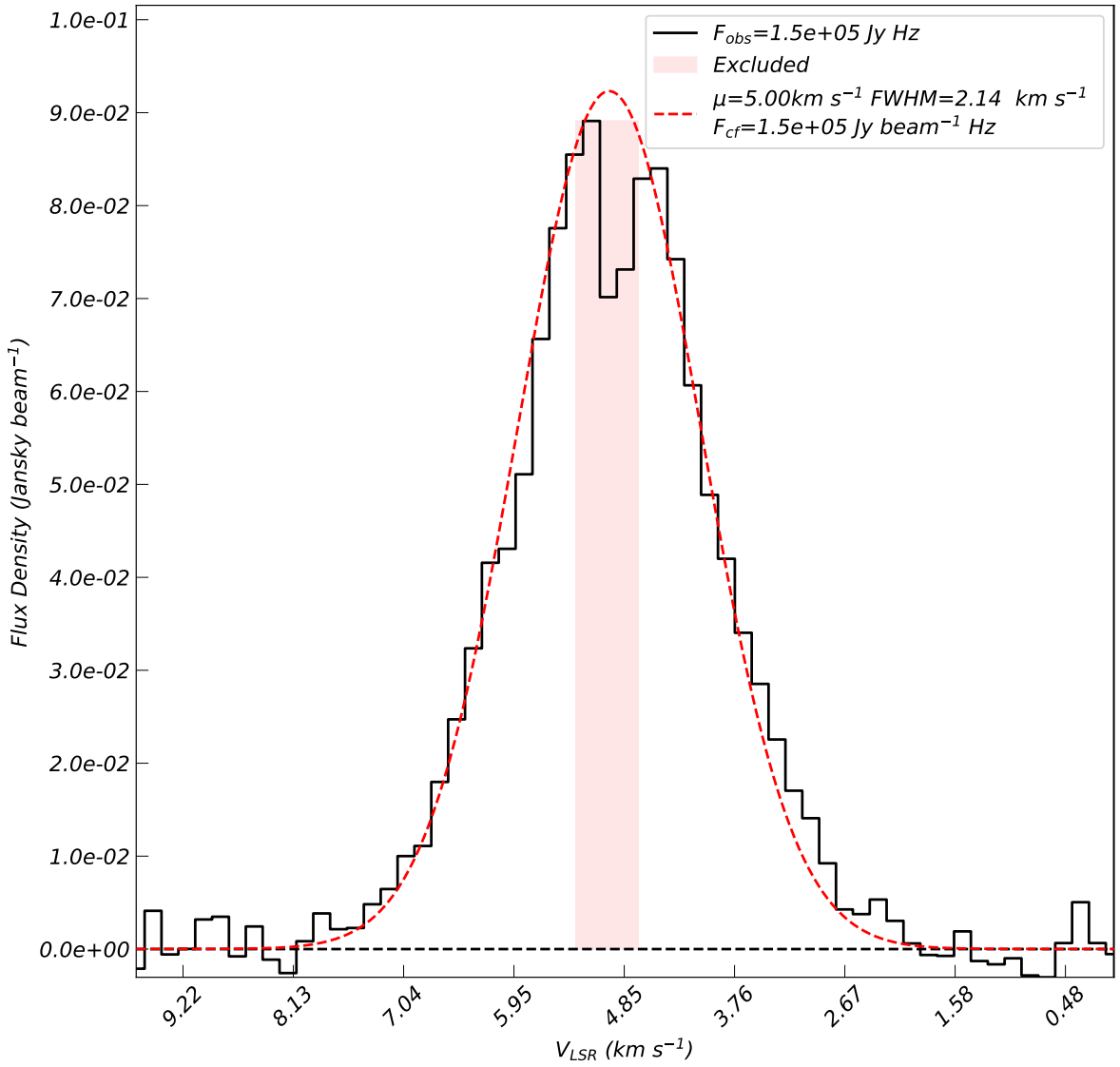

Figure 3.3.3: : The spectra of $C^{18}O$ plotted in black, extracted from a 2″ mask around the protostar BHR7-mms. The red-dashed line is a Gaussian fit to the emission, with the channels closet to line center masked out due to spatial filtering and high optical depths. The kinematics indicate a well ordered disk undergoing clear Keplerian rotation in $C^{18}O$. We discuss this further in Section 3.3.2.

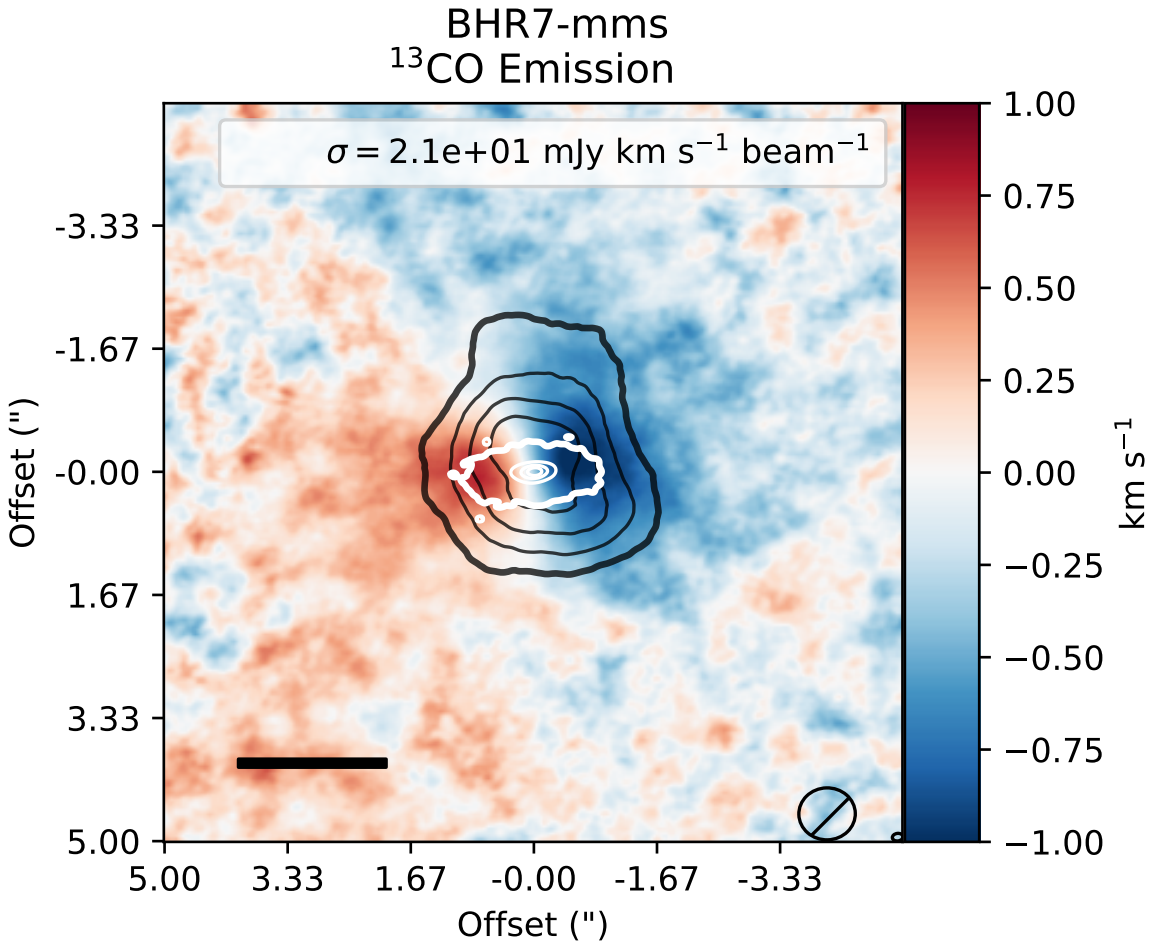

Figure 3.3.4: : The first moment map of ^{13}CO in red-blue scale, the ^{13}CO moment 0 map overplotted in the white contour line (starting at 10-σ, iterating by 6-σ) and finally the compact black contours at the center of the image indicate the 1.3 mm dust continuum (starting at 10-σ, iterating by 300-σ). ^{13}CO is more abundant than C^{18}O and has a high optical depth (large degree of spatial filtering as shown by the asymmetry in the ^{13}CO moment 0 map shown in gray contours), making it a poor tracer for the compact disk material; however, this molecule appears to trace the outer edge of the disk and the inner part of the envelope. The moment 1 background map shows the characteristic red-blue shift of velocities from one side of the disk to the opposing side across the major axis, yet there appears to be a slight kink in the velocity towards line center. We discuss this further in Section 3.3.2.

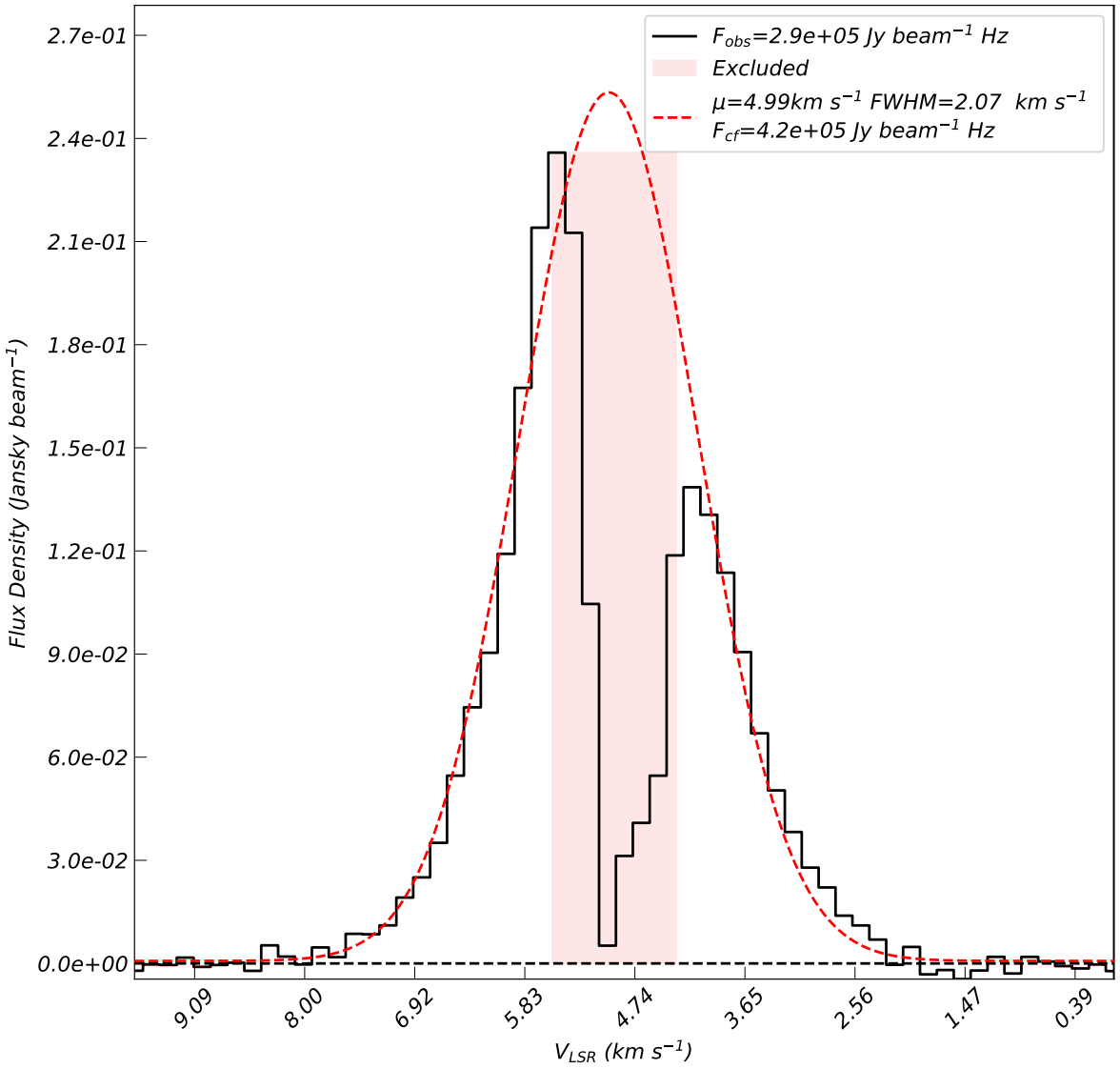

Figure 3.3.5: : ^{13}CO spectra plotted in black, extracted from a 2″ mask around the protostar BHR7-mms. The red-dashed line is a Gaussian fit to the emission, with the channels closet to line center masked out due to spatial filtering. ^{13}CO is more abundant than C^{18}O and has a high optical depth with a large degree of spatial filtering as shown in Figure 3.3.4. We discuss this further in Section 3.3.2.

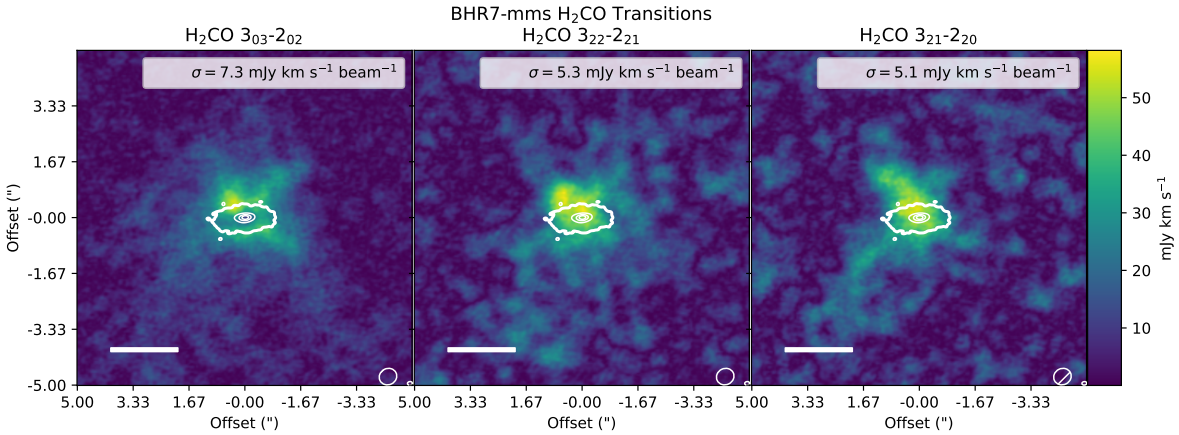

Figure 3.3.6: : The three columns show the zeroth moment map for the three different H_2CO transitions, indicated by the respective title. This molecule appears to trace the gas material just outside of the disk but appears to be in Keplerian rotation and concentrated at smaller radii. Only the H_2CO ($J = 3_{03} - 2_{02}$) transition, appears to have significant spatial filtering and at high optical depths. This is likely due to the other transitions being less abundant than the main transition. The corresponding clean beam in shown in the bottom right of each image.

select out any large scale emission and to align the extraction along the major axis of the disk. We performed the extraction for all disk tracing lines within a 2″ width along the disk major axis of 87°, east-of-north. We centered the extraction to the location of the continuum emission peak of BHR7-mms, such that the positions are defined at offsets from where we would expect the gravitational potential to be.

The PV diagram, provides information on the velocities at positions offset from the protostar. Keplerian rotation on the size-scale of the disk ($v \propto R^{-0.5}$) and infall with rotation conserving angular momentum ($v \propto R^{-1}$), both produce radial profiles that are apparent in the PV diagram. These two effects can be difficult to distinguish in the envelope.

3.3.3.0.1 SLAM To further analyze the observations, we employed the use of public code SLAM (Spectral Line Analysis/Modeling[2]; Aso et al., 2015; Sai et al., 2020). The code computes so called "edges" (location of greatest gradient) and "ridges" (location of peak brightness) to define the fitting of the gravitational potential. The algorithm works by fitting the extracted edge/ridge positions/velocities with a double power law function by using *emcee*.

It stands to reason that the "edge" of the emission would determine the maximum velocity

[2]https://github.com/jinshisai/SLAM.git

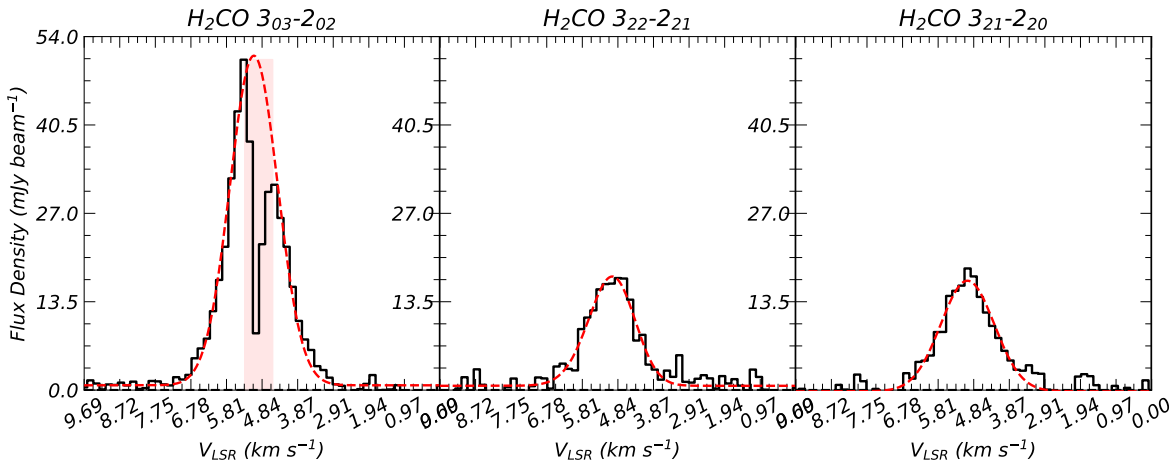

Figure 3.3.7: : The three columns show the spectra for the three different H_2CO transitions, constructed by finding the flux density per channel within a 2″ radius around the protostar BHR7-mms. Each spectra is fit with a Gaussian profile (shown in red). The fit results of the mean V_{sys} =5.0 km s^{-1}, FWHM∼1.88 km s^{-1}.

and would serve as the upper-bound for the gravitational potential while the "ridge" would determine the lower bound for the gravitational potential. We utilized the $C^{18}O$, ^{13}CO, and H_2CO molecules due to their well-ordered kinematics and spatial locations coinciding with the disk.

The code fits several parameters which we will summarize: R_b is the break radius, where the power-law switches from Keplerian rotation into infall, V_{sys} is the systemic velocity, R_{range} and V_{range} define the range of observations fit, M_{in} is the mass fit by the R_{in}, and M_{out} is the mass fit by the full range of radii.

3.3.3.1. $C^{18}O$

The PV diagram of $C^{18}O$ in Figure 3.3.8 shows a velocity spread <2.5 km s^{-1}, indicative of low-velocity gas. $C^{18}O$ appears to trace the kinematics of the disk and envelope and appears to extend out to scales ∼5″ from the central potential. The emission also appears spatially asymmetric, as apparent in the moment 0 map, with more emission appearing on the east side, at red Doppler-shifted velocities, despite the spectrum appearing relatively symmetric. The SLAM fit shown in Figure 3.3.8 fit the mean intensities along each channel and the location of steepest gradient to determine representative points of the PV diagram. From SLAM, we fitted a lower-bound mass (M_b) of 0.41±0.32 $M_\odot$ and an upper-bound of 1.38±0.08 $M_\odot$ (Table 3.3.1).

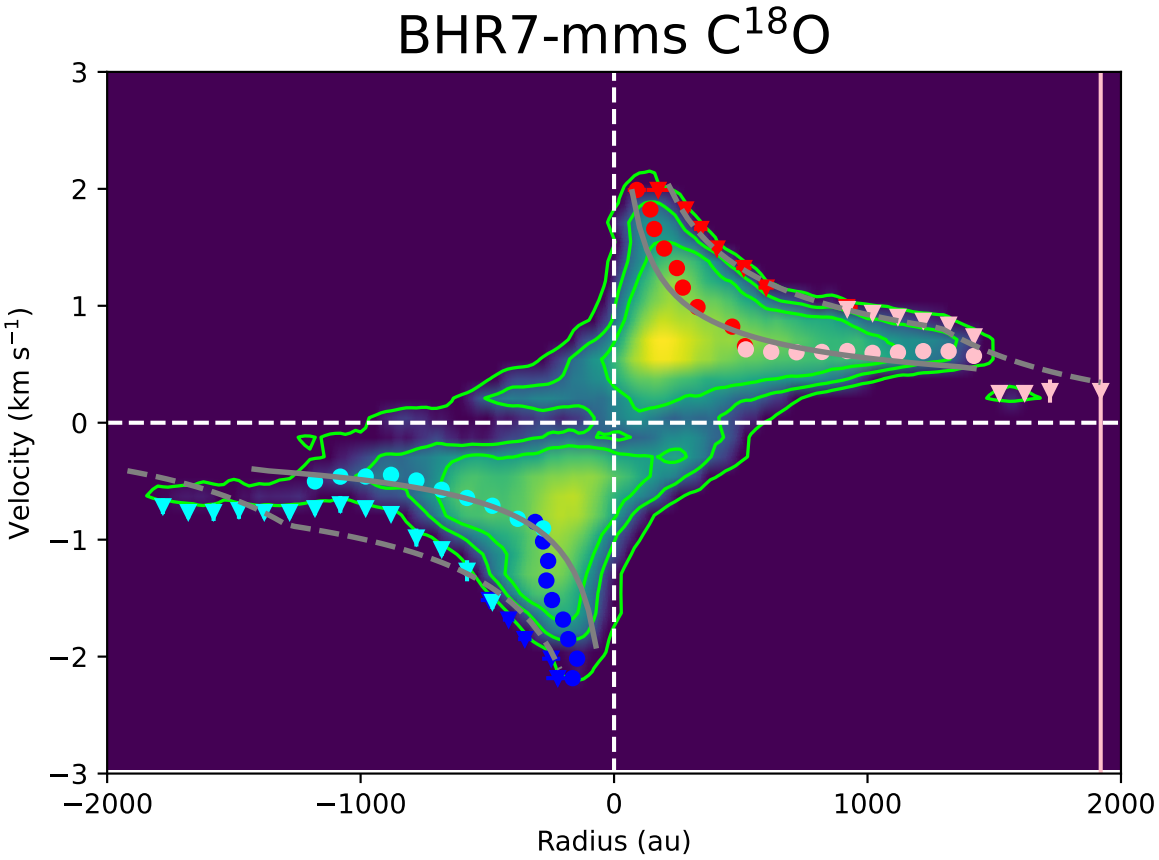

Figure 3.3.8: : The Position-Velocity (PV) diagram for $C^{18}O$, constructed by summing the pixels in a 2″ width slice along the minor axis of the disk. The points indicate the "edge" (exterior) and "ridge" (interior) points fit by SLAM. The horizontal dashed white line indicates the system velocity, which is left as a free parameter, ∼4.9 km s^{-1} and the offset from the center of BHR7-mms. The full summary of results if given in Table 3.3.1.

Table 3.3.1: Best fit parameters for $C^{18}O$ SLAM

Parameter		unit
	edge	
R_b	1294.45±45.19	au
V_{sys}	4.824±0.009	km s^{-1}
R_{range}	207 ∼1290	au
V_{range}	0.401 ∼2.128	km s^{-1}
M_{in}	1.410±0.078	$M_\odot$
M_{out}	0.464±0.139	$M_\odot$
M_b	1.379±0.075	$M_\odot$
	ridge	
R_b	1358.15±655.46	au
V_{sys}	4.890±0.011	km s^{-1}
R_{range}	64.96 ∼1420	au
V_{range}	0.520 ∼2.128	km s^{-1}
M_{in}	0.442±0.439	$M_\odot$
M_{out}	0.577±0.581	$M_\odot$
M_b	0.406±0.320	$M_\odot$

NOTE—The best fit parameters provided from public code SLAM, which fits the position-velocity diagram with a double-power law function. The program computes surface of greatest gradient as the "edge" and the Gaussian center of each particular channel as the "ridge". A full description is provided in Chapter 3.3.3.0.1.

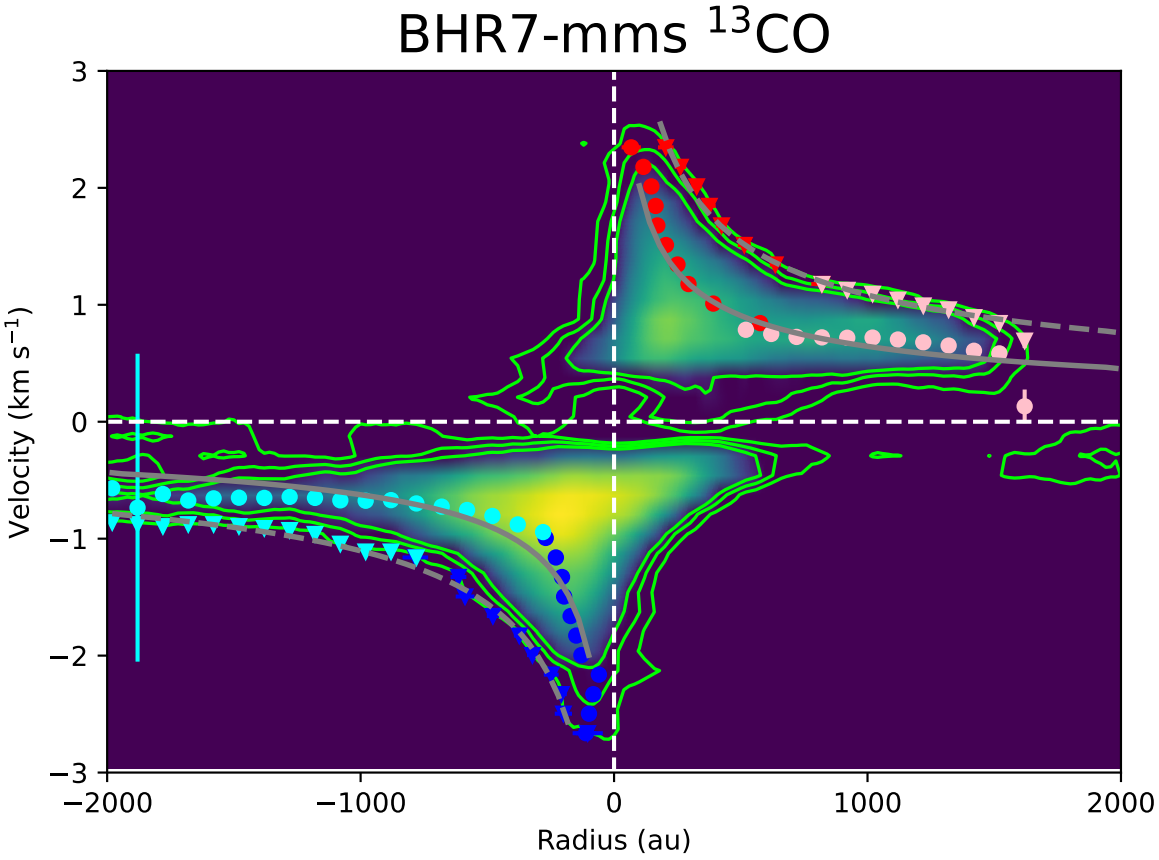

Figure 3.3.9: : The Position Velocity (PV) diagram for ^{13}CO, constructed by summing the pixels in a 2″ width slice along the minor axis of the disk. The points indicate the "edge" (exterior) and "ridge" (interior) points fit by SLAM. The white dashed lines indicate the system velocity offset of ∼4.8 km s^{-1} on the horizontal axis and the offset from the center of BHR7-mms, which are left as free parameters. The ^{13}CO emission is asymmetric across the major axis of the disk, with more emission found on the blue shifted emission. There is a deficit of emission towards line center due to resolving out the large-scale emission. The full summary of results if given in Table 3.3.2.

3.3.3.2. ^{13}CO

We show the PV diagram of the ^{13}CO molecule (Figure 3.3.9). The ^{13}CO molecule appears to trace a similar velocity structure to the C^{18}O molecule, believed to be the disk and inner envelope, extending out to scales >3″ from the central potential. This emission is highly asymmetric, both spatially and in the spectra, with more emission appearing in the blue shifted velocities. From the SLAM analysis, we fitted a lower-bound mass of 0.61±0.14 M$_\odot$ and an upper-bound of 1.79±0.60 M$_\odot$.

Table 3.3.2: Best fit parameters for ^{13}CO SLAM

Parameter		unit
	edge	
R_b	1916.49±686.93	au
V_{sys}	4.825±0.004	km s^{-1}
R_{range}	175 ∼1980	au
V_{range}	0.798 ∼2.629	km s^{-1}
M_{in}	1.823±0.600	$M_\odot$
M_{out}	1.896±0.668	$M_\odot$
M_b	1.788±0.569	$M_\odot$
	ridge	
R_b	1932.28±283.44	au
V_{sys}	4.845±0.003	km s^{-1}
R_{range}	60 ∼1980	au
V_{range}	0.491 ∼2.629	km s^{-1}
M_{in}	0.626±0.148	$M_\odot$
M_{out}	0.717±0.224	$M_\odot$
M_b	0.605±0.143	$M_\odot$

NOTE—The best fit parameters provided from public code SLAM, which fits the position-velocity diagram with a double-power law function. The program computes surface of greatest gradient as the "edge" and the Gaussian center of each particular channel as the "ridge". A full description is provided in Chapter 3.3.3.2.

3.3.3.3. H_2CO

While we observed several transitions of the H_2CO molecule (Figure 3.3.6), only the least energetic transition, H_2CO (J = 3_{03} - 2_{02}), has sufficient SNR for kinematic analysis. The H_2CO molecule appears similar in brightness, spatial scales, and features as the $C^{18}O$ molecule, with asymmetric emission in towards the red shifted emission on the east side of the disk. The velocity structure is also consistent with a FWHM $<$2.5 km s^{-1}, indicative of primarily low-velocity gas. H_2CO appears to trace the kinematics of the disk and envelope and appears to extend out to scales $>4''$ from the central potential. From the SLAM analysis, we fitted a lower-bound mass of 0.39$\pm$0.24 $M_\odot$ and an upper-bound of 1.15$\pm$0.09 $M_\odot$.

3.4. Radiative Transfer Modeling

To more robustly model the disk kinematics, we used Bayesian inference methods to determine the most probable parameters that are consistent with the observations. The methods are extensively detailed in (Sheehan & Eisner, 2017b; Sheehan et al., 2019, disk mass and protostar mass, respectively). The underlying modeling framework uses RADMC-3D (Dullemond et al., 2012) to calculate the synthetic channel maps using 2D axisymmetric radiative transfer models in the limit of local thermodynamic equilibrium and *galario* (Tazzari et al., 2018) to generate the model visibilities from those synthetic channel maps. We sampled the posterior distributions of the parameters to provide fits to the visibilities by utilizing a nested sampling approach (*dynesty*; Skilling, 2004; Feroz et al., 2009; Speagle, 2020). *pdspy* uses the full velocity range given by the frequency limit of the input visibilities in modeling. Our focus for the kinematic models are position angle (p.a.), inclination (inc.), stellar mass (M_*), disk radius (R_D), and system velocity (V_{sys}). We provide a summary of our model results in Table 3.4.1. The combined fitting of the models is computationally expensive (250 models simultaneously generated per "walker integration time step"), requiring on average 10^4 core-hours per source to reach convergence.

Analytic Models : Keplerian rotation in the disk appears in channel maps as a butterfly pattern. The specific pattern is highly sensitive to the particular physical parameters of the system,

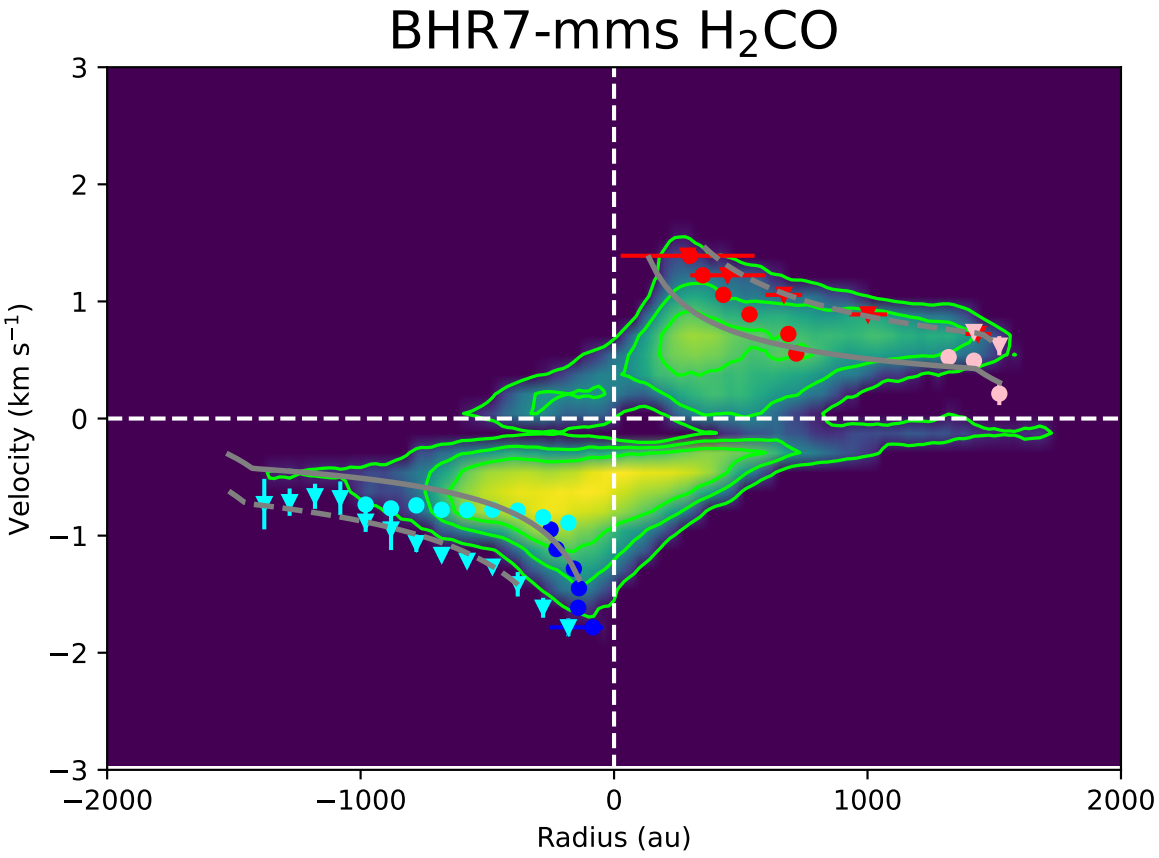

Figure 3.3.10: : The Position Velocity (PV) diagram for H_2CO (J = 3_{03} - 2_{02}), constructed by summing the pixels in a 2″ width slice along the minor axis of the disk. The points indicate the "edge" (exterior) and "ridge" (interior) points fit by SLAM. The white dashed line indicate the system velocity of ∼4.8 km s^{-1} and the center of the gravitational potential, which are left as free parameters. The lower energy transition of the three observed transitions, H_2CO (J = 3_{03} - 2_{02}), is the most abundant (Figure 3.3.6) and provides the best molecule to test Keplerian rotation of the three. The full summary of results if given in Table 3.3.3.

Table 3.3.3: Best fit parameters for H_2CO (J = 3_{03} - 2_{02}) SLAM

Parameter		unit
	edge	
R_b	1451.15±70.96	au
V_{sys}	4.956±0.013	km s^{-1}
R_{range}	353 ∼1520	au
V_{range}	0.779 ∼1.627	km s^{-1}
M_{in}	1.405±0.117	$M_\odot$
M_{out}	1.388±0.491	$M_\odot$
M_b	1.148±0.094	$M_\odot$
	ridge	
R_b	1427.94±423.93	au
V_{sys}	4.957±0.006	km s^{-1}
R_{range}	120 ∼1520	au
V_{range}	0.459 ∼1.627	km s^{-1}
M_{in}	0.478±0.297	$M_\odot$
M_{out}	0.481±1.066	$M_\odot$
M_b	0.390±0.242	$M_\odot$

NOTE—The best fit parameters provided from public code SLAM, which fits the position-velocity diagram with a double-power law function. The program computes surface of greatest gradient as the "edge" and the Gaussian center of each particular channel as the "ridge". A full description is provided in Chapter 3.3.3.3.

such as the protostellar mass, the disk radius, the disk position angle, and the disk inclination. Thus, given an analytic form, we can fit the observations for these parameters. See Sheehan et al. (2019) for details regarding the specific radial, vertical, and kinematic analytic structure, following models of viscous disk evolution (Lynden-Bell & Pringle, 1974) and assuming hydrostatic equilibrium. The specific parameters we sampled are: f_{cav} the density scaling relative to the calculated envelope density, γ the surface density profile exponent, *i* the inclination, M_{gas} the gas mass component of the disk, M_{env} the mass of the envelope, M_{star} the mass of the central protostar, R_{disk} the radius of the disk after which the disk becomes exponentially tapered, R_{env} the radius of the envelope, T_0 is the temperature at 1 au, a_{turb} is the microtublent line width, ξ is the outflow cavity power law exponent, *pa* is the position angle, and x_0/y_0 are the coordinate centers for the protostar.

Convergence : One of the main advantages of dynamic nested sampling over other methods such as Markov-Chain Monte Carlo is the well defined convergence criteria. The *dynesty* implementation of dynamic nested sampling allows the user to define the remaining prior volume as the convergence bound. We set the bound to be equal to 5% meaning only 5% of the prior volume remains unsampled. We found this provides a good trade-off between a well-sampled posterior and time-for-convergence, which scales exponentially as the unsampled volume decreases.

3.4.1. $C^{18}O$

As stated, the $C^{18}O$ molecule appears to trace the Keplerian rotation and from less rigorous analysis of the PV diagrams, we estimated the gravitational potential to be $\sim$1.1 $M_\odot$. We then used sophisticated radiative transfer models coupled with Bayesian posterior estimators to fit the *uv*-visibilities (Figure 3.4.1). The top panel shows the channel map for velocities $\pm$2.5 km s^{-1} from system velocity, reconstructed from the visibilities. The middle row is reconstructed from the model visibilities, within the same velocity range. The final row is the residual of the model - observations. The model, as shown, fits the observations well, with no significant residual except for the channel near to the kinematic center, likely due to contamination from the envelope emission. Our results strongly constrain the $V_{sys}\approx$ $4.7874\pm\sim$0.0017 km s^{-1}, $M_* \approx 1.1894\pm\sim$0.0094 $M_\odot$, inclination $\approx 50.90°\pm\sim$0.35°, and

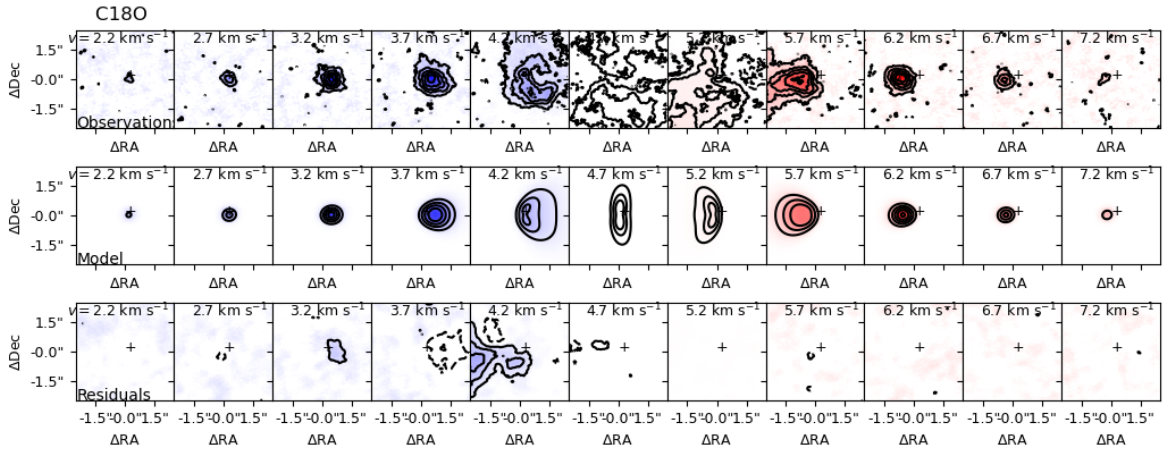

Figure 3.4.1: : A model channel map constructed from *pdspy*, show in color with the red-blue Doppler shifted emission indicated by the respective color. The first row overplots the observed data in black contours with the model shown in color. The second row overplots the model contours. The final row plots the residual, of the model - observations. The position of the central potential is indicated in the black cross. The channel map ranges ± 2.5 km s^{-1} from the central velocity. A full description of the modeling procedures is described in Section 3.4 and the result of the Bayesian estimators is in Table 3.4.1.

the position angle $\approx 90.322° \pm \sim 0.0088°$, with the full fitting results given in Table 3.4.1.

3.4.2. Disk Stability

Typically, from the radial surface brightness and the dust mass from isothermal, thin-disk assumptions we could construct radial surface density profiles of the disk. High resolution radial surface density profiles would provide a method to search for possible substructure by analyzing asymmetries in the disk brightness profiles. However, with highly inclined and vertically thick disks, the construction of the radial profiles becomes contaminated with the vertical height structure. To disentangle the two, we would need to make assumptions regarding the specific geometries of the system, such as the vertical scale height and the inclination. Further observations at higher resolution and longer wavelengths will be needed to probe the high optical depths of the disk to determine the exact geometry, but for the purpose of this paper, we are under the assumption the structure we observed is reasonably described with power law geometry.

We found the mass of the disk to be large from both integrating the total flux density in the image-plane ($M_{disk} \sim 0.16\ M_\odot$) and by determining amplitude from the most compact base-

Table 3.4.1: Best Fit Parameters for $C^{18}O$

Parameter		units
f_{cav}	$0.68^{0.20}_{0.17}$	
γ	$0.5801^{0.0081}_{0.0096}$	
i	$50.90^{0.39}_{0.30}$	$^\circ$
ξ	$1.03^{0.28}_{0.23}$	
M_{gas}	$0.06066^{0.00035}_{0.00030}$	$M_\odot$
M_{env}	$0.0426^{0.0050}_{0.0416}$	$M_\odot$
M_{star}	$1.1894^{0.0094}_{0.0096}$	$M_\odot$
R_{disk}	$481.6^{3.9}_{2.2}$	au
R_{env}	766^{94}_{103}	au
T_0	$999.03^{0.71}_{0.98}$	K
a_{turb}	$0.13310^{0.00015}_{0.00063}$	km s^{-1}
pa	$90.322^{0.113}_{0.082}$	$^\circ$
v_{sys}	$4.7874^{0.0017}_{0.0018}$	km s^{-1}
x0	$0.0552^{0.0016}_{0.0015}$	$''$
y0	$-0.02660^{0.00163}_{0.00096}$	$''$

NOTE—The best fit parameters from the *pdspy* Bayesian fitting, given as the 50^{th}, 32^{nd}, and 68^{th} confidence intervals, respectively.

lines (M_{disk}~0.32 $M_\odot$). We note the lower mass measurement than reported from Tobin et al. (2018a), due to our higher disk temperature $T_{disk} \approx 75$ K as compared to their 30 K. It has been shown that the gas-to-dust ratio, which provides a correcting factor from the dust mass to the total disk mass, can evolve from the ISM-derived values (Ansdell et al., 2016), but it is unclear if it changes significantly at such a young evolutionary age.

We can characterize the stability of the disk to its self-gravity via the Toomre Q parameter ("Q"). Typically it is defined as the ratio of the rotational shear and thermal pressure of the disk versus the self-gravity of the disk, susceptible to fragmentation, of the form,

$$Q = \frac{c_s \Omega}{\pi \Sigma G}, \tag{3.2}$$

where the sound speed is c_s, the orbital frequency Ω, the surface density is Σ, and G is the gravitational constant.

However, this specific form of the equation relies on the accurate determination of c_s, Ω, and Σ, which are subject to the exact geometry of the system. We instead can rewrite the equation for a disk (Kratter & Lodato, 2016; Tobin et al., 2016a, 2018a) in the form,

$$Q \approx 2 \frac{M_*}{M_d} \frac{H}{R}, \tag{3.3}$$

where H=c_s/Ω is the disk scale height, M_d is the disk mass, M_* is the star mass, and R is the disk radius. By plugging in the values we estimated, M_d =0.16 $M_\odot$, M_* =1.19 $M_\odot$, T_{disk}=75 K, H=$\frac{0.47\ km\ s^{-1}}{1.7\times10^{-10}\ s^{-1}}$ = 16 au, R=166 au, we found the upper bound disk-averaged Q≈2.5. We performed the same analysis for T_{disk}=20 K (M_d =0.76 $M_\odot$), finding Q≈0.3 and for a more modest T_{disk}=48 K (M_d =0.26 $M_\odot$), finding Q≈1.2.

It should be noted, several parameters are unconstrained and the specific Q value can vary based on the underlying assumptions. In particular, the parameter with the most uncertainty is the dust mass measurement. The chosen opacity (for this work, $\kappa_\lambda = 0.899$ cm^{2}g^{-1}) will directly change the measured mass by the same factor. Additionally, we assumed the disk is optically thin and without scattering, which inherently cannot be the case when viewing an edge on disk.

When the Q parameter is $<$1, it indicates a gravitationally unstable region of the disk, which could be apparent if significant substructure exists (Andrews et al., 2018; Reynolds et al., 2021). Simulations have shown that values of Q$<$1.7 (calculated in 1D) can be sufficient for self-gravity to drive substructure formation within massive disks, while Q$\approx$1 is required for fragmentation to occur in the disks (Kratter et al., 2010a). Due to the high inclination of the system, substructure can be masked by high optical depths. Sierra & Lizano (2020) show that for wavelengths $\sim$1 mm and particle sizes $\sim$100 μm , only a $\Sigma \approx 3.2$ g cm^{-2}, (compared to our $\Sigma \approx 25$ g cm^{-2} for R=166 au and M$_{disk}$ $\approx$0.26 M$_\odot$) is needed for the particles to be optically thick. Furthermore, scattering reduces the emission of optically thick regions of the disk, thus causing an underestimate of the mass. Zhu et al. (2019) showed in the outer disks (R$\sim$100s of au), this effect underestimates the disk masses by a factor of 2 and towards the inner regions, up to factors $>$10. The uncertainty can lead to values a few factors higher or lower than the reported value, thus we adopt a balanced value.

3.5. Discussion

3.5.1. Protostellar Mass Comparison

Comparing the mass of BHR7-mms (1.19 M$_\odot$) to the initial mass function (young cluster initial mass function toward binaries; Chabrier, 2005) shows this protostar will probably enter the main sequence higher than a typical mass protostar, once mass accretion from the infalling envelope and massive disks completes. BHR7-mms is likely to continue accreting matter from the disk (M$_{disk}$ $>$0.236 M$_\odot$) and envelope (M$_{env}$ $\sim$1.3 M$_\odot$ Tobin et al., 2018a) and grow substantially in size (likely M$_*$$>$ 1.6 M$_\odot$).

We assumed the majority of the accretion from the disk (M$_d$ $\sim$ 0.26 M$_\odot$) and envelope (M$_{env}$ $\sim$ 1 M$_\odot$) happens within the first $\sim$0.5 Myr of star formation, the source will most likely form an A-type star (M$_*$$\approx$1.6–2.4 M$_\odot$), depending on the efficiency of accretion (10%–15%; Jørgensen et al., 2007). Yen et al. (2017) conducted a survey of several well-known Class 0 protostars to determine any evolutionary tracer from the star and disk characteristics. They derived an empirical power-law protostellar mass and Keplerian radii relation for, Class 0 sources $R_d = (44 \pm 8) \times \left(\frac{M_*}{0.1 M_\odot}\right)^{(0.8\pm0.14)}$ au and Class 0+I sources $R_d = (161 \pm 16) \times \left(\frac{M_*}{1 M_\odot}\right)^{(0.24\pm0.12)}$ au. From our mass of 1.1894$\pm$0.0095 M$_\odot$, we found $R_d = 313 \pm 62$ au and

$R_d = 167 \pm 8$ au, for the Yen et al. (2017) Class 0 and Class 0+I relations, respectively. From the constraints of our observations, we found the Keplerian disk may extend to 480 au, placing BHR7-mms above all of the Class 0 sources found in Yen et al. (2017).

3.5.2. Mass Accretion

The circumstellar disk and envelope of BHR7-mms provides a reservoir for additional mass transfer onto the protostar (envelope contains >1 $M_\odot$ Tobin et al., 2018a). Thus we need to determine the maximal mass accretion rate of the system to determine whether viscous transport can efficiently carry away enough momentum to facilitate accretion or if winds are required to carry away angular momentum to enable accretion (Wilkin & Stahler, 1998). While these observations do not place a direct constraint on $\dot{M}$, since we cannot directly observe the mass accretion indicators, from our constraints on M_* and the observed total luminosity (9.3 $L_\odot$; Tobin et al., 2018a), we can estimate the mass accretion rate. In a viscous, accreting disk, the total luminosity is the sum of the stellar and accretion luminosity:

$$L \approx L_* + L_{acc}, \tag{3.4}$$

where

$$L_{acc} = \frac{GM_*\dot{M}}{R_*}. \tag{3.5}$$

Prior observations constrain the bolometric luminosity and from our observations, we can directly constrain the stellar mass from the kinematic observations (M_* ≈1.18 $M_\odot$). Using the stellar birth line in Hartmann et al. (1997) (adopting the models with protostellar surface cooling that provides lower estimates), we can then estimate the protostellar radius (R_* ≈2.5 $R_\odot$). From Figure 3 in Hartmann et al. (1997), we estimated the stellar luminosity to be 3.6 $L_\odot$, for a stellar mass of 1.18 $M_\odot$.

Considering the bolometric luminosities (9.3 $L_\odot$) we found the $\dot{M}$∼3.9×10^{-7} $M_\odot$ year^{-1}. This estimate is likely a lower bound, as we adopt models that introduce protostellar surface cooling). These accretion rates are unable to build up the observed protostellar masses within the typical lifetime of the Class 0 stage (lifetime∼150 kyr, buildup from mass accretion rate ∼3 Myr) and thus require periods of higher accretion events to explain the observed protostellar

masses. Furthermore, we compared the derived accretion rate with a similar survey toward Class 0+I protostars (Yen et al., 2017) and found the derived accretion rate is consistent with TMC-1 and TMC-1A, other Class 0+I sources.

3.6. Summary

We have characterized the disk of the protostar BHR7-mms using ALMA dust continuum observations at 1.3 mm and kinematic molecular line observations, $C^{18}O$, ^{13}CO, and H_2CO transitions. The results and our analysis of the observations is as follows:

1. We resolved the minor and major axis of the continuum disk, determining the disk size to be $\sim$0.″580$\times$0.″253 ($\approx 232\times101$ au) with a position angle of $\sim$87°. The continuum disk appears relatively smooth and symmetric in brightness, with an flux density of $\sim$0.21 Jy. Assuming an optically thin, isothermal ($T_d \approx 48$ K) dust continuum disk, we found the disk mass to be $\sim$0.26 $M_\odot$.
2. We further confirmed Keplerian rotation on the size scale of the disk using the kinematic tracers $C^{18}O$, ^{13}CO, and H_2CO. We analyzed the source using public code (SLAM; Aso et al., 2015; Sai et al., 2020) to analyze the PV diagrams of the disk tracing molecules to fit Keplerian rotation and potential infall kinematics using Bayesian estimators (emcee; Foreman-Mackey et al., 2013). From this method, we find $C^{18}O$, ^{13}CO, and H_2CO we found the maximum mass consistent with $\sim$1.6 $M_\odot$and the minimum mass consistent with $\sim$0.5 $M_\odot$(summarized in Tables 3.3.1,3.3.2, &3.3.3).
3. We performed a more rigorous fit directly to the observed $C^{18}O$ *uv*-visibilities, using nested sampling, and find the central potential is consistent with a mass of $M_* = 1.19\pm \sim 0.01$ $M_\odot$ (full table of parameters found in Table 3.4.1).
4. From these constraints, we found the disk is consistent with being on the edge of gravitational instability, with the upper bound for the Toomre Q parameter, the measure of disk stability, to be 0.9.
5. Using the protostar mass of $M_*= 1.19 \pm 0.01$ $M_\odot$, the known bolometric luminosity of 9.3 $L_\odot$, and stellar birthline models, we found the accretion rate to be $\approx 3.9\times10^{-7}$ $M_\odot$ yr^{-1}.

Chapter 4

Decoupling Infall and Rotation in the isolated protostar BHR7-mms[1]

Preface

We present Atacama Large Millimeter/submillimeter Array observations toward the isolated protostar, BHR7-mms (d$\sim$400 pc) at 3 mm (resolution of $\sim$1.$''$5$\approx$ 600 au) and complementary observations at 1.3 mm (R$\sim$0.$''$1$\approx$ 40 au). We observed several gas tracers, such as the outflow tracer ^{12}CO, cold and dense gas tracers, N_2D+ and N_2H+, and the gas tracers SO, ^{13}CS and HNC. We identified infall signatures of envelope material. We also traced the scales of mass transfer from the $\sim$1000s of au scales of the envelope, across the cavity, and down to the disk. We estimated the total dust component of the surrounding material from the unresolved 3 mm observations to be $\sim$0.9 $M_\odot$.

[1]Chapter reproduced from work in submission.

4.1. Introduction

The origins of stars and planets begin at the collapse of cold, dense clouds. The infall of the parent cloud plays a critical role in forming and regulating the protostar and circumstellar disk. This mass transport from large ($\sim$ 0.1 pc scales) down to the protostar and disk scales must be probed in order to understand the formation of protostars.

During the earliest stages of star formation, most of the mass is contained within the envelope (1000s of au) and infalls to the circumstellar disk (<100s of au) (Bergin & Tafalla, 2007). This circumstellar disk is comprised primarily of gas and further accretes to the protostellar surface, building up mass of the central protostar. The earliest stage of the protostars, the Class 0 stage (<150 kyr), are defined by the steep spectral index ($\alpha_\lambda < -2$ Lada & Wilking, 1984; Lada, 1987; Greene et al., 1994), strong excess of their submillimeter luminosity (Andre et al., 1993), and very low bolometric temperatures (<70 K e.g., Chen et al., 1995b), indicative of cold, dense envelopes. Class 0 sources are often associated with powerful bi-polar outflows/-jets, circumstellar disks, and the envelope containing most of the mass of the system. These outflows and accretion events act to deplete the mass of the envelope, eventually halting the accretion process onto the protostellar surface (Shu et al., 1987).

Rotationally supported disks have been observed at every protostellar stage, from Class 0 sources (Lada, 1987; Andre et al., 1993; Tobin et al., 2018b), up to protoplanetary disk (Andrews et al., 2018), which strongly suggests nascent rotation in the parent cloud prior to collapse. The formation of protostellar disks is a natural consequence of gravitational collapse of protostellar cores, even without the complete conservation of angular momentum, due to the many orders-of-magnitude in specific angular momentum between the large scale core (R$\sim$0.1 pc, v$\sim$5 km s^{-1}, $j > 10^{21} cm^2 s^{-1}$) and the compact disks (R$\sim$10 au, v$\sim$5 km s^{-1}, $j \sim 10^{16} cm^2 s^{-1}$).

Since these class 0 objects are heavily embedded in envelopes of dust and gas, observations of molecular line rotational transitions in addition to multi-wavelength continuum observations, can be used to infer kinematics, column densities, temperatures, and chemical abundances (van Dishoeck & Blake, 1998; Evans, 1999). The advancement of state-of-the-art radio interferometers allows for simultaneous continuum and molecular line observations with sub-arcsecond

resolution and high sensitivity (Wilner et al., 2000; Jørgensen et al., 2005; Tobin, 2011). Recent studies with the Atacama Large Millimeter/submillimeter Array (ALMA) show hosts of protostars with a plethora of molecules (Jørgensen et al., 2016; Tychoniec et al., 2018; Lee et al., 2019b; Tobin et al., 2018b, 2022), which can be used to trace the angular momentum transport in protostars.

The surface mass density distribution of the disk, which directly regulates the mass of the protostar, results from the transport of the angular momentum of the infalling protostellar envelope, modified by transport processes within the disk (Cassen & Moosman, 1981; Terebey et al., 1984). At this stage, pressure gradients, turbulence, self-gravity, outflows, accretion rates, and magnetic fields heavily influence the structure of the disk and envelope (Crutcher, 1999; McKee & Ostriker, 2007; Kim & Ostriker, 2007; Boss & Keiser, 2013; Inutsuka et al., 2015). The exact weighted importance of these processes is still being explored.

Thus magnetic braking due to the compression of the magnetic fields is thought to assist (Allen et al., 2003b,a; Allen, 2004) with the dispersal of angular momentum, but due to the high efficiency to transport angular momentum, either does not produce rotationally supported disks or produces disks much smaller than observed (Mellon & Li, 2008). Many higher order processes can be applied; such as outflows carrying away the magnetic field (Dapp et al., 2012) and Ohmic dissipation (Nakano et al., 2002).

Additionally, the exact contribution by which angular momentum is carried away after material is accreted from large scales is not well known. The envelope, which accretes onto the disk, could build up mass to a critical point, by which the thermal properties of the disk can no longer hydrostatically support against gravitational collapse, and thus the disk fragments.

Furthermore, disk accretion to near the protostellar surface would launch bi-polar outflows, which can carry away momentum. These processes are likely time-variable, with periods of high accretion events (Hartmann & Kenyon, 1996). In order to form Sun-like stars ($M_* \approx 1\ M_\odot$) over a-few-10^5 yr requires accretion rates of at least 2-3$\times 10^{-5}$ $M_\odot$ yr^{-1}, which is 1-2 orders of magnitude larger than what is observed (Kenyon et al., 1990; Evans et al., 2009; Kryukova et al., 2012).

We are approaching this study via two methods. First we obtained the 1.3 mm ALMA extended configuration in order to charactertize Keplerian rotation on the size scales of the

disk. Furthermore we characterize the dust component of the continuum disk and estimate the total disk mass by assuming a gas-to-dust ratio. Rigorous analysis and characterization of the Keplerian disk is summarized in Reynolds et al. (2023 subm.), herein Paper I. In this work, we combine these disk tracers with large scale processes, such as shock tracers (SO), the outflow tracers (CO), and the envelope tracer (N_2D+) to characterize all scales of the system. We obtained complementary 3 mm ALMA+ACA observations of the envelope (N_2H+ and HNC) with high sensitivity. From these observations we can construct a complete picture of the protostar BHR7-mms, building the bridges of mass and angular momentum transport from large scales to small scales.

The setup of this paper (Paper II) is as follows: in Section 4.2 we detail our observations of BHR7-mms at 3 mm, in Section 4.3 we analyze the ALMA ACA+TP observations, and we summarize our findings in Section 4.4.

4.2. Observations

Our observations were taken by the state-of-the-art radio interferometer ALMA, located on Llano de Chajnantor plateau in the Atacama region of Chile at an elevation of $\sim$5000 meters. We present observations of a nearby (d$\sim$400$\pm$10 pc; Woermann et al., 2001) isolated protostar BHR7-mms, located in the dark cloud BHR7, within the Vela cometary globule, using Band 3 (3 mm). The observations took place across two sets of observations, associated with project 2019.1.00463.S.

The correlator was configured to observe both continuum and molecular line emission with a central frequency of 93 GHz; with spectra windows set to observe N_2H+ (J = 1-0) and ^{13}CS (J = 2-1). The lines were each observed with 59 MHz and an additional two spectral windows were added with 2 GHz bandwidth to obtain high sensitivity. The aggregate continuum bandwidth after flagging line emission is 3.75 GHz.

4.2.0.0.1 ACA+TP Observations The first set of observations utilized the Atacama Compact Array (ACA) with an average of eleven, 7-meter antennas between 2019 October 15 to November 07 for 16 total execution blocks. The total on source time for the compact baseline observations across the 16 executions blocks was 22 hours, with an average time per execution

block of 1.5 hours, and covered baselines between 8 meters to 47 meters. The raw visibility data were pipeline calibrated by the North American ARC staff using Common Astronomy Software Applications (CASA) version 5.6.1-8. The observations have a typical angular resolution of 17.″5 (7,000 au) with a continuum sensitivity of 0.12 μJy beam^{-1} when reconstructed with Briggs robust weighting parameter of 0.5 and a signal-to-noise ratio (SNR) of $\sim$1,300. No self-calibration was performed on the dataset.

4.2.0.0.2 Compact ALMA Configuration The second set of observations utilized the most compact ALMA configuration, with an average of 46 antennas between 2019 October 31 to November 04 for 16 total execution blocks. The total on source time for the compact baseline observations across the 4 executions blocks was 4.2 hours, with an average time per execution block of 1.1 hours, and covered baselines between 15 meters to 700 meters. The raw visibility data were pipeline calibrated by the North American ARC staff using Common Astronomy Software Applications (CASA) version 5.6.1-8. The observations have a typical angular resolution of 1.″7 (680 au) with a continuum sensitivity of 10 μJy beam^{-1} when reconstructed with Briggs robust weighting parameter of 0.5 and a signal-to-noise ratio (SNR) of $\sim$1,200. No self-calibration was performed on the dataset. These observations took place in 3 pointings, creating a mosaic on the field, providing the most overlap and therefore sensitivity over the central region where the protostar is.

4.2.0.0.3 Imaging With the calibrated uv-visibilities in hand, we utilized the *CASA* (McMullin et al., 2007) task *tclean* (version 6.5) to reconstruct the molecular line data cubes and continuum images. Rather than combining the uv-visibilities, we opted to provide the task *tclean* with the "mosaic" field in the imaging mode to image the full field-of-view.

In order to take advantage of the full spectral range of line-free continuum emission, we used the multi-frequency synthesis (MFS) imaging mode. We also utilized the multi-Taylor-term, multi-scale (MTMFS) algorithm on the continuum with the scales set to "0" (point like), "5" (minor axis of the beam), and "30" ($\sim$3$\times$ beam major axis), applying conservative masks around the regions of emission as to not inadvertently introduce structure. Images were produced at a range of Briggs robust weighting parameter from -2 to 2, but for the purpose of this

work, we show the Briggs robust 0.5 image, which balances the compact and extended baseline weights to achieve moderate resolution and sensitivity. The pixel size of the continuum images was set to $0.''02$, which achieves $\sim$5 pixels across the minor beam axis for the Briggs robust 0.5 synthesized beam. The images were constructed $\sim 30''$ wide, centered on the protostar, to recover any emission compact or large-scale, that could be found at high separations.

The continuum-subtracted molecular line uv-visibilities were reconstructed using the "cube" imaging mode, in order to retain information regarding the velocity structure. We utilized the well known "Clark" algorithm during the imaging process, also applying conservative masks around the regions of emission as to assist the deconvolve process and not clean the sidelobes of the beam. Images were produced at a range of Briggs robust weighting parameter from 0 to 2, and for the purpose of this work, we show the Briggs robust weighting parameter of 2, corresponding to "natural" weighting. The pixel size of the continuum images was set to $0.''02$, which achieves $\sim$20 pixels across the minor beam axis for the natural synthesized beam.

4.3. Results

4.3.1. Spectral Energy Distribution

We constructed the SED combining prior observations (Tobin et al., 2018a), our 1.3 mm observations, and our 3 mm observations to characterize the protostar. TheSED is shown in Figure 4.4.3. We integrated the SED using the *numpy*, trapezoidal technique to determine the bolometric luminosity (L_{bol}), the submillimiter luminosity (L_{submm}), and the bolometric temperature (T_{bol}), which are typical indicators for the evolutionary state of protostars (Andre et al., 1993; Chen et al., 1995a). We found the $L_{bol}= 9.26\ L_{\odot}$, the $L_{submm}/L_{bol}\approx 0.031$, and $T_{bol}= 46$ K.

4.3.2. 3 mm Dust Continuum

While the 3 mm continuum observations remain unresolved, the continuum observations constrain the dust component of the envelope and disk. The source appears to be nearly edge-on in NIR images (see Figure 8, models of the dark lane across the disk major axis and the cavity cleared out by the outflow; Whitney et al., 2003) and from continuum radiative transfer modeling of the 1.3 mm observations, we estimated an inclination of $\sim$60°. With nearly edge-on sources, we are usually limited by the disk optical depth and are less sensitive to the azimuthal sub-structures that may be present (Bate, 2018). However, the 3 mm observations were optimized to observe the large scale envelope, thus these observations do not detail the circumstellar disk which was resolved in previous works (Tobin et al., 2018a; Reynolds et al., 2023 subm.).

From the 3 mm observations, we did not resolve the BHR7-mms as the source appears nearly beam-like (Briggs robust weighting 0.5; Figure 4.4.1). To estimate the dust properties, we used the *CASA imfit* to estimate the size of the emission by fitting a multi-component 2D Gaussian to the emission. The deconvolved size (major and minor axis given by *imfit*) of the continuum source is $0.''849\pm0.047\times0.''686\pm0.034\approx340\times274$ au with a position angle of $88°\pm14°$ at the assumed distance of 400 pc. The peak flux is 11.797 ± 0.085 mJy beam^{-1} with an integrated flux density of 14.2 ± 0.17 mJy.

Spectral Index Conducting observations across multiple wavelengths is crucial for holistically characterizing the source, in particular, the submillimeter/millimeter observations can constrain the dust properties by computing the spectral index, defined as,

$$\alpha_\lambda = \frac{dlog(F_\lambda)}{dlog(\lambda)}, \tag{4.1}$$

which is valid over finite wavelengths. When evaluated in the range of the Rayleigh-Jeans law, this can detail the deviation from the Rayleigh-Jeans law, where $\alpha_\lambda \simeq 2$ in the Rayleigh-Jeans regime.

We used the 1-D, radially averaged uv-visibility amplitude of the observations to estimate the spectral index (given in Figure 4.4.2). The peak (shortest baseline) of the 1.3 mm prior observations is 0.234 Jy and the peak (shortest baseline) of the 3 mm observations is 0.019 Jy. To estimate the spectra index, we baseline-matched the two datasets by choosing the shortest baseline in the 1.3 mm ($\langle\lambda\rangle = 1325.57$ μm) and interpolated the 3 mm ($\langle\lambda\rangle = 3286.07$ μm) baseline to fill the same coverage. This gave 0.234 Jy for the 1.3 mm and 0.014 Jy for the 3 mm. We found the $\alpha_\lambda = 4.1$ which corresponds to $\beta = 2.1 \pm 0.1$, where β is defined as,

$$\alpha_\lambda = 2 + \beta, \tag{4.2}$$

indicative of ISM-like dust grain distributions.

4.3.2.0.1 Mass Estimates We assumed the dust emission comes from a dust population that is isothermal, optically thin, and without scattering, and derived the dust properties from the equation:

$$M_{dust} = \frac{D^2 F_\lambda}{\kappa_\lambda B_\lambda(T_{dust})}, \tag{4.3}$$

where D is the distance to the region (400 pc), F_λ is the flux density, κ_λ is the dust opacity, B_λ is the Planck function for a dust temperature, and T_{dust} is taken to be the average temperature of a thermally emitting region. The κ_λ at λ = 3 mm was adopted from dust opacity models with value of 0.2 cm^2 g^{-1}, corresponding to an extrapolation of Ossenkopf & Henning (1994),

using $\beta = 1.7$,$\lambda = 1.3$ mm, for thin ice mantles after 10^5 yr of coagulation at a gas density of 10^6 cm^{-3}. The authors note the opacity chosen will directly determine the estimated dust mass by the equivalent factor, but the value should be between 0.15-0.3 cm^2 g^{-1}. This M_{dust} is thought to be a proxy for the total mass by applying a correction factor that accounts for the gas contribution. We adopted a gas-to-dust ratio (GDR) of 100:1, typical for Class 0 protostars and the ISM (Bohlin et al., 1978b).

There are several ways to approximate the average temperature of the dust in the envelope. One method is to adopt T_{disk} =43 K$\left(\times\frac{L_*}{L_\odot}\right)^{1/4}$ = 75 K, which is larger than temperatures derived from protostellar models (43 k; Tobin et al., 2013) and much larger than temperatures assumed for the more evolved protoplanetary disks (25 K; Andrews et al., 2013). If we assume the dust component probed by the 3 mm observations is isothermal, this would constitute the upper value for temperature of the emitting region. We adopted the temperature of ∼20 K, consistent with the freeze out temperature of CO. Finally, we took the lower bound of the average T_{env} to be 10 K, typical of the cold environment of the protostellar envelope.

We found the total mass of the envelope to be 0.29 $M_\odot$ (T=75 K) and 2.7 $M_\odot$ (T=10 K). For the purpose of this work, we adopted the average of these two values, equal to 1.5 $M_\odot$.

4.3.3. Molecular Lines

An isolated Class 0 source with an inclination of >60° is an ideal candidate to examine the kinematic properties of the infalling envelope. The lack of nearby sources and the clear geometric orientation simplify the interpretation of molecular line kinematic data. The 3 mm observations were optimized for observing the large-scale envelope with high sensitivity, using the tracers N_2H+ and ^{13}CS. The ^{13}CS is not strongly detected in this source and thus we did not use it for the purpose of our analysis. We also discuss the 1.3 mm observations in Reynolds et al. (2023 subm.), which included other large-scale tracers such as the envelope tracer N_2D+, the shock tracer SO, and the outflow tracer ^{12}CO.

4.3.3.1. Molecular Line Observations

To aid in the analysis of the molecular line observations, we employ several methods to reduce the 3D datacubes. We constructed moment 0 maps, which integrate the data cube over the frequency axis, to reduce the 3D nature of data cubes to 2D images. These images show

spatial locations of strong emission and deficits. To help preserve frequency information from the data cubes, we performed velocity-weighted integrated emission, so-called moment 1 maps. However, when integrating over any velocity ranges, we do not preserve the full velocity information of the emission; thus we provide spectral profiles of the molecular lines as well, integrated within a specified region. We detail each of the specific molecular line observations, but in particular we constructed several maps to show where the emission of certain molecules coincides,

$$\text{Figure 4.4.9} : C^{18}O(\text{disk}), {}^{12}CO(\text{outflow}), SO,$$
$$\text{Figure 4.4.10} : C^{18}O(\text{disk}), H_2CO(\text{outer disk}), N_2H\text{+}(\text{envelope}),$$
$$\text{Figure 4.4.11} : C^{18}O(\text{disk}), N_2D\text{+}(\text{envelope}), N_2H\text{+}(\text{envelope}).$$

CO is the next most abundant molecule to H_2 (ISM abundance $H_2/CO \approx 10,000$, Wilson & Rood, 1994), with relatively well understood gas phase chemistry. However, despite being 4 orders of magnitude less abundant, the ^{12}CO molecule is still optically thick in these regions making it a poor tracer for compact regions, but appropriate for observations towards less dense scales like that of the outflows (moment 0 map shown in Figure 4.4.4). The CO appears in the 1.3 mm observations to reach scales beyond 20″ (8,000 au), with deprojected velocities $>$30 km s^{-1} (Figure 4.4.5), tracing the outflow components of the protostar. The CO appears to launch from the center of the continuum observations and have an opening that is comparable to the size of the disk (Figure 4.4.9). It is likely that the outflow is entraining gas from the disk and colliding with the large scale envelope.

SO is spatially resolved and shows morphological features that are, on compact scales near to the continuum disk, similar to C^{18}O and H^{13}CO+ (Figure 4.4.9). The narrow line emission of SO (Figure 4.4.8 & 4.4.7) rules out an accretion shock origin (Sakai et al., 2014). A spatial comparison between the moment 0 maps of C^{18}O, ^{12}CO, and SO is shown in Figure 4.4.9. The SO emission, appears to trace out the cavity of the CO outflow, consistent with observations of other energetic sources (TMC1A and HH212, Tabone et al., 2017; Lee et al., 2018, respectively). Towards the compact continuum disk (Figure 4.4.8), the linewidth and spatial

distribution of SO is comparable to the Keplerian disk as traced by $C^{18}O$, indicative that they are both tracing the gas component of the disk. Whereas, the off-center emission, found at both red and blue Doppler shifted channels, is likely tracing the outflow cavity wall, evident by the low velocity component in Figure 4.4.7.

N_2D+ observations were conducted as part of Reynolds et al. (2023 subm.) at 1.3 mm. On disk scales, where the gas is heated up by thermal motion and the central protostar, CO exists in gas phase and reacts destructively with nitrogen-bearing molecules. Further out in the disk, the temperature reaches $\sim$10 K, freezing out CO and other carbon-bearing molecules onto the dust grains, while remaining dense (n$\sim10^5$ cm^{-2}), allowing for nitrogen-bearing species to exist (Turner, 1974; Green et al., 1974; Caselli et al., 1995, 2002a; Crapsi et al., 2005). While the 1.3 mm observations were constructed to simultaneously observed N_2D+ (J = 3-2) at 231.321828 GHz, the emission remains mostly resolved out due to incomplete compact baseline sampling (Crapsi et al., 2005; Tobin et al., 2013).

N_2H+ molecular line was the primary target of the 3 mm observations, to detail the kinematics of the protostellar envelope. The envelope appears at large scales (Figures 4.4.10 & 4.4.11), well beyond the scales of the disk. This is due to the destructive chemical reactions of N_2H+ with carbon-bearing species of molecules like CO, which sublimate from the dist grains at temperatures $>$20 K. This makes N_2H+ particularly ideal for tracing the cold (T$\sim$10 K), dense gas in the envelope.

4.3.4. Position-Velocity Diagram Analysis

In order to reduce the 3D nature of the data cubes into lower-dimensions, we constructed 2D position-velocity (PV) diagrams of the data cubes. The PV diagrams are extracted by summing the pixels within a defined region at each pixel along a particular axis of the disk. When probing disk kinematics, it is useful to restrict the PV diagram to widths to the size of the disk to select out any large scale emission and to align the extraction along the major axis of the disk. Otherwise, when probing envelope structure, larger widths are required to encompass the entirety of the emission. We performed the extraction for the compact component of SO within a 1$''$ cut along the disk major axis of 87°, east-of-north. For the outflow, we extracted

a 10″ wide cut along the outflow axis of -5°. For the envelope, we extracted a 60″ wide cut along the velocity gradient axis, which appears to be ∼42°. We centered all extractions to the location of the continuum emission peak of BHR7-mms, 08h14m23.323s -34d31m03.42s, such that the positions are defined as offsets from the gravitational potential. The PV diagram, inherently, provides information on spatial distribution of the velocities with positions offset from the protostar, which, for the case of protostars, is understood to be possible Keplerian rotation ($v \propto R^{-0.5}$) and infall (conservation of angular momentum; $v \propto R^{-1}$) effects.

H_2CO/$C^{18}O$ both appear to trace similar components (Figure 4.4.15) when the two PV diagrams align. From fitting the lines of H_2CO and $C^{18}O$, we found the FWHM of the linewidth is >1 km s^{-1}, which is indicative of Keplerian rotation when found on the size-scales of the continuum disk.

N_2H+/$C^{18}O$ appear to trace distinct components of the protostellar system (Figures 4.4.14 & 4.4.16). The $C^{18}O$ emission is found on more compact spatial scales and occupies the higher velocity ranges as compared to the large scale, narrow linewidth N_2H+ envelope. The N_2H+ emission is also blue-Doppler-shift dominated, indicative of an infalling envelope while the $C^{18}O$ appears more symmetric.

SO , when extracted along an angle consistent with the Keplerian disk ($\theta \simeq 87°$), appears to trace Keplerian motions around the central protostar (Figure 4.4.13). It is likely that the SO material is tracing along the cavity wall, exposed and perturbed by the outflow. This material is probably infalling along the cavity and as the material falls to the scales of the continuum disk, begins to undergo Keplerian rotation and become a part of the gaseous flared disk.

4.3.5. Masses and Column Densities

In Figure 4.4.6 we show the 7-component, hyperfine N_2H+ spectra in black, extracted within a 45″ (18,000 au) annulus centered on BHR7-mms. We utilized the published code *pyspeckit* with the N_2H+ module to simultaneously fit all of the hyperfine structure components (indicated in dashed red). The *pyspeckit* code is based off of a well known hyperfine fitting program, implemented in CLASS (Forveille et al., 1989), with the rest frequencies adopted from

Caselli et al. (1995) and weights adopted from Womack et al. (1992). From the fit we are able to determine the local-standard-of-rest velocities (V_{LSR}), intrinsic line width (Δv, corrected for instrumental effects), total optical depths (τ_{tot}), and excitation temperatures (T_{ex}). Here τ_{tot} is the sum of the peak optical depths of the seven hyperfine components (Benson & Myers, 1989). In comparing the optical depth of the isolated N_2H+ (J = 1-0) component, we found the main component is small (< 0.5) and is $\approx 0.3\ \tau_{tot}$, thus the N_2H+ emission can be considered optically thin everywhere.

We calculated the mass of the N_2H+ component and relating back to the abundance, determined the total mass in the envelope. We assumed that the observed N_2H+ line widths are not dominated by systematic gas motions, thus the column density of the N_2H+ molecule has been calculated as

$$N(N_2H+) = 3 \times 10^{11} \frac{\tau \Delta v T_{ex}}{1 - e^{-4.47/T_{ex}}} cm^{-2}, \tag{4.4}$$

given by (Benson et al., 1998), where τ is the total optical depth (6.13), Δv is the intrinsic linewidth (0.28 km s^{-1}), and T_{ex} is the excitation temperature (2.74 K). From the hyperfine structure fit (Figure 4.4.6) we determined the N(N_2H+)$\approx 1.96 \times 10^{12}$ cm^{-2}.

The gas-phase N_2H+ mass can then be calculated by

$$M(N_2H+) \approx N(N_2H+)_{peak} \times m_{N_2H+} \times D^2 \times \Omega_{FWHM}, \tag{4.5}$$

where D is the distance to the protostar (400 pc), and Ω_{FWHM} is the area enclosed by the contour level at 50% of the peak value for the envelope, corresponding to an R_{avg} $\approx$2970 au. We found the M(N_2H+)$\approx 2.94 \times 10^{-10}$ $M_\odot$. To convert to M_{H_2}, we assumed a conservative abundance value of $\chi(N_2H+) \approx 3 \times 10^{-10}$, typical of other studies (Chen et al., 2007), and calculated M_{H_2} $\approx$0.98 $M_\odot$. This indicates a majority of the core's mass is still available for further accretion from the large-scale envelope.

4.4. Summary

We present high sensitivity observations tracing the envelope kinematics of the isolated protostar BHR7-mms. Our observations complement the disk kinematics outlined in Reynolds

et al. (2023 subm.) by targeting the cold, dense gas tracer N_2H+. Furthermore, we traced the transfer of mass and angular momentum from the envelope down to the disk, while simultaneously resolving several processes that can disperse the excess of angular momentum buildup from collapse.

Our results are as summarized:

1. We determined the bolometric temperature of BHR7-mms to be $\sim$46 K, confirming BHR7-mms status as a Class 0 protostar.
2. We resolved the envelope with the cold, dense gas tracer N_2H+, and found the column density to be $N(N_2H+) = 1.96 \times 10^{12}$ cm^{-2} and the total mass $M(N_2H+) >= 2.94 \times 10^{-10}$ M$_\odot$.
3. The ^{12}CO observations seem to originate from the disk surface, as the outflow starting width is the same as the 1.3 mm continuum disk.
4. The ^{12}CO jet originates from the central protostellar and has deprojected velocities exceeding 30 km s^{-1}.
5. The spatial coincidence of SO, a warm gas tracer, likely indicates it originates from the outflow cavity wall, as it forms a "S" pattern around the outflow and traces down to the disk.
6. While N_2D+ is spatially filtered in the high resolution observations, the emission appears at scales outside of the C^{18}O emission and comparable scales to the N_2H+ emission. This is due to the destructive chemistry that occurs between the nitrogen and carbon bearing gas species.

Through our analysis of the compact and large scale kinematics, we found the envelope (M$_{env} \approx 0.98$ M$_\odot$) is likely efficiently building up mass in the disk (M$_d \approx 0.3$ M$_\odot$). The mass infall rate from the envelope, is $\sim 3 \times 10^{-6}$ M$_\odot$ while the disk accretion rate is $\sim 1 \times 10^{-6}$ M$_\odot$ The disk appears to be marginally unstable through Toomre Q analysis, with a value likely $<$1.2, averaged across the disk. However, due to the high inclination of the system, we did not observe any disk substructure which would visually confirm disk instability.

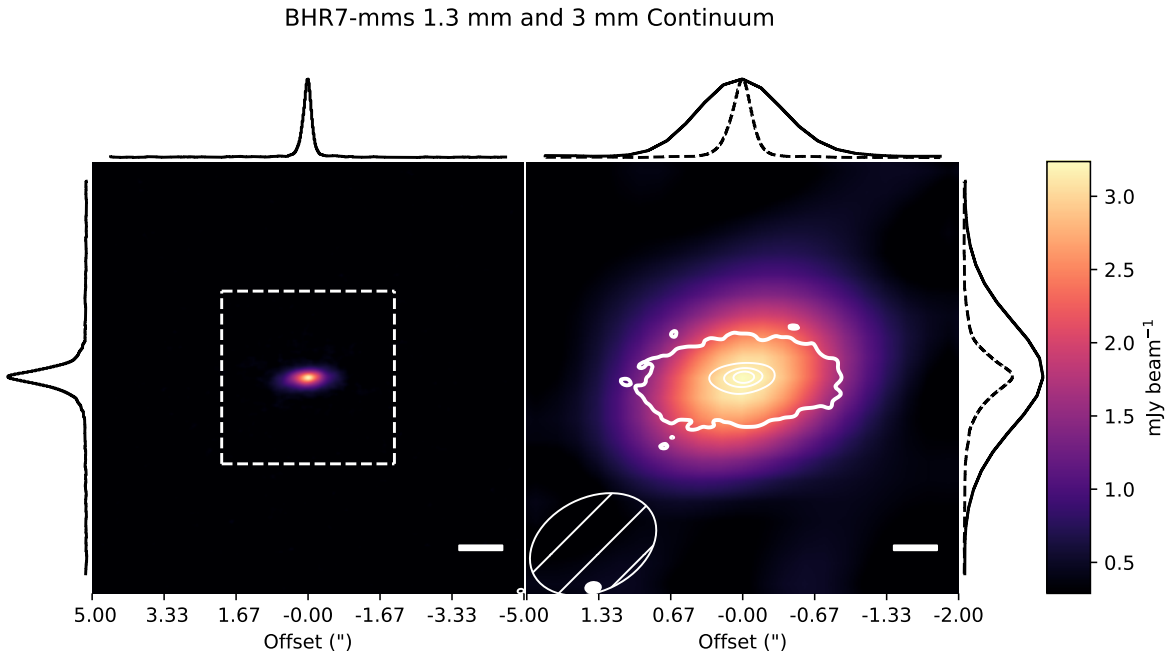

Figure 4.4.1: : Dust continuum image of BHR7-mm, at 1.3 mm (left panel) and 3 mm (right panel), constructed with Briggs robust weighting parameter of -2. The left panel indicates a 10″ wide 1.3 mm color image and a zoom-in window 4″ wide. On the right panel, the 3 mm color image overlayed with 1.3 mm white contours (levels=5, 10, 15, 20 σ). Along each axis, a histogram summing the respective pixels along the opposing axis. A 0.″5 (200 au) scalebar is shown in the lower right of each panel. The restoring beam is shown in the panels near the center, with the 1.3 mm beam indicated by a filled in ellipse and the 3 mm beam indicated by the hashed ellipse. The color bar is indicated on the very right of the panels.

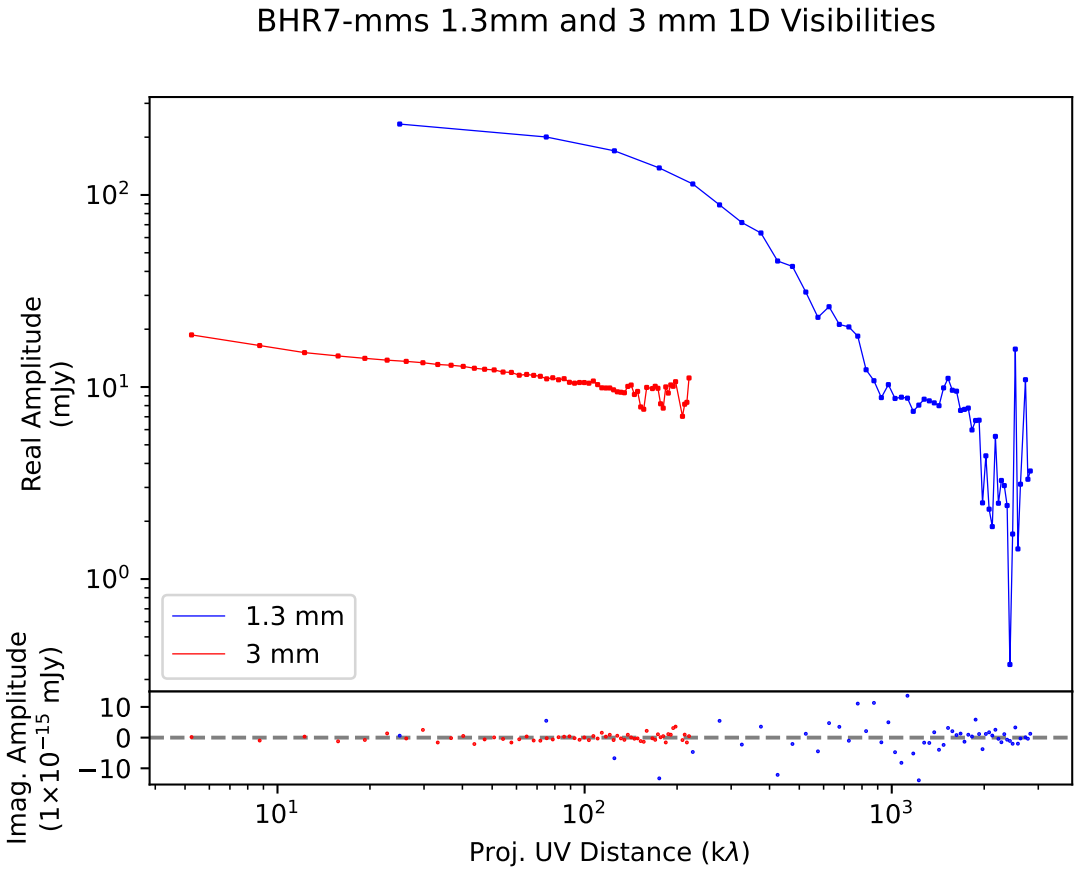

Figure 4.4.2: : The real (top panel) and imaginary (bottom panel), radially averaged (1.3 mm averaging=500 kλ) uv-visibility amplitudes for BHR7-mms. The peak (shortest baseline) of the 1.3 mm (blue) is 0.256 Jy and the peak (shortest baseline) of the 3 mm (red) is 0.019 Jy. To estimate the spectra index, we can baseline-match the two datasets by choosing the shortest baseline in the 1.3 mm and interpolate the 3 mm baseline to fill the same coverage. This gives 0.256 Jy for the 1.3 mm and 0.015 Jy for the 3 mm. We find the $\alpha_\lambda = -3.2$ which corresponds to $\beta = 1.2$.

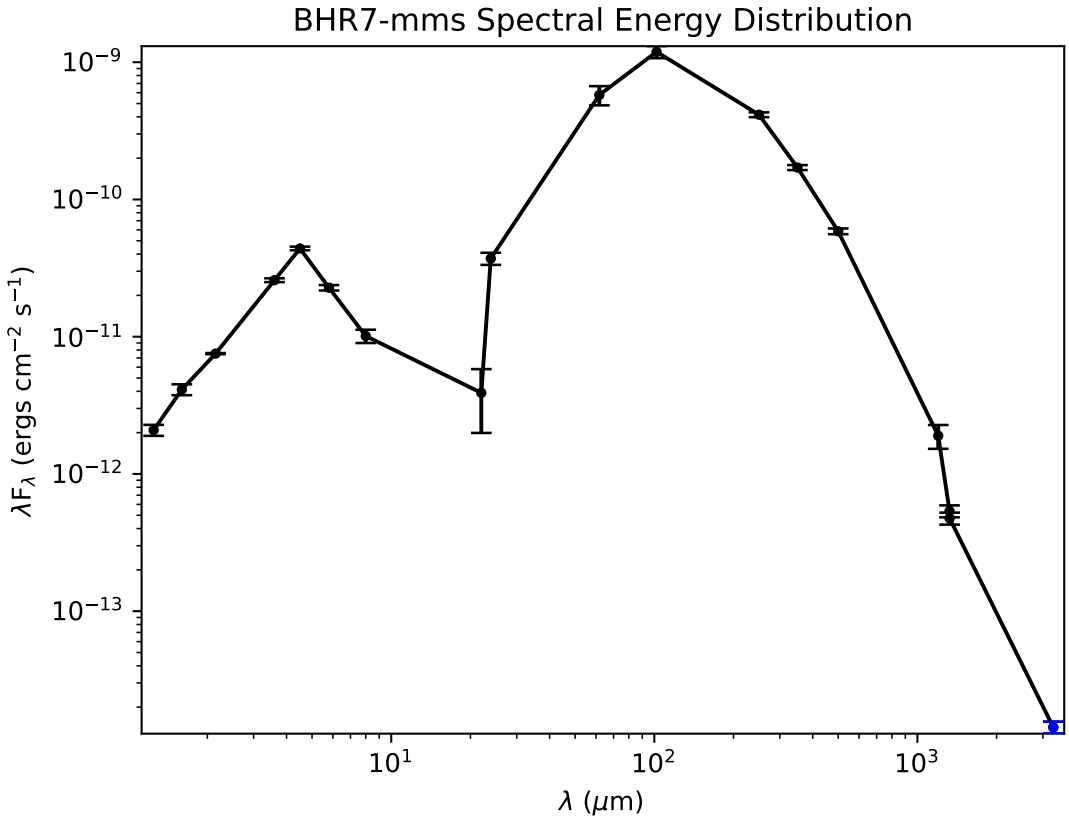

Figure 4.4.3: : The spectral energy distribution of BHR7-mms, as observed by Tobin et al. (2018a), with our additional observations indicated in blue. We find the bolometric luminosity to be 9.26 $L_\odot$, the ratio L_{submm}/L_{bol} =0.14, and the bolometric temperature to be 50 K, confirming the source is a Class 0 protostar.

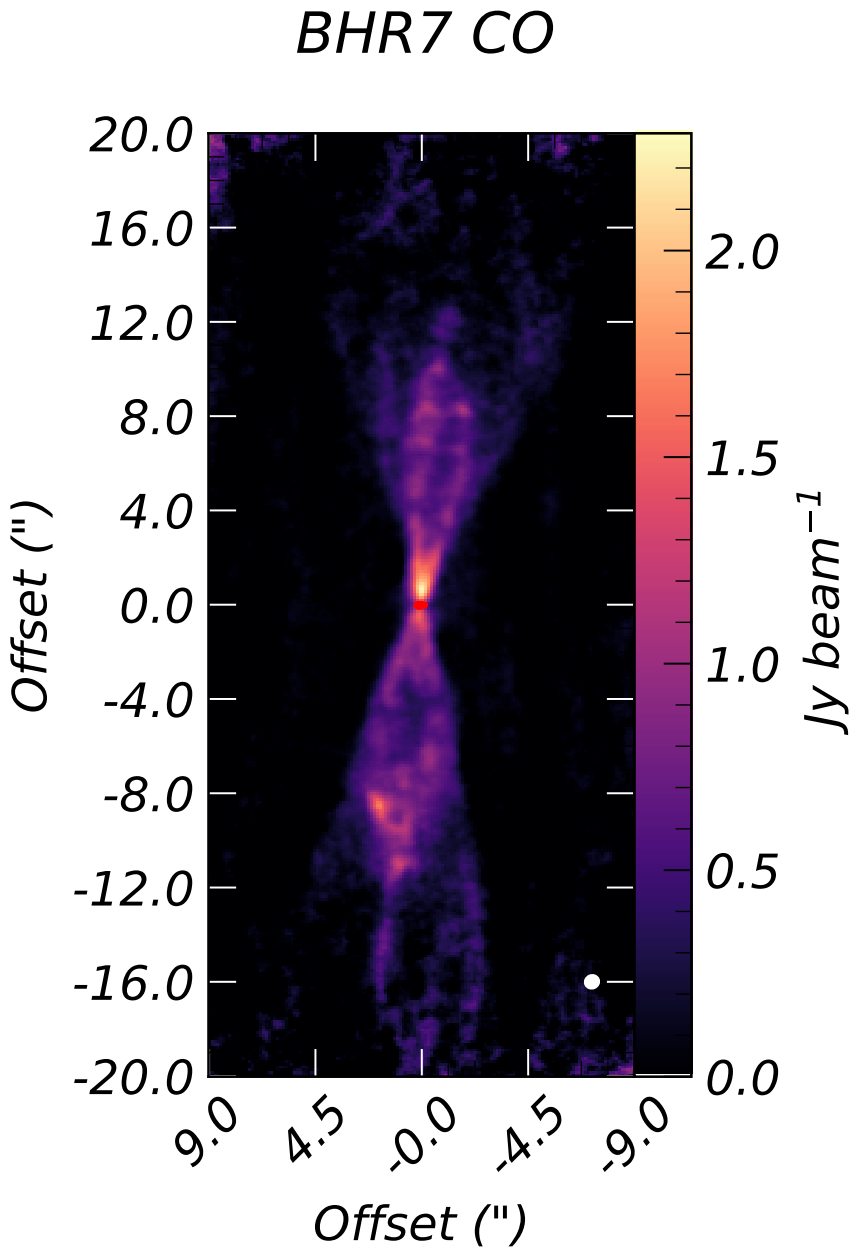

Figure 4.4.4: : The ^{12}CO moment 0 map, constructed by integrating along the frequency axis. The red contour at the center indicates the 3 σ of the 1.3 mm continuum image. We observe the slower, wide angle ($\sim$45°) component and a faster, collimated jet originating from the protostar. The outflows span $\sim$20″ ($\sim$8,000 au) from the protostar. The restoring beam is indicated in the lower right.

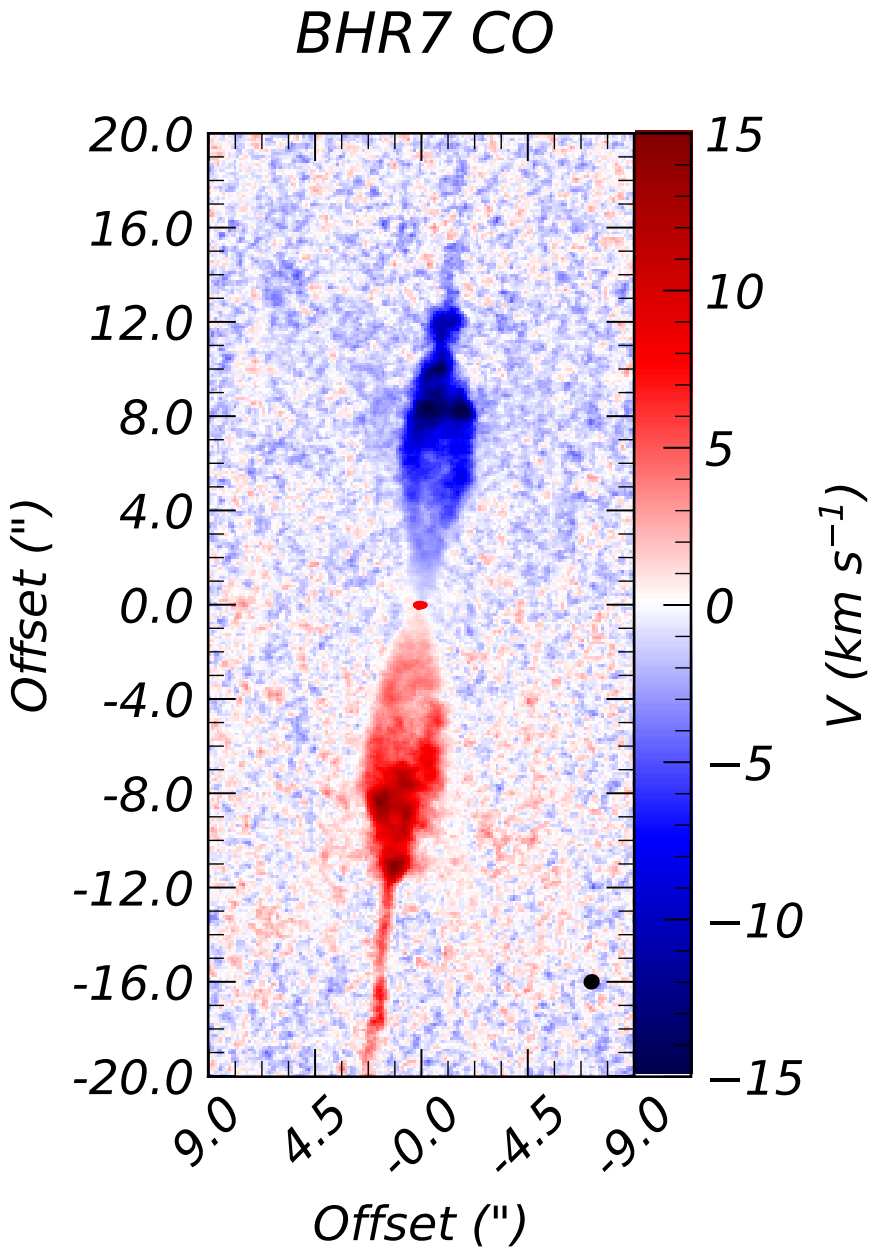

Figure 4.4.5: : The ^{12}CO moment 1 map, with the respective Doppler shifted emission indicate as red and blue. This is constructed by integrating along the frequency axis and weighting the values by the respective intensities. The red contour at the center indicates the 3 σ of the 1.3 mm continuum image. The restoring beam is indicated in the lower right.

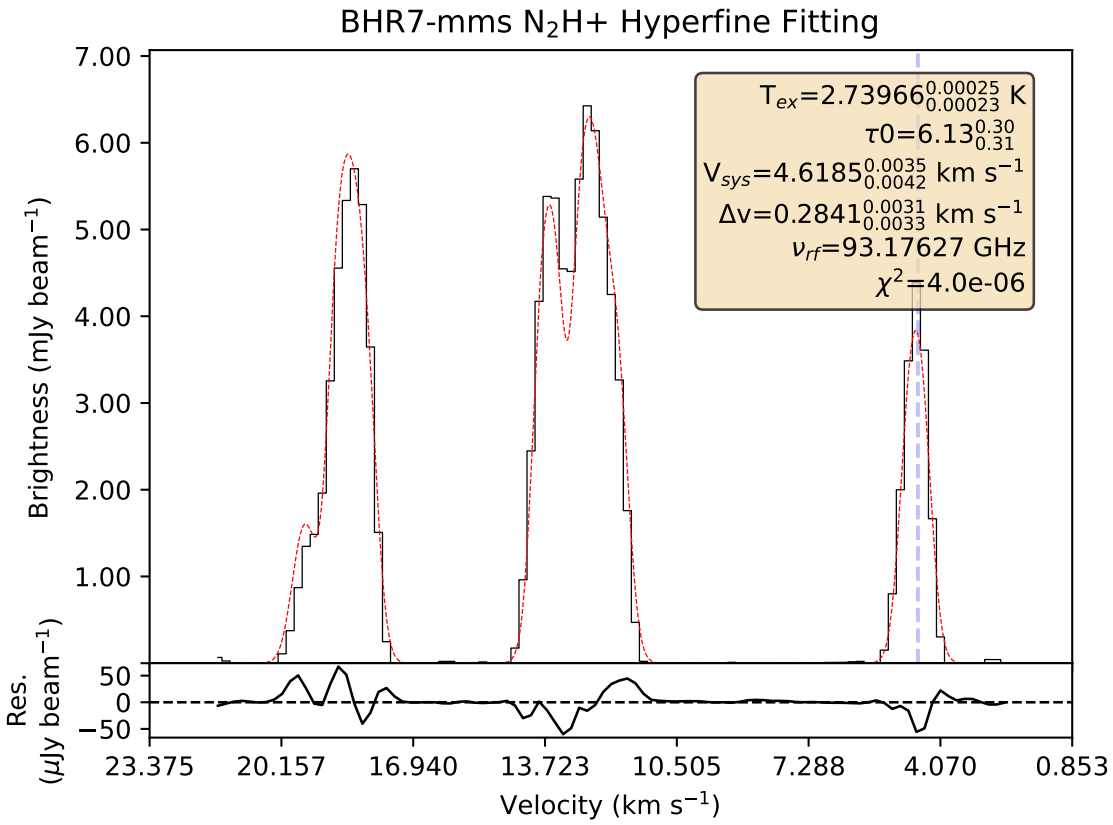

Figure 4.4.6: : A R$\leq$ $40''$ circle of integrated N_2H+ emission towards the source BHR7-mms. We utilized the published code *pyspeckit* with the module N_2H+ spectra fitter to simultaneously fit all hyperfine structure components (indicated in dashed red). We fit the excitation temperature to be T_{ex} $=2.73966^{0.00025}_{0.00023}$ K, the total optical depth of all components τ_0 $=6.13^{0.30}_{0.31}$, the linewidth to be $\Delta v = 0.2841^{0.0031}_{0.0033}$ km s^{-1}, and the $V_{sys} = 4.6185^{0.0035}_{0.0042}$.

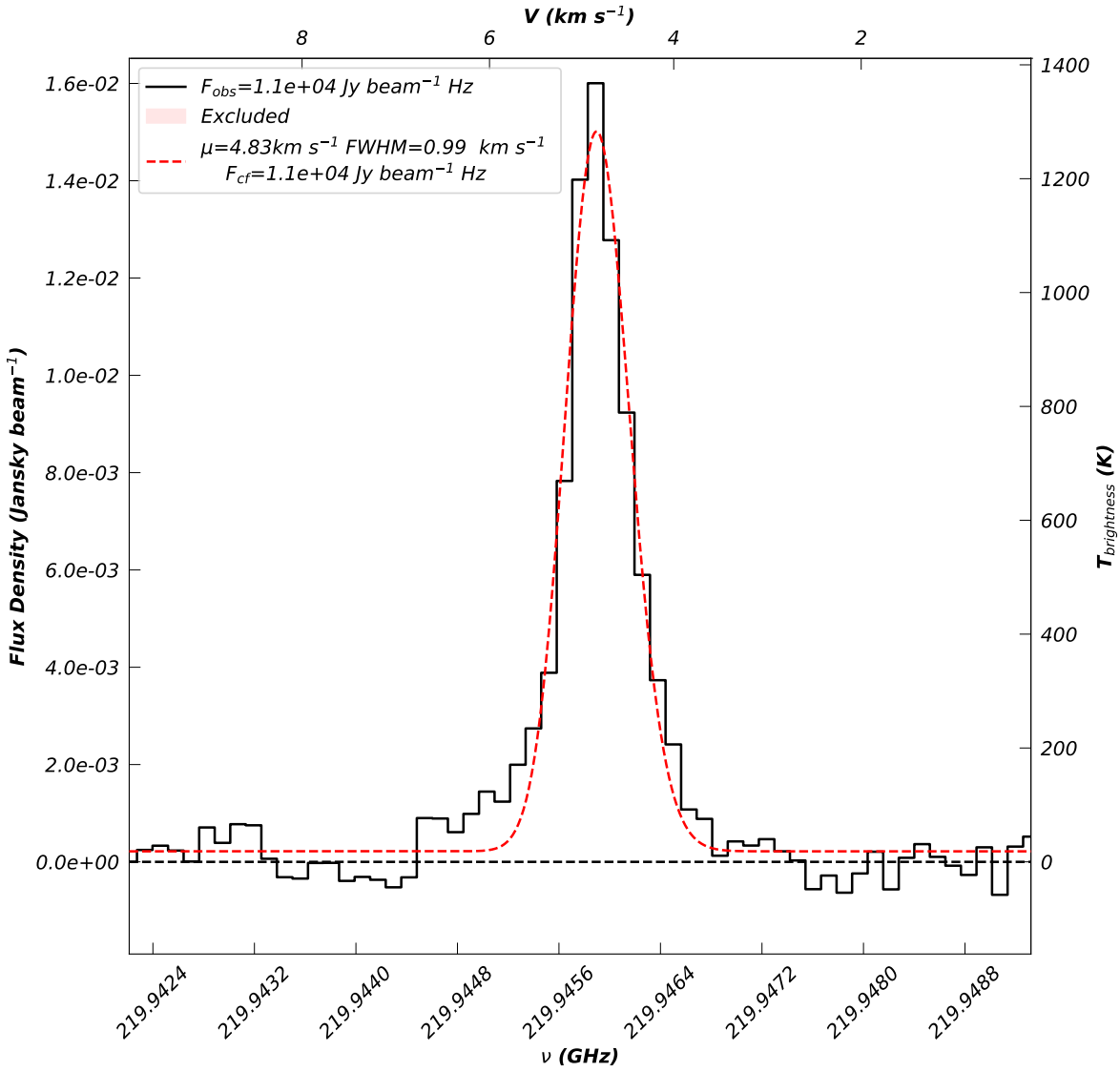

Figure 4.4.7: : A $R_{in} = 1, R_{out} = 2''$ annulus of integrated SO emission towards the source BHR7-mms. A Gaussian profile least-squares fit was performed (indicated in dashed red), and the V_{sys} is fit to be 4.83 km s^{-1}. The emission is narrow (FWHM$\approx$ 0.99 km s^{-1}) and deviates from a Gaussian profile, indicating it is likely not tracing Keplerian motion alone.

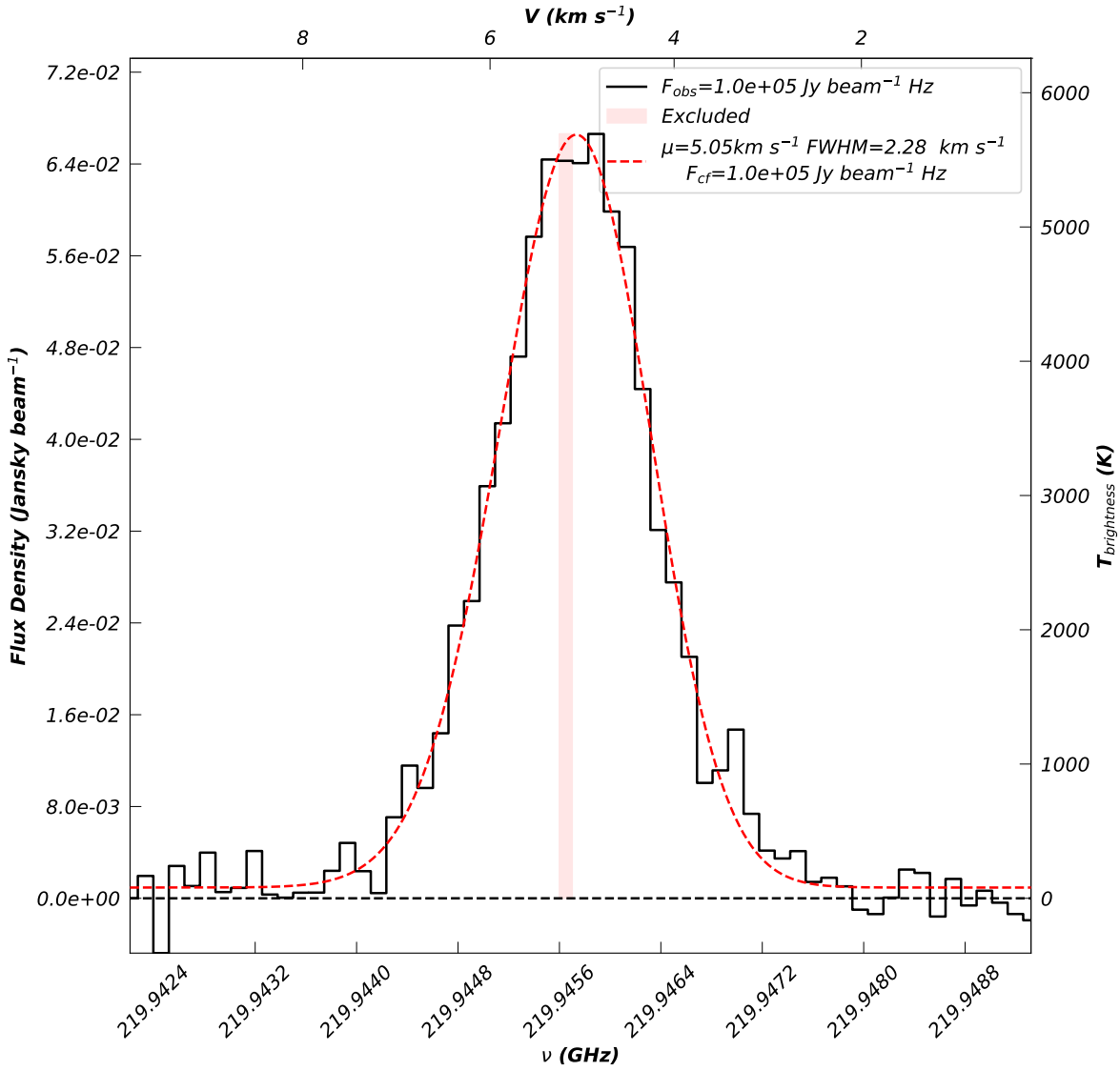

Figure 4.4.8: : A R$\leq 1''$ circle of integrated SO emission towards the source BHR7-mms. A Gaussian profile least-squares fit was performed (indicated in dashed red), and the V_{sys} is fit to be 5.05 km s^{-1}. The emission line is wide (FWHM$\approx$ 2.48 km s^{-1}) and is well described by a Gaussian profile, similar to H_2CO and $C^{18}O$, indicating it is likely tracing Keplerian motion of the outer disk.

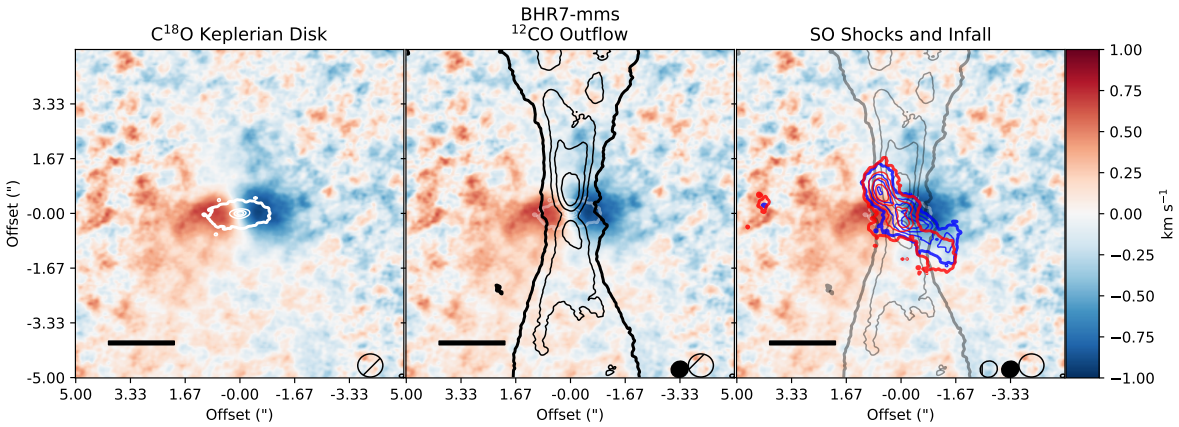

Figure 4.4.9: : Spatial coincidence of molecular line tracers. For all panels, $C^{18}O$ moment 1 map is shown in red-blue color, indicating the respective Doppler shift from system velocity. **Left panel:** the 1.3 mm continuum is overlaid with the contours indicating the 5,10,15 σ levels. The Keplerian rotation indicate in $C^{18}O$ spatially coincides with the continuum disk.**Center panel:** overlays the ^{12}CO moment 0 map ontop of the previous panel in black contours. The levels indicate the 10, 13,16,19 σ levels. The outflows launch from the center of the continuum disk and the width of the starting outflow is similar to the width of the continuum disk.**Right panel:** overlays the SO moment 0 map ontop of the previous panel, with the red and blue contours indicating the integration over all red and blue Doppler shifted emission. The levels indicate the 5, 8, 11,14, 17 σ levels. The SO appears to trace the cavity, cleared by the wide angle outflow. With red and blue emission found at the same scales, it is likely this molecule is tracing the turbulent surface along the cavity, as material is entrained by the winds and some material is infalling. The 1.3 mm continnum, $C^{18}O$, CO, and SO beams are shown in the lower right, right to left , respectively

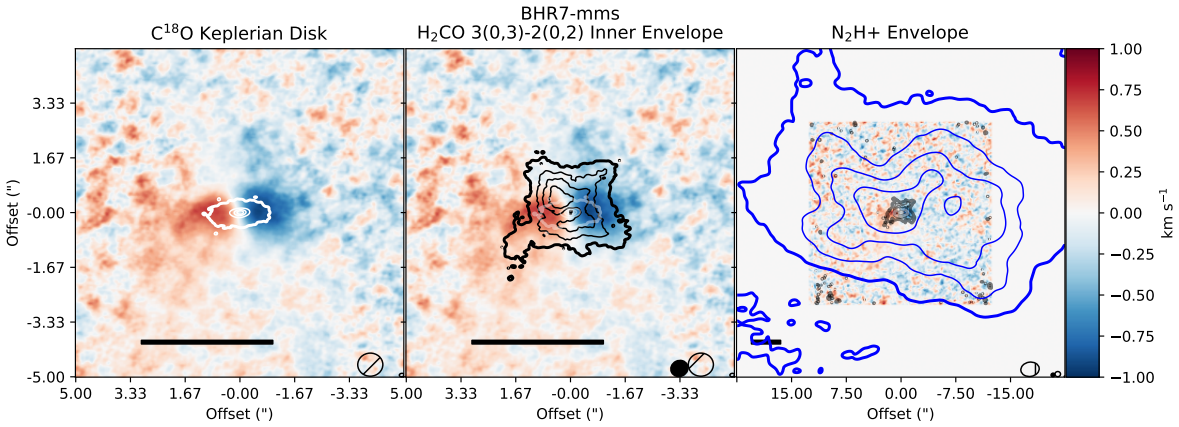

Figure 4.4.10: : Spatial coincidence of molecular line tracers. For all panels, $C^{18}O$ moment 1 map is shown in red-blue color, indicating the respective Doppler shift from system velocity. **Left panel:** the 1.3 mm continuum is overlaid with the contours indicating the 5,10,15 σ levels. The Keplerian rotation indicate in $C^{18}O$ spatially coincides with the continuum disk.**Center panel:** overlays the H_2CO (J = 3_{03} - 2_{02}) moment 0 map ontop of the previous panel in black contours. The levels indicate the 3, 5, 8, 11, 14 σ levels. The gaseous disk extends to scales similar to the $C^{18}O$. **Right panel:** zoom out to scales 60″, with the N_2H+ moment 0 map overlaid the previous panel, indicated in blue contours. These observations utilize the compact ALMA arrays and this are more sensitive to the large scale emission. The envelope is centered on the continuum emission but is highly asymetric. The 1.3 mm continnum, $C^{18}O$, H_2CO, and N_2H+ beams are shown in the lower right, right to left , respectively

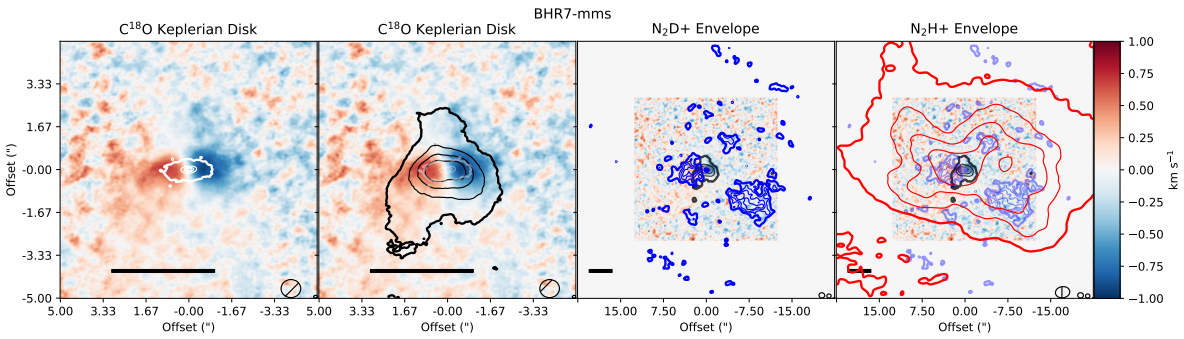

Figure 4.4.11: : Spatial coincidence of molecular line tracers. For all panels, $C^{18}O$ moment 1 map is shown in red-blue color, indicating the respective Doppler shift from system velocity. **Leftmost panel:** the 1.3 mm continuum is overlaid with the contours indicating the 5,10,15 σ levels. The Keplerian rotation indicate in $C^{18}O$ spatially coincides with the continuum disk.**Left panel:** overlays the $C^{18}O$ moment 0 map ontop of the previous panel in black contours. The levels indicate the 5, 8, 11, 14 σ levels. The gaseous disk extends to scales just beyond the continuum disk and appears asymmetric. **Right panel:** the scale changes to $\sim 60''$ wide and overlays the N_2D+ moment 0 map ontop of the previous panel as blue contour. The levels indicate the 3,5,7,9 σ levels. The N_2D+ and CO react destructively, and this cannot exist on the sam e spatial scales. The N_2D+ is found at regions just beyond the $C^{18}O$ spatial scales. Additionally, due to spatial filtering, we resolve out most of the large scale emission from the N_2D+ observations. **Rightmost panel:** the N_2H+ moment 0 map overlaid the previous panel, indicated in red contours. These observations utilize the compact ALMA arrays and this are more sensitive to the large scale emission. The envelope is centered on the continuum emission but is highly asymetric. The 1.3 mm continnum, $C^{18}O$, N_2D+, and N_2H+ beams are shown in the lower right, right to left , respectively

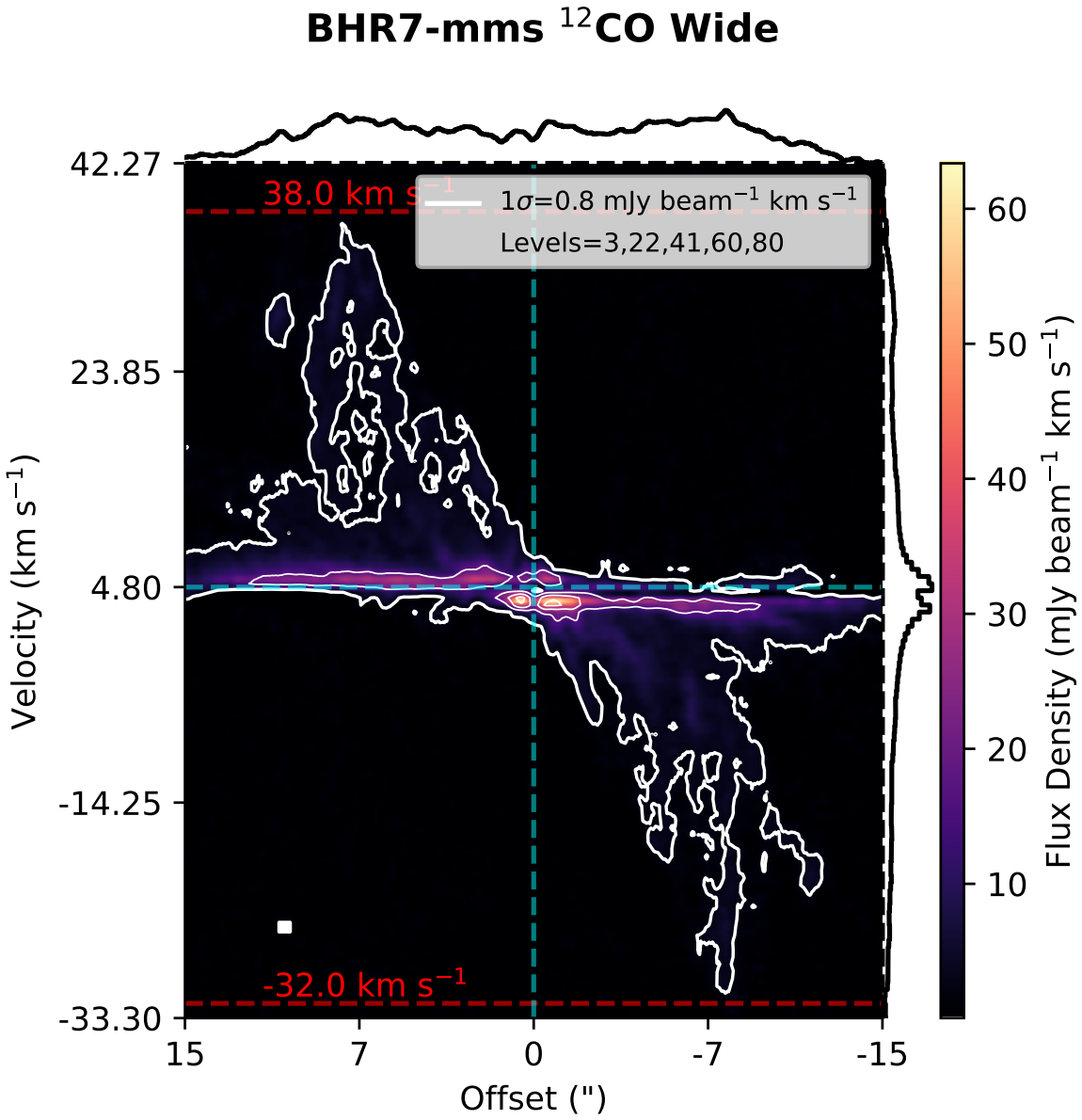

Figure 4.4.12: : The ^{12}CO position-velocity (PV) diagram, with the y-axis indicated by velocity and the x-axis indicated by offsets from the peak of the 1.3 mm continuum. The contours indicate the 3,22,41,60, and 80 σ levels with 1 σ = 0.8 mJy beam^{-1} km s^{-1}. The PV diagram is constructed by cutting a 10$''$ wide box along the major axis of the outflow ($\theta \sim -5°$) and summing the pixels across the minor axis. The outflow emission has a fast $\sim$38 km s^{-1}($\sim$44 km s^{-1}, deprojected) narrow component and a slower, wide angle component. A 1$''$ scalebar is shown on the lower-left. Along each axis is a histogram, constructed by integrating the pixels along the opposing axis and a colorbar is shown on the right.

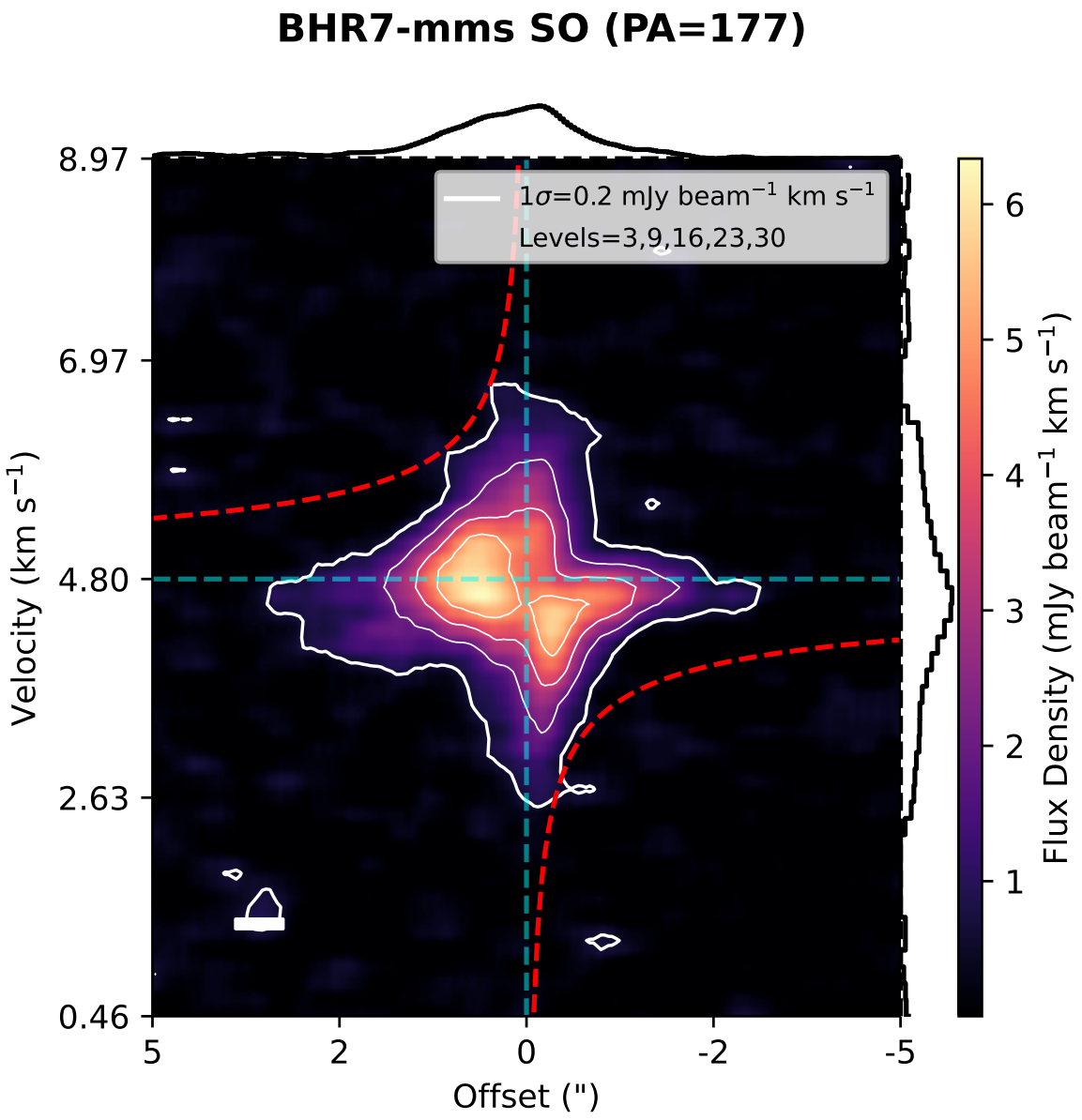

Figure 4.4.13: : The SO position velocity (PV) diagram, constructed by extracting summing the pixels along the minor axis at an angle of 177°. This gemoetry selects the disk scales and the resulting PV diagram reflects disk kinematics. The emission has a relatively wide linewidth ($\sim$2.2 km s^{-1}) and found to scales 2″ from the disk. A 1″ scalebar is shown on the lower-left. Along each axis is a histogram, constructed by integrating the pixels along the opposing axis and a colorbar is shown on the right.

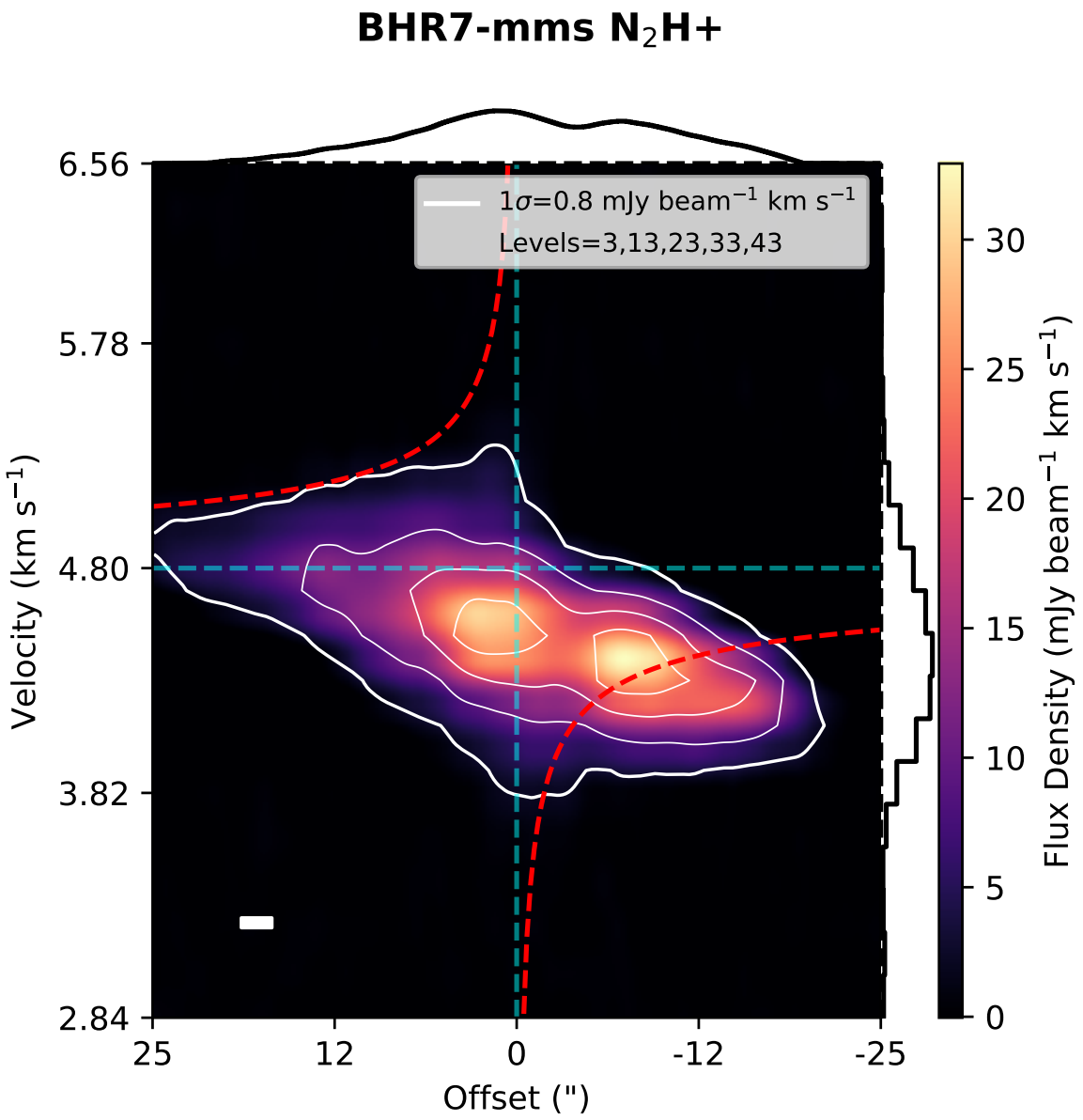

Figure 4.4.14: : The N_2H+ position-velocity (PV) diagram, with the y-axis indicated by velocity and the x-axis indicated by offsets from the peak of the 1.3 mm continuum. The contours indicate the 3,13,23,33, and 43 σ levels with 1 $\sigma = 0.8$ mJy beam^{-1} km s^{-1}. The PV diagram is constructed by cutting a 30$''$ wide box along the major axis of the envelope velocity gradient ($\theta \sim 42°$) and summing the pixels across the minor axis. The envelope line emission is narrow and we only show the isolated hyperfine line at 93.17627 GHz. A 2$''$ scalebar is shown on the lower-left. Along each axis is a histogram, constructed by integrating the pixels along the opposing axis and a colorbar is shown on the right.

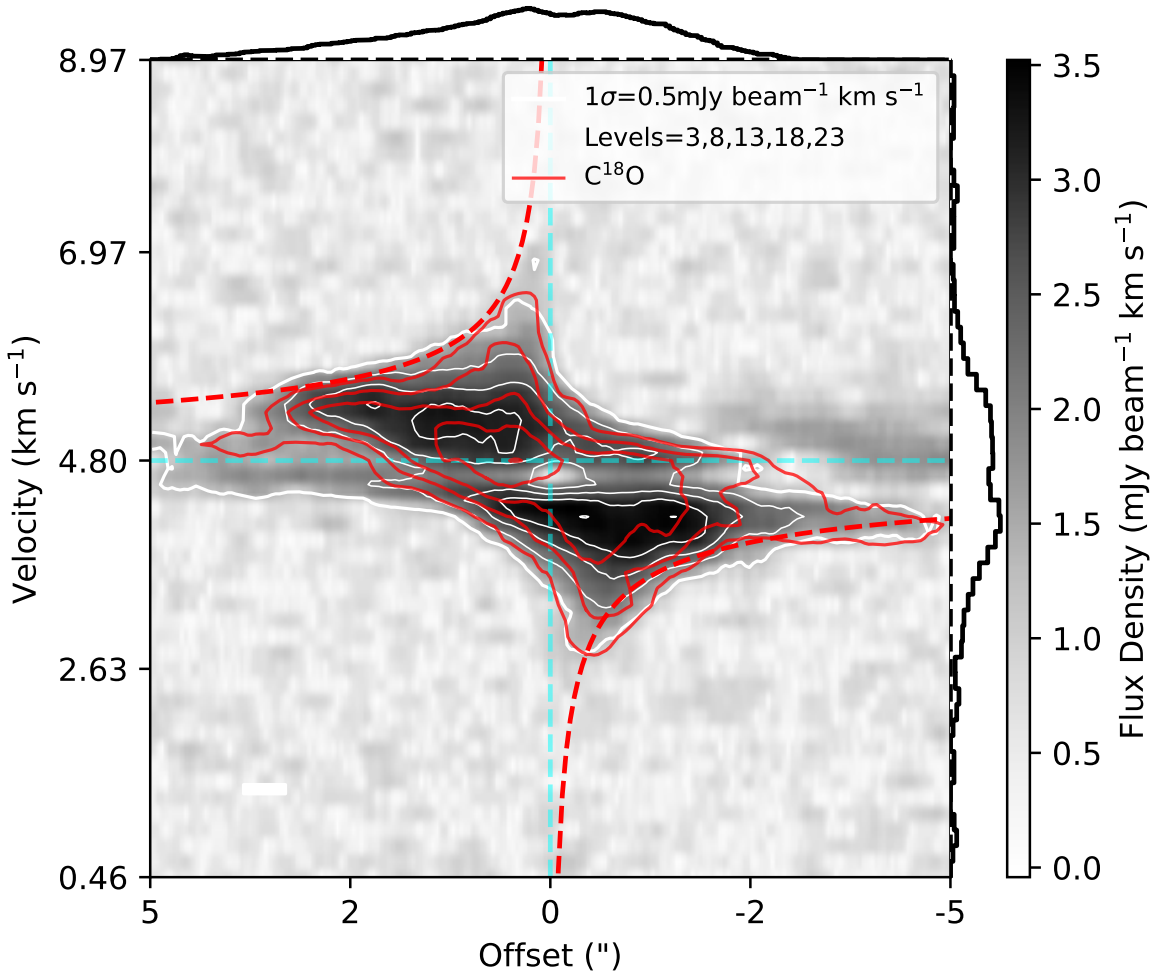

Figure 4.4.15: : The H_2CO (J = 3_{03} - 2_{02}) and $C^{18}O$ position-velocity (PV) diagram, similar to Figure 4.4.14. The white contours indicate the H_2CO 3,13,23,33, and 43 σ levels with 1 σ = 0.8 mJy beam^{-1} km s^{-1}. The red contours indicate the $C^{18}O$ emission with the levels 3,8, 13, 18, and 23 σ levels with 1 σ = 0.5 mJy beam^{-1} km s^{-1}. The $C^{18}O$ and H_2CO emission trace similar regions and are comparable to the size scale of the disk. Both molecules appear to closely follow Keplerian rotation as indicated in the red-dashed line. The H_2CO emission is likely optically thick at compact scales.

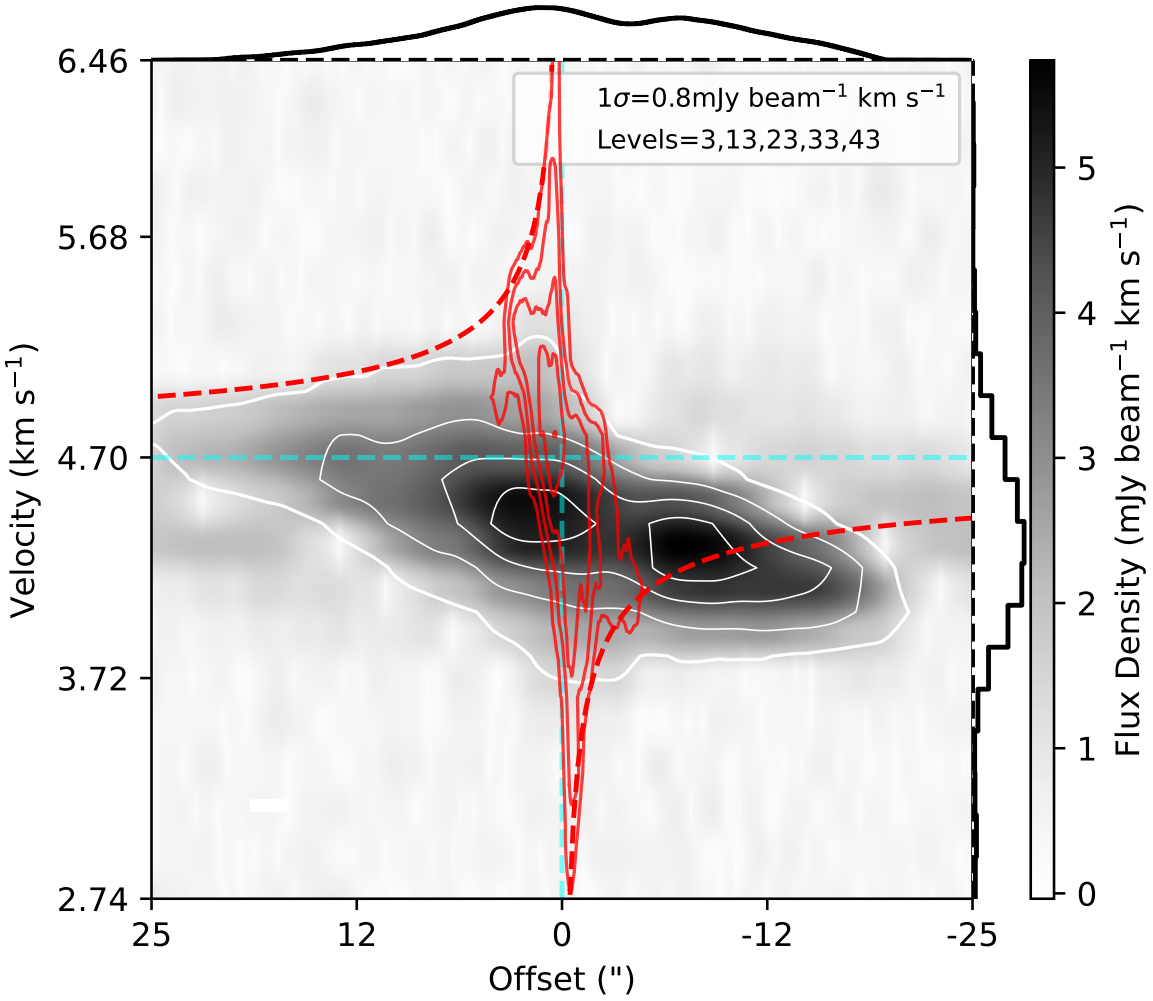

Figure 4.4.16: : The N_2H+ and $C^{18}O$ position-velocity (PV) diagram, similar to Figure 4.4.14. The white contours indicate the N_2H+ 3,13,23,33, and 43 σ levels with 1 σ = 0.8 mJy beam^{-1} km s^{-1}. The red contours indicate the $C^{18}O$ emission with the levels 3,13,23,33, and 43 σ levels with 1 σ = 0.8 mJy beam^{-1} km s^{-1}. The $C^{18}O$ emission is comparable to the size scale of the disk and appears to more closely follow Keplerian rotation as indicated in the red-dashed line. The N_2H+ emission is found at much larger scales and a much narrower line width. These two molecules cannot spatially coincide due to the destructive chemical reactions that occur.

Chapter 5

The Disk Orientations of Perseus Protostellar Multiples at ∼8 au Resolution[1]

Preface

We present a statistical characterization of circumstellar disk orientations toward 12 protostellar multiple systems in the Perseus molecular cloud using the Atacama Large Millimeter/submillimeter Array at Band 6 (1.3 mm) with a resolution of ∼25 mas and ∼8 au. This exquisite resolution enabled us to resolve the compact inner disk structures surrounding the components of each multiple system and enables us to determine the projected 3-D orientation of the disks (position angle and inclination) to high precision. We performed a statistical analysis on the relative alignment of disk pairs to determine whether the disks are preferentially aligned or randomly distributed. We considered three subsamples of the observations selected by the companion separations, a <100 au, a >500 au, and a < 10,000 au. We found for the compact (< 100 au) subsample, the distribution of orientation angles is best described by an underlying distribution of at least 30% preferentially aligned sources (within 30°). The wide companion (>500 au) subsample appears to be consistent with at most, a distribution of ∼70% preferentially aligned sources but does not rule out any distributions out to 100% uncorrelated sources. Thus our results imply the compact sources (<100 au) and the wide companions (>500 au) are statistically different.

[1]Chapter reproduced from work in submission.

5.1. Introduction

Recent studies in the past several decades have shown nearly half of all solar-type star systems are multiples (Raghavan et al., 2010b; Duchêne & Kraus, 2013; Moe & Di Stefano, 2017; Offner et al., 2022a). It has been discovered that stellar multiplicity is even more common for young stars (Mathieu, 1994; Chen et al., 2013; Tobin et al., 2020), and protostars in the midst of the stellar assembly process have the highest multiplicity fractions (Connelley et al., 2008a; Chen et al., 2013; Tobin et al., 2016b). During the earliest stages of star formation, the deeply-embedded protostellar phase, the largest reservoir of mass is available to form multiples (Tohline, 2002). This is the stage of stellar evolution that must be examined to reveal the origins of stellar multiplicity.

Multiple star systems are thought to primarily form via two processes that operate on distinct scales: massive disks undergoing disk fragmentation on 10s-100s au scales (e.g., Kratter et al., 2010a) and turbulent core fragmentation on $\sim$1000s au scales (e.g., Offner et al., 2010). These processes can operate simultaneously, possibly giving rise to populations of close ($<$500 au) and wide ($>$1000 au) multiple systems (Tobin et al., 2016b). However, while the scales by which these processes form multiples are distinct, the systems formed via turbulent fragmentation may migrate to $\sim$100s au separations (or less) in $\sim$10s of kyr (Offner et al., 2010; Lee et al., 2019b) depending on their relative gravitational attraction with the core and the relative velocities of the sources at the times of formation. This makes it difficult to uniquely identify the dominant formation mechanism from separation measurements alone. Studies of protostellar multiplicity within the Orion molecular cloud by Tobin et al. (2022) found that current simulations of turbulent collapse alone did not account for all of the observed multiples found between 20-500 au, and thus an additional mechanism was needed to explain the observations. Meanwhile, Murillo et al. (2016) characterized the relative evolutionary states for wide and compact YSO multiples using SED modeling and found $\sim$33% of multiple systems were inconsistent with "co-eval" formation mechanisms.

Distinguishing if there is a primary mechanism for close multiple star formation is important for understanding the origin of stellar multiples, their evolution, and the potential impact they might have on their circumstellar disks and the planet formation potential. A close multi-

ple system formed within a circumbinary disk may undergo relatively smooth evolution, while a close multiple system that forms as a result of migration from large separations can greatly disturb the system, leading to misalignment of outflows (Offner et al., 2016) and possibly disrupting accretion disks.

The VLA Nascent Disk And Multiplicity (VANDAM) Survey characterized the multiplicity of the entire protostar population in the Perseus molecular cloud (Tobin et al., 2016a), finding 17 multiple systems with separations less than 2.″0 (600 au) out of 90 sources observed. This sample of close multiples was followed-up with ALMA observations of 1.3 mm continuum and molecular lines that likely trace disk kinematics (^{13}CO, C^{18}O, SO, and H_2CO), enabling the most likely formation mechanism to be inferred for 12 systems (Tobin et al., 2018b). Eight out of 12 systems were found to be consistent with disk fragmentation and four were inconsistent. The systems that were consistent with disk fragmentation had apparent rotating circumbinary structures surrounding the binary/multiple system. However, even with this evidence, turbulent fragmentation could not be completely ruled-out. This is because a system formed from turbulent fragmentation could migrate inward, interact, and form a close multiple system with a new circumbinary disk (e.g., Bate, 2018).

However, the compact circumstellar disks around each component of the close multiple systems could provide more definitive evidence on the formation mechanism. If the close multiple system is formed via disk fragmentation, the angular momentum axis of each component and the circumbinary disks should be relatively aligned due to forming within a common disk with the same net angular momentum (Offner et al., 2016; Bate, 2018). On the other hand, Lee et al. (2019a) and Offner et al. (2022b) found that in simulations of turbulent core collapse, multiples preferentially formed as randomly aligned systems whose (mis-)alignment angles would persist throughout the calculation, suggesting randomly distributed alignment angles should be a signature for this formation mechanism.

At such a young age, protostars are deeply embedded, making direct measurements of the stellar rotation axis impossible. Bate et al. (2010) found that the stellar rotation axis (the inferred stellar angular momentum axis) would not differ significantly from the inner disk rotation axis ($<5°$). The outflow position angle can be a proxy for the angular momentum axis, can be difficult to separate for compact systems. These outflows may be entangled and/or mis-

aligned from the rotation axis due to n-body interactions (Ohashi et al., 2022). Tobin et al. (2018b) confirmed and resolved the companion separations, but given the resolution were not able to resolve the compact circumstellar disks or the individual outflows around the sources. Furthermore, Segura-Cox et al. (2018) conducted high resolution VLA observations and identified Per-emb-5 potential compact multiple, requiring high-sensitivity follow-up to confirm the multiplicity. Thus high-resolution and high-sensitivity studies of compact and wide multiples are needed to accurately determine the angular momentum vectors of the disks.

We carried out a novel method of empirically testing multiple protostar formation mechanisms by observing 12 known wide and compact multiples with 25 mas angular resolution ($\sim$8 au), with the ability to resolve small protostellar disks. This type of survey can best recover the projected disk rotation axis, the implied orientation vector, of the nascent circumstellar disk.

We present our findings of 12 protostellar multiple systems within the Perseus molecular cloud and detail the collection of observations in Section 5.2. We present our analysis of the protostellar sample in Section 5.4. Further, we interpret our findings in the broader aspect of star formation and with the specific sources of the sample in Section 5.5.

5.2. Observations and Data Analysis

The Atacama Large Millimeter/submillimeter Array (ALMA) is a state-of-the-art interferometer located on Llano de Chajnantor in the Atacama region of Chile at an elevation of $\sim$5000 meters). We conducted observations of protostellar multiple systems in Perseus primarily using Band 6 (1.3 mm) with some supplementary observations in Band 3 (3 mm).

Definitions

For consistency we utilized the following definitions for this work:

1. **source**: A single protostar that can have a compact and/or extended disk.
2. **system**: A collection of sources within a defined separation that may be interacting.
3. **aligned**: A pair of sources whose dot product of the orientation vectors would correspond to a value of $<30°$ (Lee et al., 2019b).
4. **misaligned**: A pair of sources whose dot product of the normalized orientation vectors would correspond to a value of $>30°$.

The definitions of alignment are for ease of qualitative referencing and is not relied on for the analysis detailed in Section 5.4. In the analysis, we utilized the alignment angles and the corresponding observational errors. The demarcation of alignment between two orientation vectors of 30° are chosen to remain consistent with studies of simulated data (Lee et al., 2019b).

5.2.1. Band 6 (1.3 mm) Observations

The observations were taken as part of project 2019.1.01425.S with 48 antennas included between 2019 September 11-18 at Band 6 (1.3 mm) toward 12 protostellar systems in the Perseus molecular cloud (d$\sim$300 pc). The observations were carried out in the most extended configuration C-9/10 (baselines 150 m$\sim$14.9 km) and have an effective angular resolution of 42 mas$\times$23 mas to 66 mas$\times$29 mas, with a continuum sensitivity of 13-76 μJy beam^{-1}, when reconstructed with the Briggs robust 1 weighted imaging. The correlator was configured with 3 spectral windows setup for 1.875 GHz bandwidth and 3840 channels and four spectral windows used 117.19 MHz bandwidth and centered on the ^{13}CO ($J = 2 \rightarrow 1$), C^{18}O ($J = 2 \rightarrow 1$), SO ($J = 6(5) \rightarrow 5(4)$), and SiO ($J = 5 \rightarrow 4$) transitions. However, the spectral lines were not well-detected given that the integration times were chosen for continuum sensitivity.

The first set of observations for 5 of the sources took place across a 1.5-hour block, with each time-on-source scan$\approx$9 minutes. The remaining 7 sources were observed in 4 execution blocks, across 3 days, with the average time-on-source $\sim$14 minutes. While the absolute flux density scale is expected to be accurate to $\sim$10%, for the purpose of the results presented, all flux uncertainties only consider statistical uncertainties. A summary of the scheduled observations and execution blocks is given in Tables 5.2.1 and 5.2.2.

Table 5.2.1: 1.3 mm Pointings

Name	Other names	α (J2000)	δ (J2000)	beam (mas×mas)	RMS (μJy beam^{-1})	S/N	Class	L_{bol} ($L_\odot$)	T_{bol} (K)
L1448 IRS1	···	3:25:9.45	30:46:21.84	43×23	13	391	I	2	None
Per-emb-2	IRAS 03292+3039	3:32:17.93	30:49:47.7	61×27	38	19	0	0.9	27
Per-emb-5	IRAS 03282+3035	3:31:20.94	30:45:30.19	61×28	47	101	0	1.3	32
NGC1333 IRAS2A	Per-emb-27	3:28:55.57	31:14:36.92	62×27	53	368	0/I	19	69
Per-emb-17	L1455 IRS1	3:27:39.11	30:13:2.98	42×23	13	429	0	4.2	59
Per-emb-18+	NGC1333 IRAS7	3:29:11.27	31:18:30.99	63×28	17	181	0	2.8	59
Per-emb-21+	···	3:29:10.67	31:18:20.09	63×28	17	359	0	6.9	45
Per-emb-22	L1448 IRS2	3:25:22.42	30:45:13.16	43×23	13	448	0	3.6	43
L1448 IRS3B+	Per-emb-33	3:25:36.32	30:45:14.81	43×23	14	169	0	8.3	57
L1448 IRS3A+	···	3:25:36.5	30:45:21.83	43×23	14	365	I	9.2	47
L1448 IRS3C	L1448 NW	3:25:35.68	30:45:34.26	43×23	20	192	0	1.4	22

Table 5.2.1 continued on next page

Table 5.2.1 *(continued)*

Name	Other names	α (J2000)	δ (J2000)	beam (mas×mas)	RMS (μJy beam^{-1})	S/N	Class	L_{bol} ($L_\odot$)	T_{bol} (K)
Per-emb-35	NGC1333 IRAS1	3:28:37.1	31:13:30.72	62×28	18	307	I	9.1	103
NGC1333 IRAS2B	Per-emb-36	3:28:57.38	31:14:15.67	66×29	37	294	I	5.3	106
SVS13A+	Per-emb-44	3:29:3.77	31:16:3.71	64×28	76	194	0/I	32.5	188
SVS13A2+	···	3:29:3.39	31:16:1.53	64×28	76	59	0/I	32.5	188
SVS13B+	···	3:29:3.08	31:15:51.64	64×28	76	32	0	1	20

NOTE—References: Enoch et al. (2009); Sadavoy et al. (2014)

NOTE—L1448IRS3B also contains L1448IRS3A within the field of view. SVS13A also contains SVS13B within the field of view. Per-emb-18 also contains Per-emb-21 within the field of view.

NOTE—RMS is specified as the root-mean-squared of the Briggs robust 1 weighted image with the upper 95% of emission clipped. The beam specified is the self-calibrated, multi-frequency synthesis *clean* beam using Briggs robust 1 weighting. S/N is the signal-to-noise ratio defined as the emission peak divided by the respective RMS. Class, T_{bol}, and L_{bol} are given in Tobin et al. (2018b); Connelley et al. (2008b).

Table 5.2.2: 1.3 mm Scheduling Block

Identifier	# E.B.	Date (Sept 2021)	Phase Cal.	Bandpass Cal.	Flux Cal.
(1)	1	11	J0336+3218	J0237+2848	J0341+3352
(2)	3	13,16,18	J0336+3218	J0237+2848	J0338+3106

NOTE—Identifier (1) corresponds to the Member Observation Unit Set (MOUS) of uid://A001/X1465/Xd60 and (2) corresponds to uid://A001/X1465/Xd63

NOTE—# E.B. is the number of execution blocks.

The raw visibility data were calibrated by the North American ARC staff using Common Astronomy Software Applications (CASA) version 6.2.1 automated pipeline. The high sensitivity of the observations (pre-self-calibration$\sim$40 μJy) and signal-to-noise ratios (S/N) of at least 50, enabled self-calibration to be attempted for all sources except for Per-emb-2. We performed 4 to 5 rounds of phase-only self calibration, with the first round of intervals starting at the full length of the EB, then round two of intervals starting at the full length of the on-source scans, then progressing to 18.14 s, 9.07 s, and ending at the single integration timestep. Per-emb-18, Per-emb-35, NGC1333 IRAS2B, and L1448 IRS3B were unable to be phase self-calibrated down to the shortest timestep due to the S/N degrading but were phase-only self-calibrated down to 9.07 s. The final average sensitivity resulting from the phase-only self calibrations was $\sim$30 μJy and an average increase of S/N by a factor of 1.5. A summary of the observations is detailed in Table 5.2.1.

The data were imaged using CASA version 6.5.0-15 with the task *tclean*, and the images using Briggs weighting with the robust parameter 1.0 are shown in Figures 5.3.1 and 5.3.2 with image sizes of 9000$\times$9000 and 4 mas per pixel. All images are shown with square-root stretch colormaps and a common RMS value of 20 μJy beam^{-1}. To restore the images, we used the Multi-(Taylor-)term Multi-Frequency Synthesis (MTMFS) with scale sizes of 0, 5, and 20 pixels and 2 Taylor terms to correct the effects of spectral smearing, which should be minimal on small spatial scale maps. The scale sizes were chosen to recover dominant features in the disk and correspond to physical sizes of point source, typical size of the beam minor axis, and 2$\times$ the typical beam major axis. We utilized the "auto-multithresh" masking technique to

non-interactively mask and clean the data in a reproducible manner by defining the threshold sub-parameter to be 1.5× the root-mean-square of the final image. The final images were checked by simultaneously cleaning the data with a conservative user-defined mask.

5.2.2. Band 3 (3 mm) Observations

ALMA Band 3 data were taken toward three targets, a subset of the Band 6 observations: Per-emb-2, Per-emb-18, and Per-emb-5, within ALMA project 2016.1.00337.S. Data were taken in two ALMA configurations, C40-6 (2017 Aug 1) and C40-9 (2017 September 27), summarized in Table 5.2.3. For both datasets, the phase calibrator was J0336+3218, the flux calibrator was J0238+1636 and the bandpass calibrator was J0237+2848. The baselines sampled in the combined dataset ranged from 16 m to 14,500 m.

The correlator was configured with 3 spectral windows setup for 1.875 GHz bandwidth and 128 channels and two spectral windows used 58.59 MHz bandwidth and centered on the ^{13}CO and C^{18}O ($J = 1 \rightarrow 0$) transitions. However, the spectral lines were not well-detected given that the integration times were chosen for continuum sensitivity. The central frequency of the observations is ∼102 GHz.

The data were pipeline processed by the observatory using the pipeline included in CASA 4.7.2 (r39732). The data were also self-calibrated and imaged using this same version of CASA. The C40-6 data went through 3 rounds of phase-only self-calibration with solution intervals of one scan, 24.15s, and 6.05s (a single integration). The C40-9 data also went through three rounds of phase-only self-calibration but the second interval used a 12.10s solution interval, and the final solution interval of 6.05s corresponded to 3 integrations.

The final self-calibrated data were imaged together using the CASA task *clean* with image sizes of 2048×2048 pixels and 5 mas pixels. We made use of MTMFS imaging given the wide fractional bandwidth, restoring the images with super-uniform weighting scheme to closely match the beamsize of the 1.3 mm observations, and interactively cleaned using hand-drawn masks. The images were cleaned down to ∼1.5× the noise in each image (Figure 5.3.3).

Table 5.2.3: 3 mm Pointings

Name	α (J2000)	δ (J2000)	beam (mas×mas)	RMS (μJy beam^{-1})	S/N
Per-emb-2	3:32:17.93	30:49:47.73	108×48	18	75
Per-emb-5	3:31:20.94	30:45:30.23	108×48	18	168
Per-emb-18+	3:29:11.26	31:18:31.04	90×41	27	34
Per-emb-21+	3:29:10.67	31:18:20.14	187×110	10	475

NOTE—Per-emb-18 also contains Per-emb-21 within the field of view.

NOTE—RMS is specified as the root-mean-squared of the superuniform weighted image with the upper 95% of emission clipped. The beam specified is the self-calibrated, multi-frequency synthesis *clean* beam using superuniform weighting. S/N is the signal-to-noise ratio defined as the emission peak divided by the respective RMS.

5.2.3. Gaussian Fitting the *uv*-visibilities

For the most compact companion sources (Per-emb-18, L1448 IRS3B, L1448 IRS3C, and SVS13A), the compact disk emission is only slightly larger than the size of the beam, so the deconvolved PA and i derived from image-plane analysis will be less well-constrained. Moreover, we desired an alternate fitting method to measure the source parameters independent of the images produced with the CLEAN algorithm. For completeness, we conducted the image-plane analysis in Appendix 5.C and find the results between the *uv*-visibility and image plane analysis are consistent.

In order to utilize the full spatial constraints afforded by the observations, we constructed a number of Gaussians equal to the number of sources in the *uv*-visibilities. Similar techniques were applied to protoplanetary disks (Jennings et al., 2022a,b) to recover substructure with $> 2\times$ longer effective baselines than the reconstruction from CLEAN by fitting the visibilities directly. We constrained the sources using Bayesian inference, fitting multi-component 2-D Gaussians to the visibilities of each individual source using (*emcee*, *dynesty*, *pdspy*; Foreman-Mackey et al., 2013; Speagle, 2020; Sheehan, 2022). We restricted the *uv*-visibilities fitting to scales smaller than 0.″5 (by restricting the *uv*-distance >400 kλ) to ensure we fit the compact disk and not the extended emission of the envelope or circum-multiple material that was not resolved out in the observations. We also limited the fit phase center to be within 0.″5 of

previously published results, and in the cases of new detections, we utilized the centering from the CASA task *imfit* to form the *prior* (a summary of the *imfit* results and the comparison with the *uv*-visibility results is described in Appendix 5.C).

A summary of the fitted parameters is provided in Table 5.2.4 , and a summary of the projected 3D orientation vectors solved from fitting the *uv*-visibilities is shown in Figure 5.4.1. The errors reported are derived as the 1 σ uncertainty from the median of the sampled posterior. While all sources could be described by a Gaussian, the source L1448 IRS3A was best described with a ring (see Appendix 5.A). The detailed analysis of L1448 IRS3A falls outside of the scope of this paper and we leave analysis of its disk structure for a future paper. While the *uv*-visibilities enable a more complete picture of the system and accurate representation of the sources, without bias from the inherent beam geometries and subsequent clean procedure, the image-plane analysis characterizes the spatial orientations of the continuum data in an intuitive manner.

Table 5.2.4: UV-plane Fitting Results

Name	RA	δ	Sep.	σ_{maj}	σ_{min}	PA	i	T_B	Int. Intensity
	(J2000)	(J2000)	(au)	(mas)	(mas)	(°)	(°)	(K)	(mJy)
L1448 IRS1 -A	+03:25:09.455	$+30:46:21.83^{+0.0002}_{-0.0002}$		$193^{+0.7}_{-0.8}$	$93^{+0.5}_{-0.5}$	$28.0^{+0.2}_{-0.2}$	50.7	397.7	48.6
··· -B	+03:25:09.418	$+30:46:20.53^{+0.0007}_{-0.0007}$	416	59^{+2}_{-2}	41^{+2}_{-2}	120.0^{+5}_{-5}	44.2	28.9	3.8
Per-emb-2 -A	+03:32:17.932	$+30:49:47.70^{+0.004}_{-0.004}$		41^{+10}_{-9}	18^{+10}_{-10}	64.0^{+20}_{-20}	51.6	17.5	0.8
··· -B	+03:32:17.936	$+30:49:47.63^{+0.002}_{-0.002}$	25	60^{+8}_{-7}	50^{+6}_{-6}	66.0^{+40}_{-30}	38.5	54.6	2.5
··· -C	+03:32:17.935	$+30:49:47.27^{+0.003}_{-0.003}$	129	117^{+9}_{-9}	67^{+9}_{-8}	126.0^{+6}_{-5}	48.1	6.9	4.7
··· -D	+03:32:17.947	$+30:49:46.28^{+0.002}_{-0.002}$	430	36^{+6}_{-5}	6^{+5}_{-3}	122.0^{+10}_{-10}	56.6	19.3	0.9
··· -E	+03:32:17.920	$+30:49:48.17^{+0.005}_{-0.005}$	150	64^{+10}_{-10}	43^{+10}_{-20}	108.0^{+40}_{-40}	45.1	4.6	1.1
Per-emb-5	+03:31:20.942	$+30:45:30.19^{+0.0006}_{-0.0006}$		341^{+2}_{-2}	221^{+1}_{-1}	$30.0^{+0.4}_{-0.4}$	45.7	60.1	184.4
NGC1333 IRAS2A -A	+03:28:55.575	$+31:14:36.92^{+0.0002}_{-0.0002}$		$85^{+0.5}_{-0.5}$	$71^{+0.6}_{-0.6}$	112.0^{+2}_{-1}	38.6	291.9	92.5
··· -B	+03:28:55.568	$+31:14:36.31^{+0.001}_{-0.001}$	186	56^{+3}_{-4}	39^{+2}_{-2}	13.0^{+6}_{-5}	44.2	59.3	9.7
Per-emb-17 -A	+03:27:39.112	$+30:13:02.97^{+0.0001}_{-0.0001}$		$50^{+0.3}_{-0.3}$	$37^{+0.4}_{-0.4}$	120.0^{+1}_{-1}	42.2	135.6	16.5

Table 5.2.4 continued on next page

Table 5.2.4 *(continued)*

Name		RA (J2000)	δ (J2000)	Sep. (au)	σ_{maj} (mas)	σ_{min} (mas)	PA (°)	i (°)	T_B (K)	Int. Intensity (mJy)
···	-B	+03:27:39.123	$+30:13:02.74^{+0.0004}_{-0.0004}$	83	96^{+2}_{-2}	52^{+1}_{-1}	161.0^{+1}_{-1}	49.1	41.7	10.7
Per-emb-18+	-A	+03:29:11.267	$+31:18:30.99^{+0.0006}_{-0.0006}$		45^{+2}_{-2}	19^{+3}_{-3}	73.0^{+3}_{-3}	52.3	22.1	4.1
···	-B	+03:29:11.260	$+31:18:30.97^{+0.0006}_{-0.0006}$	25	62^{+3}_{-2}	14^{+5}_{-6}	80.0^{+2}_{-2}	55.8	15.1	4.3
Per-emb-21+		+03:29:10.674	$+31:18:20.09^{+0.0003}_{-0.0003}$		$51^{+0.7}_{-0.7}$	$49^{+0.8}_{-0.9}$	74.0^{+20}_{-20}	32.8	87.4	16.3
Per-emb-22	-A	+03:25:22.417	$+30:45:13.16^{+0.0001}_{-0.0001}$		$50^{+0.4}_{-0.4}$	$32^{+0.3}_{-0.3}$	$39.0^{+0.9}_{-0.9}$	45.8	141.5	13.9
···	-B	+03:25:22.359	$+30:45:13.07^{+0.0003}_{-0.0002}$	227	42^{+1}_{-1}	23^{+1}_{-1}	19.0^{+2}_{-2}	48.6	102.1	5.4
L1448 IRS3B+	-A	+03:25:36.324	$+30:45:14.81^{+0.0004}_{-0.0004}$		52^{+2}_{-2}	$23^{+0.6}_{-0.6}$	25.0^{+1}_{-2}	51.8	86.1	5.3
···	-B	+03:25:36.319	$+30:45:15.06^{+0.0004}_{-0.0004}$	78	101^{+2}_{-2}	$63^{+0.9}_{-0.9}$	12.0^{+1}_{-1}	46.3	61.2	13.9
···	-C	+03:25:36.387	$+30:45:14.64^{+0.0002}_{-0.0002}$	247	$201^{+0.8}_{-0.7}$	$176^{+0.7}_{-0.7}$	$25.0^{+0.9}_{-0.9}$	36.6	56.1	78.3
L1448 IRS3A+		+03:25:36.506	$+30:45:21.80^{+0.0004}_{-0.0003}$		$364^{+0.5}_{-0.5}$	$142^{+0.5}_{-0.5}$	$142.0^{+0.2}_{-0.2}$	49.1	11.4	75.4
L1448 IRS3C	-A	+03:25:35.675	$+30:45:34.02^{+0.0002}_{-0.0002}$		$135^{+0.5}_{-0.5}$	$58^{+0.3}_{-0.3}$	$38.0^{+0.2}_{-0.2}$	52.1	55.3	35.2
···	-B	+03:25:35.679	$+30:45:34.26^{+0.0002}_{-0.0002}$	72	$66^{+0.7}_{-0.7}$	$31^{+0.4}_{-0.4}$	$38.0^{+0.6}_{-0.6}$	51.3	69.3	11.9
Per-emb-35	-A	+03:28:37.097	$+31:13:30.71^{+0.0003}_{-0.0003}$		$82^{+0.9}_{-0.8}$	$34^{+0.4}_{-0.4}$	$32.0^{+0.5}_{-0.4}$	52.4	81.0	15.1

Table 5.2.4 continued on next page

Table 5.2.4 *(continued)*

Name	RA	δ	Sep.	σ_{maj}	σ_{min}	PA	i	T_B	Int. Intensity
	(J2000)	(J2000)	(au)	(mas)	(mas)	(°)	(°)	(K)	(mJy)
···	-B +03:28:37.225	$+31:13:31.67^{+0.001}_{-0.001}$	570	114^{+6}_{-6}	18^{+2}_{-3}	48.0^{+1}_{-2}	56.6	14.1	2.9
NGC1333 IRAS2B	-A +03:28:57.379	$+31:14:15.67^{+0.0002}_{-0.0002}$		$163^{+0.6}_{-0.6}$	$97^{+0.7}_{-0.6}$	$104.0^{+0.3}_{-0.4}$	47.4	122.0	97.3
···	-B +03:28:57.373	$+31:14:15.98^{+0.0008}_{-0.0007}$	95	50^{+2}_{-2}	44^{+3}_{-3}	92.0^{+10}_{-20}	36.8	48.4	8.9
SVS13A+	-A +03:29:03.772	$+31:16:03.71^{+0.0003}_{-0.0003}$		$73^{+0.9}_{-0.9}$	68^{+1}_{-1}	80.0^{+8}_{-9}	33.9	209.4	59.9
···	-B +03:29:03.748	$+31:16:03.73^{+0.0005}_{-0.0005}$	92	142^{+1}_{-1}	115^{+1}_{-1}	74.0^{+2}_{-2}	39.5	105.6	87.6
SVS13A2+	+03:29:03.392	$+31:16:01.52^{+0.002}_{-0.001}$		54^{+5}_{-5}	36^{+3}_{-3}	26.0^{+10}_{-9}	44.8	64.6	9.4
SVS13B+	+03:29:03.085	$+31:15:51.64^{+0.002}_{-0.002}$		302^{+9}_{-9}	180^{+8}_{-8}	83.0^{+2}_{-3}	47.4	36.8	48.1

NOTE—The separations (sep.) are given in units of au, which is derived based on the average distance to the Perseus molecular cloud of 300 pc.

NOTE—The *uv*-plane nested sampling results. The models fit multiple Gaussians to the *uv* data rather than the image-plane, which is sensitive to image reconstruction efforts and the specific beam shape, particularly towards marginally-resolved or un-resolved sources.

5.3. Results

With these observations, we detected all the circumstellar disks toward each multiple system within the survey at ∼8 au resolution for the 1.3 mm observations and ∼26 au resolution for the 3 mm observations, and most circumstellar disks are at least marginally-resolved. The ALMA images are shown in Figure 5.3.1 with the respective beam sizes in the lower-right corner. While we resolved out much of the >100 au (>0.″3) scale disk structures previously resolved (Tobin et al., 2018b), we did recover a large variety of disk sub-structures never previously resolved toward these sources. We briefly discuss the morphologies of the individual sources in Appendix 5.A.

5.4. Statistical Analysis of Orientations

5.4.1. Companion Finding

In order to facilitate the analysis of the relative disk orientations in each multiple system, we must first determine which systems are associated with each other. While companions <100 au are mostly trivial to assign, systems with >3 sources and separations that range out to ∼10,000 au require a more automated approach. We made use of a method similar to the one implemented by Tobin et al. (2022) which will automatically create the companion associations given an input catalog of positions. The systems constructed by this algorithm are verified to be consistent with prior studies (Tobin et al., 2016b, 2018b) and the algorithm is discussed in detail in Appendix 5.B.

5.4.2. Geometric Orientations

To investigate the proto-multiple disk orientation alignments, we measured the projected angular difference of the inclination and position angle of the disks. With the full 2-D Gaussian fit parameters provided from the CASA *imfit* and *uv*-visibility fitting, we constructed the orientation vectors for each of the sources. We assumed that the disks are axisymmetric and geometrically thin and solved for the inclination of the disk from the major and minor axis lengths, deconvolved from the synthesized beam, via $\arccos(\frac{\sigma_{minor}}{\sigma major})$. The position angle of the disk is directly output from the 2-D Gaussian fits as the angle of the major axis, deconvolved from the synthesized beam, oriented to the standard east-of-north.

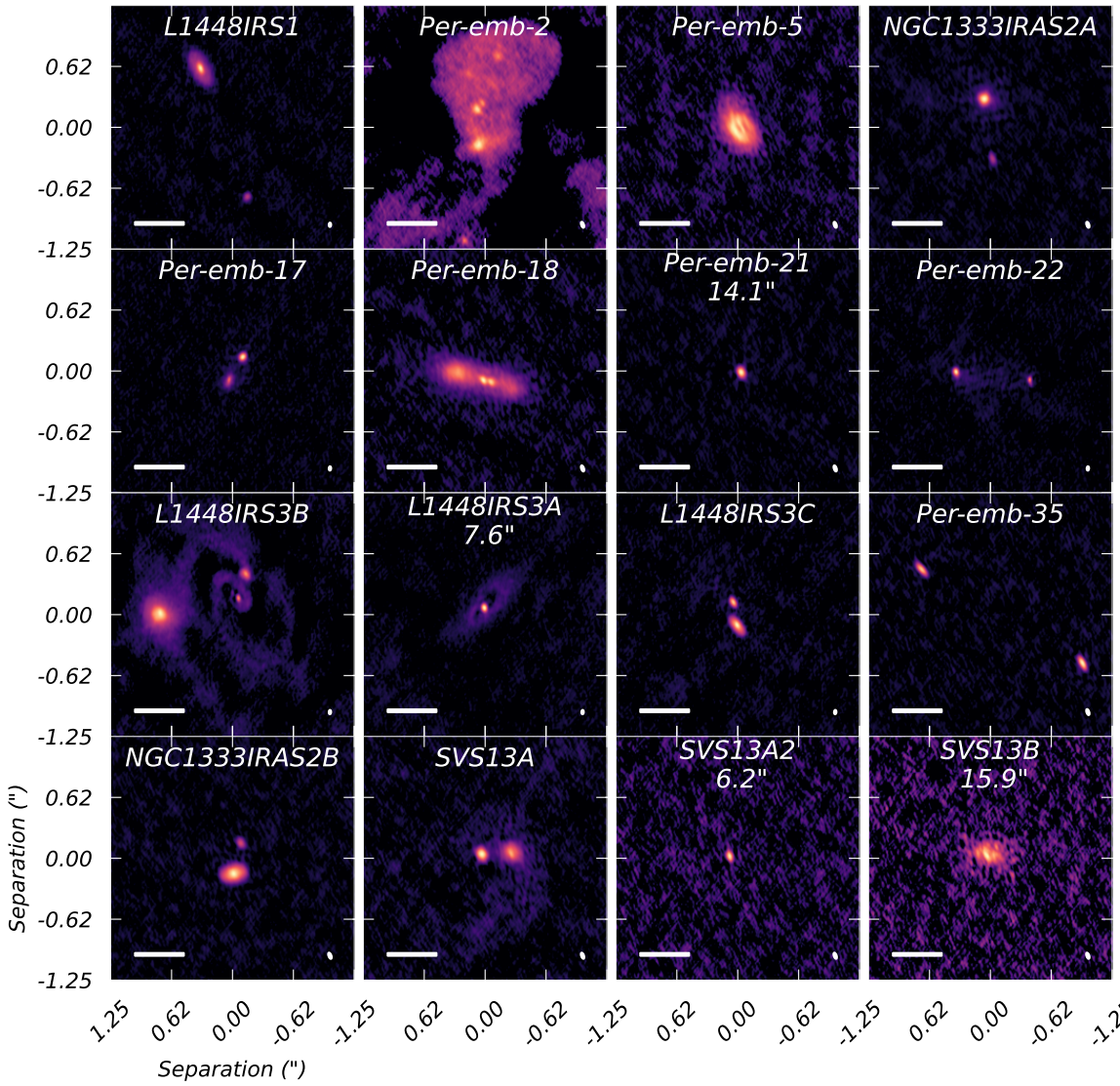

Figure 5.3.1: : ALMA 1.3 mm continuum images of the Perseus multiples, constructed with a Briggs robust weighting parameter of 1. The sources are contained within 12 pointings detailed in Table 5.2.1. The distance given underneath the source name indicates the distances of that companion to the primary pointing source (the prior source in the list). If no distance is given, the center of the image is near to the center of the primary pointing. A 0.″5 (150 au) scalebar is shown in the lower left, and the respective restoring beam is shown in the lower right. The colorscale is square-root scaled, with the lower bound set by a common RMS value of 20 μJy beam^{-1}

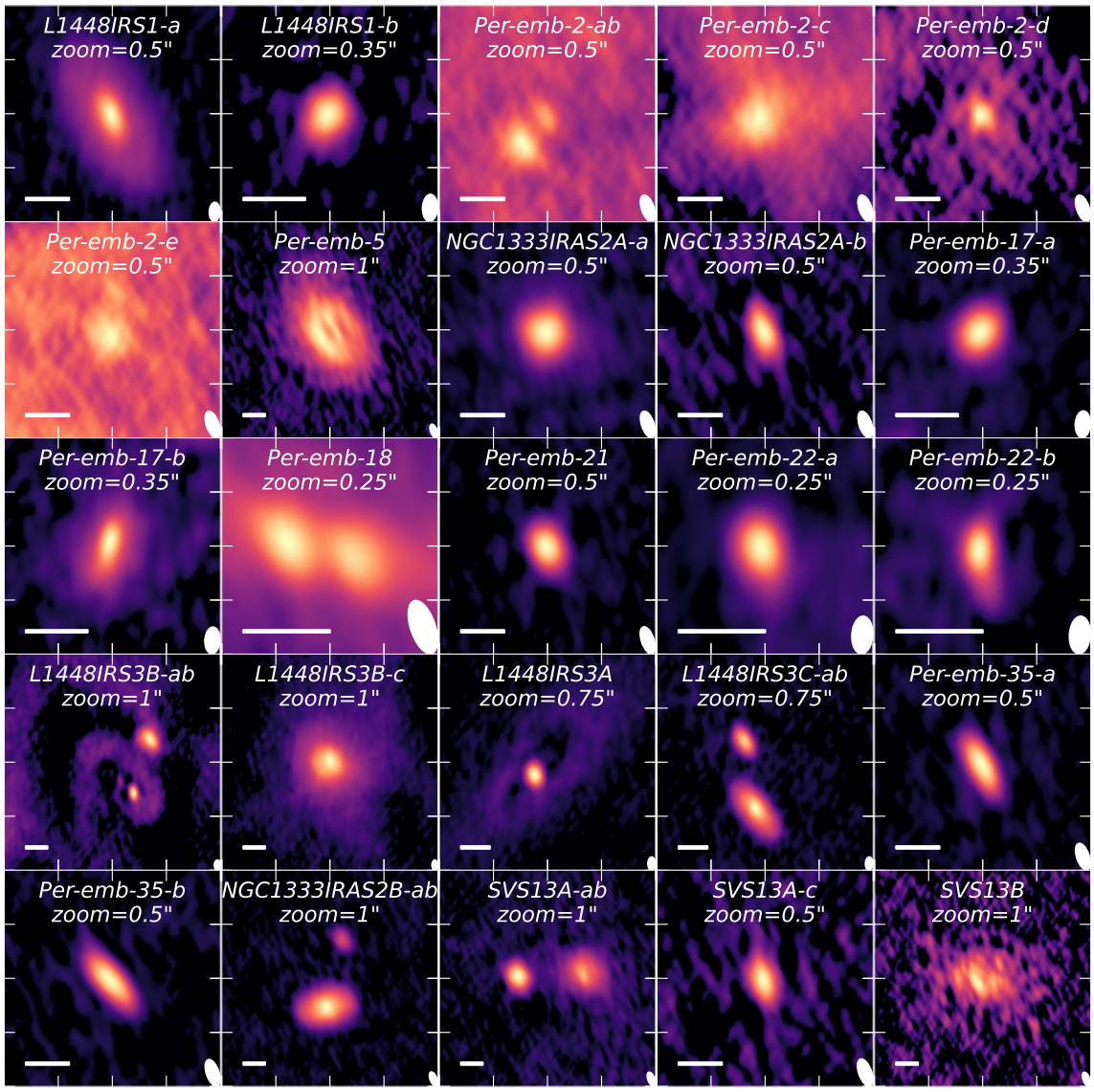

Figure 5.3.2: : Similar image to Figure 5.3.1 but zoomed in to each fitted source in Table 5.2.4. The box size for each plot is given and denotes the width and height of the plot. A 0.″1 (30 au) scalebar is shown in the lower left and the respective restoring beam is shown in the lower right.

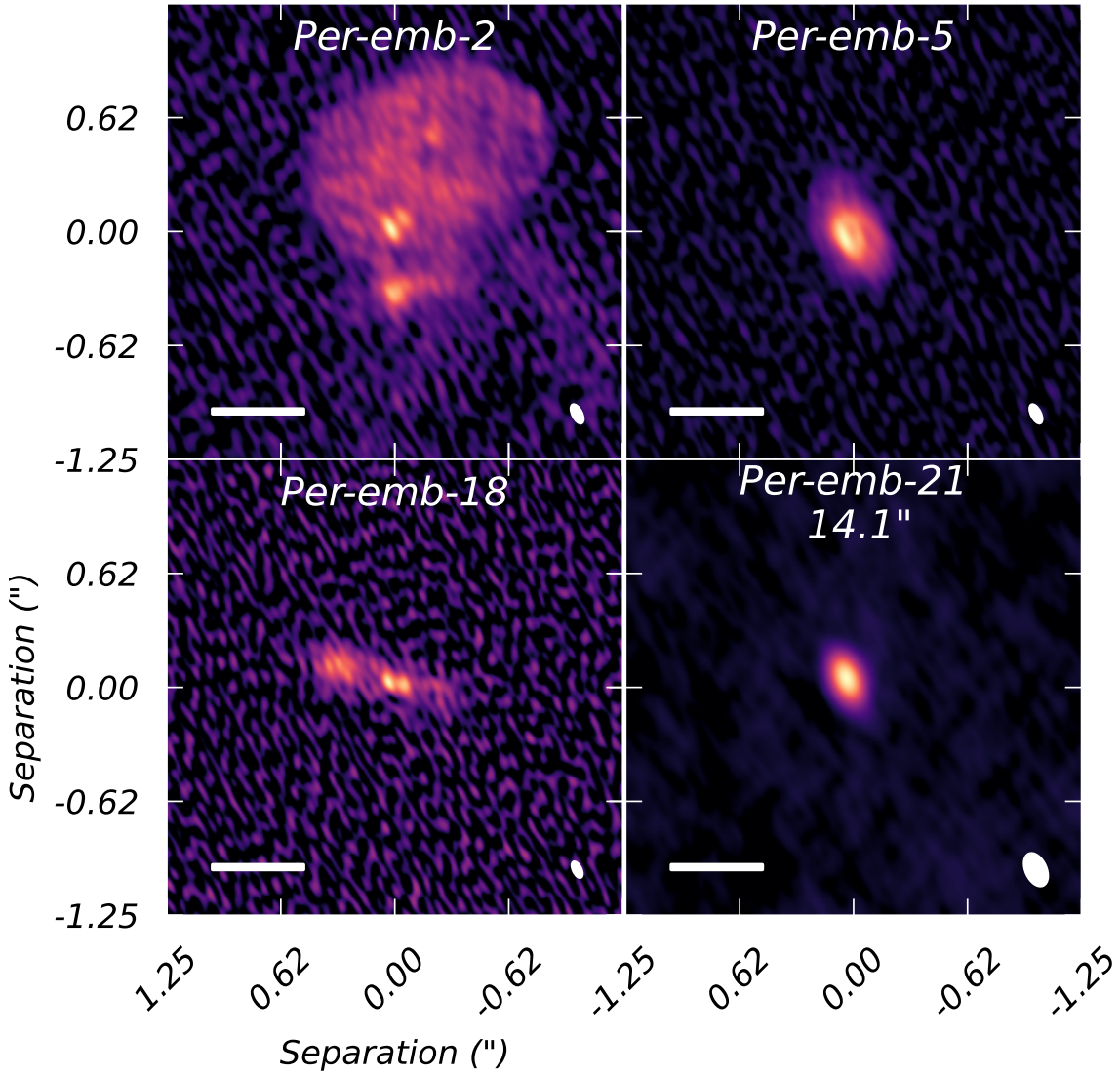

Figure 5.3.3: : Continuum images at 3 mm of the Perseus multiples, constructed with superuniform weighting. The sources are contained within 3 pointings detailed in Table 5.2.3. The distance given underneath the source name indicates the distances of that companion to the primary pointing source (the prior source in the list). If no distance is given, the center of the image is near to the center of the primary pointing. A 0.″5 (150 au) scalebar is shown in the lower left and the respective restoring beam is shown in the lower right.

From a single continuum observation alone, we are insensitive to the orbital motions of the disk, thus we were unable to differentiate between aligned and anti-aligned disks. So for our analysis, we restricted i to range from 0-90° (such that face-on is 0°) and the PA to range from 0-180°. The resulting dot product of the angular momentum vectors is normalized to fall between 0-1, and we constructed the summary plot in Figure 5.4.1 by overlaying resulting orientation vectors on the continuum image from Figure 5.3.1. In most sources the image-plane and the *uv*-visibility derived orientation vectors are nearly aligned, however for the sources where the compact disks are either unresolved or marginally resolved, the methods yield slightly different vectors. In these cases, for the purpose of interpretation, we favored the *uv*-visibility derived results as these results will take full advantage of the spatial-dynamic range in the data.

5.4.3. Models of Companion Orientations

Our goal is to statistically analyze the companion orientations within the sample and provide a robust way to characterize the ensemble sample of orientations. To do so, we need to generate a sample of model protostellar configurations to determine the most probable formation pathways for the observed sample. The protostellar configurations we considered for the analysis are disks that are preferentially aligned with each other, representing the expectation of companions formed via disk fragmentation, and randomly aligned disks as would be expected to result from turbulent fragmentation.

To generate these configurations, the parameters we considered to generate a single system are: stellar multiplicity, the position angle, and inclination of the compact circumstellar disks (ignoring circum-multiple disks and under the assumption the stellar angular momentum axis and disk angular momentum axis are aligned). From these parameters alone, we constructed our model distributions. To model a empirically-driven distribution of proto-multiple systems, we sampled multiplicity for separations between 20-10,000 au, following the distribution of Perseus protostellar multiples of Tobin et al. (2022).

From these constructed systems, we generated a range of possible protostellar configurations with various fractions of aligned and randomly-aligned orientations. That is to say, a system with a multiplicity of 4 sources and a fractional orientation of 0.75 to 0.25, preferentially aligned to randomly aligned, will have, on average, 3 preferentially aligned sources and

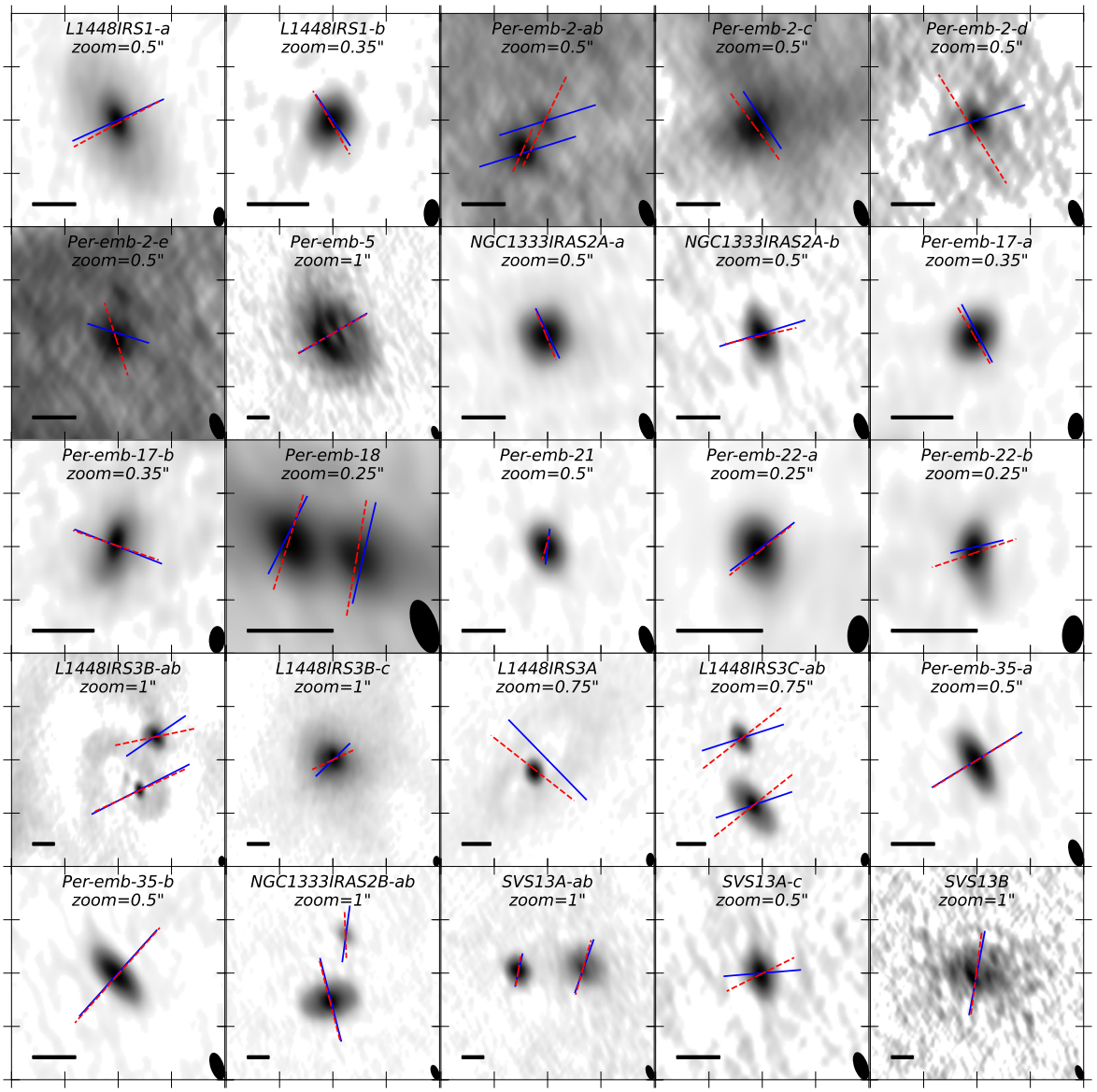

Figure 5.4.1: : Summary of the source fitting technique overlaid on the same image as Figure 5.3.2. The orientation vectors (angles orthogonal to the disk major axis) are indicated as colored lines for each of the fit sources. The blue line indicates the image-plane derived orientation vectors while the dashed red line indicates the *uv*-visibility derived orientation vectors. Several sources have orientation vector centers that do not align between the two fitting techniques. This is likely due to the image-plane fitting is influenced by the larger scale emission structure that is present such as Per-emb-2-c/-d, while the *uv*-visibilities are selected to remove spatial scales larger than $0.''5$ from the fit. We adopt the *uv*-visibility fit for the purpose of the analysis and note the *image*-plane analysis are entirely consistent with the presented results.

1 randomly aligned source. We inserted no bias or preferential weighting corresponding to the separations of the sources with regards to alignment.

Preferentially aligned systems are constructed by drawing the position angle and inclination from a normal distribution described by a full-width-half-maximum value of 30° (Lee et al., 2019b). The choice of 30° is chosen to be consistent with similar studies carried out but the results presented are not significantly changed if moderate deviations (±5°) from 30° is chosen. The resulting distributions of predominantly preferentially aligned systems are similar to population synthesis simulations conducted by Bate (2018). Randomly aligned systems are constructed by drawing the position angle and inclination from a uniform distribution of inverse cosine from 0 to 1.

For a rigorous statistical analysis, the observations need to be compared against a continuous distribution of models. Thus we generated 10,000 model systems (each system will have at least two sources) for each of the different fractions of systems with fractional orientations, ranging from fully preferentially aligned to completely random alignments. When extracting the orientation vectors of the constructed systems, we applied the same 2D projection bias the empirical continuum observations are subject to (i.e. we normalized the p.a. to $<180°$ and the inclination to $<90°$). This provides an observation-like set of models to compare directly with the observations. A visual representation of the median empirical cumulative distribution function (ECDF) for each of the constructed fractional alignment distributions is shown in Figure 5.5.1, with the median ECDF of the observations with uncertainties is overlaid in black.

5.4.4. Statistical Tests

For the observational and model data, we evaluated the dot product of orientation vectors for unique disk pairs in every system (counting each disk pair only once; Table 5.2.4). We utilized an algorithm similar to the companion finding approach, where each compact binary within a system is compared first. We then randomly selected a source from each compact binary to use for further comparison. This gives us $N_s - 1$ number of pairs per system where N_s is the number of sources within a given system (more detailed explanation in Appendix 5.D).This resulting dot product is a derived from the results of the *uv*-visibility fitting (*imfit* analysis remains entirely consistent with the uv-visibility results and is detailed in Appendix 5.C). To

account for the uncertainties in the observations and to resample the particular sources chosen for the pairs, we recalculated each of the dot products 10,000 times sampling the fit errors assuming Gaussian uncertainties. This gave a suite of 10,000 realizations of the empirical distribution which are all consistent with the observations within the uncertainties.

We need to construct a distribution of alignments that could form the basis for the observational underlying distribution. Since this underlying distribution is not known, we constructed a grid of distributions that would cover the range of possible alignment distributions. Each particular constructed distribution is an aggregate sample of preferentially aligned and randomly aligned distributions, sampled via some fractional ratio (e.g. $C_{0.75}UC_{0.25}$ =3-to-1, aligned to randomly-aligned, etc).

We then calculated the probability of each of the 10,000 resampled observed distributions being drawn with each of the fractional ratios (i.e. the null hypothesis, see Appendix 5.E) by utilizing the 2-sample Kolmogorov-Smirnov, Anderson-Darling, and Epps-Singleton probability tests (Scholz & Stephens, 1987; Hodges, 1958; Epps & Singleton, 1986; Goerg & Kaiser, 2009, respectively). We set a null-hypothesis rejection threshold of 0.3% (3 σ), such that if the probability test can reject the null hypothesis at the 3 σ threshold, we discarded that particular empirical distribution. We then counted up all of the distributions that pass this threshold and summarize the full statistics in Tables 5.5.1. A full description of the tests and methodologies is given in Appendix 5.E.

When the sample is limited to $<$100 au separations (Left panel: Figure 5.5.1), the statistical tests imply the fractional ratio of orientations is comprised with at least 30% preferentially aligned sources, but are unable to place any upper limit on the contribution of preferentially aligned sources.

When the sample is limited to only extended companions with separations $>$500 au separations (Right panel: Figure 5.5.1), 24 source pairs are analyzed and we ruled out fully preferentially aligned distributions up to 80% correlated. The statistical tests are nearly uniform with at most half of the of the tests rejecting the null hypothesis for all fractional alignment ratios corresponding to a greater ratio of randomly aligned distributions to preferentially aligned sources.

Our analysis found the full observed sample (Middle panel: Figure 5.5.1), separations out to

10,000 au, is most consistent with a hybrid population of multiples with some contribution from multiple systems with preferentially aligned orientation vectors (up to 70% aligned sources) and some contribution with randomly orientations (up to 70% randomly-aligned sources) to remain consistent. We strongly ruled out fully aligned and fully randomly aligned distributions of disk orientation pairs. While it would be expected for distributions of highly separated sources to consist of a higher fractional ratio of randomly aligned systems, we found this distribution is consistent with roughly an equal fractional ratio.

The results are not significantly different whether we used the result from the image-plane or *uv*-visibility analysis, but the results from the *uv*-plane analysis tend to be favored as the uncertainties in the fits are more constrained.

5.5. Discussion

5.5.1. Formation Pathways

There are two primary mechanisms for multiple star formation which operate at various scales, disk fragmentation and turbulent fragmentation during core collapse. Disk fragmentation operates on ∼100s au scales in massive disks ($\frac{M_d}{M_*} >= 0.1$) that are gravitationally unstable (i.e. Toomre Q < 1), if the disk cools sufficiently fast (Gammie, 2001). The outcomes of gravitational instability can be observed directly (such as; Tobin et al., 2016a; Reynolds et al., 2021) but also has been extensively modeled (Kratter & Matzner, 2006; Boley, 2009; Kratter et al., 2010b; Vorobyov et al., 2013; Vorobyov & Elbakyan, 2018). However clear cases of ongoing disk fragmentation are somewhat elusive aside from L1448 IRS3B, perhaps due to the short timescales before the disk self-stabilizes by redistributing the angular-momentum. Turbulent fragmentation typically operates on 1000s of au scales in turbulent cloud cores. Moreover, simulations show that systems may migrate significantly from their nascent locations (Ostriker, 1999; Lee et al., 2019a) due to gravitational attraction and initial velocities with respect to the cloud core. Stars in these environments can become bounded and unbounded with empirical evidence that suggests multiples frequently form via turbulent fragmentation (Murillo et al., 2016). Therefore, it is likely that gravitational instability produces companions with compact separations (< 100 au), both pathways can produce companions with moderate separations (<500 au), and a single mechanism may populate the more extended configurations at scales

of >500-10,000s of au.

While we cannot directly infer the evolution of any one particular system, we can use statistical approaches to modeling and determine the most probable formation pathway for an ensemble of multiple systems. Particularly, Bate (2018) conducted hydrodynamic simulations of proto-multiples undergoing gravitational collapse in a viscous medium, and found for a set of unbiased sources, the relative alignment angles are not correlated with hierarchy number, separation distributions, or age (see Figures 19 and 24 in; Bate, 2018). Additionally Offner et al. (2016) showed that systems formed through turbulent fragmentation are randomly aligned and found that partial misalignment persists even after inward orbital migration. This was further supported by Lee et al. (2016) in observing companions with separations a >1,000 au who found a nearly complete random distribution of alignment angles. Analyzing our statistics (Tables 5.5.1), we can statistically infer the fractions of preferentially aligned and randomly aligned orientation pairs that are in the given sample.

We found for our particular Perseus sample, for the distribution of companions with separations <10,000 au, distributions of a majority preferentially aligned orientation pairs are ruled out (for ratios 100% correlated to 70% correlated), with more than 90% of tests rejecting the null hypothesis, on average. The a <10,000 au sample also disfavors distributions of majority randomly aligned sources when considering the *uv*-visibility fit results, with more than 95% of tests rejecting the null hypothesis for as much as 90% randomly aligned systems. The *uv*-visibility derived tests have better constraints on the fitted uncertainties. With the relatively low number of statistics (at most 44 pairs of sources), we were not able to determine the exact underlying fractional alignment ratio that best describes the sample of sources. This characterization of the subsamples and full sample is consistent with synthetic radiation hydrodynamical simulations of protostellar clusters (Bate, 2018).

It is likely the more compact companions of our sample (a <100 au, left panel: Figure 5.5.1), which do not rule out the null hypothesis in fractional ratio tests from 100% correlated down to 30% correlated (Table 5.5.1), are formed primarily via gravitational instability, forming preferentially aligned pairs. This is similar to surveys of compact ($a \approx 50$ au) star-planet binaries (Dupuy et al., 2022) which were observed to have mutual orbital inclinations <30°. The large spread in the fractional ratio tests is likely due to the low number of sources

(n= 7) that have separations a <100 au). Bate (2018) shows an EDCF of compact companions that appears to be most consistent with 80% correlated sources.

The extended samples (a >500 au, right panel: Figure 5.5.1) appear uniform in fractional ratios that do not reject the null hypothesis, consistent with having at least 30% randomly aligned sources.

The full sample (a <10,000 au, middle panel: Figure 5.5.1) appear less uniform in fractional ratios that do not reject the null hypothesis, clustering around 50% correlated to 50% correlated, and are likely more constrained due to the higher number of sources (n=44).

5.5.2. Formation Mechanism of Individual Systems

The statistical tests alone are not able to tell a complete picture of an individual system, but it can provide a statistical way to characterize a sample of systems. To best determine the formation mechanism of any particular system, a combination of multi-wavelength observations of continuum and molecular lines are needed. We would expect sources that have formed via gravitational instability to have separations on the order of the continuum disk size (a ≈100s au) and the kinematics of the system to be organized. Whereas, formation of system via turbulent fragmentation happens on much larger scales (a ≈1,000-10,000s au). The sources formed at larger scales could further migrate to ∼100s of au, preserving no preferential alignment of the kinematics. We discuss the likelihood of the observed systems with these two formation mechanisms based on the previous observations and our 1.3 mm and 3 mm ALMA continuum observations.

5.5.2.1. Likelihood of Disk Fragmentation

We detected circum-multiple material in nine of the 11 observed sources (Per-emb-5 is now classified as a single source) in these observations (source designation; Figure 5.3.2); however our array configuration is less sensitive to large scale emission. In all detected cases, the circum-multiple material was observed around Class 0 sources, while sources that show significant misalignment do not show much circum-multiple material within the detection limits of our observations. In selecting a subsample consisting of only Class 0 sources from our full sample of sources, we found the median relative disk orientation angle is 24° for the Class 0 sources.

More than half of the observed multiple systems are consistent with having their <500 au

companions formed via disk fragmentation of an unstable disk. The sources Per-emb-2, Per-emb-17, Per-emb-18, Per-emb-22, L1448 IRS3B, L1448 IRS3C, and SVS 13A appear most consistent with the disk fragmentation formation pathway.

In particular for Per-emb-2, Pineda et al. (2020) found the mass-infall rate exceeds that of the accretion rate derived from the bolometric luminosity. This scenario provides favorable conditions to trigger gravitational instabilities that lead to the fragmentation of the disk (Kratter et al., 2010a).

These compact circumstellar disks appear to be strongly aligned and deeply embedded Class 0 systems, with bright circum-multiple disks (in some cases).

5.5.2.2. Likelihood of Turbulent Fragmentation

There are several other systems with separations a <1,000 au which are not consistent with disk fragmentation and likely formed via a combination of other methods. The sources L1448 IRS1 and NGC1333 IRAS2A are relatively compact proto-multiple systems, with strongly misaligned disks.

The sources Per-emb-21, L1448 IRS3A, and SVS13 B are wide ($a > 1000$ au) companion sources and additionally appear to not be preferentially aligned towards the outer sources in the respective systems, and are thus likely formed via turbulent fragmentation.

The companion ($a \approx 418$ au) of L1448 IRS1 is nearly orthogonal to the brighter primary source. This source could have formed via turbulent fragmentation and then evolved via dynamical interactions to more compact scales (a$\sim$1.$''$4$\approx$420 au).

The companion of NGC1333 IRAS2A is nearly orthogonal to the brighter primary source with a much higher inclination within the limits of our observations. Our observations for the disk position angle are consistent with an angle orthogonal to prior observations of the outflow position angles (Tobin et al., 2015a). Similar to L1448 IRS1, this source could have formed via turbulent fragmentation and then evolved via dynamical interactions to more compact scales (a$\sim$617 mas$\approx$185 au).

Per-emb-35 appears to be two similar sources, with aligned relative disk orientations, at a wide separation of 1.$''$9 ($\sim$570 au). While the orientations are aligned with an average relative orientation angle of $\sim$19°, the source is not likely to have formed via gravitational instabil-

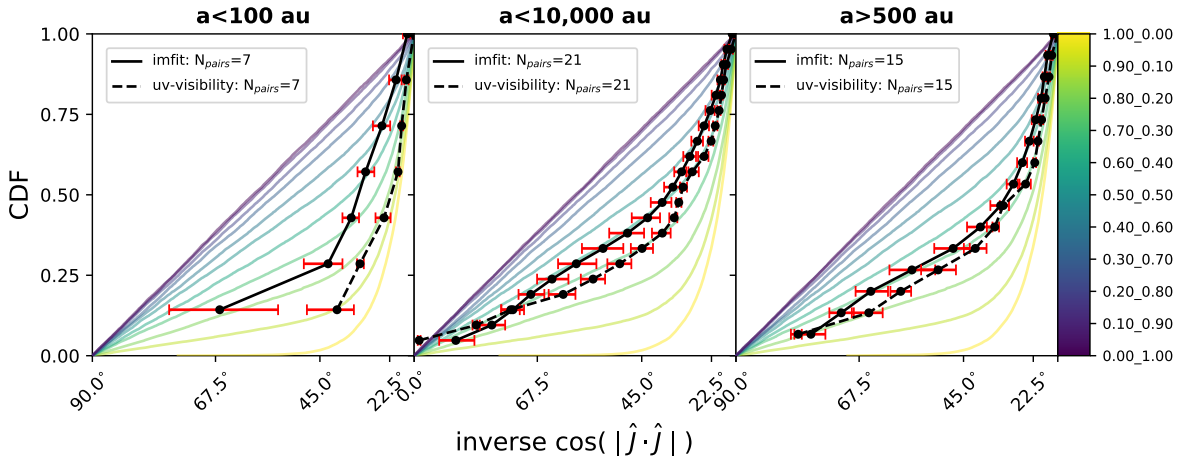

Figure 5.5.1: : Left panel: corresponds to the subsample of compact companion separations ($<$ 100 au); Middle panel: the full companion sample with separations (a$<$10,000 au); Right panel: subsample of extended companions (a$>$500 au). Median CDFs of the dot-product of the orientation vectors for each of the fitting techniques and of the various distributions of fractional alignment ratio. Each of the colored lines corresponds to a particular sample of fractional ratio distributions between a fully preferentially aligned distribution to fully randomly aligned distribution, with the given ratio in the colorbar, as detailed in Section 5.4.4. We resample the data with Gaussian errors considering the observation uncertainties and construct empirical CDFs. The solid black line is a median CDF for the CASA *imfit* results. The dashed black line is a median CDF for the *uv*-plane fit results. The red, horizontal error bars associated with each ECDF, represent the 1 σ uncertainty for the lower and upper bound, respectively. The compact ($<$100 au) subsample is consistent with preferentially aligned distributions, with $>$80% of all sources having a dot-product within 30°. The full sample and extended companion subsample are consistent with a ratio of aligned orientations, with 60% of all sources having a dot-product within 30°. The full statistical analysis is given in Table 5.5.1 and further discussed in Appendix 5.E.

ity. We report no detection of circumbinary material or any dust continuum between the two sources. This coupled with the wide separation means Per-emb-35 is likely to have formed via large-scale (1000s of au) mechanisms, likely turbulent fragmentation or dynamical capture, and migrated to more compact scales (100s of au).

5.5.2.3. Ambiguous Formation

It is not readily apparent via which formation pathway NGC 1333 IRAS2B ($a \approx 95$ au) formed. The orientation vectors are relatively aligned within 40° but this could be happenstance as there is no circum-multiple material found in these or prior observations. The system could have formed at long separations and migrated to compact scales.

Table 5.5.1: Model uv-visibility Fitting Statistics

Fractional Alignment	<100 au			<10,000 au			>500 au		
	$\%_{KS}$	$\%_{AD}$	$\%_{ES}$	$\%_{KS}$	$\%_{AD}$	$\%_{ES}$	$\%_{KS}$	$\%_{AD}$	$\%_{ES}$
$C_{1.00}$ $UC_{0.00}$	100.0	100.0	32.5	0.0	0.0	0.7	0.0	0.0	19.9
$C_{0.90}$ $UC_{0.10}$	100.0	100.0	2.1	0.9	0.1	48.3	46.6	5.3	99.9
$C_{0.80}$ $UC_{0.20}$	100.0	100.0	0.0	85.6	80.8	84.1	100.0	100.0	100.0
$C_{0.70}$ $UC_{0.30}$	100.0	100.0	0.0	100.0	100.0	99.9	100.0	100.0	100.0
$C_{0.60}$ $UC_{0.40}$	99.5	99.0	0.0	99.9	100.0	99.2	100.0	100.0	99.4
$C_{0.50}$ $UC_{0.50}$	69.7	82.6	0.0	91.6	99.0	93.4	98.0	100.0	94.1
$C_{0.40}$ $UC_{0.60}$	48.1	44.2	0.0	51.3	72.4	73.8	55.2	90.5	68.6
$C_{0.30}$ $UC_{0.70}$	33.4	5.7	0.0	7.9	8.2	37.6	9.0	3.8	26.8
$C_{0.20}$ $UC_{0.80}$	6.9	0.5	0.0	1.0	0.1	13.2	0.5	0.0	7.7
$C_{0.10}$ $UC_{0.90}$	3.4	0.0	0.0	0.1	0.0	4.4	0.0	0.0	2.5
$C_{0.00}$ $UC_{1.00}$	2.7	0.0	0.0	0.0	0.0	2.2	0.0	0.0	1.3

NOTE—The fractional alignment column details the fractional ratio of aligned vs randomly aligned as indicated by the subscripts. $\%_{KS}$, $\%_{AD}$, and $\%_{ES}$ correspond to the % of resampled observation dot products that cannot reject the null hypothesis in favour of the alternative for Kolmogorov-Smirnov, Anderson-Darling, and Epps-Singleton statistical tests respectively. The rejection criteria is evaluated at 0.3%. The total number of resampled observation dot products are 10,000. The null hypothesis tested is the empirical distributions and the corresponding constructed fractional distributions are drawn from the same underlying distribution.

5.6. Conclusion

We have presented very high resolution data (resolution $\sim$8 au) towards 12 Perseus protostellar multiple systems, resolving 31 sources within 10,000 au. We observed the dust continuum at 1.3 mm and a subset of the sources with supplemental data at 3 mm. Our results can be summarized as follows:

1. We detected and confirmed all previously detected multiple systems from the VANDAM observations (Tobin et al., 2018b, 2016b), except one, and we detected a total of 32 sources. Per-emb-5 is the only source that we reclassified as a single source.
2. We detected circum-multiple continuum emission in seven of the 12 systems consistent with other observations at lower resolution that do not resolve out the larger-scale emission.
3. We statistically characterized our full sample of 11 Perseus protostellar multiples (N_{pairs}=21), with separations $<$10,000 au, to be consistent with forming from a combination of gravitational instability and turbulent fragmentation pathways, with the underlying distribution described as 30%-70% preferentially aligned systems.
4. If we select a compact subsample of the sources, with separations $<$100 au (N_{pairs}=7), we found the underlying distribution of at least 30% preferentially aligned and we ruled out distributions that are randomly aligned dominated.
5. Combining our statistical approach with prior observations, we determined 7 of 12 of our systems are more consistent with disk fragmentation; while 3 systems (and 3 wide companions) are more consistent with turbulent fragmentation. One system, NGC1333 IRAS2B requires additional follow up to determine the formation pathway. Determining the formation mechanism via the statistical approach gives the likelihood of the sample being consistent with the same underlying distribution; whereas, combining this approach with multi-band observations detailing larger scale structures and molecular line features will give the most holistic determination.
6. Towards Per-emb-2, we detected the previously reported compact (a =24 au) binary Per-emb-2-a/-b, 2 additional possible companions Per-emb-2-c/-d, and additionally a potential fifth companion Per-emb-2-e, embedded within the northern part of the disk.

7. Per-emb-5 is now resolved in these observations and appears as a ringed disk with a single spiral arm extending to the west. The double peaks as appeared in the VLA data were likely caused by limited long baseline sampling and subsequent imaging.
8. Toward L1448 IRS3B, we resolved the compact ring of the inner disk and resolved the previously detected IRS3B-a, -b as compact sources just inside and outside of the ring, respectively. Additionally, toward L1448 IRS3B, while faint, we confidently detected an additional continuum source at the geometric center of the inner disk ring. This might be emission surrounding a more central protostellar source that could dominate the gravitational potential given that it is near the two kinematic centers as described with the molecular lines $C^{17}O$ and $C^{18}O$.
9. Towards L1448 IRS3A we resolved the disk to be a ring and an unresolved compact continuum source surrounding the central protostar at the geometric center of the ring. No source is detected within the gap between the central source and ring.

These results, while unable to determine with certainty the relative contribution of the different formation pathways due to the low number of systems, suggest a path for characterizing multiple star formation with future surveys. To best utilize the methods described, the highest resolution surveys towards larger samples of multiples are required to confidently resolve the most compact scales of the circumstellar disks around the protostars.

Appendix

5.A. Notes on Specific Sources

5.A.1. Class 0

5.A.1.0.1 Per-emb-2 This source was previously reported to be a close multiple <50 au with the VLA at 9 mm (Tobin et al., 2016b) and was further observed in Tobin et al. (2015b, 2018b) as a smooth continuum surface brightness distribution at 1.3 mm (Figure 5.A.1). We resolved the compact binary (a$\sim$80 mas$\approx$ 24 au) in both the 1.3 mm and 3 mm observations. Our observations resolved much of the large scale emission, but further revealed a possible additional 3 compact sources with separations of $\sim$0.$''$431 ($\sim$129 au), $\sim$1.$''$432 ($\sim$430 au), and $\sim$0.$''$5 ($\sim$150 au) for the southern (SNR$\approx$25), northern-most (SNR$\approx$22), and southern-most (SNR$\approx$15) sources respectively, relative to the Per-emb-2-a source of the compact binary. All of these compact sources (except the southern-most companion) are found within regions of relatively enhanced surface brightness within the Tobin et al. (2018b) observations, presumed to be a massive extended disk. The sources are present at least the 5 σ level in the 1.3 mm and the 3 mm observations. It should be noted that only the compact sources -a,-b and a marginal detection of the brighter southern source -c appear in 9 mm VLA observations (Tobin et al., 2016b) whereas more diffuse sources, the northern-most -d and and southern-most -e sources do not.

Tobin et al. (2018b) observed a velocity gradient in ^{13}CO and C^{18}O centered on the compact binary of Per-emb-2-ab. Several other studies have also detected the outflow from Per-emb-2-ab (e.g., Tobin et al., 2015a; Yen et al., 2015; Stephens et al., 2018), but none have had the resolution or sensitivity to detect which of the two compact components is driving the outflow. Also, there do not appear to be detectable outflows originating from any of the companion sources.

5.A.1.0.2 Per-emb-5 Per-emb-5 was also previously reported to be a close multiple <50 au with the VLA at 9 mm (Tobin et al., 2016b). We instead found continuum emission that ap-

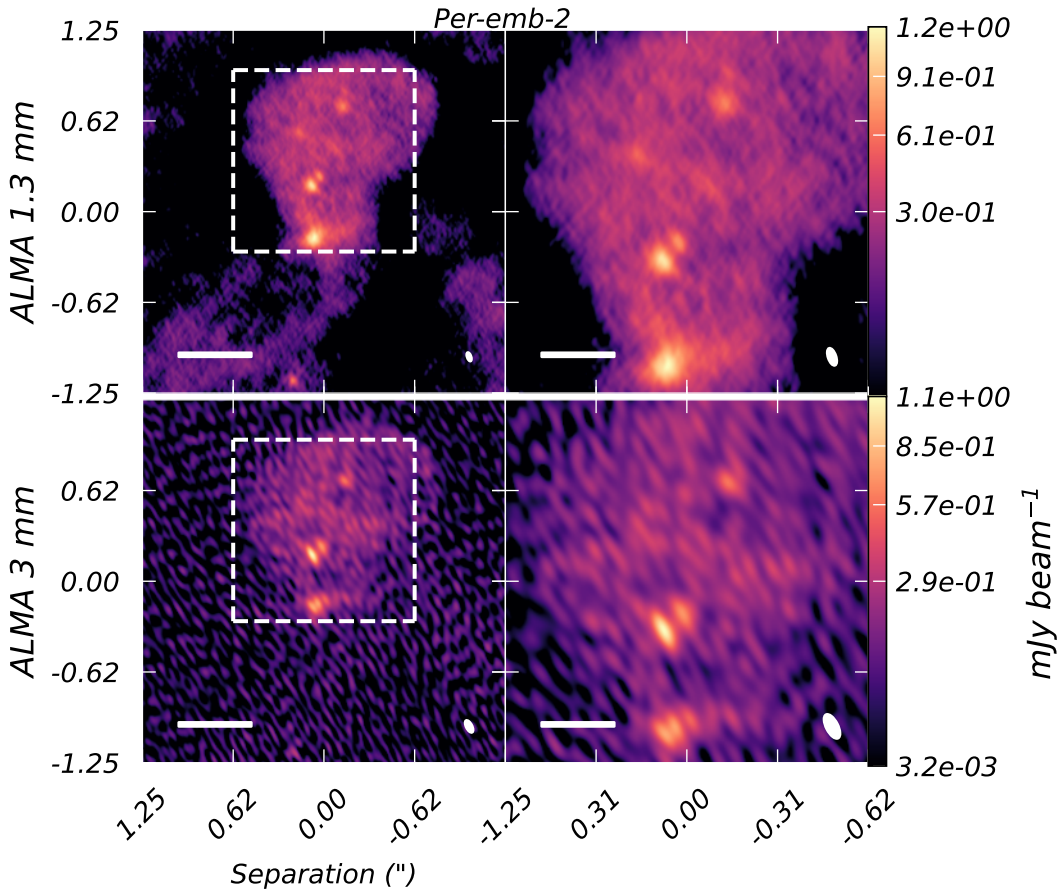

Figure 5.A.1: : Left side is a 2.″5 image of the Per-emb-2 system whose inner binary has been resolved. The right side is a 2× zoom in on the source. The top row is the ALMA 1.3 mm observations and the bottom row is the ALMA 3 mm observations. In both observations, we resolve the compact inner binary but also report potentially 3 additional companions, 2 more within the disk and the southern-most companion falls just on the edge of the image. This would make Per-emb-2 a possible 5 companion protostellar system. A 0.″5 (150 au) scalebar is shown in the left panels and a 0.″25 scalebar in the right panels. The beam is located in the lower right of both images. The colormap is square-root scaled.

pears consistent with that of a disk surrounding what appeared as two peaks in the VLA data (Figure 5.A.2). The disk appeared to have a central cavity (centered between the two VLA peaks), and maybe a single spiral arm to the west. There is an asymmetry across the minor axis of the disk and a flux enhancement in the south-east portion of the disk.

Previous Submillimeter Array (SMA) observations towards Per-emb-5 at 1.3 mm targeting $C^{18}O$ (2-1) and CO (2-1) molecular lines indicate a rich gas presence in the disk and envelope (Stephens et al., 2018; Heimsoth et al., 2022). The source also exhibits bi-polar outflows as evident in the SMA data, which are orthogonal to the major axis of the continuum disk in these observations. The $C^{18}O$ observations shown in Heimsoth et al. (2022) exhibit a velocity gradient that is in the same direction as the outflow with $\sim 3''$ (900 au) resolution, along the minor axis of the disk that we detect. Thus, the envelope may be influenced by the outflow (Arce & Sargent, 2006), or there is infall from a flattened envelope (Yen et al., 2011). Higher resolution kinematic observations are required to determine at what scale the disk rotation is detectable.

5.A.1.0.3 NGC1333 IRAS2A We resolved the binary of NGC1333 IRAS2A and resolved the brighter compact source NGC1333 IRAS2A-a. We also detected faint extended emission around NGC1333 IRAS2A-a at low surface brightness. The compact faint component NGC1333 IRAS2A-b does not appear to have much extended emission and is marginally resolved in these observations. The sources appeared oriented nearly orthogonal to each other in continuum. Bipolar outflows have been observed toward IRAS2A in several studies (Jørgensen et al., 2005; Plunkett et al., 2013; Codella et al., 2014; Tobin et al., 2015a; Jørgensen et al., 2022). The two outflows are nearly orthogonal to each other and appear to originate from the two components of the system. The outflow position angles are approximately orthogonal to the major axis of each presumed driving source. Other molecular gas emission has been characterized toward IRAS2A (Tobin et al., 2018b). There is a possible velocity gradient in $C^{18}O$, but the kinematics do not appear highly organized on scales $>0.''3$.

5.A.1.0.4 Per-emb-17 We resolved the compact disks toward each component of the binary (a$\sim$86 au) and detected the faint circumbinary material; circumbinary gas emission was also

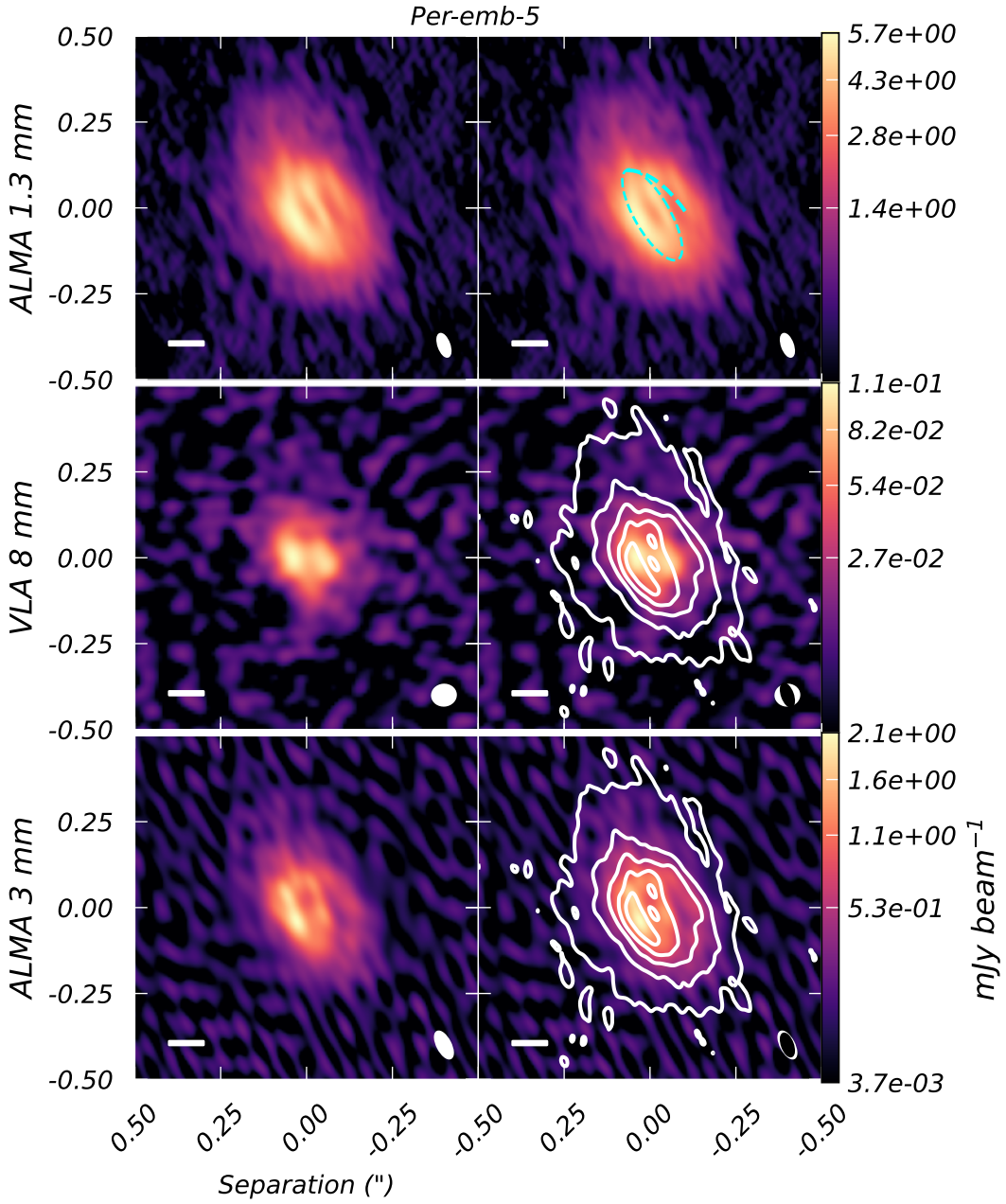

Figure 5.A.2: : Multiwavelength observations of the Per-emb-5 system. The upper panels are naturally weighted clean images from the 1.3 mm ALMA data. The middle panels are from Tobin et al. (2016b) robust 0.25 VLA 9 mm. The bottom panels are super-uniform clean images from the 3 mm ALMA data set reported here. The disk is asymmetric and appears as a ring and a single-arm spiral structure. We overlay an ellipse and line to assist in defining the substructure of Per-emb-5. A 0.″1 (30 au) scalebar is shown in the lower left and the representative beam is in the lower right. The white contours start at the 5 σ level and iterate by 20 σ, where the 1 $\sigma = 50$ μJy beam^{-1}. The colormap is square-root scaled.

previously detected by Tobin et al. (2018b). The northern source, Per-emb-17-a, is brighter and less extended than the southern source, Per-emb-17-b, which appears appears more edge-on. The circumbinary gas detected in $C^{18}O$ and ^{13}CO show a clear velocity gradient in the same plane as the companions. A bipolar outflow is also seen by (Tobin et al., 2018b), but the extended emission of the outflow is better recovered by observations from Stephens et al. (2018). The outflow position angle is orthogonal to the orientation of the binary system and the orientation of Per-emb-17-a.

5.A.1.0.5 Per-emb-18 We detected both the extended circumbinary structure reported in Tobin et al. (2018b) and resolved the separation between the compact binary (a$\sim$32 au) as reported in Tobin et al. (2016b). The binaries are situated in the near geometric center of the circumbinary disk (Figure 5.A.3). There is an apparent surface brightness asymmetry that could appear as an azimuthal asymmetry if viewed more face-on (e.g., van der Marel, 2015). When viewed at 9 mm the circumbinary disk appeared one-sided, which could be due to a combination of lower surface brightness sensitivity from the VLA and dust trapping due to a vortex created by the inner binary pair (van der Marel, 2015). The binaries themselves are similar in physical structure and brightness between the 1.3 mm and the 3 mm observations. The circumbinary material is shown to have a clear velocity gradient in ^{13}CO, $C^{18}O$, and H_2CO in Tobin et al. (2018b). These velocity gradients are orthogonal to the outflow traced by ^{12}CO (Stephens et al., 2018; Tobin et al., 2018b; Heimsoth et al., 2022).

5.A.1.0.6 Per-emb-21 Within the same pointing of Per-emb-18, Per-emb-21 is detected 14.$''$ (4230 au) from Per-emb-18. The disk surrounding Per-emb-21 is marginally resolved. In lower resolution observations, there appears to be $C^{18}O$ emission connecting Per-emb-18 to Per-emb-21, and in Heimsoth et al. (2022) they found that there is a $\sim$1 km s^{-1} line of sight velocity difference between the two sources. Rotation on $<$100 au scales has not yet been detected toward Per-emb-21.

Per-emb-18 and Per-emb-21 also appear to have entangled CO outflows as reported in Stephens et al. (2018). The Per-emb-21 outflow appears much brighter and wider than the Per-emb-18 outflow. The wide-angle ($\sim$90°) outflow spans $\sim$9000 au and encapsulates both

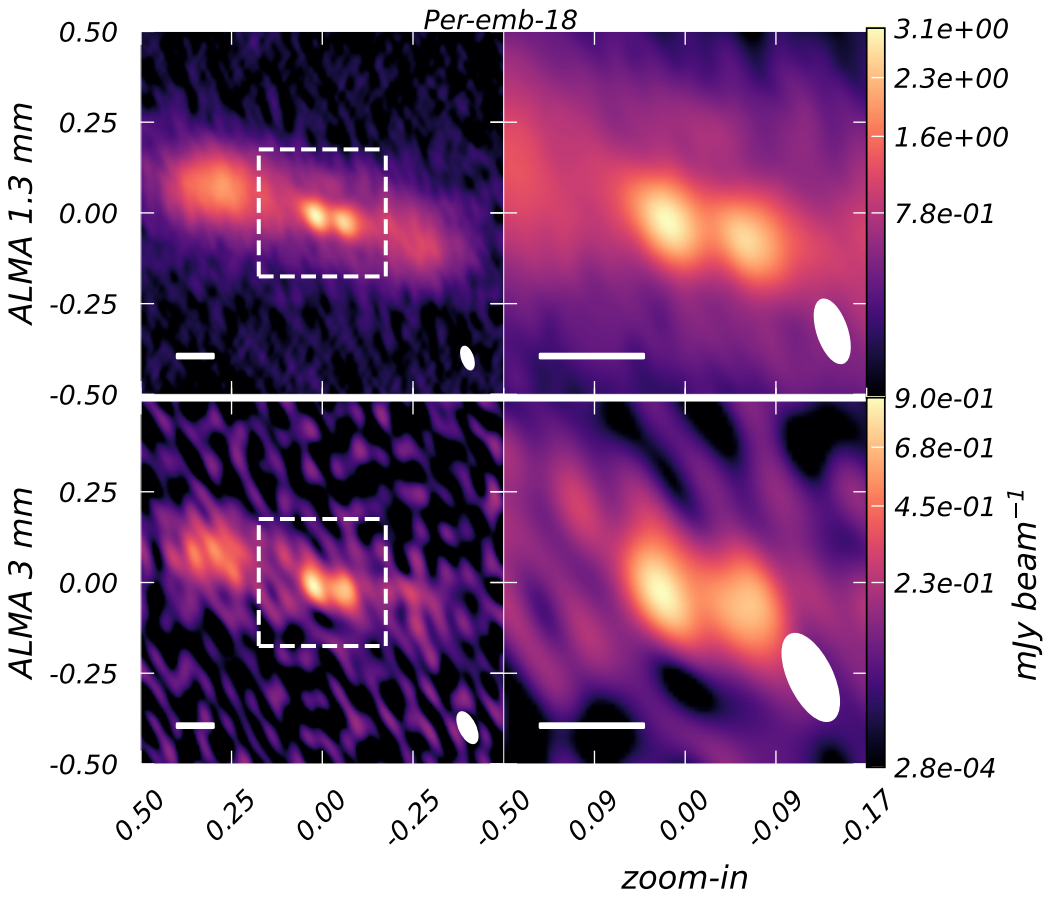

Figure 5.A.3: : Left side is an 1.″0 image of the Per-emb-18 system, and the right column is a $\sim$4$\times$ zoom-in. The upper panels are Briggs weighted with robust parameter 1, clean images from the 1.3 mm ALMA data. The bottom panels are super-uniform clean images from the 3 mm ALMA data. We resolve the compact inner binary of Per-emb-18 and resolve the circumbinary disk. We report in both 1.3 mm and 3 mm observations the circumbinary disk is asymmetric in flux, with the east side being enhanced as compared to the west side. The compact inner binary is located at the geometric center of the circumbinary disk. The compact disks of the individual sources remain unresolved in both observations. A 0.″1 (30 au) scalebar is shown in the lower left and the representative beam is in the lower right. The colormap is square-root scaled.

sources in the plane of the sky. However, our reported position angles of the disk major axis are consistent with being orthogonal to the CO outflow emission as reported in Stephens et al. (2018).

5.A.1.0.7 Per-emb-22 Towards Per-emb-22 we marginally resolved the compact disks around each compact (a$\sim$263 au) source, and we detected a connecting "bridge" between the sources in continuum. Additionally, Per-emb-22-b, appears to have an asymmetric oblate disk, extending towards the south and has a large, possibly rotating circumbinary structure in continuum and molecular lines (Tobin et al., 2015b). The velocity gradient was more evident at $\sim$1$''$(300 au) resolution than at $\sim$0.$''$3 (90 au) resolution in Tobin et al. (2018b). There is a clear outflow from Per-emb-22 (Stephens et al., 2018) that is at a $\sim$45 angle with respect to the plane of the binaries. Higher resolution maps of CO from Tobin et al. (2018b) seem to show that the more prominent outflow originates from Per-emb-22-b while there might be some evidence for a second outflow from Per-emb-22-a.

5.A.1.0.8 L1448 IRS3B L1448 IRS3B is certainly a exceptional source (Figure 5.A.4). The system is home to at least 4 compact continuum sources within 8$''$, 3 of which are within 1$''$ of each other. The brightest feature, the tertiary companion commonly known as L1448 IRS3B-c is likely optically thick. The tertiary companion is embedded within one of the large spiral arms that stems from the inner disk to the outer disk. Zooming into the center of the system, two bright continuum sources are obvious, one just inside of an inner spiral arm/disk structure and one just outside. We apparently resolved the "clump" as reported in Reynolds et al. (2021) as the north-east portion of the inner disk and now report an additional faint compact source near the geometric center of the inner disk. The bright point L1448 IRS3B-a is now resolved as the south-west portion of the ring and a bright source just inside of the "ring" of the inner disk. L1448 IRS3B-b is just outside of the "ring".

We reproduced Figure 16 from Reynolds et al. (2021) in Figure 5.A.4, denoting the locations of the kinematic centers for the L1448 IRS3B system using various disk tracing molecular line observations and techniques. We visually depict the new geometric center of the inner ring, which coincides with the center of the "deficit" previously reported and overlaps, within ob-

servation uncertainties, with the center-point of the kinematic centers. It is possible this newly resolved source is another deeply embedded protostellar source and the disk could harbor as many as 4 protostellar sources. For the purpose of the analysis conducted later in the paper, we do not consider this small point source at the center as another independent source; instead, we only consider the two confirmed compact continuum sources as protostar sources. The new source, while confidently detected, is too faint to have its geometric parameters well-constrained from Gaussian fitting. We refer to this new source as L1448 IRS3B-d, centered at 03h25m36.326s 30:45:14.93. The designation of sources in L1448 IRS3B may need reassignment in the future once the nature of the source and the inner disk are better characterized with additional observations.

Reynolds et al. (2021) observed $C^{17}O$ in the disk of IRS3B. $C^{17}O$ appears to trace well-ordered Keplerian rotation on the scale of the continuum disk (see Figure 4; Reynolds et al., 2021). Considering only the high velocity Doppler-shifted channels of the $C^{17}O$ emission, which should trace scales closest to the center of mass, the kinematic center of $C^{17}O$ coincides with the position of L1448 IRS3B-d. In Figure 5.A.4, we compile our observations at 1.3 mm and observations by Reynolds et al. (2021). We plot the kinematic centers of the $C^{17}O$ molecular line observations using the position-velocity diagram fitting technique (i.e. "1") and the Bayesian analysis of kinematic flared disk *uv*-visibility modeling ("2") with the *pdspy* software (Sheehan, 2022). We also indicate the position of L1448 IRS3B-a,-b, derived from previous observations, which we now resolved as two sources just inside and outside of the ring, respectively. Finally we draw a visual aid indicating the proposed geometric configuration of the inner disk, which now appears as a ring with a faint, but confidently detected, continuum source located at the geometric center of the ring.

5.A.1.0.9 L1448 IRS3C We resolved both disks of the compact (a$\sim$72 au) binary L1448 IRS3C. We detected faint circum-binary continuum emission at the limit of our observations. The disks appear nearly aligned and the southern source is much brighter than the northern source. This system is also a wide companion to the L1448 IRS3A/IRS3B system, located $\sim$5300 au away.

Tobin et al. (2018b) reported observations of L1448 IRS3C with disk tracing molecules $C^{18}O$ and ^{13}CO, and found position angles of the velocity gradients corresponding to 220°,

consistent with the major axes of the disk we observed here. There is also a velocity gradient in the circumbinary emission, consistent with orientation of the binary, in both ^{13}CO and C^{18}O. Outflows have been observed from L1448 IRS3C (Lee et al., 2015; Tobin et al., 2015b), but even the highest resolution ^{12}CO maps thus far from Tobin et al. (2018b) only detect a single outflow.

5.A.1.0.10 SVS13 A is a compact (a$\sim$92 au) binary with prominent spiral arms that were also seen in Tobin et al. (2018b) and Diaz-Rodriguez et al. (2022). We detected the circumbinary one-armed spiral continuum and resolved each compact circumstellar disk. We also detected the unresolved wide (a$\sim$1830 au) companion SVS13 A2. Additionally, we detected the wide (a$\sim$4770 au) companion SVS13 B. We resolved SVS13 B, but due to limited sensitivity far out in the primary beam, the image is very noisy. Tobin et al. (2018b) found apparent rotation in the circumbinary spiral structure, while higher resolution data from Diaz-Rodriguez et al. (2022) found rotation across the two binary sources and circumstellar rotation from one.

Stephens et al. (2018) found the outflow position angle to be 150°$\pm$10°, which is approximately orthogonal to our reported disk position angle of $\sim$70°. Tobin et al. (2018b) found the disk position angle to be $\sim$220° (180° symmetry yields angle $\sim$50°) by evaluating the angle of the velocity gradient in the disk tracing molecules C^{18}O and ^{13}CO. This is consistent with the average of the position angles for the two compact sources SVS13A-ab.

5.A.1.0.11 RAC1999 VLA20 We detected the continuum source RAC1999 VLA20. However it is believed to be an extra-galactic source (Rodríguez et al., 1999; Tobin et al., 2016b) so the source is not considered for the purpose of the analysis conducted in this paper. A summary of the observed source is in Table 5.A.1.

5.A.2. Class I/II Protostars

5.A.2.0.1 L1448 IRS1 The bright disk of L1448 IRS1-a, the northern source, is well-resolved and is likely the most evolved source in our sample. This source has a bright, compact (62$\times$28 mas $\approx$ 19$\times$8 au) disk and a fainter extended (25 $\times$12 mas $\approx$ 75$\times$36 au) disk. The fainter, southwest companion is marginally resolved orthogonal to the beam. Previous observations of L1448 IRS1 reported a disk position angle of 24° based on continuum observations (Tobin

et al., 2018b), and we report a consistent position angle of 25°. Analyzing the CO emission, which is tracing the disk toward L1448 IRS1-a, coincides with the major axis of the disk and is likely tracing only the gas component of the disk and not the outflows.

5.A.2.0.2 L1448 IRS3A Within the pointing of L1448 IRS3B (Section 5.A.1.0.8), we detected this wide (a∼2280 au), more evolved companion. Furthermore, we resolved the substructure of the continuum disk to be a clear circumstellar ring. The compact inner disk centered at the geometric center of the ring remains unresolved in these observations, and the relative orientation cannot be determined to be different with respect to the outer ring.

Previous observations of L1448 IRS3A reported the disk position angle to be ∼130° (Tobin et al., 2018b; Reynolds et al., 2021) based on the PA of the ring and apparent orthogonality to the outflows observed by Lee et al. (2015); Tobin et al. (2018b). As such, for the purpose of the statistical analysis later in the paper, we assumed the inner compact disk orientation would be comparable to the orientation of the ring. Rotation of the outer disk has been traced in $C^{18}O$, ^{13}CO, and $C^{17}O$, and the inner disk, close to the scales of the inner compact continuum source, has been traced in SO_2, consistent with the outer disk (Tobin et al., 2018b; Reynolds et al., 2021). The origin of the ring is beyond the scope of this paper, but we can report that we do not detect a continuum source within the gap between the inner continuum source and the ring.

5.A.2.0.3 Per-emb-35 We marginally resolved the continuum emission toward each source, which are separated by ∼644 au and report no obvious detection of any continuum emission between the two compact sources.

Observations of the the CO outflows in Stephens et al. (2018) show an outflow position angle of 123°, and Tobin et al. (2018b) detected what appear to be parallel outflows from each protostar. Due to the compact nature of the circumstellar disks, rotation within them is not clear, though Tobin et al. (2018b) did detect compact blue and red-shifted H_2CO and SO that could be from the disks. With our higher resolution 1.3 mm observations, we report a disk position angle of 31° for Per-emb-35-a, which is consistent with being orthogonal to the outflow as reported in Stephens et al. (2018).

Table 5.A.1: RAC1999 VLA20

imfit results	
R.A.	03:29:4.256
δ	31:16:9.03
separation	9″ (2700 au)
Int. Intensity	1.80 mJy
Peak	0.48 mJy beam^{-1}
P.A.	142°
σ_{major}	73 mas
σ_{minor}	31 mas

NOTE—The CASA *imfit* fitting results for the source RAC1999 VLA20, which was detected in the field of SVS13 A. This source is believed to be extra-galactic and not considered part of the SVS13 A system.

5.A.2.0.4 NGC1333 IRAS2B The disk around the brighter southern source, NGC1333 IRAS2B-a is well-resolved. The companion source ∼95 au away, is marginally resolved and visually appears mis-aligned to the brighter source. Stephens et al. (2018) reported the outflow position angle of 24°±10°, which is consistent with an earlier map by Plunkett et al. (2013). We reported the disk position angle of the larger source to be 104°, which is nearly orthogonal with the reported outflow position angles. While the companion IRS2B-b appears misaligned in the image, when deconvolved from the beam the position angles are relatively aligned. This appearance of misalignment in the 2D image is possibly due to projection of the true 3D orientations and true 3D positions of the sources, which we are unable to discern from these observations alone. Clear rotation across the binary or toward either disk has not been observed, although Tobin et al. (2018b) found emission to generally be concentrated northeast of IRAS2B-a, towards IRAS2B-b, with SO having the greatest likelihood of exhibiting a velocity gradient. ^{13}CO and H_2CO appear on the north-east side of IRAS2B-a while $C^{18}O$ appears almost entirely on the far side of IRAS2B-b.

5.B. Companion Finding Algorithm

The algorithm[2] first attempts to find the most compact pair within the defined distance criteria and groups them together, re-inserting the geometric center of the group into the source list. The algorithm then re-derives the most compact pair within the maximum distance allowed and groups these two, again re-inserting the new geometric center into the list. In Figure 5.B.1, we show an example case of 8 total sources. indicated as red crosses. At "Step 1", the algorithm finds the most compact pair and groups them (System 1). In "Step 2" the next most compact pair is a companion to the first binary, thus making a triple source system (System 1). At "Step 3", the next most compact pair is a separate pair further away (System 2). At "Step 4", another group is made from separate sources (System 3). "Step 5", the systems 2 and 3 meet the distance criteria, and thus are merged together to form System 2, now a quad-source system. The algorithm continues until no more sources meet the distance criteria, arriving at a quad-source system, a triple-source system, and a single source system for this particular model. This produces nine pairs of comparison disk orientations.

5.C. Gaussian Fitting in the Image Plane

Using the CASA task *imfit*, we fit all of the sources using 2-D Gaussians in the image plane. The estimates provided were single 2-D Gaussians on each individual companion with a Gaussian peak flux density equal to the peak flux density in the image and the beam characteristics as the Gaussian geometry. A few sources needed to be represented with two components, an unresolved point source and an extended 2-D Gaussian: L1448 IRS1, L1448 IRS3B-c, and L1448 IRS3C, NGC1333 IRAS2B. The results of the deconvolved 1.3 mm image-plane fits are summarized in Table 5.C.1 , and the results of the deconvolved 3 mm image-plane fits are summarized in Table 5.C.2. We also

The results of Gaussian fitting enable us to analyze the disk geometries of all of the sources. For faint, marginally-resolved (<3 beams) or unresolved sources, the recovered structure of the source approaches the inherent beam geometry. For well-resolved sources with bright emission, these effects are less important; however, towards the more compact and marginally-resolved continuum sources, the Gaussian fits are less-well constrained.

[2]Codes are made public in https://github.com/nickalaskreynolds/ALMAc7-PerseusMultiples-Statistics

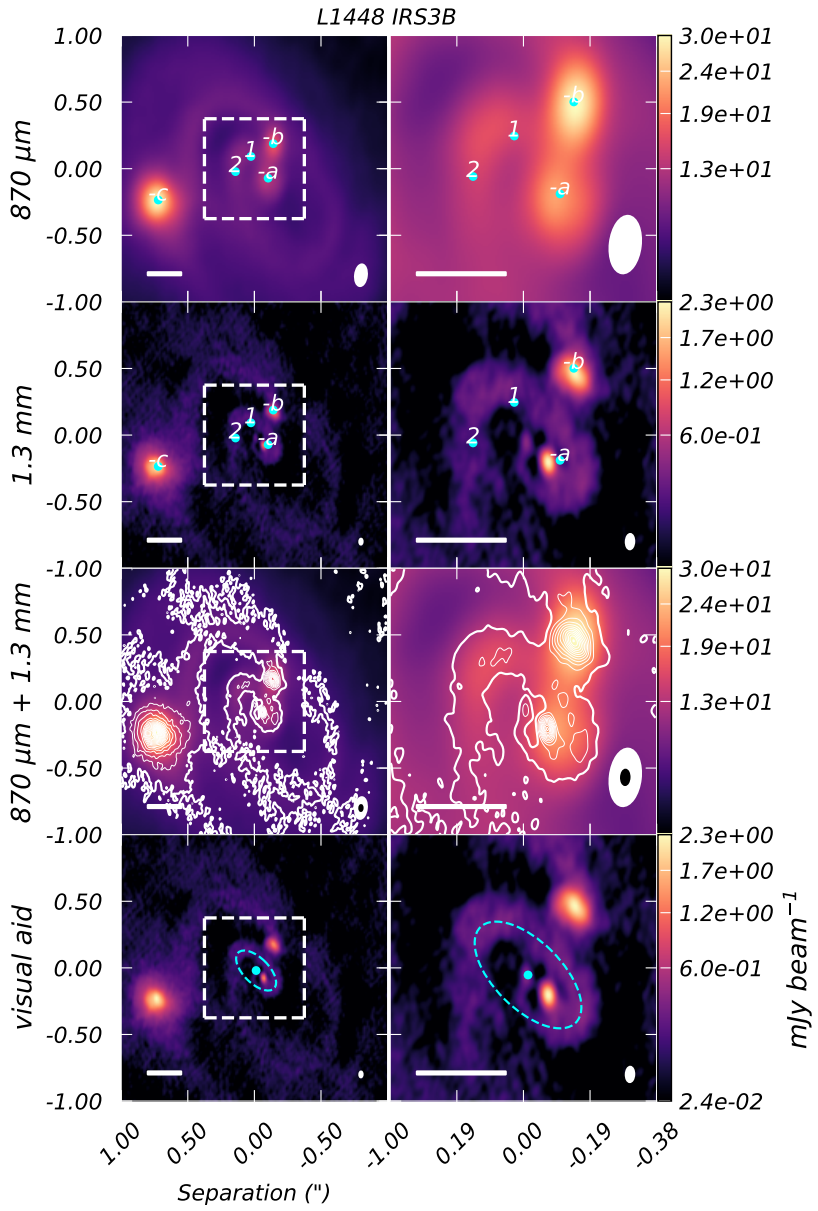

Figure 5.A.4: : The left side is the 2″ view of the system L1448 IRS3B, in which you can clearly see the triple component companion system and the spiral arm substructures. Right side is a ∼4× zoom in on the inner disk of the binary L1448 IRS3B-ab. The top row is reproduced from Reynolds et al. (2021) using ALMA 870 μm continuum emission. The upper-middle row is the current 1.3 mm, high resolution observations. The lower-middle row has the 870 μm data as the background and the 1.3 mm data is overlayed as white contours. The lower row is the same 1.3 mm data but with diagrams to aid in visualizing the likely configuration of the disk. We now resolve the inner disk to be a ring and the so called "clump" (see Figure 2; Reynolds et al., 2021), is the north-east side of the ring. We report the L1448 IRS3B-a source is now resolved as just inside of the ring and L1448 IRS3B-b is now resolved as just outside of the ring. The separation between the two sources is well resolved and the L1448 IRS3B-b source is resolved. Towards the geometric center of the ring there is compact emission. We also reproduce the kinematic centers as the numbers "1" and "2" in the plot, as reported in Reynolds et al. (2021). The 0.″25 (75 au) scalebar is shown in the lower left and the representative beam is in the lower right. The white contours start at the 3 σ level and iterate by 10 σ, where the 1 σ = 20 μJy beam^{-1}. The colormap is square-root scaled. The contour representative beam is overlayed in black at the lower right.

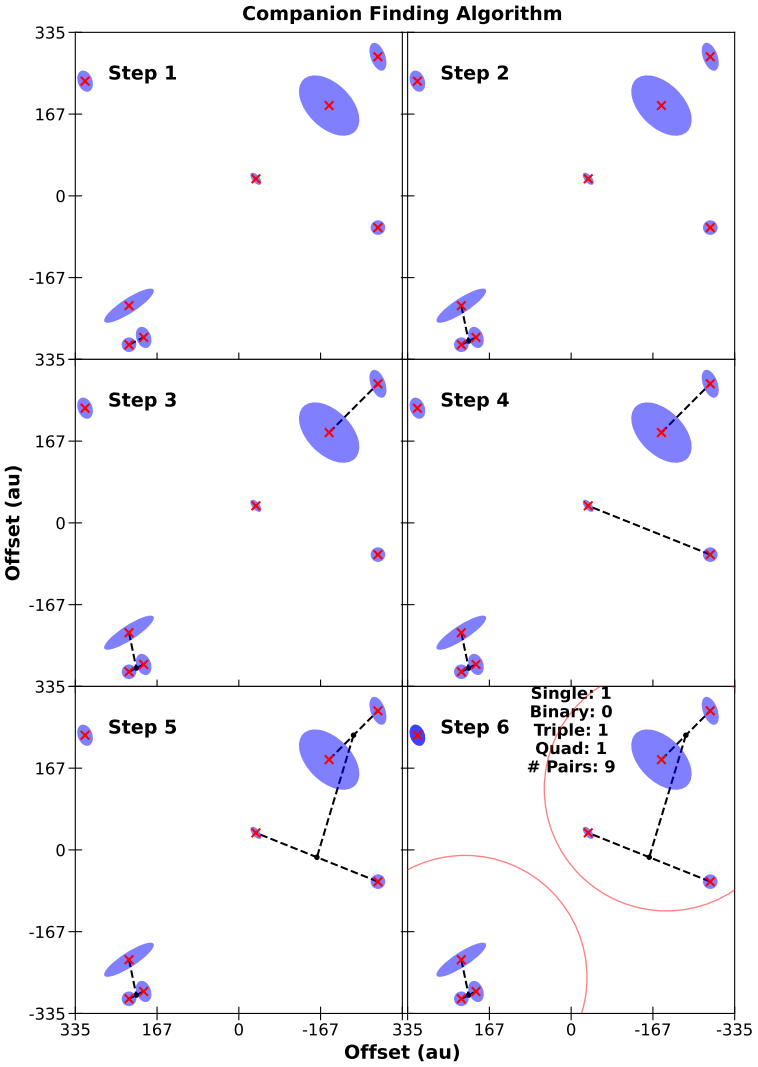

Figure 5.B.1: : Demonstration of the companion finding algorithm used to sort the survey data. In this case, the companion maximum distance is 500 au. The algorithm first attempts find the most compact pair within the maximal defined distance and groups them together, re-inserting the geometric center of the group into the source list. The algorithm then finds the most compact pair within the maximum distance allowed and groups these two. In the plot, all of the example sources are shown in red crosses. At "Step 1", the algorithm finds the most compact pair. In "Step 2" the next most compact pair is a companion to the first binary, thus making a triple source system. The algorithm continues until no more sources meet the distance criteria, arriving at a quad-source system, a triple-source system, and a single source system for this example.

Table 5.C.1: 1.3 mm Image-plane Fitting Results

Name	α (J2000)	δ (J2000)	Sep. (au)	$\sigma_{maj} \times \sigma_{min}$ [a] (mas × mas)	σ_{error} (mas)	PA [a] (°)	PA error (°)	i (°)	T_B (K)	Int. Intensity (mJy)
L1448 IRS1 -A	+03:25:09.455	+30:46:21.84		62 × 29	2	24.7	1.6	62.7	80.4	9.8
··· -B	+03:25:09.418	+30:46:20.53	418	51 × 40	4	124.0	13.7	38.3	30.7	4.1
Per-emb-2 -A	+03:32:17.932	+30:49:47.70		49 × 22	36	17.5	90.0	63.0	9.8	0.4
··· -B	+03:32:17.935	+30:49:47.63	26	49 × 22	36	17.5	90.0	63.0	6.0	0.3
··· -C	+03:32:17.934	+30:49:47.28	126	141 × 104	13	123.5	15.4	42.7	11.9	8.1
··· -D	+03:32:17.946	+30:49:46.30	424	49 × 22	36	17.5	90.0	63.0	10.5	0.5
··· -E	+03:32:17.920	+30:49:48.19	153	76 × 58	24	162.5	56.6	39.9	5.9	1.4
Per-emb-5	+03:31:20.942	+30:45:30.19		331 × 215	6	30.4	2.2	49.5	57.4	176.2
NGC1333 IRAS2A -A	+03:28:55.575	+31:14:36.92		80 × 66	2	115.6	7.9	34.0	264.1	83.6
··· -B	+03:28:55.568	+31:14:36.31	185	63 × 35	4	17.0	4.0	55.8	66.3	10.9
Per-emb-17 -A	+03:27:39.112	+30:13:02.98		48 × 37	1	117.8	4.4	40.6	130.4	15.9

Table 5.C.1 continued on next page

Table 5.C.1 *(continued)*

Name	α (J2000)	δ (J2000)	Sep. (au)	$\sigma_{maj} \times \sigma_{min}$ a (mas × mas)	σ_{error} (mas)	PAa (°)	PA error (°)	i (°)	T_B (K)	Int. Intensity (mJy)
··· -B	+03:27:39.123	+30:13:02.73	84	99 × 52	3	158.5	2.5	58.6	32.2	8.2
Per-emb-18+ -A	+03:29:11.267	+31:18:30.99		62 × 36	10	63.4	16.2	54.3	30.4	5.7
··· -B	+03:29:11.260	+31:18:30.97	28	94 × 40	12	77.0	8.7	64.8	25.5	7.3
Per-emb-21+	+03:29:10.674	+31:18:20.09		50 × 47	2	83.1	26.1	21.8	85.4	15.9
Per-emb-22 -A	+03:25:22.417	+30:45:13.16		44 × 28	2	37.0	4.7	50.0	130.5	12.9
··· -B	+03:25:22.359	+30:45:13.08	227	18 × 15	2	13.7	52.5	33.4	74.8	4.0
L1448 IRS3B+ -A	+03:25:36.324	+30:45:14.81		32 × 12	8	27.1	12.5	68.6	54.3	3.3
··· -B	+03:25:36.318	+30:45:15.06	78	78 × 55	4	34.3	8.7	44.6	49.3	11.2
··· -C	+03:25:36.387	+30:45:14.64	248	193 × 168	4	44.0	7.1	29.2	54.5	76.1
L1448 IRS3A+	+03:25:36.502	+30:45:21.83		677 × 233	24	134.2	1.7	69.9	4.5	30.1
L1448 IRS3C -A	+03:25:35.675	+30:45:34.02		149 × 96	5	18.9	3.9	50.1	115.8	73.7
··· -B	+03:25:35.678	+30:45:34.26	72	72 × 43	16	17.9	37.0	53.4	79.6	13.7
Per-emb-35 -A	+03:28:37.097	+31:13:30.72		81 × 33	2	31.6	1.0	66.0	78.6	14.7

Table 5.C.1 continued on next page

Table 5.C.1 *(continued)*

Name	α	δ	Sep.	$\sigma_{maj} \times \sigma_{min}$ [a]	σ_{error}	PA[a]	PA error	i	T_B	Int. Intensity
	(J2000)	(J2000)	(au)	(mas × mas)	(mas)	(°)	(°)	(°)	(K)	(mJy)
··· -B	+03:28:37.225	+31:13:31.67	570	91 × 27	2	48.0	1.1	72.8	62.3	12.7
NGC1333 IRAS2B -A	+03:28:57.379	+31:14:15.67		163 × 97	2	104.3	1.1	53.7	126.1	100.6
··· -B	+03:28:57.373	+31:14:15.98	95	51 × 42	6	82.3	37.9	35.1	49.0	9.0
SVS13A+ -A	+03:29:03.772	+31:16:03.71		70 × 66	4	77.3	47.4	20.6	199.3	57.0
··· -B	+03:29:03.748	+31:16:03.73	92	146 × 120	5	70.6	9.4	35.1	102.8	85.3
SVS13A2+	+03:29:03.391	+31:16:01.53		49 × 33	7	4.7	23.1	48.2	59.0	8.6
SVS13B+	+03:29:03.085	+31:15:51.64		218 × 131	18	79.4	8.5	53.2	21.4	28.0

NOTE—The Gaussian image-plane fit results utilizing the CASA *imfit* routine. The sources were given estimates to begin the fitting routine but were otherwise not restricted by any bounding values.

NOTE—The separations (sep.) are given in units of au, which is derived based on the average distance to the Perseus molecular cloud of 300 pc.

[a]The values for PA are defined as the angle of the major axis, oriented east-of-north. The values for σ_{maj}, σ_{min}, and PA are deconvolved from the beam.

Table 5.C.2: 3 mm Image-plane Fitting Results

Name		RA	δ	Separation	$\sigma_{maj} \times \sigma_{min}$*a*	PA*a*		i	T_B	Int. Intensity
		(J2000)	(J2000)	(mas)	(mas × mas)	(°)	(°)		(K)	(mJy)
Per-emb-2	-A	+03:32:17.93	+30:49:47.73		108 × 48	26.4		63.3	16.2	0.7
···	-B	+03:32:17.94	+30:49:47.68	85	108 × 48	26.4		63.3	28.5	1.3
···	-C	+03:32:17.93	+30:49:47.34	393	152 × 82	114.2		57.1	17.2	3.1
···	-D	+03:32:17.92	+30:49:48.19	491	88 × 69	11.6		38.0	8.7	0.4
···	-E	+03:32:17.94	+30:49:46.32	1424	108 × 48	26.4		63.3	5.1	0.2
Per-emb-5		+03:31:20.94	+30:45:30.23		264 × 180	28.8		47.1	55.1	24.8
Per-emb-18	-A	+03:29:11.26	+31:18:31.04		34 × 16	97.1		62.3	24.7	1.0
···	-B	+03:29:11.26	+31:18:31.02	86	87 × 61	27.0		45.8	20.1	0.9
Per-emb-21		+03:29:10.67	+31:18:20.14		57 × 34	166.7		53.1	26.1	5.1

NOTE—The Gaussian image-plane fit results utilizing the CASA *imfit* routine. The sources were given estimates to begin the fitting routine but were otherwise not restricted by any bounding values.

[a]The values for PA are defined as the angle of the major axis, oriented east-of-north. The values for σ_{maj}, σ_{min}, and PA are deconvolved from the beam.

5.D. Comparison of Orientation Vectors

We determine the orientation vectors of each source via independent fitting of the image-plane using the CASA task *imfit* and by fitting 2-D multi-component Gaussians to the *uv*-plane. While the image-plane derived results do not differ significantly from the *uv*-plane results, for the marginally-resolved sources, the image-plane results are less reliable. This is because for marginally-resolved sources, the inherent shape of any recovered source will be nearly identical to the beam geometry, albeit this affect is mitigated in using the deconvolved values. We show the *uv*-plane and image-plane fit inclination and position angles in Figure 5.C.1. The two techniques are in good agreement within the observational uncertainties.

With the inclination and position angle of each of the companions within a system, we can determine the relative orientations of each of the sources. We compute the relative orientation pairs in a way consistent with the companion finding algorithm previously described by first comparing the most compact binaries within each system. For sources within a multi-body system which are not in a compact configuration, a source from the compact binary is chosen for comparison. Similar studies of synthetic simulations compared the orientation of the compact circumstellar disks against the known bound orbit of the constructed protostars (Bate, 2018). In our observations, for sources with a typical separation of > 50 au, the orbital time would be $>$300 years, thus the orbital parameters are not well constrained. While other observational studies compared outflow angles to the relative orientation of the larger filamentary structure (Stephens et al., 2017), it is known the outflow angles can be highly misaligned from the disk orientation axis (Offner et al., 2016; Ohashi et al., 2022).

One can conceive of several methods to determine relative orientation pairs and to verify our results, we explore these methods. For reference, we note the method carefully chosen in our analysis as the "primary" method. Other methods could include: computing a pairwise permutation (N choose 2 comparisons) of all sources ("A") or designate a particular protostar as a "primary" (perhaps the geometric center or most massive protostar if known) and compute every other source against this primary only once ("B"). The result of Method B is highly sensitive to which particular source is determined to be the "primary" and any resampling of the chosen binary would result in the same pairs as method A. The results presented in this

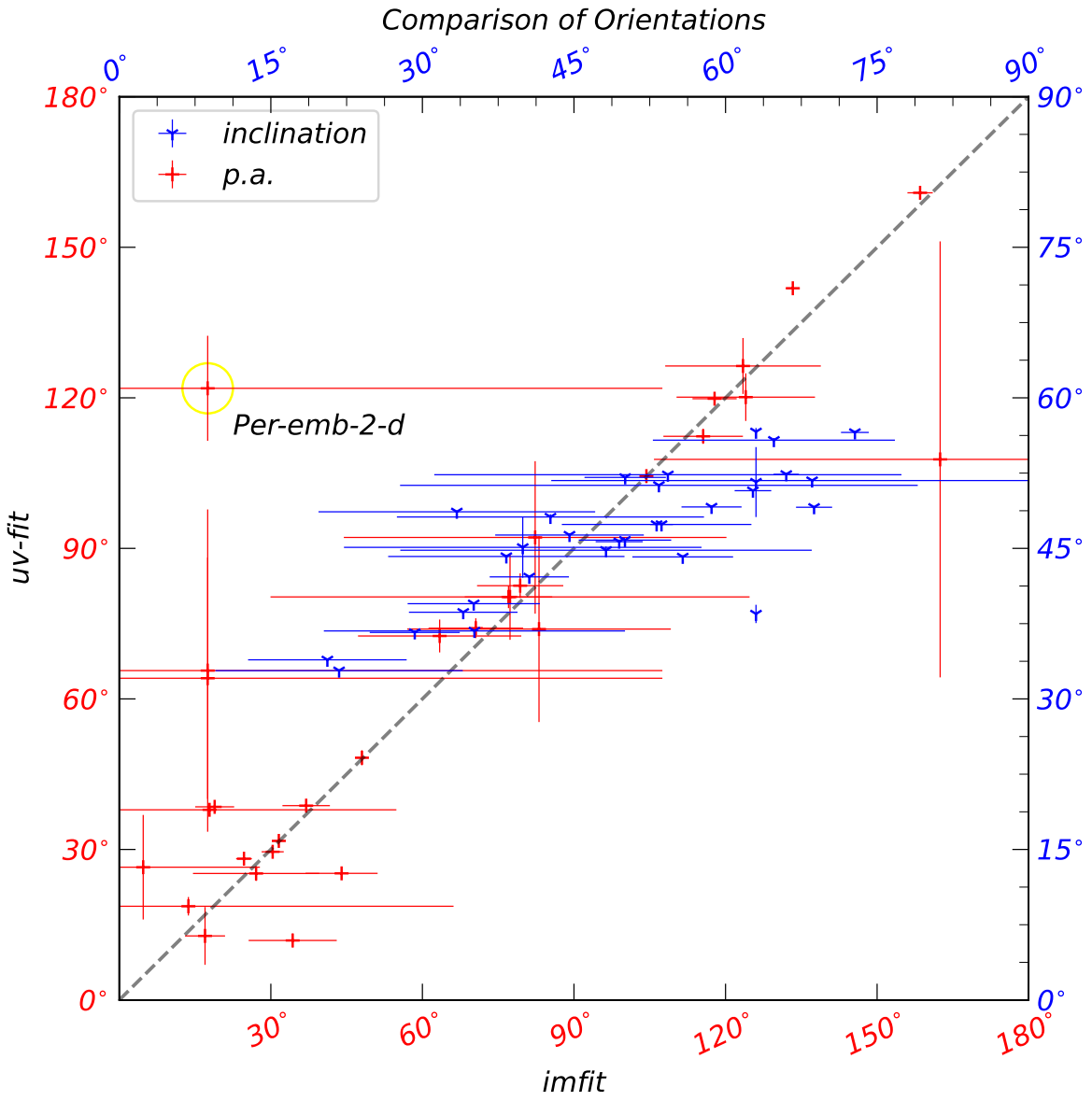

Figure 5.C.1: : Comparison of the *uv*-visibility fit and imfit derived inclination and position angle orientations for each of the sources. In the cyan, "Y" the inclination orientations are shown between 0°-90° and in the red "+", the position angle orientations are shown between 0°-180°. The respective errorbars for each fit are also shown, where the *uv*-visibility errors correspond to the isometric 1 σ average uncertainty in the posterior. The one-to-one line demonstrating the two fit methods return the same result is plot in black. There appears to be no clear systematic difference for the two fitting schema. The only significant outlier, Per-emb-2-d, is unresolved in these observations, so the imfit fit would be biased towards the beam geometry. The *uv*-visibility fit would be able to achieve higher resolution fits as compared to the image-plane fit, thus the *uv*-visibility fit is likely more consistent with the true compact disk orientation.

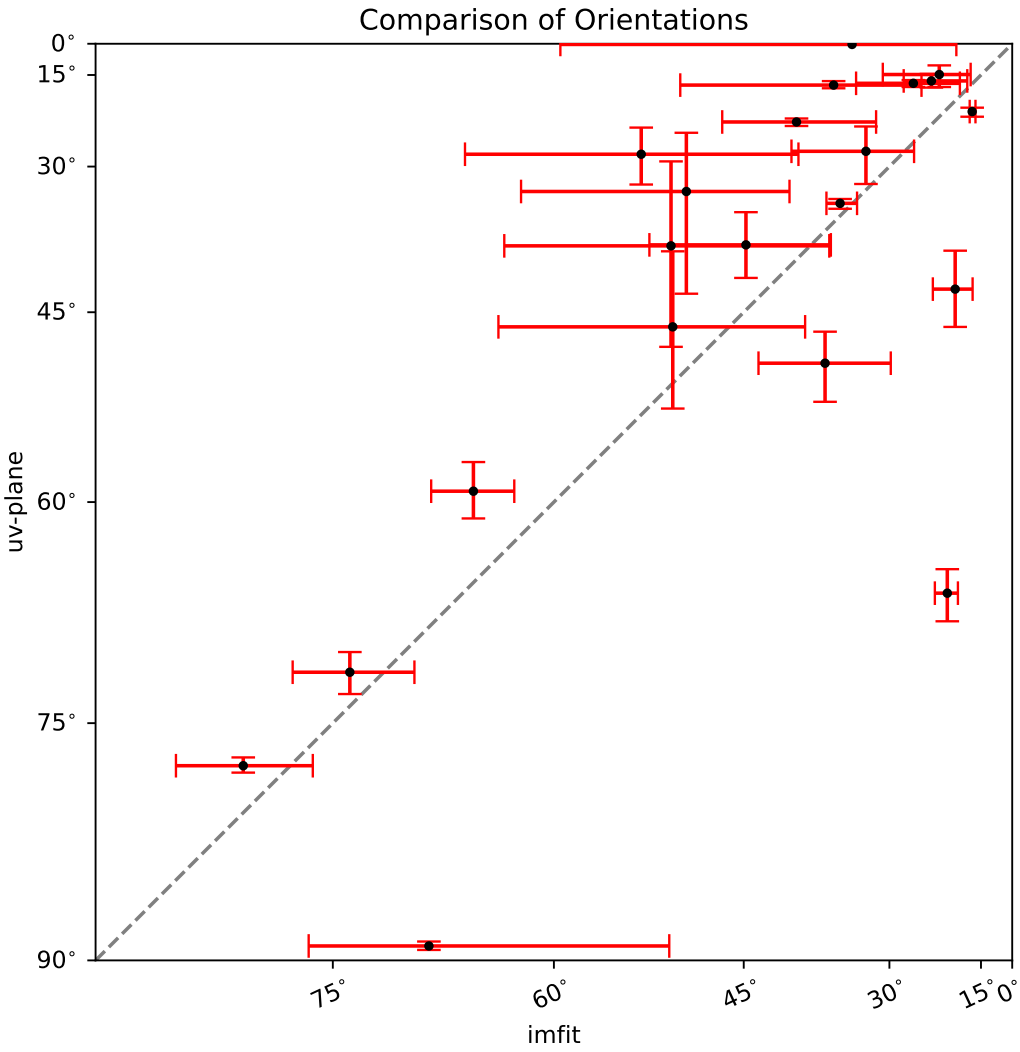

Figure 5.C.2: : Comparison of the uv-visibility fit and imfit derived dot-product orientations for each of the sources. The red errorbars represent the 32/68% confidence interval while the black points represent the median of the resampled distributions. for the The one-to-one line demonstrating the two fit methods return the same result is plot in black, with the upper left half corresponding to targets that appear more aligned with the uv-visibility fitting while the lower right half corresponding to targets that appear more aligned with the image-plane fitting. There appears to be no clear systematic difference for the two fit. The only outlier system L1448 IRS3C, fits higher position angle in the image-plane as compared to the uv-visibility. The uv-visibility fit would be able to achieve higher resolution fits as compared to the image-plane fit, thus the uv-visibility fit is likely more consistent with the true compact disk orientation.

work do not change significantly for each of the methods.

Given two unit vectors ($\vec{v}_1$ and $\vec{v}_2$), defined in spherical coordinates with the angles i (defined such that 0° is face-on) and *p.a.* (defined east-of-north), we can define the magnitude of the relative orientation (the dot product; $\vec{v}_1 \cdot \vec{v}_2$) of these two vectors as $\vec{v}_1 \cdot \vec{v}_2 = sin(i_1)sin(i_2)cos(p_1 - p_2) + cos(i_1)cos(i_2)$. Furthermore, with continuum-only detections at this resolution, we cannot differentiate the position angle of the disk from +180°. We also cannot differentiate if the disk is "face-on" versus "anti-face-on" (+90°), we normalize the inclinations to be 0-90° and normalize the position angles to be 0-180°.

We show a comparison of the derived orientations with the *uv*-plane and image-plane fitting techniques in Figure 5.C.2. The points are the median value of the resampled dot products when considering the observation and fitting uncertainties. The only source that stands out is L1448 IRS3A, which has elevated uncertainties due to restricting the *uv*-plane and image-plane fitting to only consider the larger scale structure of the ring.

We summarize our results in Table 5.D.1 which details the median separation and the median derived dot-product, considering observation uncertainties, for each of the companions. We also indicate if the particular pair is consistent with being aligned within 30° as a ✓ or if the system is not aligned as a "X".

Table 5.D.1: Comparison of Derived Dot-products

Source A	Source B	Separation (au)		Dot-product		Aligned (<30°)
		imfit	*uv*-plane	*imfit*	*uv*-plane	
L1448IRS1-a	L1448IRS1-b	$418^{0.08}_{0.08}$	$416^{0.14}_{0.14}$	$0.28^{0.07}_{0.06}$	$0.31^{0.03}_{0.03}$	X
L1448IRS3A	L1448IRS3B-a	$2215^{3.12}_{3.12}$	$2213^{0.02}_{0.02}$	$0.16^{0.08}_{0.07}$	$0.2^{0.01}_{0.01}$	X
	L1448IRS3B-b	$2151^{3.06}_{3.06}$	$2149^{0.02}_{0.02}$	$0.14^{0.04}_{0.05}$	$0.21^{0.01}_{0.01}$	X
	L1448IRS3B-c	$2201^{2.98}_{2.98}$	$2196^{0.03}_{0.03}$	$0.3^{0.03}_{0.03}$	$0.15^{0.00}_{0.00}$	X
	L1448IRS3C-a	$4858^{3.04}_{3.04}$	$4874^{0.06}_{0.06}$	$0.08^{0.03}_{0.02}$	$0.02^{0.00}_{0.00}$	X
	L1448IRS3C-b	$4904^{2.18}_{2.18}$	$4920^{0.05}_{0.05}$	$0.36^{0.26}_{0.13}$	$0.02^{0.00}_{0.00}$	X
L1448IRS3B-a	L1448IRS3B-b	$78^{0.08}_{0.08}$	$78^{0.01}_{0.01}$	$0.89^{0.05}_{0.06}$	$0.96^{0.00}_{0.00}$	✓
	L1448IRS3B-c	$248^{0.34}_{0.34}$	$247^{0.02}_{0.02}$	$0.76^{0.09}_{0.08}$	$0.82^{0.01}_{0.01}$	X
	L1448IRS3C-a	$6285^{0.36}_{0.36}$	$6286^{0.07}_{0.07}$	$0.92^{0.04}_{0.04}$	$0.98^{0.00}_{0.00}$	✓
	L1448IRS3C-b	$6346^{1.45}_{1.45}$	$6347^{0.06}_{0.06}$	$0.75^{0.12}_{0.24}$	$0.98^{0.00}_{0.00}$	✓
L1448IRS3B-b	L1448IRS3B-c	$292^{0.12}_{0.12}$	$290^{0.03}_{0.03}$	$0.96^{0.01}_{0.02}$	$0.92^{0.00}_{0.00}$	✓

Table 5.D.1 continued on next page

Table 5.D.1 *(continued)*

Source A	Source B	Separation (au)		Dot-product		Aligned (<30°)
		imfit	*uv*-plane	*imfit*	*uv*-plane	
	L1448IRS3C-a	$6208^{0.29}_{0.29}$	$6209^{0.07}_{0.07}$	$0.97^{0.01}_{0.01}$	$0.9^{0.00}_{0.00}$	✓
	L1448IRS3C-b	$6268^{1.38}_{1.38}$	$6269^{0.05}_{0.05}$	$0.86^{0.07}_{0.22}$	$0.91^{0.00}_{0.00}$	✓
L1448IRS3B-c	L1448IRS3C-a	$6431^{0.25}_{0.25}$	$6430^{0.02}_{0.02}$	$0.89^{0.01}_{0.01}$	$0.8^{0.00}_{0.00}$	X
	L1448IRS3C-b	$6490^{1.33}_{1.33}$	$6490^{0.01}_{0.01}$	$0.81^{0.07}_{0.16}$	$0.82^{0.00}_{0.00}$	X
L1448IRS3C-a	L1448IRS3C-b	$72^{1.15}_{1.15}$	$72^{0.01}_{0.01}$	$0.83^{0.11}_{0.32}$	$1.0^{0.00}_{0.00}$	✓
NGC1333IRAS2A-a	NGC1333IRAS2A-b	$185^{0.26}_{0.26}$	$186^{0.25}_{0.25}$	$0.41^{0.04}_{0.05}$	$0.52^{0.03}_{0.03}$	X
	NGC1333IRAS2B-a	$9424^{0.07}_{0.07}$	$9424^{0.02}_{0.02}$	$0.93^{0.01}_{0.01}$	$0.94^{0.00}_{0.00}$	✓
	NGC1333IRAS2B-b	$9346^{0.19}_{0.19}$	$9346^{0.19}_{0.19}$	$0.91^{0.03}_{0.06}$	$0.97^{0.01}_{0.02}$	✓
NGC1333IRAS2A-b	NGC1333IRAS2B-a	$9320^{0.18}_{0.18}$	$9320^{0.22}_{0.22}$	$0.37^{0.03}_{0.03}$	$0.4^{0.03}_{0.03}$	X
	NGC1333IRAS2B-b	$9243^{0.08}_{0.08}$	$9243^{0.06}_{0.06}$	$0.65^{0.12}_{0.11}$	$0.67^{0.05}_{0.04}$	X
NGC1333IRAS2B-a	NGC1333IRAS2B-b	$95^{0.23}_{0.23}$	$95^{0.16}_{0.16}$	$0.84^{0.05}_{0.08}$	$0.89^{0.03}_{0.04}$	X
Per-emb-17-a	Per-emb-17-b	$84^{0.35}_{0.35}$	$83^{0.08}_{0.08}$	$0.81^{0.02}_{0.01}$	$0.83^{0.01}_{0.01}$	X
Per-emb-18-a	Per-emb-18-b	$28^{0.45}_{0.45}$	$25^{0.09}_{0.09}$	$0.92^{0.03}_{0.06}$	$0.97^{0.01}_{0.01}$	✓

Table 5.D.1 continued on next page

Table 5.D.1 *(continued)*

Source A	Source B	Separation (au)		Dot-product		Aligned (<30°)
		imfit	*uv*-plane	*imfit*	*uv*-plane	
	Per-emb-21	$3987^{0.51}_{0.51}$	$3985^{0.12}_{0.12}$	$0.8^{0.07}_{0.07}$	$0.63^{0.04}_{0.04}$	X
Per-emb-18-b	Per-emb-21	$3966^{0.71}_{0.71}$	$3966^{0.17}_{0.17}$	$0.69^{0.05}_{0.06}$	$0.46^{0.05}_{0.04}$	X
Per-emb-2-a	Per-emb-2-b	$26^{0.46}_{0.46}$	$25^{0.57}_{0.57}$	$0.63^{0.17}_{0.18}$	$0.8^{0.08}_{0.12}$	X
	Per-emb-2-c	$126^{0.57}_{0.57}$	$129^{0.38}_{0.38}$	$0.63^{0.14}_{0.19}$	$0.6^{0.10}_{0.15}$	X
	Per-emb-2-d	$424^{0.17}_{0.17}$	$430^{0.61}_{0.61}$	$0.56^{0.21}_{0.19}$	$0.48^{0.15}_{0.13}$	X
	Per-emb-2-e	$153^{1.27}_{1.27}$	$150^{0.25}_{0.25}$	$0.64^{0.11}_{0.18}$	$0.69^{0.13}_{0.16}$	X
Per-emb-2-b	Per-emb-2-c	$103^{0.07}_{0.07}$	$109^{0.14}_{0.14}$	$0.65^{0.12}_{0.19}$	$0.68^{0.09}_{0.09}$	X
	Per-emb-2-d	$401^{0.36}_{0.36}$	$408^{0.09}_{0.09}$	$0.66^{0.14}_{0.23}$	$0.4^{0.12}_{0.08}$	X
	Per-emb-2-e	$178^{0.78}_{0.78}$	$174^{0.79}_{0.79}$	$0.58^{0.16}_{0.19}$	$0.79^{0.09}_{0.10}$	X
Per-emb-2-c	Per-emb-2-d	$299^{0.44}_{0.44}$	$300^{0.23}_{0.23}$	$0.68^{0.12}_{0.16}$	$0.89^{0.03}_{0.02}$	X
	Per-emb-2-e	$276^{0.69}_{0.69}$	$278^{0.64}_{0.64}$	$0.8^{0.08}_{0.11}$	$0.84^{0.08}_{0.12}$	X
Per-emb-2-d	Per-emb-2-e	$575^{1.1}_{1.1}$	$578^{0.87}_{0.87}$	$0.6^{0.17}_{0.19}$	$0.66^{0.14}_{0.14}$	X
Per-emb-22-a	Per-emb-22-b	$227^{0.04}_{0.04}$	$227^{0.04}_{0.04}$	$0.81^{0.10}_{0.17}$	$0.95^{0.00}_{0.00}$	✓

Table 5.D.1 continued on next page

Table 5.D.1 *(continued)*

Source A	Source B	Separation (au)		Dot-product		Aligned (<30°)
		imfit	*uv*-plane	*imfit*	*uv*-plane	
Per-emb-35-a	Per-emb-35-b	$570^{0.06}_{0.06}$	$570^{0.48}_{0.48}$	$0.96^{0.00}_{0.00}$	$0.93^{0.00}_{0.00}$	✓
SVS13A-a	SVS13A-b	$92^{0.32}_{0.32}$	$92^{0.07}_{0.07}$	$0.91^{0.04}_{0.03}$	$0.96^{0.01}_{0.01}$	✓
	SVS13A2	$1603^{0.14}_{0.14}$	$1603^{0.33}_{0.33}$	$0.73^{0.10}_{0.12}$	$0.78^{0.03}_{0.04}$	X
	SVS13B-a	$4483^{1.91}_{1.91}$	$4482^{0.88}_{0.88}$	$0.78^{0.06}_{0.08}$	$0.83^{0.02}_{0.02}$	X
SVS13A-b	SVS13A2	$1522^{0.24}_{0.24}$	$1522^{0.27}_{0.27}$	$0.71^{0.09}_{0.11}$	$0.84^{0.03}_{0.04}$	X
	SVS13B-a	$4433^{1.65}_{1.65}$	$4433^{0.82}_{0.82}$	$0.94^{0.02}_{0.02}$	$0.95^{0.01}_{0.01}$	✓
SVS13A2	SVS13B-a	$3190^{1.35}_{1.35}$	$3190^{0.41}_{0.41}$	$0.61^{0.08}_{0.10}$	$0.73^{0.04}_{0.04}$	X

NOTE—The separations are given in units of au, which is derived based on the average distance to the Perseus molecular cloud of 300 pc.

NOTE—Compiled comparison table between the *uv*-plane derived results and the image-plane derived results for each of the sources. The "source A" and "source B" columns correspond to each pair where the comparison was performed to derive the orientation vector correlations. Where "source A" is not listed, the previously listed "source A" is to be assumed. All separations are defined with respect to the "source A". The dot-product is given in cosine coordinates. The final column, "Aligned ($<30°$)" compares the derived dot-product values by averaging the two values and if the value corresponds to $<30°$, the sources are considered aligned, while values $>30°$ are considered misaligned.

Table 5.D.2: Model image-plane Fitting Statistics

Fractional Alignment	<100 au			<10,000 au			>500 au		
	$\%_{KS}$	$\%_{AD}$	$\%_{ES}$	$\%_{KS}$	$\%_{AD}$	$\%_{ES}$	$\%_{KS}$	$\%_{AD}$	$\%_{ES}$
$C_{1.00}$ $UC_{0.00}$	77.7	51.6	40.8	0.0	0.0	4.2	0.3	0.0	35.6
$C_{0.90}$ $UC_{0.10}$	95.8	98.6	16.8	0.9	0.1	10.6	18.2	5.8	55.0
$C_{0.80}$ $UC_{0.20}$	99.8	100.0	6.8	29.1	21.4	28.7	78.2	70.6	67.3
$C_{0.70}$ $UC_{0.30}$	100.0	100.0	5.0	95.6	97.0	73.6	99.9	100.0	87.6
$C_{0.60}$ $UC_{0.40}$	99.9	99.9	4.3	100.0	100.0	87.5	100.0	100.0	89.4
$C_{0.50}$ $UC_{0.50}$	98.1	99.5	3.8	98.5	99.6	86.5	98.6	99.7	84.9
$C_{0.40}$ $UC_{0.60}$	90.5	97.5	3.5	90.2	94.1	79.8	88.4	94.1	77.4
$C_{0.30}$ $UC_{0.70}$	80.4	86.9	3.3	67.6	67.3	67.5	64.0	62.7	64.2
$C_{0.20}$ $UC_{0.80}$	70.0	74.1	3.1	45.9	38.8	52.7	45.4	37.3	50.1
$C_{0.10}$ $UC_{0.90}$	62.1	62.6	2.9	32.6	21.2	41.3	33.9	21.6	41.0
$C_{0.00}$ $UC_{1.00}$	58.5	58.5	2.9	27.6	16.5	37.2	29.8	17.5	37.3

NOTE—Same as Table 5.D.2, except using the image-plane results from the deconvolved *imfit* task from CASA.

5.E. Statistical Tests

Across all scientific fields, many statistical tests have been used to test whether two independent empirical samples were drawn from the same underlying distribution. This procedure of testing the the distributions usually involves solving the inverted hypothesis, whether the "null hypothesis" can be rejected. The null hypothesis being that the two distributions are drawn from the same underlying distribution against the alternative hypothesis, that the two distribution are not drawn from the same underling distribution. If we reject the null hypothesis at some significance level, then we can confidently say the underlying distributions are not identical at that significance level. However, careful consideration is needed as proving the inverse is not necessarily proving the distributions are drawn from the same underlying population. That is to say if we cannot reject the null hypothesis in favor of the alternative, that simply means the underlying distributions are consistent with being drawn from the same distribution at a particular significance level, and does not state the two distributions themselves are identical.

The most well-known statistical test is the Kolmogorov–Smirnov test (KS test), in the case of k-samples, tests the empirical cumulative distribution functions (ECDFs) of each sample

against the null hypothesis that they were drawn from the same distribution (under the assumption one distribution is continuous). The KS test is sensitive to changes in the mass center and shape of the ECDF by computing the maximum difference of the distributions (higher sensitivity towards CDF center). The Anderson-Darling test (AD test) belongs to a family of quadratic rank tests and thus places more weight on the differences in the tails of the distributions. However, both the KS and AD tests assume the samples are drawn from continuous distributions and that the underlying distribution is stochastically larger than the drawn distribution. This is the so-called directional alternative hypothesis.

The Epps-Singleton test (ES test), is an empirical rank test that compares the characteristic functions (CFs) of the distributions, not the distributions themselves as compared to the KS and AD test. The test performs a quadratic form of differences between the CFs. The ES test is more powerful in that it does not assume the directional-alternative hypothesis or the continuous criteria, as it can be applied to discrete distributions. The primary prerequisite for the ES test, however, is the samples are fully independent, both across samples and within the samples (Epps & Singleton, 1986; Goerg & Kaiser, 2009), but otherwise is shown to provide a more robust statistical test.

For the purpose of our analysis, we apply all three tests, KS, AD, and ES test (as implemented in *scipy*), with k-samples, against the empirical distributions of the Perseus samples and the suites of mixture models. To satisfy the conditions of the KS and AD tests' directional alternative hypothesis and continuous prerequisite, we construct well-sampled models of 10,000 systems (each system comprised of at least 2 sources). To statistically characterize the observations, we resample all of the observation parameters (α, δ, σ_{major}, σ_{minor}, i, and *p.a.*) with Gaussian errors representative of the uncertainties of the observations 10,000 times. We then compute the statistic and probability for each of the KS, AD, and ES tests for every resample of the observations against every constructed distribution of fractional ratios. We finally compile the number of resampled distributions that cannot reject the null hypothesis at the 0.3% (3 σ) significance level and provide these numbers in Tables 5.5.1. This yields six numbers per mixture ratio suite that describes the number of distributions that cannot reject the null hypothesis.

5.F. Full Statistics

In Section 5.4.4, we discussed the statistics of the subsamples for separations <100 au, <10,000 au, and >500 au. Surveys of protostellar multiplicity (Tobin et al., 2016b, 2020; Encalada et al., 2021; Tobin et al., 2022) found the average separation of companions to be ∼75 au, thus we chose 100 au as the compact subsample. Since turbulent fragmentation can form on 1000s au scales and then migrate down to 100s au scales, we select scales >500 au to select the subsample with a different underlying distribution. However, our selection of subsample noticeably foregoes the sources that fall within the range of separations $100 < a < 500$ au. This selects out ∼13 source pairs. While performing such a selection cut reduces the overall number of sources included in the subsamples, the authors do not detect any major difference that would change the findings. This particular cut of $100 < a < 500$ au was chosen to ensure sources selected by the two subsamples < 100 au and >500 au would probe different underlying distributions, minimizing the overlap in these particular distributions, making the resulting statistical test more sensitive to differences in the underlying distributions.

CHAPTER 6

Summary and Conclusions

The results of this dissertation help provide crucial observational constraints to test theories of multiple star formation. Disks around Class II have been extensively studied but we need to understand how the disk formed to this point. I examined the properties and kinematics of isolated disks and proto-multiple disks, shedding light into the formation of protostellar disks. I will outline the specific results of each chapter in more detail.

Gravitational Instability in a Massive Disk

In this chapter, I presented high resolution observations at 879 μm, tracing the kinematics of the unique protostellar system, L1448 IRS3B and the wide ($\sim$2300 au) companion L1448 IRS3A. I observed the optically thin gas tracer $C^{17}O$ to determine the combined mass of the central potential to be 1.19 $M_\odot$. I also estimated the total mass of the disk to be $\sim$0.29 $M_\odot$ and further analyze the stability of the disk against gravitational fragmentation. When analyzing the Toomre Q parameter, which is a dimensionless quantity, relating the self-gravity against the localized sounds speed and the Keplerian velocities, I found that the disk is gravitationally unstable. This is also visually evident in the disk via the formation of spiral arms and several "clumps" (presumed protostars) found within the disk. I confirmed prior theories of formation for the system, with the compact ($<$500 au) companions of L1448 IRS3B having formed via gravitational instability and the wide companion (a$\sim$2,300 au), likely formed via turbulent collapse from the parent cloud.

Characterizing the Keplerian Disk of an Isolated Protostar

In this chapter, I performed observations at 1.3 mm towards an isolated, single protostar BHR7-mms. This protostar has yet to be characterized with a Keplerian disk and thus the mass of the protostar remains unconstrained. I performed several analyses along with robust modeling of $C^{18}O$ using radiative transfer codes in order to constrain the central protostar to be

1.18 $M_\odot$. From the observations, I estimated the total disk mass to be $\sim$0.26 $M_\odot$ from the dust continuum observations, which is consistent with the mass measurements given from the radiative transfer models. The circumstellar disk around BHR7-mms is quite large when compared to other protostellar objects ($\sim$470 au) and massive ($\sim$0.26 $M_\odot$). Due to the nearly edge-on nature of the source, substructures were not readily detected in the source, despite the high disk-to-star mass ratio and I found the Toomre Q parameter is $<$1.5. Thus it is likely the source is marginally gravitationally unstable, likely efficiently dispersing the envelope momentum from accretion.

Decoupling Infall and Rotation from the Envelope to the Disk

I continued my study of BHR7-mms, seeking to link the flow of angular momentum from large scales to the compact scales previously observed. I added additional analysis to prior observations at 1.3 mm, with molecules SO, N_2D+, and CO along with additional observations at 3 mm, with cold, dense gas tracers ^{13}CS, HNC, and N_2H+. I identified infall in the envelope and traced the infall of material from the envelope, down the cavity wall of the outflow, and down to the disk scale. I estimated the total material from the unresolved 3 mm observations to be $\sim$1.2 $M_\odot$, consistent with observations of other protostars where a majority of the mass is locked in the large scale envelope.

Formation Mechanisms of Protostellar Multiples

In this final chapter, I conducted a survey at very high resolution ($\sim$8 au) of 12 known Perseus protostellar multiples at 1.3 mm. I resolved 31 total sources within 10,000 au separations with the goal of constraining the relative disk orientation vectors with respect to the orbital plane between each of the sources to determine the most probable formation pathway. I found that our compact subsample of sources, with separations $<$ 100 au are most consistent with preferentially aligned distributions of angles $<$30°, and ruled out randomly aligned distributions. I found the wide companions ($>$500 au) were consistent with a distribution of randomly aligned sources. These differences are likely signatures of the formation pathways, where gravitational instabilities preferentially form close, aligned multiples, while turbulent fragmentation forms randomly aligned sources at originally large separations, that may undergo dynamical 3-body interactions to further decay or excite orbital changes. Tangentially,

through the high resolution observations, I discovered Per-emb-5, previously categorized as a compact binary, is actually a ring+spiral arm disk. These features are indicative of massive disk formation or unresolved multiple dynamical interactions and warrant follow up. I also discovered, from the same observations, L1448 IRS3B is likely a 4-star system, with a faintly detected (5 σ) central emission at the geometric center of the inner disk. This is consistent with the previously determined Keplerian centers and outflow launch locations.

6.1. Broader Impacts

In Chapter 2, I examined the L1448 IRS3B system in great detail, confirming gravitational instability as the most likely formation mechanism in a Class 0 source. This provides a critical testing ground for star and disk formation theory. In Chapter 5, I conducted a survey of well known protostellar multiples, to test a novel method for determining the most probable formation pathway. I used robust statistical tests to determine at which scales the disks are aligned/misaligned which helps us to understand how the multiple systems form. In Chapters 3 & 4, I focused on the isolated Class 0 source, BHR7-mms, to establish it as a prototypical Class 0 source. The source, through my analysis, is likely gravitationally unstable ($M_* \approx 1.2\ M_\odot$, $M_{disk} \approx 0.26\ M_\odot$), unless the disk has additional thermal support or is able to efficiently transport angular momentum away, providing a pristine source for testing non-ideal MHD theory.

Beyond the analysis in this dissertation, the data collected in these works still has significant scientific potential for future studies. The models performed in this work assumed single source protostars, with great care taken to reduce the complicated and entangled observations into the constituent sources. Additionally, most of the complex structures, while they give great insights into the dynamics of the systems, impose great computation complexity during modeling. More robust models are currently under development and simultaneous fitting of proto-multiple structures can be done.

6.2. Future Work

Despite the progress that is made, there remains significant open questions in the field that require additional follow up. Several discoveries have necessitated additional follow up surveys to constrain their physical conditions and to test current star formation theories. The high reso-

lution Perseus survey conducted demonstrated the need for larger sample sizes with multi-band, high resolution capabilities. Most notably, follow up surveys in the broader Perseus regions, Taurus (d≈150 pc), and Orion (d≈400 pc) molecular clouds will add clarity to the formation of protostellar multiples. Most importantly, the surveys would require resolutions to constrain the geometries of the individual sources and detect the large scale core structures. ALMA has been revolutionary to the field over the past decade, having vastly superior sensitivities compared to prior interferometers, and with additional improvements coming, it will continue to provide high-quality science. I will detail a few forthcoming papers and possible additional studies that could be done:

High Resolution Surveys: Kinematics

The primary method by which to determine the central mass of the protostellar systems is via Keplerian rotations and analysis of data cubes. However, to observe these products, ample telescope time is required and thus not many protostars have been observed with adequate sensitivity and resolution in order to fit the kinematics. I have conducted a survey of protostellar multiples (target list in Chapter 5) with high resolution observations of $C^{18}O$ (and a plethora of other molecules), a tracer for disk kinematics, in order to determine the central protostellar masses. While I have observed these systems with continuum observations and prior studies have been conducted on these systems, very little is known regarding the circum-multiple environment or the protostar parameters. I am performing a large suite of rigorous radiative transfer modeling using Bayesian inference to fit the central protostar masses. Individual fits require months to sample enough probability space to reach convergence, requiring on average 2,000,000 core-hours per source. I have several models underway currently and this survey will provide critical rigorous constraints. Furthermore from these observations, I can analyze the complex kinematic structures around the multiples.

High Resolution Surveys: Continuum

In Chapter 5, I discussed high resolution continuum observations of twelve known Perseus multiples, and described methods to determine particular formation pathways for the sample. Expanding upon this, in upcoming ALMA cycles, I proposed for additional follow up of additional Perseus and Orion protostellar multiples systems at high very resolution(< 8 au) to build

up a large sample of Class 0/I protostars with their circumstellar disk orientations characterized. Unbiased samples of the Orion molecular cloud and the Perseus molecular cloud, whose sources are thought to be at an earlier evolutionary stage than Orion, are crucial for building up our understanding of multiples. This will provide key insights into what dominant formation pathways exist in the cloud complexes and various filamentary structures.

Per-emb-5

Per-emb-5 was previously observed with VLA observations and detected to be a protostellar binary at close separations. However, with the high resolution and sensitivities, I resolved the protostar to be a compact ring structure and spiral arm feature. These disk features are indicative of gravitational instabilities and dynamical interactions with massive, embedded companions and has yet to be extensively studied. Protostellar systems, possibly at the onset of fragmentation such as this, are incredibly rare, with only a handful observed, and are crucial to understand. This system can provide constraints on disk characteristics prior to fragmentation taking place. Thus in upcoming cycles, I proposed for high resolution follow-up, targeting Per-emb-5, with a plethora of optically thin kinematic lines in order to characterize the system.

(Near) Protostellar Surface Properties: Surveys of Class 0/I Spectra

It is of critical importance to characterize the information regarding the compact, highly energetic circumstellar material around protostars. This material is what accretes onto the protostellar surface and the excess is what is carried away known as outflows. In general, it is accepted that compact-circumstellar gas is heated and ionized prior to and after reaching the stellar surface. This results in the characteristic hydrogen emission lines found in protostars. In particular, Connelley & Greene (2010); Laos et al. (2021), show that observations of the J, H, K-band spectra can give insight into Brγ (an accretion tracer), CO "comb" overtones (energetic winds/photosphere), and H_2 (outflow) emission. I conducted a large, multi-epoch survey of Class 0/I/II protostars across Perseus and Orion with the Triplespec instrument mounted on the 3.5-meter telescope at the Apache Pointe Observatory, New Mexico. Preliminary results show the Brγ line profiles are broad and centrally peaked, with FWHMs of $\sim$150 km s^{-1} and wings extending to $>$300km s^{-1}. In several sources I observed inverse P-Cygni profiles, indicative of accretion, wide band CO, indicative of extensive disk winds, and estimated the line ratios

of the H_2 emission features, which are consistent with shock excitations.

L1448 IRS3B

In particular, the source L1448 IRS3B (Chapters 2 for 879 μm and Section 5.A.1.0.8 for 1.3 mm) is truly a remarkable system and while extensive observations and analysis have taken place, many more advancements can be made. This source, which is composed of at least 3 sources within 500 au and one wide companion at $\sim$2,300 au, could have a central protostar consistent with 1.19 $M_\odot$. The strong presence of spiral arms is thought to provide efficient dust trapping mechanisms which has not been fully characterized for a system. This system alone provides a theory testing ground for chemical evolution, protostellar multiple formation at large and small scales, dust grain growth, disk accretion, and envelope evolution, each of which are a rich subfield of protostellars. Through this work, I have taken high resolution and sensitivity observations at 879 μm and 1.3 mm for this source, with a plethora of kinematic tracers, which can be utilized in part with additional longer wavelength observations to probe the various subfields listed.

References

Abt, H. A. 1983, ARA&A, 21, 343, doi: 10.1146/annurev.aa.21.090183.002015

Adams, F. C., Ruden, S. P., & Shu, F. H. 1989, ApJ, 347, 959, doi: 10.1086/168187

Allen, A. 2004, in Astronomical Society of the Pacific Conference Series, Vol. 323, Star Formation in the Interstellar Medium: In Honor of David Hollenbach, ed. D. Johnstone, F. C. Adams, D. N. C. Lin, D. A. Neufeeld, & E. C. Ostriker, 385

Allen, A., Li, Z.-Y., & Shu, F. H. 2003a, ApJ, 599, 363, doi: 10.1086/379243

Allen, A., Shu, F. H., & Li, Z.-Y. 2003b, ApJ, 599, 351, doi: 10.1086/379242

Alonso-Albi, T., Fuente, A., Crimier, N., et al. 2010, A&A, 518, A52, doi: 10.1051/0004-6361/201014317

Alves, J., Lombardi, M., & Lada, C. J. 2007, A&A, 462, L17, doi: 10.1051/0004-6361:20066389

André, P., Di Francesco, J., Ward-Thompson, D., et al. 2014, Protostars and Planets VI, 27, doi: 10.2458/azu_uapress_9780816531240-ch002

Andre, P., Ward-Thompson, D., & Barsony, M. 1993, ApJ, 406, 122, doi: 10.1086/172425

André, P., Men'shchikov, A., Bontemps, S., et al. 2010, A&A, 518, L102, doi: 10.1051/0004-6361/201014666

Andrews, S. M., Rosenfeld, K. A., Kraus, A. L., & Wilner, D. J. 2013, ApJ, 771, 129, doi: 10.1088/0004-637X/771/2/129

Andrews, S. M., Wilner, D. J., Hughes, A. M., Qi, C., & Dullemond, C. P. 2009, ApJ, 700, 1502, doi: 10.1088/0004-637X/700/2/1502

Andrews, S. M., Huang, J., Pérez, L. M., et al. 2018, ApJL, 869, L41, doi: 10.3847/2041-8213/aaf741

Ansdell, M., Williams, J. P., van der Marel, N., et al. 2016, ApJ, 828, 46, doi: 10.3847/0004-637X/828/1/46

Arce, H. G., & Sargent, A. I. 2006, ApJ, 646, 1070, doi: 10.1086/505104

Artymowicz, P., & Lubow, S. H. 1996, Lecture Notes in Physics, Berlin Springer Verlag, Vol. 465, Interaction of Young Binaries with Protostellar Disks (Springer), 115, doi: 10.1007/BFb0102630

Aso, Y., Ohashi, N., Saigo, K., et al. 2015, ApJ, 812, 27, doi: 10.1088/0004-637X/812/1/27

Astropy Collaboration, Robitaille, T. P., Tollerud, E. J., et al. 2013, A&A, 558, A33, doi: 10.1051/0004-6361/201322068

Baehr, H. 2023, MNRAS, 523, 3348, doi: 10.1093/mnras/stad1564

Bally, J., & Langer, W. D. 1982, ApJ, 255, 143, doi: 10.1086/159812

Bally, J., Stark, A. A., Wilson, R. W., & Henkel, C. 1987, ApJS, 65, 13, doi: 10.1086/191217

Bate, M. R. 1998, ApJL, 508, L95, doi: 10.1086/311719

—. 2000, MNRAS, 314, 33, doi: 10.1046/j.1365-8711.2000.03333.x

—. 2012, MNRAS, 419, 3115, doi: 10.1111/j.1365-2966.2011.19955.x

—. 2018, MNRAS, 475, 5618, doi: 10.1093/mnras/sty169

Bate, M. R., Bonnell, I. A., & Bromm, V. 2002, MNRAS, 336, 705, doi: 10.1046/j.1365-8711.2002.05775.x

Bate, M. R., Lodato, G., & Pringle, J. E. 2010, MNRAS, 401, 1505, doi: 10.1111/j.1365-2966.2009.15773.x

Beckwith, S. V. W., & Sargent, A. I. 1993, ApJ, 402, 280, doi: 10.1086/172131

Beckwith, S. V. W., Sargent, A. I., Chini, R. S., & Guesten, R. 1990, AJ, 99, 924, doi: 10.1086/115385

Benson, P. J., Caselli, P., & Myers, P. C. 1998, ApJ, 506, 743, doi: 10.1086/306276

Benson, P. J., & Myers, P. C. 1989, ApJS, 71, 89, doi: 10.1086/191365

Bergin, E. A., & Tafalla, M. 2007, ARA&A, 45, 339, doi: 10.1146/annurev.astro.45.071206.100404

Bianchi, E., López-Sepulcre, A., Ceccarelli, C., et al. 2022, ApJL, 928, L3, doi: 10.3847/2041-8213/ac5a56

Bodenheimer, P., Yorke, H. W., Rozyczka, M., & Tohline, J. E. 1990, ApJ, 355, 651, doi: 10.1086/168798

Bohlin, R. C. 1975, ApJ, 200, 402, doi: 10.1086/153803

Bohlin, R. C., Savage, B. D., & Drake, J. F. 1978a, ApJ, 224, 132, doi: 10.1086/156357

—. 1978b, ApJ, 224, 132, doi: 10.1086/156357

Boley, A. C. 2009, ApJL, 695, L53, doi: 10.1088/0004-637X/695/1/L53

Booth, A. S., & Ilee, J. D. 2020, MNRAS, 493, L108, doi: 10.1093/mnrasl/slaa014

Boss, A. P., & Keiser, S. A. 2013, ApJ, 764, 136, doi: 10.1088/0004-637X/764/2/136

Bourke, T. L., Hyland, A. R., & Robinson, G. 1995a, MNRAS, 276, 1052, doi: 10.1093/mnras/276.4.1052

Bourke, T. L., Hyland, A. R., Robinson, G., James, S. D., & Wright, C. M. 1995b, MNRAS, 276, 1067, doi: 10.1093/mnras/276.4.1067

Bracewell, R. N. 2000, The Fourier transform and its applications (Mcgraw-Hill)

Briggs, D. S. 1995a, PhD thesis, New Mexico Institute of Mining and Technology

Briggs, D. S. 1995b, in American Astronomical Society Meeting Abstracts, Vol. 187, American Astronomical Society Meeting Abstracts, 112.02

Brouw, W. N. 1975, Methods in Computational Physics, 14, 131, doi: 10.1016/B978-0-12-460814-6.50008-5

Bruderer, S. 2013, A&A, 559, A46, doi: 10.1051/0004-6361/201321171

Burns, R. A., Uno, Y., Sakai, N., et al. 2023, Nature Astronomy, doi: 10.1038/s41550-023-01899-w

Caselli, P., Benson, P. J., Myers, P. C., & Tafalla, M. 2002a, ApJ, 572, 238, doi: 10.1086/340195

Caselli, P., Hartquist, T. W., & Havnes, O. 1997, A&A, 322, 296

Caselli, P., Myers, P. C., & Thaddeus, P. 1995, ApJL, 455, L77, doi: 10.1086/309805

Caselli, P., Walmsley, C. M., Zucconi, A., et al. 2002b, ApJ, 565, 331, doi: 10.1086/324301

Cassen, P., & Moosman, A. 1981, Icarus, 48, 353, doi: 10.1016/0019-1035(81)90051-8

Cazaux, S., Caselli, P., Cobut, V., & Le Bourlot, J. 2008, A&A, 483, 495, doi: 10.1051/0004-6361:20078612

Chabrier, G. 2005, in Astrophysics and Space Science Library, Vol. 327, The Initial Mass Function 50 Years Later, ed. E. Corbelli, F. Palla, & H. Zinnecker, 41, doi: 10.1007/978-1-4020-3407-7_5

Chen, H., Myers, P. C., Ladd, E. F., & Wood, D. O. S. 1995a, ApJ, 445, 377, doi: 10.1086/175703

Chen, H., Zhao, J. H., & Ohashi, N. 1995b, ApJL, 450, L71, doi: 10.1086/316773

Chen, J.-H. 2010, PhD thesis, University of Texas, Austin

Chen, X., Launhardt, R., & Henning, T. 2007, ApJ, 669, 1058, doi: 10.1086/521868

Chen, X., Arce, H. G., Zhang, Q., et al. 2013, ApJ, 768, 110, doi: 10.1088/0004-637X/768/2/110

Clemens, D. P., & Barvainis, R. 1988, ApJS, 68, 257, doi: 10.1086/191288

Codella, C., Maury, A. J., Gueth, F., et al. 2014, A&A, 563, L3, doi: 10.1051/0004-6361/201323024

Condon, J. J., & Ransom, S. M. 2016, Essential Radio Astronomy (Princeton University Press)

Connelley, M. S., & Greene, T. P. 2010, The Astronomical Journal, 140, 1214, doi: 10.1088/0004-6256/140/5/1214

Connelley, M. S., Reipurth, B., & Tokunaga, A. T. 2008a, AJ, 135, 2526, doi: 10.1088/0004-6256/135/6/2526

—. 2008b, AJ, 135, 2496, doi: 10.1088/0004-6256/135/6/2496

Conway, J. E., Cornwell, T. J., & Wilkinson, P. N. 1990, MNRAS, 246, 490

Cornwell, T., & Fomalont, E. B. 1999, in Astronomical Society of the Pacific Conference Series, Vol. 180, Synthesis Imaging in Radio Astronomy II, ed. G. B. Taylor, C. L. Carilli, & R. A. Perley, 187

Cornwell, T. J. 2008, IEEE Journal of Selected Topics in Signal Processing, 2, 793, doi: 10.1109/JSTSP.2008.2006388

Cornwell, T. J., Golap, K., & Bhatnagar, S. 2008, IEEE Journal of Selected Topics in Signal Processing, 2, 647, doi: 10.1109/JSTSP.2008.2005290

Cornwell, T. J., Perley, R. A., & Aurass, H. 1995, Astronomische Nachrichten, 316, 170, doi: 10.1002/asna.2103160309

Crapsi, A., Devries, C. H., Huard, T. L., et al. 2005, A&A, 439, 1023, doi: 10.1051/0004-6361:20042411

Crutcher, R. M. 1999, ApJ, 520, 706, doi: 10.1086/307483

Currie, T., Lawson, K., Schneider, G., et al. 2022, Nature Astronomy, 6, 751, doi: 10.1038/s41550-022-01634-x

D'Angelo, G., & Lubow, S. H. 2008, ApJ, 685, 560, doi: 10.1086/590904

—. 2010, ApJ, 724, 730, doi: 10.1088/0004-637X/724/1/730

Dapp, W. B., Basu, S., & Kunz, M. W. 2012, A&A, 541, A35, doi: 10.1051/0004-6361/201117876

Dartois, E., Dutrey, A., & Guilloteau, S. 2003, A&A, 399, 773, doi: 10.1051/0004-6361:20021638

D'Hendecourt, L. B., Allamandola, L. J., & Greenberg, J. M. 1985, A&A, 152, 130

di Francesco, J., Evans, N. J., I., Caselli, P., et al. 2007, in Protostars and Planets V, ed. B. Reipurth, D. Jewitt, & K. Keil, 17, doi: 10.48550/arXiv.astro-ph/0602379

Diaz-Rodriguez, A. K., Anglada, G., Blázquez-Calero, G., et al. 2022, ApJ, 930, 91, doi: 10.3847/1538-4357/ac3b50

Duchêne, G., & Kraus, A. 2013, ARA&A, 51, 269, doi: 10.1146/annurev-astro-081710-102602

Dullemond, C. P., Juhasz, A., Pohl, A., et al. 2012, RADMC-3D: A multi-purpose radiative transfer tool, Astrophysics Source Code Library, record ascl:1202.015. http://ascl.net/1202.015

Dunham, M. M., Evans, Neal J., I., Terebey, S., Dullemond, C. P., & Young, C. H. 2010, ApJ, 710, 470, doi: 10.1088/0004-637X/710/1/470

Dunham, M. M., Vorobyov, E. I., & Arce, H. G. 2014, MNRAS, 444, 887, doi: 10.1093/mnras/stu1511

Dupuy, T. J., Kraus, A. L., Kratter, K. M., et al. 2022, MNRAS, 512, 648, doi: 10.1093/mnras/stac306

Duquennoy, A., & Mayor, M. 1991, A&A, 500, 337

Dutrey, A., Semenov, D., Chapillon, E., et al. 2014, in Protostars and Planets VI, ed. H. Beuther, R. S. Klessen, C. P. Dullemond, & T. Henning, 317–338, doi: 10.2458/azu_uapress_9780816531240-ch014

Encalada, F. J., Looney, L. W., Tobin, J. J., et al. 2021, ApJ, 913, 149, doi: 10.3847/1538-4357/abf4fd

Endres, C. P., Schlemmer, S., Schilke, P., Stutzki, J., & Müller, H. S. P. 2016, Journal of Molecular Spectroscopy, 327, 95, doi: 10.1016/j.jms.2016.03.005

Enoch, M. L., Evans, II, N. J., Sargent, A. I., & Glenn, J. 2009, ApJ, 692, 973, doi: 10.1088/0004-637X/692/2/973

Epps, T. W., & Singleton, K. J. 1986, Journal of Statistical Computation and Simulation, 26, 177–203

Evans, Neal J., I. 1999, ARA&A, 37, 311, doi: 10.1146/annurev.astro.37.1.311

Evans, Neal J., I., Dunham, M. M., Jørgensen, J. K., et al. 2009, ApJS, 181, 321, doi: 10.1088/0067-0049/181/2/321

Fedele, D., Tazzari, M., Booth, R., et al. 2018, A&A, 610, A24, doi: 10.1051/0004-6361/201731978

Feroz, F., Hobson, M. P., & Bridges, M. 2009, MNRAS, 398, 1601, doi: 10.1111/j.1365-2966.2009.14548.x

Fisher, R. T. 2004, ApJ, 600, 769, doi: 10.1086/380111

Foreman-Mackey, D., Hogg, D. W., Lang, D., & Goodman, J. 2013, PASP, 125, 306, doi: 10.1086/670067

Forveille, T., Guilloteau, S., &), R. 1989, CLASS: Continuum and Line Analysis Single-dish Software (IRAM). https://books.google.com/books?id=308dMQAACAAJ

Frerking, M. A., Langer, W. D., & Wilson, R. W. 1982, ApJ, 262, 590, doi: 10.1086/160451

Frey, S., & Mosoni, L. 2009, NewAR, 53, 307, doi: 10.1016/j.newar.2010.07.005

Frimann, S., Jørgensen, J. K., Dunham, M. M., et al. 2017, A&A, 602, A120, doi: 10.1051/0004-6361/201629739

Gammie, C. F. 2001, ApJ, 553, 174, doi: 10.1086/320631

Gerin, M., Pety, J., Commerçon, B., et al. 2017, A&A, 606, A35, doi: 10.1051/0004-6361/201630187

Ginsburg, A., Bally, J., Goddi, C., Plambeck, R., & Wright, M. 2018, ApJ, 860, 119, doi: 10.3847/1538-4357/aac205

Goerg, S. J., & Kaiser, J. 2009, The Stata Journal, 9, 454–465

Goldsmith, P. F., Bergin, E. A., & Lis, D. C. 1997, ApJ, 491, 615, doi: 10.1086/304986

Goldsmith, P. F., & Langer, W. D. 1999, ApJ, 517, 209, doi: 10.1086/307195

Goodman, A. A., Benson, P. J., Fuller, G. A., & Myers, P. C. 1993, ApJ, 406, 528, doi: 10.1086/172465

Green, J. D., Evans, Neal J., I., Jørgensen, J. K., et al. 2013, ApJ, 770, 123, doi: 10.1088/0004-637X/770/2/123

Green, S., Montgomery, J. A., J., & Thaddeus, P. 1974, ApJL, 193, L89, doi: 10.1086/181639

Greene, T. P., Wilking, B. A., Andre, P., Young, E. T., & Lada, C. J. 1994, ApJ, 434, 614, doi: 10.1086/174763

Hall, C., Dong, R., Teague, R., et al. 2020, ApJ, 904, 148, doi: 10.3847/1538-4357/abac17

Harris, C. R., Millman, K. J., van der Walt, S. J., et al. 2020, Nature, 585, 357, doi: 10.1038/s41586-020-2649-2

Hartley, M., Manchester, R. N., Smith, R. M., Tritton, S. B., & Goss, W. M. 1986, A&AS, 63, 27

Hartmann, L., Cassen, P., & Kenyon, S. J. 1997, ApJ, 475, 770, doi: 10.1086/303547

Hartmann, L., & Kenyon, S. J. 1996, ARA&A, 34, 207, doi: 10.1146/annurev.astro.34.1.207

Hasegawa, T. I., Herbst, E., & Leung, C. M. 1992, ApJS, 82, 167, doi: 10.1086/191713

Heimsoth, D. J., Stephens, I. W., Arce, H. G., et al. 2022, ApJ, 927, 88, doi: 10.3847/1538-4357/ac448e

Henning, T., & Semenov, D. 2013, Chemical Reviews, 113, 9016, doi: 10.1021/cr400128p

Herbst, E., & Klemperer, W. 1973, ApJ, 185, 505, doi: 10.1086/152436

Hildebrand, R. H. 1983, QJRAS, 24, 267

Hodges, J. J. 1958, Arkiv fiur Matematik, 3, 469

Högbom, J. A. 1974, A&AS, 15, 417

Horne, K., & Marsh, T. R. 1986, MNRAS, 218, 761, doi: 10.1093/mnras/218.4.761

Hsieh, T. H., Segura-Cox, D. M., Pineda, J. E., et al. 2023, A&A, 669, A137, doi: 10.1051/0004-6361/202244183

Hunter, J. D. 2007, Computing in Science & Engineering, 9, 90, doi: 10.1109/MCSE.2007.55

Hut, P., & Bahcall, J. N. 1983, ApJ, 268, 319, doi: 10.1086/160956

Inutsuka, S.-i., Inoue, T., Iwasaki, K., & Hosokawa, T. 2015, A&A, 580, A49, doi: 10.1051/0004-6361/201425584

Jennings, J., Booth, R. A., Tazzari, M., Clarke, C. J., & Rosotti, G. P. 2022a, MNRAS, 509, 2780, doi: 10.1093/mnras/stab3185

Jennings, J., Tazzari, M., Clarke, C. J., Booth, R. A., & Rosotti, G. P. 2022b, MNRAS, 514, 6053, doi: 10.1093/mnras/stac1770

Jennison, R. C. 1958, MNRAS, 118, 276, doi: 10.1093/mnras/118.3.276

Jensen, E. L. N., & Akeson, R. 2014, Nature, 511, 567, doi: 10.1038/nature13521

Jensen, E. L. N., Mathieu, R. D., Donar, A. X., & Dullighan, A. 2004, ApJ, 600, 789, doi: 10.1086/380089

Jørgensen, J. K., Bourke, T. L., Myers, P. C., et al. 2005, ApJ, 632, 973, doi: 10.1086/433181

Jørgensen, J. K., Johnstone, D., Kirk, H., & Myers, P. C. 2007, ApJ, 656, 293, doi: 10.1086/510150

Jørgensen, J. K., Kuruwita, R. L., Harsono, D., et al. 2022, Nature, 606, 272, doi: 10.1038/s41586-022-04659-4

Jørgensen, J. K., van Dishoeck, E. F., Visser, R., et al. 2009, A&A, 507, 861, doi: 10.1051/0004-6361/200912325

Jørgensen, J. K., van der Wiel, M. H. D., Coutens, A., et al. 2016, A&A, 595, A117, doi: 10.1051/0004-6361/201628648

Kenyon, S. J., Hartmann, L. W., Strom, K. M., & Strom, S. E. 1990, AJ, 99, 869, doi: 10.1086/115380

Keppler, M., Benisty, M., Müller, A., et al. 2018, A&A, 617, A44, doi: 10.1051/0004-6361/201832957

Kim, W.-T., & Ostriker, E. C. 2007, ApJ, 660, 1232, doi: 10.1086/513176

Kirk, H., Myers, P. C., Bourke, T. L., et al. 2013, ApJ, 766, 115, doi: 10.1088/0004-637X/766/2/115

Kratter, K., & Lodato, G. 2016, ARA&A, 54, 271, doi: 10.1146/annurev-astro-081915-023307

Kratter, K. M., & Matzner, C. D. 2006, MNRAS, 373, 1563, doi: 10.1111/j.1365-2966.2006.11103.x

Kratter, K. M., Matzner, C. D., Krumholz, M. R., & Klein, R. I. 2010a, ApJ, 708, 1585, doi: 10.1088/0004-637X/708/2/1585

Kratter, K. M., Murray-Clay, R. A., & Youdin, A. N. 2010b, ApJ, 710, 1375, doi: 10.1088/0004-637X/710/2/1375

Kristensen, L. E., & Dunham, M. M. 2018, ArXiv e-prints. https://arxiv.org/abs/1807.11262

Kryukova, E., Megeath, S. T., Gutermuth, R. A., et al. 2012, AJ, 144, 31, doi: 10.1088/0004-6256/144/2/31

Kwon, W., Looney, L. W., Mundy, L. G., Chiang, H.-F., & Kemball, A. J. 2009, ApJ, 696, 841, doi: 10.1088/0004-637X/696/1/841

Lada, C. J. 1987, in IAU Symposium, Vol. 115, Star Forming Regions, ed. M. Peimbert & J. Jugaku, 1–17

Lada, C. J., & Lada, E. A. 2003, ARA&A, 41, 57, doi: 10.1146/annurev.astro.41.011802.094844

Lada, C. J., & Wilking, B. A. 1984, ApJ, 287, 610, doi: 10.1086/162719

Laos, S., Greene, T. P., Najita, J. R., & Stassun, K. G. 2021, The Astrophysical Journal, 921, 110, doi: 10.3847/1538-4357/ac1f1b

Larson, R. B. 1969, MNRAS, 145, 271, doi: 10.1093/mnras/145.3.271

Lee, A. T., Offner, S. S. R., Kratter, K. M., Smullen, R. A., & Li, P. S. 2019a, ApJ, 887, 232, doi: https://doi.org/10.3847/1538-4357/ab584b

—. 2019b, ApJ, 887, 232, doi: 10.3847/1538-4357/ab584b

Lee, C.-F., Li, Z.-Y., Codella, C., et al. 2018, ApJ, 856, 14, doi: 10.3847/1538-4357/aaae6d

Lee, C. W., & Myers, P. C. 1999, ApJS, 123, 233, doi: 10.1086/313234

Lee, K. I., Dunham, M. M., Myers, P. C., et al. 2015, The Astrophysical Journal, 814, 114, doi: 10.1088/0004-637x/814/2/114

Lee, K. I., Dunham, M. M., Myers, P. C., et al. 2016, ApJL, 820, L2, doi: 10.3847/2041-8205/820/1/L2

Li, P. S., Klein, R. I., & McKee, C. F. 2016, in From Interstellar Clouds to Star-Forming Galaxies: Universal Processes?, ed. P. Jablonka, P. André, & F. van der Tak, Vol. 315, 103–106, doi: 10.1017/S1743921316007341

Lin, C. C., Mestel, L., & Shu, F. H. 1965, ApJ, 142, 1431, doi: 10.1086/148428

Lin, D. N. C., & Pringle, J. E. 1990, ApJ, 358, 515, doi: 10.1086/169004

Lis, D. C., Keene, J., Young, K., et al. 1997, Icarus, 130, 355, doi: 10.1006/icar.1997.5833

Liseau, R., Larsson, B., Lunttila, T., et al. 2015, A&A, 578, A131, doi: 10.1051/0004-6361/201525641

Lodders, K. 2003, ApJ, 591, 1220, doi: 10.1086/375492

Lombardi, M., Bouy, H., Alves, J., & Lada, C. J. 2014a, A&A, 566, A45, doi: 10.1051/0004-6361/201323293

—. 2014b, Herschel-Planck dust optical-depth and column-density maps (Corrigendum). I. Method description and results for Orion, Astronomy & Astrophysics, Volume 568, id.C1, 3 pp., doi: 10.1051/0004-6361/201323293e

Lynden-Bell, D., & Pringle, J. E. 1974, MNRAS, 168, 603, doi: 10.1093/mnras/168.3.603

Lynds, B. T. 1962, ApJS, 7, 1, doi: 10.1086/190072

Maret, S., Maury, A. J., Belloche, A., et al. 2020, A&A, 635, A15, doi: 10.1051/0004-6361/201936798

Mathieu, R. D. 1994, ARA&A, 32, 465, doi: 10.1146/annurev.aa.32.090194.002341

Maury, A. J., André, P., Hennebelle, P., et al. 2010, A&A, 512, A40, doi: 10.1051/0004-6361/200913492

Maury, A. J., André, P., Testi, L., et al. 2019, A&A, 621, A76, doi: 10.1051/0004-6361/201833537

McBride, A., & Kounkel, M. 2019, ApJ, 884, 6, doi: 10.3847/1538-4357/ab3df9

McKee, C. F., & Ostriker, E. C. 2007, ARA&A, 45, 565, doi: 10.1146/annurev.astro.45.051806.110602

McMullin, J. P., Waters, B., Schiebel, D., Young, W., & Golap, K. 2007, in Astronomical Society of the Pacific Conference Series, Vol. 376, Astronomical Data Analysis Software and Systems XVI, ed. R. A. Shaw, F. Hill, & D. J. Bell, 127

Mellon, R. R., & Li, Z.-Y. 2008, ApJ, 681, 1356, doi: 10.1086/587542

Mestel, L., & Spitzer, L., J. 1956, MNRAS, 116, 503, doi: 10.1093/mnras/116.5.503

Michelson, A. A., & Pease, F. G. 1921, ApJ, 53, 249, doi: 10.1086/142603

Miotello, A., Kamp, I., Birnstiel, T., Cleeves, L. I., & Kataoka, A. 2022, arXiv e-prints, arXiv:2203.09818, doi: 10.48550/arXiv.2203.09818

Moe, M., & Di Stefano, R. 2017, ApJS, 230, 15, doi: 10.3847/1538-4365/aa6fb6

Moeckel, N., & Bate, M. R. 2010, MNRAS, 404, 721, doi: 10.1111/j.1365-2966.2010.16347.x

Molinari, S., Swinyard, B., Bally, J., et al. 2010, A&A, 518, L100, doi: 10.1051/0004-6361/201014659

Müller, A., Keppler, M., Henning, T., et al. 2018, A&A, 617, L2, doi: 10.1051/0004-6361/201833584

Müller, H. S. P., Schlöder, F., Stutzki, J., & Winnewisser, G. 2005, Journal of Molecular Structure, 742, 215, doi: 10.1016/j.molstruc.2005.01.027

Müller, H. S. P., Thorwirth, S., Roth, D. A., & Winnewisser, G. 2001, A&A, 370, L49, doi: 10.1051/0004-6361:20010367

Murillo, N. M., van Dishoeck, E. F., Tobin, J. J., & Fedele, D. 2016, A&A, 592, A56, doi: 10.1051/0004-6361/201628247

Myers, P. C. 2009, ApJ, 700, 1609, doi: 10.1088/0004-637X/700/2/1609

Myers, P. C., Adams, F. C., Chen, H., & Schaff, E. 1998, ApJ, 492, 703, doi: 10.1086/305048

Myers, P. C., & Ladd, E. F. 1993, ApJL, 413, L47, doi: 10.1086/186956

Myers, P. C., Linke, R. A., & Benson, P. J. 1983, ApJ, 264, 517, doi: 10.1086/160619

Nakano, T., Nishi, R., & Umebayashi, T. 2002, ApJ, 573, 199, doi: 10.1086/340587

Nyquist, H. 1928, Transactions of the American Institute of Electrical Engineers, Volume 47, Issue 2, pp. 617-624, 47, 617, doi: 10.1109/T-AIEE.1928.5055024

Offner, S. S. R., & Arce, H. G. 2014, ApJ, 784, 61, doi: 10.1088/0004-637X/784/1/61

Offner, S. S. R., Dunham, M. M., Lee, K. I., Arce, H. G., & Fielding, D. B. 2016, The Astrophysical Journal, 827, L11, doi: 10.3847/2041-8205/827/1/l11

Offner, S. S. R., Kratter, K. M., Matzner, C. D., Krumholz, M. R., & Klein, R. I. 2010, ApJ, 725, 1485, doi: 10.1088/0004-637X/725/2/1485

Offner, S. S. R., Moe, M., Kratter, K. M., et al. 2022a, arXiv e-prints, arXiv:2203.10066. https://arxiv.org/abs/2203.10066

Offner, S. S. R., Taylor, J., Markey, C., et al. 2022b, MNRAS, 517, 885, doi: 10.1093/mnras/stac2734

Ohashi, S., Codella, C., Sakai, N., et al. 2022, The Astrophysical Journal, 927, 54, doi: 10.3847/1538-4357/ac4cae

Ortiz-León, G. N., Loinard, L., Dzib, S. A., et al. 2018, ArXiv e-prints. https://arxiv.org/abs/1808.03499

Ossenkopf, V., & Henning, T. 1994, A&A, 291, 943

Ostriker, E. C. 1999, ApJ, 513, 252, doi: 10.1086/306858

Padoan, P., & Nordlund, Å. 2004, ApJ, 617, 559, doi: 10.1086/345413

Papoular, R. 2005, MNRAS, 362, 489, doi: 10.1111/j.1365-2966.2005.09313.x

Pearson, T. J., & Readhead, A. C. S. 1984, ARA&A, 22, 97, doi: 10.1146/annurev.aa.22.090184.000525

Pérez, S., Casassus, S., & Benítez-Llambay, P. 2018, MNRAS, 480, L12, doi: 10.1093/mnrasl/sly109

Perez, S., Dunhill, A., Casassus, S., et al. 2015, ApJL, 811, L5, doi: 10.1088/2041-8205/811/1/L5

Pineda, J. E., Segura-Cox, D., Caselli, P., et al. 2020, Nature Astronomy, 4, 1158, doi: 10.1038/s41550-020-1150-z

Pinte, C., Ménard, F., Duchêne, G., et al. 2018a, A&A, 609, A47, doi: 10.1051/0004-6361/201731377

Pinte, C., Price, D. J., Ménard, F., et al. 2018b, ApJL, 860, L13, doi: 10.3847/2041-8213/aac6dc

Pinte, C., van der Plas, G., Ménard, F., et al. 2019a, Nature Astronomy, 3, 1109, doi: 10.1038/s41550-019-0852-6

—. 2019b, Nature Astronomy, 3, 1109, doi: 10.1038/s41550-019-0852-6

Pinte, C., Hammond, I., Price, D. J., et al. 2023, MNRAS, doi: 10.1093/mnrasl/slad010

Plunkett, A. L., Arce, H. G., Corder, S. A., et al. 2013, ApJ, 774, 22, doi: 10.1088/0004-637X/774/1/22

Plunkett, A. L., Arce, H. G., Mardones, D., et al. 2015, Nature, 527, 70, doi: 10.1038/nature15702

Price, N. M., & Podsiadlowski, P. 1995, MNRAS, 273, 1041, doi: 10.1093/mnras/273.4.1041

Price-Whelan, A. M., Sipőcz, B. M., Günther, H. M., et al. 2018, AJ, 156, 123, doi: 10.3847/1538-3881/aabc4f

Pudritz, R. E., & Wilson, C. 1996, JRASC, 90, 310

Raghavan, D., McAlister, H. A., Henry, T. J., et al. 2010a, ApJS, 190, 1, doi: 10.1088/0067-0049/190/1/1

—. 2010b, ApJS, 190, 1, doi: 10.1088/0067-0049/190/1/1

Rau, U., Bhatnagar, S., Voronkov, M. A., & Cornwell, T. J. 2009, IEEE Proceedings, 97, 1472, doi: 10.1109/JPROC.2009.2014853

Rau, U., & Cornwell, T. J. 2011, A&A, 532, A71, doi: 10.1051/0004-6361/201117104

Readhead, A. C. S., & Wilkinson, P. N. 1978, ApJ, 223, 25, doi: 10.1086/156232

Reipurth, B., & Mikkola, S. 2012, Nature, 492, 221, doi: 10.1038/nature11662

Reipurth, B., & Zinnecker, H. 1993, A&A, 278, 81

Reynolds, N. K., Tobin, J. J., Sheehan, P., et al. 2021, ApJL, 907, L10, doi: 10.3847/2041-8213/abcc02

Reynolds, N. K., Tobin, J. J., Bos, S. P., et al. 2023 subm., ApJ

Rodríguez, L. F., Anglada, G., & Curiel, S. 1999, ApJS, 125, 427, doi: 10.1086/313283

Rosenfeld, K. A., Andrews, S. M., Hughes, A. M., Wilner, D. J., & Qi, C. 2013, ApJ, 774, 16, doi: 10.1088/0004-637X/774/1/16

Sadavoy, S. I. 2013, PhD thesis, University of Victoria

Sadavoy, S. I., & Stahler, S. W. 2017, MNRAS, 469, 3881, doi: 10.1093/mnras/stx1061

Sadavoy, S. I., Di Francesco, J., André, P., et al. 2014, ApJL, 787, L18, doi: 10.1088/2041-8205/787/2/L18

Safron, E. J., Fischer, W. J., Megeath, S. T., et al. 2015, ApJL, 800, L5, doi: 10.1088/2041-8205/800/1/L5

Sai, J., Ohashi, N., Saigo, K., et al. 2020, ApJ, 893, 51, doi: 10.3847/1538-4357/ab8065

Sakai, N., Oya, Y., Sakai, T., et al. 2014, ApJL, 791, L38, doi: 10.1088/2041-8205/791/2/L38

Scholz, A., Wood, K., Wilner, D., et al. 2010, MNRAS, 409, 1557, doi: 10.1111/j.1365-2966.2010.17397.x

Scholz, F. W., & Stephens, M. A. 1987, Journal of the American Statistical Association, 82, 918

Segura-Cox, D. M., Looney, L. W., Tobin, J. J., et al. 2018, ApJ, 866, 161, doi: 10.3847/1538-4357/aaddf3

Segura-Cox, D. M., Schmiedeke, A., Pineda, J. E., et al. 2020, Nature, 586, 228, doi: 10.1038/s41586-020-2779-6

Seifried, D., Sánchez-Monge, Á., Walch, S., & Banerjee, R. 2016, MNRAS, 459, 1892, doi: 10.1093/mnras/stw785

Sheehan, P. 2022, pdspy: MCMC tool for continuum and spectral line radiative transfer modeling, Astrophysics Source Code Library, record ascl:2207.026. http://ascl.net/2207.026

Sheehan, P. D., & Eisner, J. A. 2017a, ApJL, 840, L12, doi: 10.3847/2041-8213/aa6df8

—. 2017b, ApJ, 851, 45, doi: 10.3847/1538-4357/aa9990

Sheehan, P. D., Wu, Y.-L., Eisner, J. A., & Tobin, J. J. 2019, ApJ, 874, 136, doi: 10.3847/1538-4357/ab09f9

Shu, F. H., Adams, F. C., & Lizano, S. 1987, ARA&A, 25, 23, doi: 10.1146/annurev.aa.25.090187.000323

Sierra, A., & Lizano, S. 2020, ApJ, 892, 136, doi: 10.3847/1538-4357/ab7d32

Skilling, J. 2004, in American Institute of Physics Conference Series, Vol. 735, Bayesian Inference and Maximum Entropy Methods in Science and Engineering: 24th International Workshop on Bayesian Inference and Maximum Entropy Methods in Science and Engineering, ed. R. Fischer, R. Preuss, & U. V. Toussaint, 395–405, doi: 10.1063/1.1835238

Speagle, J. S. 2020, MNRAS, 493, 3132, doi: 10.1093/mnras/staa278

Spitzer, L., J., & Jenkins, E. B. 1975, ARA&A, 13, 133, doi: 10.1146/annurev.aa.13.090175.001025

Srama, R., Stephan, T., Grün, E., et al. 2009a, Experimental Astronomy, 23, doi: 10.1007/s10686-008-9088-7

—. 2009b, Experimental Astronomy, 23, doi: 10.1007/s10686-008-9088-7

Sramek, R. A., & Schwab, F. R. 1989, in Astronomical Society of the Pacific Conference Series, Vol. 6, Synthesis Imaging in Radio Astronomy, ed. R. A. Perley, F. R. Schwab, & A. H. Bridle, 83

Stamatellos, D., & Whitworth, A. P. 2009, MNRAS, 392, 413, doi: 10.1111/j.1365-2966.2008.14069.x

Stephens, I. W., Dunham, M. M., Myers, P. C., et al. 2017, ApJ, 846, 16, doi: 10.3847/1538-4357/aa8262

—. 2018, ApJS, 237, 22, doi: 10.3847/1538-4365/aacda9

Tabone, B., Cabrit, S., Bianchi, E., et al. 2017, A&A, 607, L6, doi: 10.1051/0004-6361/201731691

Tazzari, M., Beaujean, F., & Testi, L. 2018, MNRAS, 476, 4527, doi: 10.1093/mnras/sty409

Terebey, S., Shu, F. H., & Cassen, P. 1984, ApJ, 286, 529, doi: 10.1086/162628

Thomas, H. S., & Fuller, G. A. 2008, A&A, 479, 751, doi: 10.1051/0004-6361:20066499

Thompson, A. R., Moran, J. M., & Swenson, G. W. 2017, Van Cittert–Zernike Theorem, Spatial Coherence, and Scattering (Cham: Springer International Publishing), 767–786, doi: 10.1007/978-3-319-44431-4_15

Tobin, J. J. 2011, PhD thesis, University of Michigan

Tobin, J. J., Bos, S. P., Dunham, M. M., Bourke, T. L., & van der Marel, N. 2018a, ApJ, 856, 164, doi: 10.3847/1538-4357/aaafc7

Tobin, J. J., Hartmann, L., Chiang, H.-F., et al. 2012, Nature, 492, 83, doi: 10.1038/nature11610

—. 2013, ApJ, 771, 48, doi: 10.1088/0004-637X/771/1/48

Tobin, J. J., Dunham, M. M., Looney, L. W., et al. 2015a, ApJ, 798, 61, doi: 10.1088/0004-637X/798/1/61

Tobin, J. J., Looney, L. W., Wilner, D. J., et al. 2015b, ApJ, 805, 125, doi: 10.1088/0004-637X/805/2/125

Tobin, J. J., Kratter, K. M., Persson, M. V., et al. 2016a, Nature, 538, 483, doi: 10.1038/nature20094

Tobin, J. J., Looney, L. W., Li, Z.-Y., et al. 2016b, ApJ, 818, 73, doi: 10.3847/0004-637X/818/1/73

—. 2018b, ApJ, 867, 43, doi: 10.3847/1538-4357/aae1f7

Tobin, J. J., Megeath, S. T., van't Hoff, M., et al. 2019, ApJ, 886, 6, doi: 10.3847/1538-4357/ab498f

Tobin, J. J., Sheehan, P. D., Megeath, S. T., et al. 2020, ApJ, 890, 130, doi: 10.3847/1538-4357/ab6f64

Tobin, J. J., Offner, S. S. R., Kratter, K. M., et al. 2022, ApJ, 925, 39, doi: 10.3847/1538-4357/ac36d2

Tohline, J. E. 2002, ARA&A, 40, 349, doi: 10.1146/annurev.astro.40.060401.093810

Troland, T. H., & Crutcher, R. M. 2008, ApJ, 680, 457, doi: 10.1086/587546

Tsukamoto, Y., Iwasaki, K., Okuzumi, S., Machida, M. N., & Inutsuka, S. 2015, MNRAS, 452, 278, doi: 10.1093/mnras/stv1290

Turner, B. E. 1974, ApJL, 193, L83, doi: 10.1086/181638

Tychoniec, Ł., Tobin, J. J., Karska, A., et al. 2018, ApJS, 238, 19, doi: 10.3847/1538-4365/aaceae

van der Marel, N. 2015, PhD thesis, University of Leiden, Netherlands

van Dishoeck, E. F., & Black, J. H. 1988, ApJ, 334, 771, doi: 10.1086/166877

van Dishoeck, E. F., & Blake, G. A. 1998, ARA&A, 36, 317, doi: 10.1146/annurev.astro.36.1.317

Van Rossum, G., & Drake Jr, F. L. 1995, Python tutorial (Centrum voor Wiskunde en Informatica Amsterdam, The Netherlands)

van 't Hoff, M. L. R. 2019, PhD thesis, University of Leiden, Netherlands

van 't Hoff, M. L. R., Bergin, E. A., Jørgensen, J. K., & Blake, G. A. 2020, ApJL, 897, L38, doi: 10.3847/2041-8213/ab9f97

van 't Hoff, M. L. R., Tobin, J. J., Harsono, D., & van Dishoeck, E. F. 2018, IAU Symposium, 332, 121, doi: 10.1017/S1743921317007876

van Zadelhoff, G. J., van Dishoeck, E. F., Thi, W. F., & Blake, G. A. 2001, A&A, 377, 566, doi: 10.1051/0004-6361:20011137

Virtanen, P., Gommers, R., Oliphant, T. E., et al. 2020, Nature Methods, 17, 261, doi: 10.1038/s41592-019-0686-2

Visser, R., van Dishoeck, E. F., & Black, J. H. 2009, A&A, 503, 323, doi: 10.1051/0004-6361/200912129

Vorobyov, E. I., & Basu, S. 2011, in IAU Symposium, Vol. 276, The Astrophysics of Planetary Systems: Formation, Structure, and Dynamical Evolution, ed. A. Sozzetti, M. G. Lattanzi, & A. P. Boss, 463–464, doi: 10.1017/S1743921311020813

Vorobyov, E. I., & Elbakyan, V. G. 2018, A&A, 618, A7, doi: 10.1051/0004-6361/201833226

—. 2019, A&A, 631, A1, doi: 10.1051/0004-6361/201936132

Vorobyov, E. I., Zakhozhay, O. V., & Dunham, M. M. 2013, MNRAS, 433, 3256, doi: 10.1093/mnras/stt970

Ward-Thompson, D., Scott, P. F., Hills, R. E., & Andre, P. 1994, MNRAS, 268, 276, doi: 10.1093/mnras/268.1.276

Ward-Thompson, D., Di Francesco, J., Hatchell, J., et al. 2007, PASP, 119, 855, doi: 10.1086/521277

Weaver, E., Isella, A., & Boehler, Y. 2018, ApJ, 853, 113, doi: 10.3847/1538-4357/aaa481

Whitney, B. A., Wood, K., Bjorkman, J. E., & Wolff, M. J. 2003, ApJ, 591, 1049, doi: 10.1086/375415

Wilkin, F. P., & Stahler, S. W. 1998, ApJ, 502, 661, doi: 10.1086/305948

Wilkinson, P. 1990, The Observatory, 110, 98

Wilkinson, P. N. 1989, in NATO Advanced Study Institute (ASI) Series C, Vol. 283, Techniques and Applications of Very Long Baseline Interferometry, ed. M. Felli & R. E. Spencer, 69–93, doi: 10.1007/978-94-009-2428-4_1

Williams, J. P., & Best, W. M. J. 2014, ApJ, 788, 59, doi: 10.1088/0004-637X/788/1/59

Williams, J. P., & Cieza, L. A. 2011, ARA&A, 49, 67, doi: 10.1146/annurev-astro-081710-102548

Williams, J. P., & McKee, C. F. 1997, ApJ, 476, 166, doi: 10.1086/303588

Wilner, D. J., Ho, P. T. P., Kastner, J. H., & Rodríguez, L. F. 2000, ApJL, 534, L101, doi: 10.1086/312642

Wilson, C. D., Walker, C. E., & Thornley, M. D. 1997, ApJ, 483, 210, doi: 10.1086/304216

Wilson, T. L., Rohlfs, K., & Hüttemeister, S. 2009, Tools of Radio Astronomy (Springer), doi: 10.1007/978-3-540-85122-6

Wilson, T. L., & Rood, R. 1994, ARA&A, 32, 191, doi: 10.1146/annurev.aa.32.090194.001203

Woermann, B., Gaylard, M. J., & Otrupcek, R. 2001, MNRAS, 325, 1213, doi: 10.1046/j.1365-8711.2001.04558.x

Womack, M., Ziurys, L. M., & Wyckoff, S. 1992, ApJ, 387, 417, doi: 10.1086/171094

Worley, C. E. 1962, AJ, 67, 590, doi: 10.1086/108886

Yen, H.-W., Koch, P. M., Takakuwa, S., et al. 2015, ApJ, 799, 193, doi: 10.1088/0004-637X/799/2/193

—. 2017, ApJ, 834, 178, doi: 10.3847/1538-4357/834/2/178

Yen, H.-W., Takakuwa, S., & Ohashi, N. 2011, ApJ, 742, 57, doi: 10.1088/0004-637X/742/1/57

Yen, H.-W., Takakuwa, S., Ohashi, N., et al. 2014, ApJ, 793, 1, doi: 10.1088/0004-637X/793/1/1

Yorke, H. W., & Bodenheimer, P. 1999, ApJ, 525, 330, doi: 10.1086/307867

Young, C. H., & Evans, Neal J., I. 2005, ApJ, 627, 293, doi: 10.1086/430436

Zhu, Z., Zhang, S., Jiang, Y.-F., et al. 2019, ApJL, 877, L18, doi: 10.3847/2041-8213/ab1f8c

Zucker, C., Speagle, J. S., Schlafly, E. F., et al. 2019, ApJ, 879, 125, doi: 10.3847/1538-4357/ab2388